Spring 2018

Aerogels for energy storage applications: From shape memory materials to thermites and explosives

Suraj Donthula

Department: Chemistry

AEROGELS FOR ENERGY STORAGE APPLICATIONS:

FROM SHAPE MEMORY MATERIALS TO THERMITES AND EXPLOSIVES

by

SURAJ DONTHULA

A DISSERTATION

Presented to the Faculty of the Graduate School of the

MISSOURI UNIVERSITY OF SCIENCE AND TECHNOLOGY

In Partial Fulfillment of the Requirements for the Degree

DOCTOR OF PHILOSOPHY

in

CHEMISTRY

2018

Approved

Dr. Nicholas Leventis, Advisor
Dr. Chariklia Sotiriou-Leventis, Co-Advisor
Dr. Amitava Choudhury
Dr. Manashi Nath
Dr. Xinhua Liang

TO

MY PARENTS

Shri. SURESH DONTHULA

Smt. UMA DEVI DONTHULA

&

MY BELOVED WIFE

CHANDANA MANDAL

PUBLICATION DISSERTATION OPTION

This dissertation consists of the following three manuscripts that have been published or submitted for publication:

Paper I, pages 33-109, was published in *Chemistry of Materials*

Paper II, pages 110-187, was submitted in *Applied Materials and Interfaces*

Paper III, pages 188-231, was published in *Chemistry of Materials*

ABSTRACT

Aerogels are three dimensional highly porous solid objects that provide density reduction compared to dense objects. Those materials can have applications in different classes of energy storage and the two types that are focused in this dissertation are mechanical energy and thermal energy storage. Shape memory materials can store and recover elastic deformation energy when triggered by an external stimulus such as temperature. To incorporate those properties, shape memory polymeric aerogels (SMPA) were synthesized from a rigid isocyanurate containing triisocyanate (N3300 A) and four short oligomeric derivatives of ethylene glycol: $H(OCH_2CH_2)_nOH$ ($1 \leq n \leq 4$). The shape memory effect (SME) of those aerogels were evaluated via four figures of merit namely strain fixity, strain recovery, strain recovery rate and fill factor. The morphologies of skeletal frameworks of those aerogels varied from micrometer sized particles with thick necks to bicontinuous structures, that are typical of spinodal decomposition. A Marcus-type thermodynamic-kinetic relationship was identified between that shape recovery rate, $R_t(N)$, and the elastic modulus, E. Other part of the dissertation deals with the synthesis of nanoporous metallic iron (Fe(0)) aerogels via carbothermal reduction of interpenetrating networks of polybenzoxazine and iron oxide nanoparticles. Excess carbon was removed oxidatively at 600 ^oC under flowing air and the oxides of Fe(0) thus produced in the oxidative step were reduced back to Fe(0) with H_2 at different temperatures ranging from 300 - 1300 ^oC. Those final monoliths were loaded with perchlorates and ignited with a flame in open air. Based on the temperature of the reduction step, monoliths either fizzled out ($\leq$400 ^oC), exploded violently (500-900 ^oC), or behaved as thermites ($\geq$950 ^oC).

ACKNOWLEDGEMENTS

I would like to express my sincere gratitude to my advisor, Prof. Nicholas Leventis and co-advisor Prof. Chariklia Sotiriou-Leventis for their support, patience, and encouragement throughout my graduate studies. Prof. Nicholas Leventis is someone you will instantly love with his good grace and spontaneity and I hope that I could be as lively, enthusiastic, and energetic as he is. He has provided insightful discussions about the research and always compelled me and provided a good training as a scientist. I am fortunate to have got this all along the completion of my project work.

I would like to thank Dr. M. Nath, Dr. A. Choudhury, and Dr. X. Liang for serving on my PhD thesis committee and providing me their valuable suggestions throughout the completion of this dissertation. I appreciate Dr. Mary Ann B. Meador, NASA GRC for her time in designing models and analyzing data for my projects. I thank the Department of Chemistry, Missouri S&T for providing financial assistance and resources. I want to thank my past group members, Adnan, Shruti, Chakri, and Abhishek for their assistance during my research work. I would like to thank my present group members Hojat, Tara, Parwani, Chandana, Rushi, Shaheen and all my friends for their great help.

I would especially like to thank my parents, Mr. Suresh Donthula and Mrs. Uma Devi Donthula, my sister Sushmitha Donthula for their support and motivation. Also, special thanks to my father in law Mr. Madhusudan Mandal, my mother in law Mrs. Madhuri Mandal and my brother in law Mr. Koushik Mandal for their affection towards me. Finally, I would like to deeply thank my wife Chandana Mandal for her unconditional love, continued support and encouragement in my research and for standing beside me to help me get to this point.

TABLE OF CONTENTS

Page

LIST OF ILLUSTRATIONS

PAPER II

LIST OF SCHEMES

LIST OF TABLES

Page

PAPER I

PAPER III

1. INTRODUCTION

1.1. ENERGY STORAGE MATERIALS

One way to quantify the development stage of the human civilization is by the consumption of energy. Energy consumption increases of course with the population growth, and with the current demands imposed by technology and population, human civilization will face an energy crisis. Based on the current energy demands, it is predicted that the energy supply might double by 2050 and triple by 2100.[1,2] The energy cycle includes energy generation, conversion, storage, transportation, consumption and all human civilization must be vigilant about conservation, because all steps of the energy cycle impose strains on the environment, which, compounded by the population growth, bring into question the very survival of the human species. At all stages of the energy cycle, materials are called to play a pivotal role. This dissertation focuses on two special types of porous lightweight materials classified as aerogels which store energy.

Energy storage materials convert one type of energy into another and release it off with the application of an external stimulus. Those materials store energy in thermal,[3] elastic,[4] mechanical,[5] chemical,[6] solar,[7] or electromagnetic form.[8,9] The storage of electrical energy in a rechargeable battery is based on reversible chemical reactions in an electrochemical cell. Mechanical energy storage occurs mainly in the form of potential energy. Hydrogen storage is a form of chemical energy: electrical energy storage in the form of electrolysis which uses electricity to reduce water into hydrogen and oxygen. Thus, solar energy, an important source of renewable energy can be converted to electricity and stored as chemical energy. Another way to store electrical energy is via superconductive magnetic energy storage, which can be achieved by charging a superconducting coil at

cryogenic temperatures; the magnetic field over the coil is created by the flow of current in the coil that can be sustained indefinitely. The heat source for thermal batteries belongs to thermal energy storage in the form of chemical energy. Shape memory materials store mechanical energy using nano-structuring, molecular design, surface modification and tuning the pore structures.

This dissertation deals with the latter two categories of energy storage materials. Shape memory polymeric aerogels (SMPAs) with varying glass transition temperatures were prepared to remember and recover back to initial shapes from high elastic strains when triggered by heat. Those SMPAs may find applications in deployable panels e.g., for space applications, and in biomedical engineering like bionic hands and casts for broken body parts. Nanoporous iron aerogels prepared via carbothermal reduction of interpenetrating networks of polybenzoxazine and iron oxide nanoparticles were loaded with lithium perchlorate and may serve as heat sources that activate thermal batteries.

1.2. AEROGELS – BRIEF HISTORY

Aerogels are lightweight, highly porous solids. The IUPAC definition for aerogels is "gels comprised of a microporous solid in which the dispersed phase is a gas."[10] That definition is not satisfactory, in fact is wrong, because for example microporous materials like zeolites are not aerogels. Given that weakness, and also controversy arising by several authors attempting to define aerogels by the way they are prepared, very recently Vareda et al. suggested to redefine aerogels as "highly porous nanostructured solid materials derived from gels, in which the pores filling phase is a gas and whose properties/structures are not significantly affected by the removal of swelling agents regardless of the drying

approach used."[11] That definition follows closely the definition by the inventor of aerogels, S. S. Kistler who defined aerogels as "gels in which liquid has been replaced by air, with very moderate shrinkage of the solid network."[12] Those definitions do account for the "aero" part of the aerogels but do not address the "gel" part. In that regard, a more complete definition of the term "aerogel" that also differentiates them from closed-cell foam one from xerogels has been proposed by Leventis: "an open non-fluid colloidal network or polymer network that is expanded throughout its whole volume by a gas, and is formed by the removal of all swelling agents from a gel without substantial volume reduction or network compaction."[13] All in all, aerogels are derived from wet-gels where the pore-filling solvent is converted to a supercritical fluid and is vented off as a gas. The process preserves the porous skeletal framework of the wet-gel into the final solid object with a minimum volume compromise (shrinkage).

In addition to low densities and high porosities, aerogels combine high surface areas, low thermal conductivities, good elastic properties, acoustic attenuation, and possibilities for easy surface modification.[14] Thereby, they have been used as absorbents,[15] sensors,[16,17] catalyst supports,[18-21] thermal insulators,[22] templates for solar cells,[23] aerospace applications,[24] clothing and thermal insulation blankets,[25] energy storage materials,[26,27] dielectrics,[28,29] and capacitors.[30]

1.3. AEROGELS THROUGH THE PARADIGM OF SILICA

Silica aerogels were invented by S. S. Kistler and are highly porous, high surface area, extremely lightweight, good thermal insulators consisting of hierarchical assemblies of particles (see scanning electron micrograph in Figure 1.1).[31] Generally, silica aerogels

are transparent exhibiting a light blue tint because of the Rayleigh scattering of the short wavelengths of light from the primary particles. Silica aerogels are very fragile materials which limits their applications. The mechanical properties of the silica aerogel can be enhanced by manipulating their nanostructure, which requires a detailed understanding of their skeletal and porous structure, which in turn requires a detailed understanding of their formation via the so-called sol-gel chemistry.

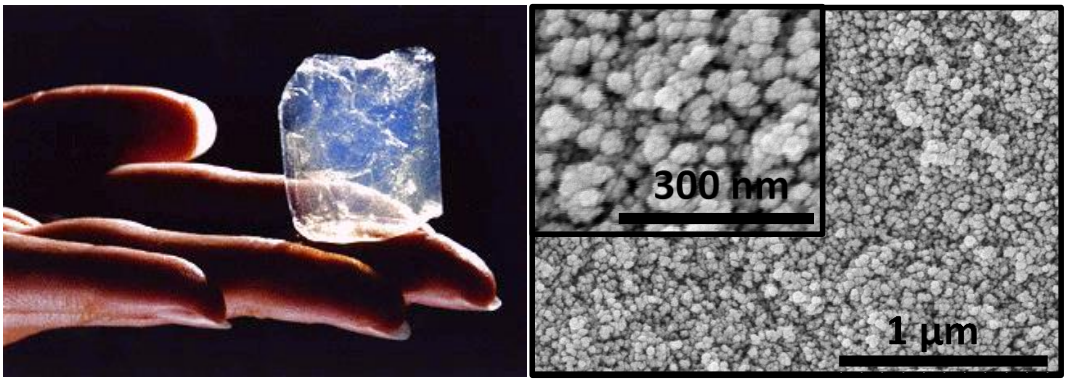

Figure 1.1. Macroscopic and microscopic view through scanning electron microscope of a silica aerogel.[32]

In a typical sol-gel chemistry, the gel precursors are mixed in a solvent to form a colloidal solution of primary particles (referred to as a sol). In the case of silica, the silica precursors can be tetramethylorthosilicate (TMOS) which is dissolved in a solvent e.g., methanol and is mixed with water (for hydrolysis), and a catalyst (base or acid, for hydrolysis and condensation). At first, hydrolysis of TMOS gives silanols which condense to form Si-O-Si bridges. The resulting polymer phase separates into tiny primary silica particles, that aggregate into mass-fractal secondary particles, that again agglomerate into

higher mass-fractal aggregates until the percolation threshold is reached, and a continuous network of particles is formed that is referred to as a wet-gel (Figure 1.2). Wet-gels are aged in order to gain mechanical stability. During aging, silica dissolves from the surface of the primary particles and reprecipitates at the interparticle necks rendering necks wider, which enhances the mechanical strength of the network.

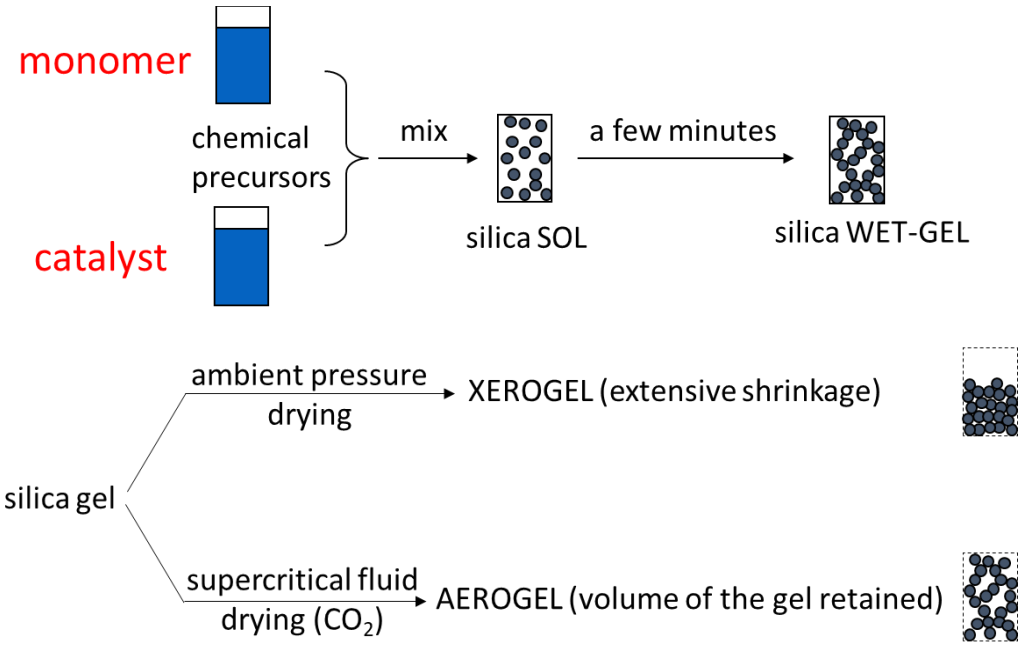

Figure 1.2. Sol-gel process for the synthesis of silica aerogel and xerogel.

Finally, wet-gels are dried in an autoclave exchanging the pore filling solvent with liquid CO_2 that is finally converted to a supercritical fluid (SCF) and is vented off like a gas. When pore filled solvent is dried at atmospheric pressure and temperature, structural collapse leads to extensive shrinkage and the final product is referred to as xerogel. Aerogels were prepared showing flexibility for insulation applications in subsea systems,

insole for shoes, industrial buildings and refrigerators.[33] Fiber reinforced aerogel composite blankets are commercially available from Aspen aerogels which can be bent and rolled over.[34] Process for the manufacturing of these blankets is shown in Figure 1.3.[35]

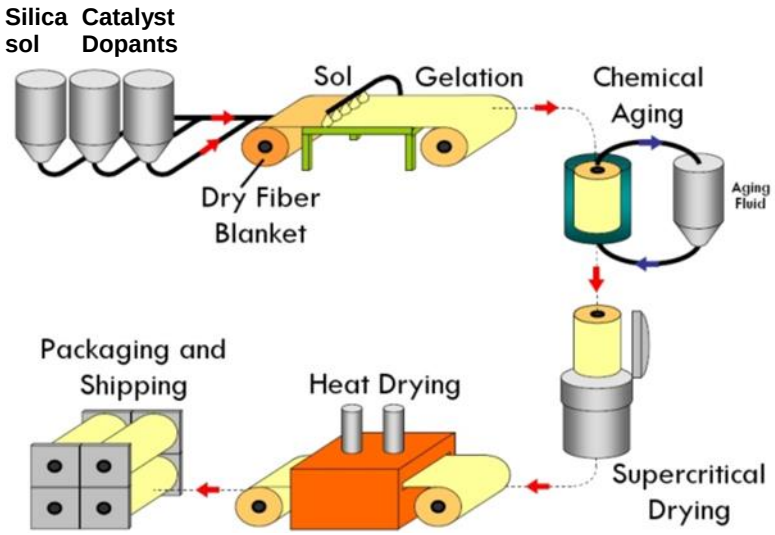

Figure 1.3. Manufacturing process of fiber reinforced aerogel composite blankets.

1.4. ADDRESSING THE FRAGILITY ISSUE OF SILICA AEROGELS: FROM POLYMER CROSSLINKED TO ALL-POLYMER AND ISOCYANATE-DERIVED POLYMERIC AEROGELS

The fragility issue of silica aerogels has limited their use in certain types of thermal insulation,[36] catalyst supports,[37] and space exploration for example in capturing cosmic dust in outer space (refer to NASA's Stardust program).[38,39] In order to address the fragility issue, Leventis et al. developed the so-called polymer crosslinked aerogels (X-aerogels).[40] In those, the free hydroxyl groups on the surface of the silica network reacted with commercial triisocyanate forming urethane linkages and eventually a conformal coating on the skeletal framework keeping mostly intact the open porosity of the native silica

framework. That X-linking process increased the flexural strength of typical silica aerogels by almost 300 times with just an increase in density by a factor of 3. Since that exceptional increase in mechanical strength was brought about by adding polymer, the Leventis group shifted attention to purely organic aerogels and one major category of those was based on isocyanate chemistry. Such aerogels included conventional polymers that are associated with the isocyanate chemistry, that is polyureas and polyurethanes, but also polyimides and polyamides.

1.5. THE ISOCYANATE CHEMISTRY

The isocyanate group, -N=C=O, is highly reactive. Because of the partial positive charge induced on the carbon atom by the electron withdrawing abilities of both the nitrogen and oxygen atoms, it acts as an electrophile (Scheme 1.1).

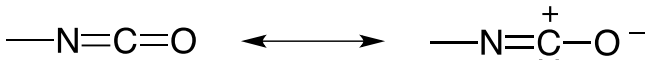

Scheme 1.1. The isocyanate group.

The attack of a nucleophile on the -N=C=O group is shown in Scheme 1.2. The reactivity of alkyl and aryl isocyanates with different kinds of nucleophiles like H_2O, alcohols (R-OH), amines (R-NH_2), carboxylic acids (R-COOH) etc. have been studied extensively as summarized in Scheme 1.3.

Initially, those reactions are described as pseudo second-order reactions, but later it was reported to follow third-order kinetics.[41,42]

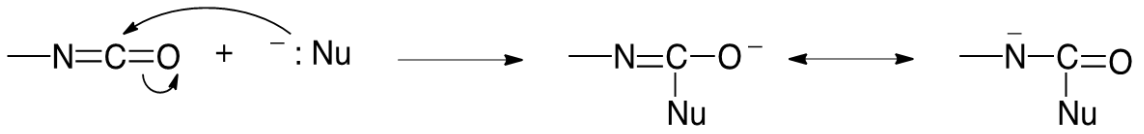

Scheme 1.2. Nucleophilic attack on the isocyanate group.

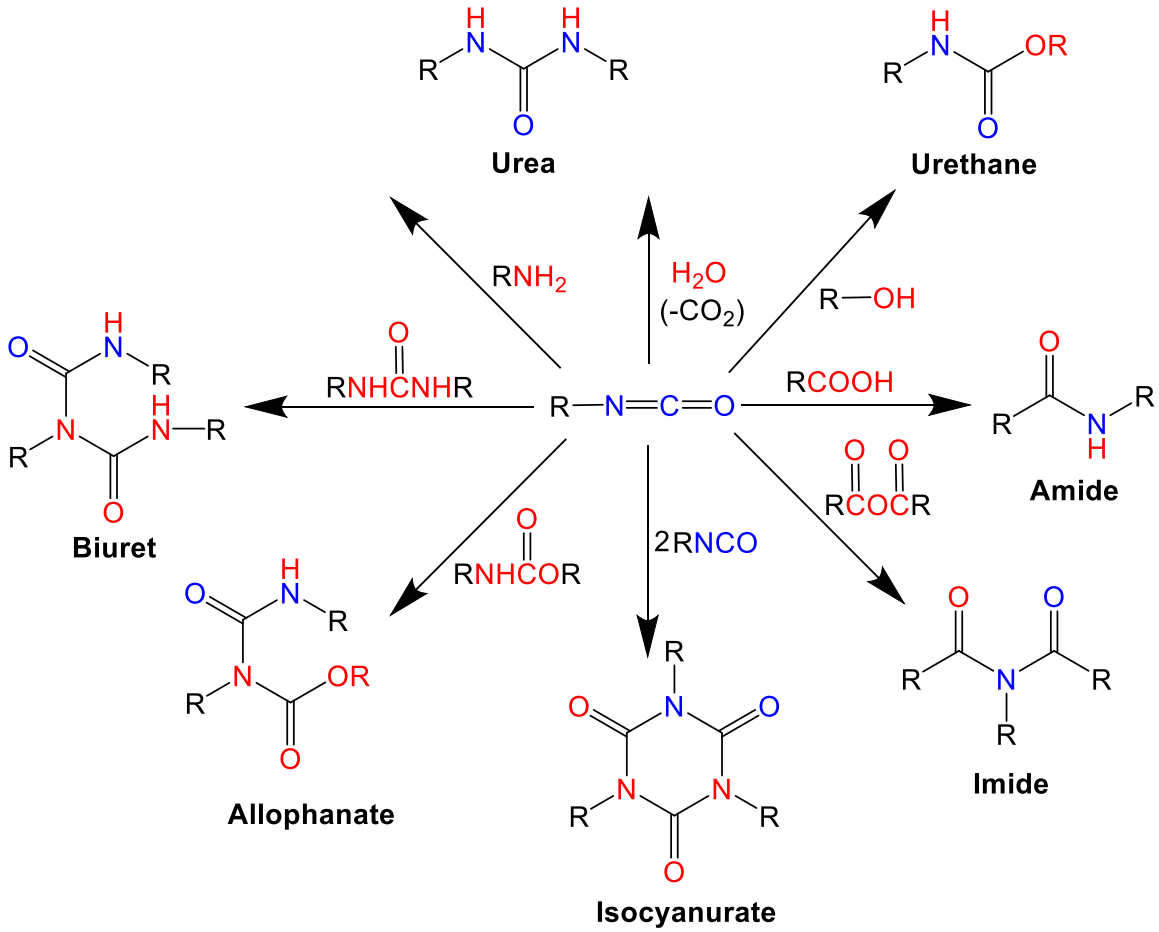

Scheme 1.3. The chemistry of isocyanates with different nucleophiles.

Solvents best suited for those reactions include toluene-DMSO or toluene-DMF mixtures which can form strong hydrogen bonds.[43,44] Part of this dissertation is based on

the reaction of isocyanate with alcohols to polyurethanes and therefore, those reactions are discussed in more detail below.

Polyurethanes belong to a special class of versatile polymeric materials that have been incorporated into different products such as elastomers, insulators, foams, paints, liquid coatings, etc. Polyurethanes are based on the urethane repeat unit, which is formed by the addition reaction of the isocyanate group with an alcohol in the presence of a catalyst. Dibutyltin dilaurate (DBTDL) is a typical acid catalyst favored by many researchers.

1.5.1. Polyurethanes (PU). Polyurethanes were discovered in 1947 by Bayer and his coworkers through the reaction of diisocyanates and polyester diols.[45] The properties of polyurethanes can be varied by using the different types of polymer building blocks, i.e., the alcohol and the isocyanate in combination with different catalysts, as well as chain extenders, stabilizers, and surfactants. In general, high molecular weight polyols yield soft elastic polyurethanes, whereas low molecular weight polyols form rigid and hard polyurethanes. Those structure-property relationships give polyurethanes great potential for use in different applications.[46] Thus, various improvements in processing, selection of additives and formulation enabled use of polyurethanes in construction, transportation, textiles, fibers, adhesives, foams, bedding and electronic appliances.[47,48,49] Because of easy tuning of their mechanical strength and elastic modulus, polyurethanes have been used as a replacement for other plastics, rubber, and metals.[50-52]

Polyurethanes can be broadly classified into following four types based on the applications of the final materials: flexible foams, rigid foams, elastomers and coatings/adhesives.[53]

1.5.1.1. Flexible foams. Most of the flexible polyurethane foams finds applications in furniture cushions, bedding, automotive seating, and carpet underlaying.[54-57] Two major processes are involved in the synthesis of flexible PU foams: blowing and gelling. In the first process (blowing), urea is produced in parallel with polyurethane via reaction of the isocyanate with water, releasing carbon dioxide that acts as a blowing agent. The second process involves polymerization that forms urethane linkages from isocyanate and polyols.[58] The most commonly used isocyanates for foams are 2,4 and 2,6-toluene diisocyanate, while the alcohols are polyether polyols with the general formula H-$(CHOH)_m$-CH_2O-$(C_2H_5O)_n$-H, that is, typical polyols are polyethers from active hydrogen compounds like glycerol, sorbitol, sucrose etc. Few PU foams have been synthesized from lignin; the flexibility of those materials could be improved incorporating either by a flexible segment in the backbone of the PU using a chain extender that would lower the glass transition, or by lowering the crosslinking density, which could be achieved by reducing the NCO/OH ratio. Textile based fibers of carbon, basalt and aramids were added to increase the tensile properties of those PU foams.[59]

1.5.1.2. Rigid foams. The major application of rigid PU foams is in energy saving thermal insulation in refrigerators, building walls, refrigerated trucks and commercial appliances that work with heating and cooling.[60] Rigid foams can also provide structural strength to the appliances and vehicles.[61] Generally, rigid foams are strongly cross-linked, closed-pore materials prepared from polyether or polyester polyols and methylene diphenyl diisocyanates. In order to decrease the overall thermal conductivities of the foams, pentane isomers are frequently used as solvents, because the thermal conductivity of pentane that remains trapped in the closed pores is well below that of air.[62]

For additional requirements in the field of fire protection, rigid PU embedded with polyisocyanurate (PIR) foams are used to insulate buildings.[63] PIRs belong to a special class of isocyanate derived polymers. They are synthesized from the trimerization of aliphatic or aromatic isocyanates upon heating whose forward reaction is more favored than the backward reaction. The high thermal stability of PIRs permits their application in elastomers, coatings and adhesives.[63] Those polymers by themselves are friable and hence are generally modified with urethanes by mixing an excess of diisocyanate with a diol using a catalyst and the resulting polymers cannot be crumbled easily but are mostly elastomeric. The dissociation temperature can be increased to 250 ^{o}C from 150 ^{o}C by the incorporation of isocyanurates in the polymer.

1.5.1.3. Elastomers. Elastomers represent a wide range of materials for a variety of applications. They fall into two categories: cast elastomers, and thermoplastic polyurethane elastomers (TPUs). The elastomers market includes footwear, fibers, TPU, spray elastomers, synthetic leather, gaskets, seals, O-rings, and biomedical devices.[64-66] Other special applications include the noise and vibration-damping properties of the elastomers. Diisocyanates like 1,5-naphthalene diisocyanate (NDI), 1,4-para-phenylene diisocyanate (PPDI) and novel fatty acid-based diisocyanates are generally used for the synthesis of elastomers. Polyols are based on polytetrahydrofuran diols, polyester polyols or polyether polyols, while chain extenders range from short chain glycols to aromatic diamines. Applications of PU elastomers are enhanced by using additives like flame retardants, accelerators, antidegradants, colorants, fillers and softeners.[67]

1.5.1.4. Coatings/adhesives.[68,69] Extensive research in this area has led to the development of chemical resistant hyperbranched PU coatings for wood, metal, and high

gloss finishes for aeroplanes.[70] For flame-retardant applications in nano composites and nano coatings, hyperbranched PUs were incorporated with Bisphenol-A.[71] Other major applications of PUs in coatings include marine antifouling materials, castor oil-based PUs as advanced surface coating materials, automotive coatings, corrosion resistant coatings, and coatings for everyday usage materials like wood, plastic, and textile.[72] Solvent based PUs were replaced with waterborne PU dispersions that offer sustainable coating of textiles. PU adhesives are preferred over other types of adhesives because of the fast development of strength on curing and capability to bond with substrates. Adhesive PUs are cured above the crystalline melting temperature of the material. Those adhesives are used in footwear and flexible packaging industries.[73] Those PUs are generally prepared from aromatic isocyanates and low molecular weight diols.

In general, flexible long tethers of alcohol and long aliphatic chains on isocyanates yield soft elastic polymers whereas small aliphatic chains of alcohol or isocyanate form rigid and hard polymers.[74]

1.5.2. Shape Memory Polymers (SMP). SMPs belong to a special group referred to as functional polymers. Application of those materials in a specific area is decided by their properties in relation to the desired function. Those materials store deformation energy and recover elastic strains triggered by temperature, light, electric or magnetic fields. That shape memory effect (SME) was first observed in certain metal alloys that are referred to as shape memory alloys (SMA). SMPs are differentiated from SMAs by their high tolerance for strains, low density, and low stresses. A prerequisite for showing the SME is superelasticity, which can be observed in both polymers and alloys. Superelasticity is the property of a material to recover back to its original shape after an extreme

deformation. The differentiation between a shape memory material and a superelastic material is that it regains its permanent shape not by simple removal of stress, but when an external stimulus like temperature change is applied after the sample has been fixed in a temporary shape. For the SME to occur, the sample should be elastic above and hard below a certain temperature. That temperature might be the point of a phase transition (e.g., melting point), or simply a glass transition (T_g) in superelastic polymers.

The SME of SMAs is based on the fact that those materials can exist in two stable phases: austenitic phase (at higher temperature) and a martensitic phase (at lower temperature or under stress). Therefore, at higher temperature upon stress, these materials are converted to a martensitic phase that is fixed (i.e., stabilized) by cooling the deformed object. By heating up, the material returns to austenitic phase, and the object recovers to its original shape. The most widely known shape memory alloy is Nitinol (a nickel-titanium alloy) and it was discovered in 1963. Desirable properties of Nitinol include bio-compatibility, and a transition temperature near to body temperature.[75] Shape memory polymers were introduced in the 1990s.

1.5.2.1. Overall literature review of SMAs and SMPs. Notable reviews include: A book by K. Otsuka and C. M. Wayman covered from fundamentals to applications of SMAs, offered also an introduction to the SME in ceramics and polymers, and described the mechanistic assessment of the SME in alloys.[76] Beloshenko et al. reviewed the SME in glassy polymers, crystallisable polymers, polymer blends, polymer gels and polymer matrix composites.[77] Those authors focused on temperature dependence of recoverable strain, relaxation stress, thermal shrinkage, and shrinkage stress. Later, A. Lendlein and S. Kelch focused on the theromechanical characterization of SMPs, the molecular

mechanisms of the SME, and then different kinds of shape memory polymer systems.[78] Lately, Liu et al. classified all SMPs into four categories based on their shape fixing and shape recovery abilities via a quantifiable property referred to as the Fill Factor.[79] They emphasized biomedical applications of SMPs. A recent review on shape memory polymers by Hager et al. provided a broad view on the overall developments on SMPs until 2015.[80] They discussed the underlying reasoning behind the different kinds of SME observed in polymers and classified reversible shape memory effects based on melting transitions, glass transitions, reversible bond formation (e.g., covalent bonds vs supramolecular interactions), light irradiation and liquid crystal effects. Even more recently, a review of SMP based on supramolecular interactions like hydrogen bonding, host-guest interactions, hydrophobic interactions, metal-ligand coordination, and ionic interactions have been reported.[81] Those materials have widened the range of applications from industrial to bio-medical to aerospace.[82,83]

1.5.2.2. Key developmental milestones in SMPs. SMPs can be synthesized using chemistries leading to SME that can be triggered at different temperatures. Xiao et al. synthesized SMPs based on polyimides resulting in T_gs in the range of 299 - 322 ^oC, which were among the highest Tg reported for SMMs.[84] They discussed the importance of covalent crosslinking and the crosslink density observed in thermosets compared to thermoplastics in terms of the potential impact on physical properties like the storage modulus. Those polyimides were good for high temperature applications, and their properties could be modified via the chemical structure of the monomers and the molecular weight, and crosslink density of the polymer. Dual and triple shape memory polymers were synthesized based on multiple phase transitions achievable via bilayer system.[85-87] Xie et

al. demonstrated for instance, using bilayer polymers, the triple shape memory effect with three temporary shapes at different temperatures (Figure 1.4), T. Xie has also synthesized shape memory polymers using perfluorosulphonic acid ionomer which can display multi-shape memory effects without any variation in the material composition.

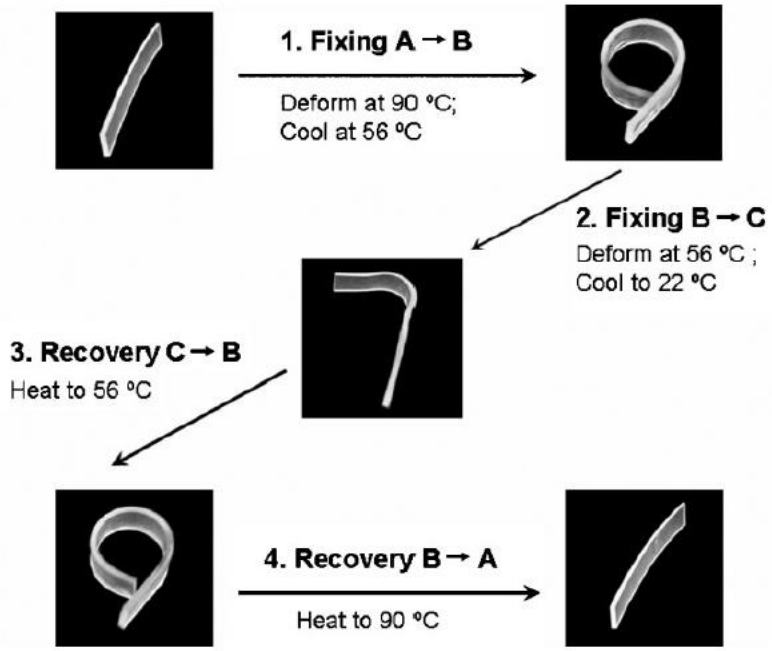

Figure 1.4. Photographs of a bilayer polymer demonstrating a triple shape memory effect.

These SMPs have a single broad T_g which can help in tuning the recovery behavior by changing the strain control and temperature while the sample is being fixed.[88]

Rivero et al. has prepared furan-based shape memory assisted self-healing polymers where, Diels-Alder chemistry was used to form covalent bonds, introduced as crosslinkers into polycaprolactone (PCL) containing polyurethane material. Those

covalent bonds were thermoreversible, meaning that, once the bonds were broken by the introduction of a crack forming free furan/maleimide functional groups, shape memory effect (i.e., temperature driven) assisted the crack closure at temperatures above the melting point of PCL.[89] Interestingly, the structural integrity of that crosslinked polymers was not affected by the breaking and self-healing process as there was no complete melting of the polymer.

Another interesting approach to multi temporary SMPs has been demonstrated with crosslinked poly (butyl methacrylate-co-methyl methacrylate) triggered with high intensity focused ultrasound (HIFU) directed at selected regions of the material.[90] HIFU heats the sample instantaneously locally and initiates the shape recovery process as shown in Figure 1.5. In an interesting twist, these materials have been demonstrated to release a drug that is loaded on the sample simultaneously with the changes in the macroscopic shape of the polymer. It was suggested that the controlled release of the drug was due to the swelling of the polymer network as it was heated during shape recovery that allowed the drug to diffuse into the surrounding medium through osmosis.

1.5.2.3. Transition from flexible aerogels to superelastic and shape memory aerogels. Silica aerogels made from methyl trimethoxysilane demonstrate flexibility by reducing the overall bonding because of the methyl group present in the monomer.[91] Flexible polyimide aerogels were produced by Meador et al. from aromatic anhydride and aromatic triamines.[92] Those materials have potential applications as high temperature insulation for launch vehicles and aerospace industry. More recently, flexible aerogels from hyperbranched polyurethanes were synthesized by Leventis group and along the way

studying the importance of molecular source for flexibility by comparing aerogels from urethane acrylate as opposed to urethane norbornene.[93]

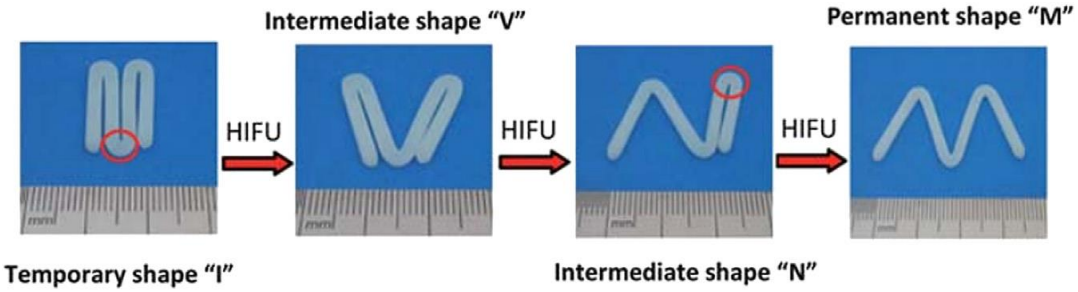

Figure 1.5. Shape memory cycles induced by ultrasound in a random copolymer of poly(butyl methacrylate-co-methyl methacrylate).[90]

Lately, shape memory aerogels were successfully synthesized from thiol-ene networks of 1,6-hexanedithiol, pentaerythritol tetrakis (3-mercaptopropionate), and triallyl-1,3,5-triazine-2,4,6,-trione. They possessed T_g values in the range of 42-64 ^oC which assists in the shape recovery process. Samples were characterized using compression testing for five cycles.[94] The first and second part of the dissertation introduces to new type of shape memory aerogels that are discussed below.

1.5.3. Shape Memory Poly (urethane-isocyanurate) Aerogels. Shape memory poly(urethane-isocyanurate) aerogels were prepared from commercially available aliphatic triisocyanate (N3300A) and ethylene glycol-based diols ranging from ethylene glycol (EG) to tetraethylene glycol (TTEG) in a solvent mixture of acetonitrile and acetone.

1.5.3.1. Characterization of shape memory aerogels. Selected aerogels were chemically characterized via ^{13}C-NMR and FTIR. Solid state ^{13}C NMR of triethylene glycol (TEG) based sample is shown below stacked with its corresponding liquid ^{13}C NMR

of monomers (Figure 1.6.A). The peak at around 155 ppm corresponds to the urethane carbon. A stacked FTIR figure of four samples prepared from different alcohols is also shown in the Figure 1.6.B. The isocyanurate carbonyl stretch shows up near 1680 cm^{-1}, while the urethane carbonyl stretch is observed at 1729 cm^{-1}, and the C−N stretch near 1240 cm^{-1}. The free N−H stretching is observed as a shoulder or a broad peak at around 3600 cm^{-1} and the hydrogen-bonded N−H stretching near 3350 cm^{-1}.

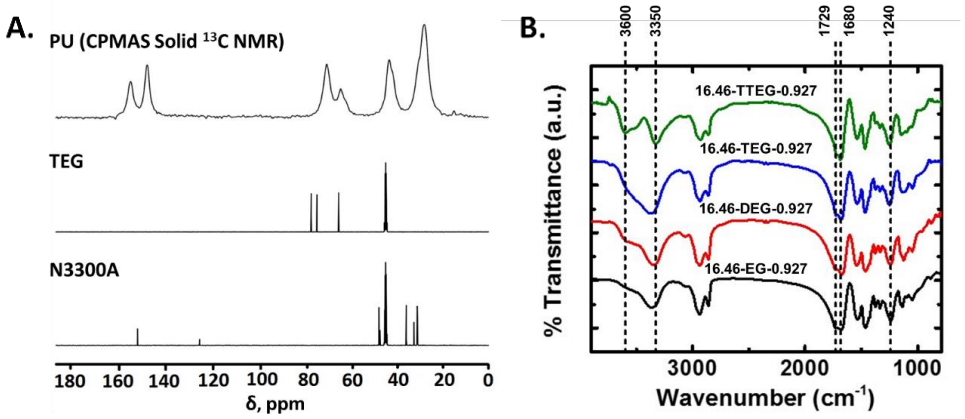

Figure 1.6. Chemical characterization of selected SMA aerogels. (a). Solid CPTOSS ^{13}C NMR spectrum stacked with liquid ^{13}C NMR of monomers TEG and N3300A. (b). FTIR Spectra.

It was observed that upon increasing the chain length of the alcohol and incorporating flexible –(CH_2)– tethers from N3300 renders the polymer more soluble resulting in larger particle sizes. This change in the chain length of alcohol also yielded aerogels which have varying T_g. Aerogels synthesized from EG showed higher Tg compared to that of the aerogels from TTEG. This decrease in the T_g could be reasoned

based on the fact that longer alcohols increase the segmental motions inside the polymer, thereby reducing T_g.

T_g values were obtained from single frequency strain oscillation experiments while ramping the temperature from -150 ^oC to 150 ^oC using a Dynamic Mechanical Analyzer

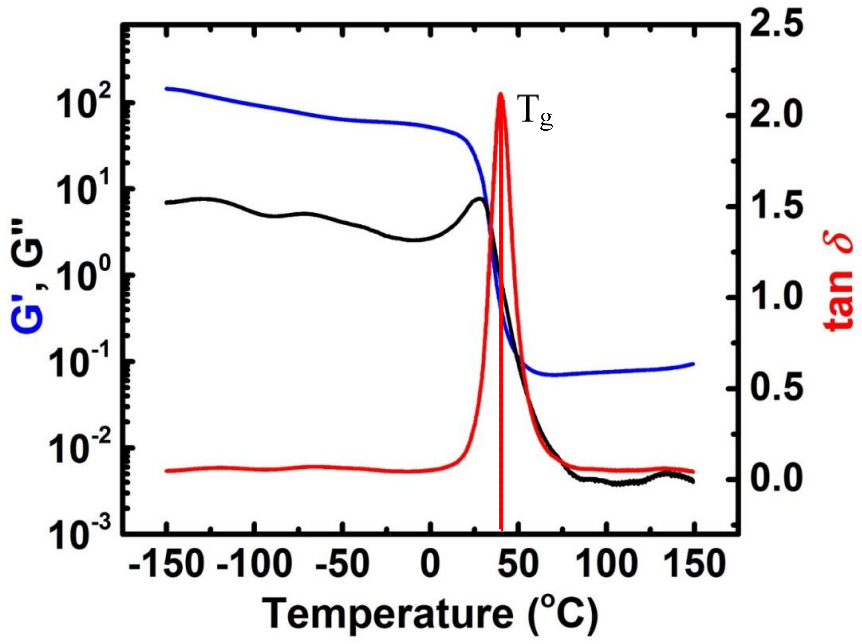

Figure 1.7. Storage modulus (G'), Loss modulus (G"), and tan δ for a representative TEG-based polyurethane aerogel under single frequency (1 Hz) strain (0.3%) oscillation as the temperature was ramped from -150 ^oC to 150 ^oC.

(DMA). As shown in Figure 1.7, initially at low temperatures, samples were rigid and as the temperature was increased, the storage modulus (G') decreased by 1000 times while the loss modulus (G") increased up to a particular temperature and then decreases along with G' leading to a peak for tanδ (=G"/G'). The maximum in tanδ is defined as T_g. Samples before T_g were stiff and hard while above this temperature, they became rubbery.

The SME for the aerogels that were studied here was generally observed within 10 – 15 ^{o}C below and above T_g.

1.5.3.2. Quantification and possible explanation for SME. As shown in Figure 1.8, in a typical shape memory experiment, a sample was first heated to T_g + 10 ^{o}C and then deformed (stretched in our case) near its maximum strain. Next, the force required to stretch the sample was kept constant, while the temperature was decreased to a low temperature of T_g - 40 ^{o}C. At this point, the sample became stiff and the shape was fixed. Then the force was released instantaneously and subsequently the temperature was ramped back up to T_g + 10 ^{o}C at a constant heating rate resulting in gradual shape recovery. This shape memory cycle was repeated for 5 times in order to investigate how robust its shape memory behavior was. Three different strain values are recorded along the shape memory experiment viz. the maximum strain (ε_m), fixation strain (ε_u), and residual strain (ε_p) as shown in the Figure1.9.A. In order to quantify the shape memory effect, four figures of merit were calculated from these values: strain fixity (R_f, Eq 2) strain recovery (R_r, Eq 3), recovery rate (m_r, Eq 4), and fill factor (FF). The Fill Factor is a combined index of all the three figures of merit and was calculated from the ratio of the shaded area under the S-shaped curve to the total box area, as shown in Figure 1.9.B. All samples showed excellent strain fixities, strain recoveries and fill factors when compared to other SMPs.[95]

$$R_f(N) = \frac{\varepsilon_u(N)}{\varepsilon_m(N)} \times 100 \quad (2)$$

$$R_r(N) = \frac{\varepsilon_m(N) - \varepsilon_p(N)}{\varepsilon_m(N)} \times 100 \quad (3)$$

$$R_t(N) = \max\left[-\frac{dStrain}{dt}\right] \quad (4)$$

The unrecoverable strain after the first cycle was attributed to the settling in the sample at the molecular level and was studied and explained using ATR-FTIR in the N-H stretching region (3000 – 3800 cm^{-1}). It was found that native aerogel sample had three types of N-H stretchings viz. two kinds of H-bonded N-H stretches (H-bonded to glycol units and H-bonded to carbonyl groups) and one free N-H stretching. When the sample was heated, the free N-H stretching region was partially converted to the H-bonded N-H stretches and eventually, it was completely converted to H-bonded N-H upon stretches.

Due to the increased H-bonding, the stiffness increased after the first cycle. The alcohols chosen for this study showed high tendency for H-bonding with the neighboring polyurethane groups which increased as the diol chain length increased from EG to TTEG. That tendency for H-bonding extends to H-bonds with solvent, and was the reason for the different morphologies observed in the final aerogels, depending on the diol. EG based aerogels showed micron sized particles with narrow necks between them. Particles in TTEG based aerogels were merging forming thicker necks. That has been attributed to the longer aliphatic chains of TTEG which have higher solubility than the smaller aliphatic chains of EG, leading to secondary polymer accumulation in the TTEG based aerogels on the interparticle necks rendering them wider.

Figure 1.10 shows the scanning electron microscope (SEM) images of A. TEG and B. TTEG based aerogels.

1.5.3.3. Applications of shape memory aerogels. The superelastic behavior and shape memory effect described in this thesis are illustrated in Figure 1.11. Those properties have been put to practice with deployable panels and with bionic hand mimicking the muscle coordination of a human hand grabbing a pen.

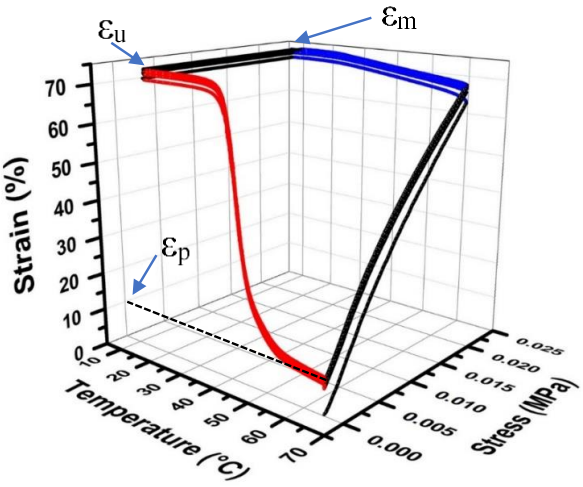

Figure 1.8. 3D representation of five shape memory cycles for a diethylene glycol (DEG) based sample. Temperature dependent steps are colored with blue and red.

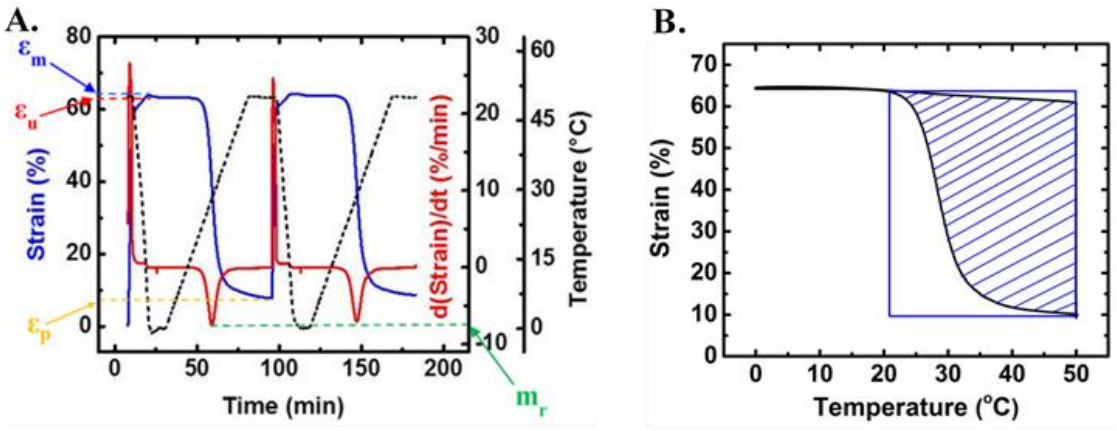

Figure 1.9. Projections of the entire 3D representation of Figure 1.8 to different planes in order to calculate the figures of merit of the shape memory effect. (a). Projection to the Strain-Temperature plane unfolding Temperature into Time (Temperature vs. Time is also included as a dotted line). (b). Projection of the 3D curve to the Strain vs. Temperature plane.

1.5.4. Tuning the T_g of Shape Memory Aerogels. For a better understanding relative importance of the various system parameters upon the shape memory effect, we used mixed alcohols and varied the mole ratio of the three alcohols, DEG, TEG, TTEG,

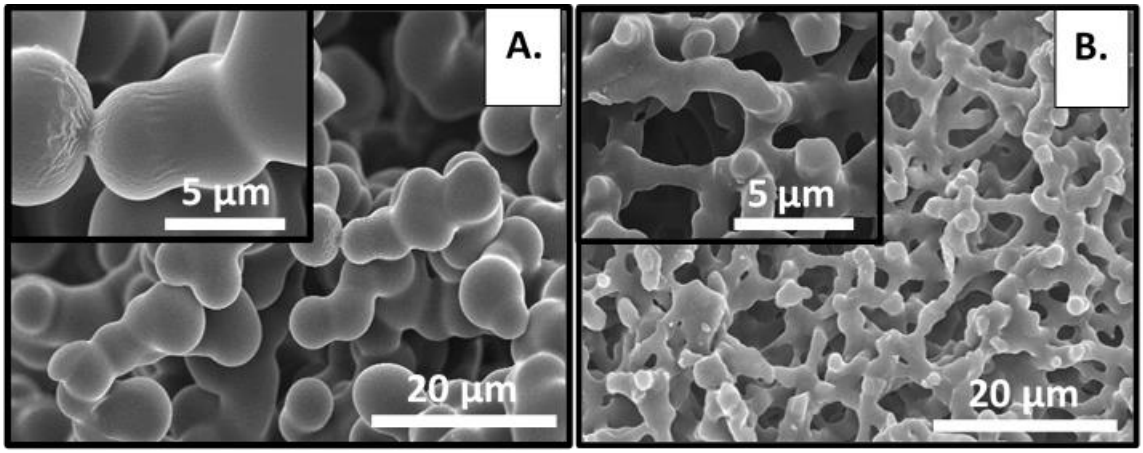

Figure 1.10. SEM images of (a). TEG based SMA and (b). TTEG based SMA.

the total monomer concentration and the solvent fraction. Initial data showed that high acetone content in the solvent (up to 0.5% v/v) resulted in an unacceptable high proportion of samples that collapsed.

Then, the solvent fraction of acetonitrile/(acetonitrile+acetone) was fixed to an intermediate value 0.875 and we varied three other system parameters namely the monomer concentration, the mole fraction of DEG, and the mole fraction of TTEG. The T_g values varied in the range of 25 – 49 ^oC. The micromorphology depended on all three independent variables and ranged from micron-sized particles with thick necks, to bicontinuous structures, typical of spinodal decomposition. The major finding was that the recovery rate of these shape memory aerogels had an inverse relationship with the elastic modulus of the corresponding samples.

1.6. ORGANIC POLYMERIC AEROGELS VIA PHENOLIC CHEMISTRY

The first organic aerogels through phenolic chemistry were based on resorcinol-formaldehyde (RF) resins invented by Pekala.[96] Phenolic chemistry involves the

condensation reaction of phenolic derivatives with formaldehyde. Those aerogels have been the primary precursors for the synthesis of carbon aerogels and xerogels.[97] Many other phenolic resin based aerogels were introduced thereafter like that of melamine-formaldehyde, cresol-formaldehyde, and phenol-furfural.[98] Due to their electrical conductivities, high surface areas (>400 m^2 g^{-1}), and high porosities (>80%), carbon aerogels have been used as electrodes for capacitors (aerocapacitors) that can release stored energy rapidly resulting in high energy and power densities.[99]

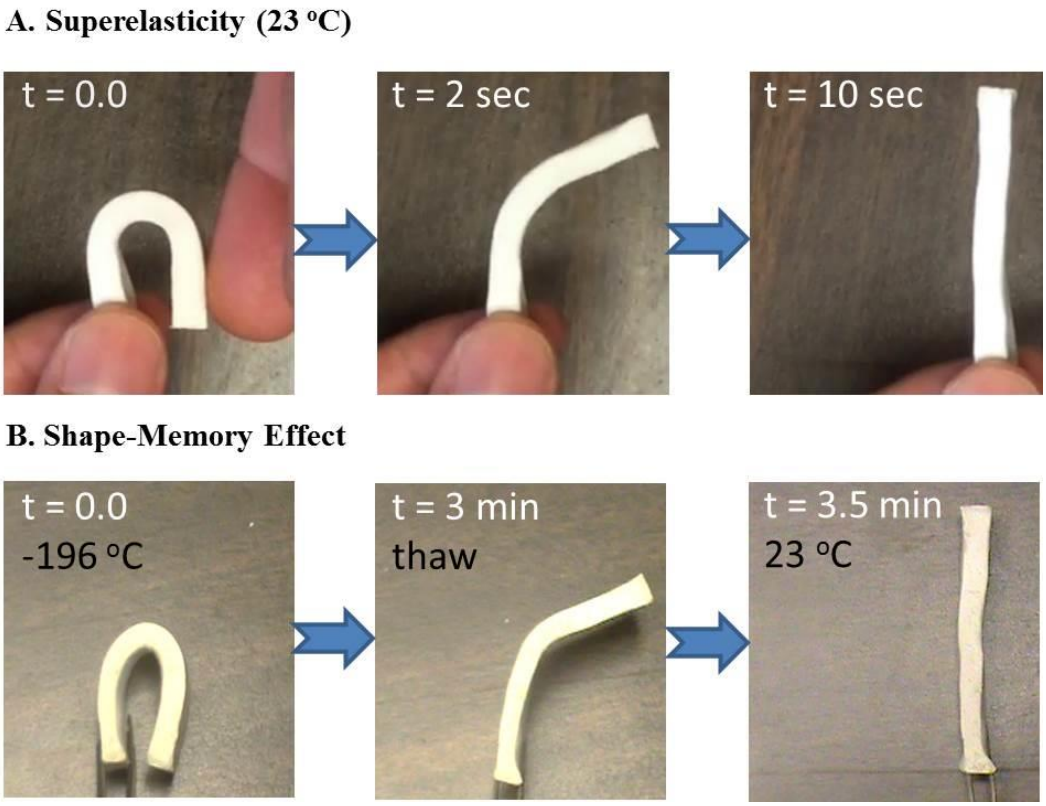

Figure 1.11. Shape memory aerogel demonstrating superelasticity at room temperature shape memory effect. (a). Sample was bent at RT allowed to recover. (b). Sample was first bent, then cooled to liquid N_2 temperature, and finally allowed to thaw at room temperature.

Pekala's procedure to RF aerogels involved base catalysis via the addition of sodium carbonate to an aqueous solution of R & F, and the pH was maintained in the range of 6.5-7.4. Gelation of these sols took 16-30 h followed by 7 days aging. To overcome the long processing times, efforts focused on gelation of RF under acidic conditions.[100] Later, a time efficient synthesis of RF aerogels developed via a HCl-catalyzed room temperature gelation process in acetonitrile.[101] Eventually, that HCl-catalyzed procedure was applied also on a special class of phenolic resins referred to as polybenzoxazines.

1.6.1. Polybenzoxazines. The first reported synthesis of the benzoxazine heterocyclic ring was in 1944 by Holly and Cope and involved a Mannich condensation of an amine (of ortho-hydroxybenzyl amine) and an aldehyde.[102] Later Burke et al. in 1949 reported a single step, one-pot synthesis of many substituted benzoxazines from phenol, amine and formaldehyde. [REF. Burke, W. J.; Glennie, E. L. M.; Weatherbee, C. "Condensation of Halophenols with Formaldehyde and Primary Amines," J. Org. Chem. 1964, 29, 909-912] Further, benzoxazines were synthesized from bisphenol-A and diamines. Those monomers can be polymerized to polybenzoxazines with high thermal and resistance, good mechanical properties.[103] Benzoxazine from bisphnol-A has the advantage over other monomers in that it involves a solventless procedure at high temperature of 85-140 ^{o}C.[104]

The mechanism of benzoxazine formed via Mannich reaction of phenolic derivatives, amines and formaldehyde is shown in Scheme 1.3. In the last part of the dissertation, benzoxazine monomer was synthesized according to Ishida's solventless procedure using bisphenol-A, aniline and formaldehyde. That benzoxazine monomer could be either polymerized using conventional heating at 130 ^{o}C,[105] which is a long procedure

or from a newly developed room-temperature acid-catalyzed process, which takes just a few hours.[106] Wet gels were washed and were dried with SCF-CO_2 to PBO aerogels. Those aerogels combine high mechanical strength, high temperature stability, high char yield (thereby, they are attractive for conversion to nano-porous carbon), low water absorption and flexibility in design.

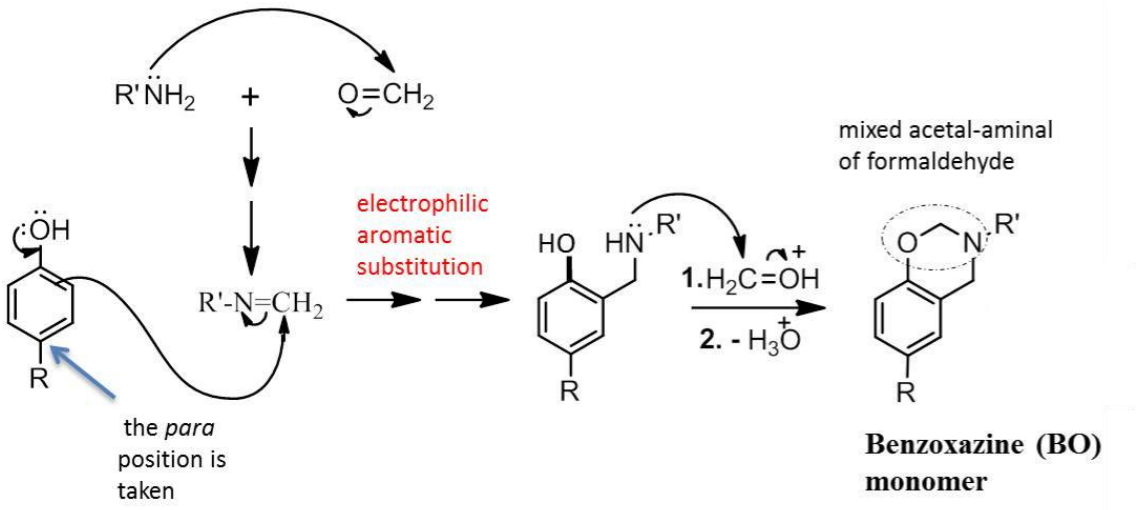

Scheme 1.4. General reaction mechanism for the synthesis of Benzoxazine monomer.

Generally ring opening reaction of benzoxazine monomers leads to the formation of polybenzoxazine. Addition of metal ions to the above reactions can act as catalysts in the ring opening reaction of benzoxazine ring. The catalytic effect of metal ions on the polymerization and degradation has been studied by various researchers. Incorporation of $TiCl_4$ into benzoxazine monomer effectively increased the thermal stability of PBO.[107] Agag et al. studied in detail the thermal stability and viscoelastic properties of PBO/Titania hybrids.[108] Later Sudo et al. studied the catalytic effect of fourth period transition metal complexes for the ring opening polymerization of benzoxazine. Among all transition

metals, iron, cobalt and manganese displayed high catalytic activity.[109] Other rare earth metal ions were also used and Ran et al. found that $LaCl_3$ increased the char yield and degradation temperature.[110]

The morphology of polybenzoxazine resins is generally dependent on two factors namely, the rate of the curing reaction and the phase separation processes. Those two processes compete in the formation of thermoset blends that produce different kinds of morphologies like bicontinuous morphologies, sea-island morphologies and interpenetrating networks.[111] Huang et al. studied the morphology changes of polybenzoxazine/polyethylene oxide (PBO/PEO) blends which showed phase separated structures.[112]

A gradual change in morphology from sea-island (PEO-PBO) to island-sea (PEO-PBO) phase was observed upon increasing the PEO content from 10 % to 40 % (Figure 1.12). Several other polymer blends have also been studied in terms of the possible variation in morphology. Some of those blends include blends of polybenzoxazine with polyimides,[113] polycaprolactone,[114] polysulfone,[115] epoxy,[116] bismaleimide,[117] and cyanate ester.[118]

1.6.2. Polybenzoxazine Aerogels. Leventis et al. observed that curing in air at around 200 ^{o}C is a necessary step for the high-yield conversion of polybenzoxazines to isomorphic carbons.[119] The air-cured samples were successfully characterized through solid state ^{13}C NMR, ^{15}N NMR and FTIR spectroscopy. It was discovered that air oxidation causes ring-fusion aromatization along the PBO back bone. It has been previously reported that PBO aerogels can be used to convert them to mesoporous carbons, with higher yields

than the bulk polymer (e.g., 51% w/w vs 27 % w/w).[120] The newly discovered ring-fusion aromatization process has explained that observation. Four other systems were also studied in detail and the mechanism involving the air-oxidation of phenolic resin aerogels like phloroglucinol-formaldehyde (FPOL), terephthalaldehyde-phloroglucinol (TPOL), resorcinol-formaldehyde (RF), and phenol-formaldehyde (PF) was explicated. Even though the yields of final carbons via direct carbonization were similar to the yields of carbons from air-oxidation followed by carbonization, still there was a definite increase in the surface areas of the carbons derived from systems that could undergo ring-fusion aromatization by low-temperature oxidation.[121] Those carbons came from TPOL and FPOL.

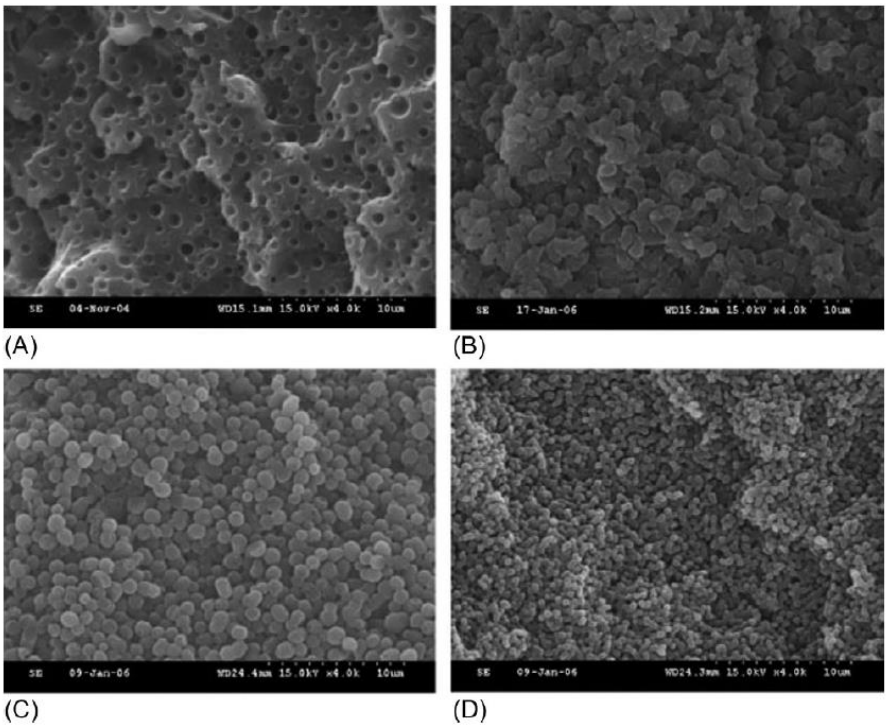

Figure 1.12. SEM images of different proportion of PBO/PEO blends. (a) 90/10, (b) 80/20, (c) 70/30, (d) 60/40.[117]

1.6.3. Nanoporous Metals. Thin films of nanoporous metals have been prepared from dealloying,[122] laser etching[123] and metal deposition onto templates.[124] Synthesis of bulk nanoporous metals: templating,[125] sol-gel chemistry,[126] and combustion synthesis.[127] Metal deposition on templates such as colloidal silica particles or polystyrene spheres is a conventional approach but, deposition becomes difficult when the pores get reduced to sub-micron size. On that note, Jiang et al. could do electroless deposition of metals like Ni, Cu, Au, Pt and Ag by penetrating through small pores of the template.[128] Other ordered templates like monodisperse polystyrenes have also been used for metal deposition enabling pore sizes in the range of 250-500 nm.[129]

1.6.4. Metal Aerogels. Noble metal (gold, palladium and platinum) aerogels were successfully synthesized by Burpo et al. via a direct solution-based method.[130] Dimethylamine borane (DMAB) and sodium borohydride were used to reduce the noble metal salt solutions. Reduction occurs fast (within seconds or minutes) and if it is carried out above a critical concentration results in gels, which could then be freeze-dried to aerogels. High surface area, capacitance and conductivity of those aerogels allows their application in catalytic, energy storage and sensor applications. Previously, noble metal aerogels (both monometallic and multimetallic) were also prepared via sol-gel process either through gelation of noble metal nanoparticles, which in turn were already prepared by reduction of noble metal precursor solutions, or by a single step spontaneous gelation process.[131]

On the other hand, S. L. Brock's group has extensively studied the synthesis of metal chalcogenide aerogels through sol-gel pathways. The general method involves synthesis of metal chalcogenide nanoparticles, followed by complexation with a thiolate

ligand, and then controlled oxidation of thiolate groups resulting in the formation of wet-gels, which could be supercritically dried to aerogels. Different metal chalcogenide aerogels like CdS, CdSe, PbS, ZnS, and CdTe were synthesized using this process.[132] Along the way, for the first time, phosphide aerogels based on InP nanoparticles were reported in 2013 followed by the synthesis of Ni_2P nanoparticle-based aerogels in 2014.[133] These phosphide aerogels show many applications in catalytic reactions namely hydrodesulfurization (HDS), hydrodenitrogenation (HDN), hydrodeoxygenation (HDO), and hydrogen evolution reaction (HER).[134]

1.6.5. Metal Aerogels via Carbothermal Reduction. Several other metal aerogels seem to serve as viable alternatives to precious metal aerogels with applications in energy conversions, biomedicine and catalysis.[135] Kumar et al. synthesized Ni-Fe alloy aerogels by using polydopamine as a carbon source for reducing nickel-iron oxide aerogels.[136] Those materials showed electrocatalytic activity towards the oxygen evolution reaction. After that, Chandrasekaran et al. reported similarly the synthesis of Ni-Fe alloy particles supported on reduced graphene oxide aerogels via the carbothermal reduction of Nickel iron oxide-graphene oxide aerogels at 800 ^{o}C in inert atmosphere.[137]

The performance of energy storage materials depends on the design, structure and properties, which has led to the development of latest energy storage and conversion devices in the form of stretchable lithium ion batteries,[138] and stretchable inorganic solar cells.[139] Those stretchable forms consist of single crystal elements that can be shaped to periodic, wavelike geometries. They can be supported by elastomeric substrates, that allows them to be stretched and compressed to high strain values without damaging the metal structure.

Practically efficient synthesis of metal aerogels through nanosmelting of polymer-metal oxide aerogels was reported by Leventis et al.[140] Here, epoxide-initiated gelation of iron chloride is mixed with resorcinol-formaldehyde and the acidity of the gelling iron oxide network catalyzes the co-gelation of RF network. Pyrolyzing these interpenetrating networks of RF-iron oxide under inert atmosphere at different temperatures ranging from 200 to 1000 ^{o}C results in the formation of porous pig iron.

Along this way, interpenetrating network of polybenzoxazine-iron oxide (PBO-FeOx) similar to RF-FeOx aerogel were synthesized and pyrolyzed at 800 ^{o}C to form iron aerogels. The main drawback about RF-FeOx route was that the resulting iron aerogels were not monolithic. Those porous iron aerogels prepared from PBO-FeOx were infiltrated with oxidizing agents like $LiClO_4$ for demonstrating the capability of those materials to function as energetic materials. But, those iron aerogels retained a small amount of carbon, which is not favorable for these applications. Hence, the final aerogels were further oxidized at 600 ^{o}C in air followed by reduction in H_2 at 800 ^{o}C to produce highly crystalline, pure iron aerogels. It was observed that these final aerogels could perform as explosives when loaded with oxidizers and ignited in air. Increasing the temperature of the final reduction step to 1200 ^{o}C resulted in aerogels that could act as thermites. So, the final part of dissertation explains the effect of final reduction temperature on the explosive versus thermite behavior of iron aerogels when infiltrated with $LiClO_4$ and ignited in air. Changes in the morphology, particle sizes through N_2 sorption, mechanical properties and electrical conductivity of the iron aerogels were also studied as a function of the final reduction temperature. The properties mentioned above were related to the ignition behavior of oxidizer-loaded iron aerogels. Iron aerogels synthesized here showing thermite

behavior can be used as heat sources for thermal batteries. Traditionally, for activating thermal batteries, the heat source was pyrotechnic pellets. Those pellets were a compressed mixture of Fe and $KClO_4$ and changing the mole ratio of Fe and $KClO_4$ gave rise to different heat release rates.[141] The technology described in this dissertation deals with the mechanical strength, cheap raw materials, and better production efficiency of PBO-FeOx derived Fe(0) thermites and explosives.

PAPER

I. SHAPE-MEMORY SUPERELASTIC POLY(ISOCYANURATE-URETHANE) AEROGELS (PIR-PUR) FOR DEPLOYABLE PANELS AND BIOMIMETIC APPLICATIONS

Suraj Donthula, Chandana Mandal, Theodora Leventis,[#] James Schisler,[#] Adnan Malik Saeed, Chariklia Sotiriou-Leventis[*] and Nicholas Leventis[*]

Department of Chemistry, Missouri University of science and Technology, Rolla, MO 65409, U.S.A.

[#]Summer students via the ARO High School Student Apprenticeship Program.

[*]Correspondence: Tel.: 573-341-4391 (NL) 573-341-4353 (CSL). E-mail: leventis@mst.edu, cslevent@mst.edu

Published in *Chemistry of Materials* **2017**, *29*, 4461-4477.

ABSTRACT

Shape memory polymers (SMPs) remember and return to an original shape when triggered by a suitable stimulus, typically a change in temperature. They are pursued as cost-effective, low-density, higher-strain-tolerant alternatives to shape memory alloys. Arguably, *porous* SMPs may offer the near-ultimate refinement in terms of density reduction. To that end, shape memory polymeric aerogels (SMPAs) may offer a viable approach. The necessary condition for SMPs is rubber-like superelasticity, which is introduced via crosslinking. Crosslinking is also a necessary condition for inducing phase separation during solution-phase polymerization of suitable monomers into 3D nanoparticle networks. Such networks form the skeletal frameworks of polymeric aerogels.

Those principles were explored here with rigid trifunctional isocyanurate crosslinking nodes between flexible urethane tethers from four short oligomeric derivatives of ethylene glycol: $H(OCH_2CH_2)_nOH$ ($1 \leq n \leq 4$). Formation of self-supporting 3D particle networks depended on the solubility of the developing polymer, which translated into specific combinations of the diol, monomer concentration, and composition of the solvent (CH_3CN/acetone mixtures). Those parameters were varied systematically using statistical design-of-experiments methods. The skeletal frameworks of the resulting poly(isocyanurate-urethane) (PIR-PUR) aerogels consisted of micron-size particles. Bulk densities were in the 0.2-0.4 g cm^{-3} range, and typical porosities between 70% and 80% v/v. Glass transition temperatures (T_g) varied from about 30 ^oC (n=4) to 70 ^oC (n=1). At and above T_g, all SMPAs showed rubber-like elasticity. They also became stiffer after the first stretching cycle, which was traced to maximization of H-bonding interactions ($NH^{\cdots}O=C$ and $NH^{\cdots}O(CH_2)_2$). Below the T_g zone, the elastic modulus of all formulations decreased by about 1000 fold. That property gave rise to a robust shape memory effect (SME), the quality of which was evaluated via several figures of merit that were calculated from tensile stretching data over five temperature cycles between T_g+10 ^oC and T_g–40 ^oC. All thermomechanical testing was carried out with dynamic mechanical analysis (DMA). The strain fixity was always >98%, pointing to very low creep. After the first cycle, strain recovery (a measure of fatigue) improved from 80-90% to about 100%, and the fill factor, a cumulative index of performance, reached 0.7, which is in the range of fast elastomers. The robust shape memory effect was demonstrated with deployable panels and bionic hands capable of mimicking coordinated muscle function.

TOC Graphic.

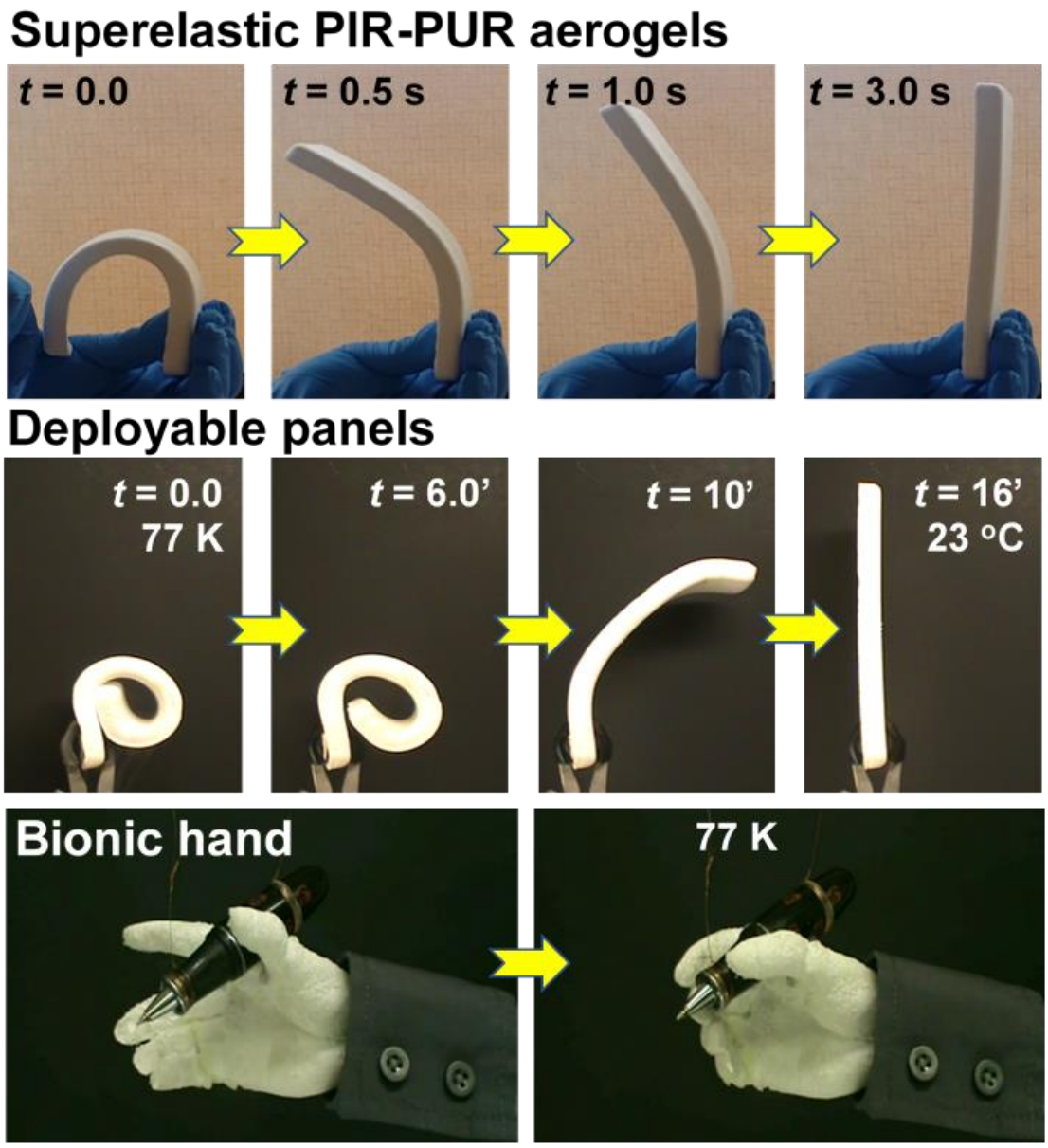

1. INTRODUCTION

Shape memory materials (SMM) remember and return to an original shape. The transition is triggered by light,[1,2] electric[3,4] or magnetic fields,[5] most frequently though by

a change in temperature.[6] The two main classes of SMMs are shape memory alloys (SMAs) and shape memory polymers (SMPs). Application areas range from aerospace (deployable structures),[7] to biomedicine (implantable devices,[8,9] surgical sutures,[10] drug delivery vehicles),[11] to transportation,[12] construction,[13] electronic,[14] textile[15] and various consumer product industries (e.g., as lightweight actuators).[16,17]

The first SMM was a Au-Cd alloy (1930s).[18] Nitinol (a Ni-Ti alloy), arguably the most well-studied material in that class, was introduced in the 1960s.[19,20] Nitinol is a superelastic material, meaning that it recovers its shape after extreme deformations – e.g., after bending by 180^{o}.[21] Superelasticity is a necessary condition for the shape memory effect, but not sufficient: just so it happens, the martensitic phase of Nitinol, which is brought about by lattice deformation under shear stress, is also stable at lower temperatures. Thus, deformation at a higher temperature followed by cooling "freezes" Nitinol to a temporary shape that is retained even after stress is removed. By raising the temperature, the martensitic phase returns to the normal stress-free austenitic phase of the material and the object recovers its original shape. SMAs develop high recovery stresses, in the range of 50-500 MPa, on the downside though they are heavy, costly, and their recoverable transformation strains are low (usually <10% – above that level, deformation causes unrecoverable lattice slippage).[22]

SMPs are high strain-tolerant, lightweight alternatives to SMAs. The first SMP was disclosed in a 1941 patent and was based on a methacrylic acid ester for dental applications.[23] The familiar crosslinked polyethylene-based heat-shrinking tubing was introduced in the 1960s,[24,25,26] however, systematic research on SMPs started picking momentum only in the 1990s.[27,28,29] Superelasticity is again a necessary condition for the

shape-memory effect, but here it is more commonly referred to as "rubber-like elasticity."[30] "Rubber-like elasticity" implies that superelastic polymers are elastomers, thus their response to tensile stress is associated with rigid covalent crosslinking nodes between extendable (i.e., linear) polymeric strands. But, for such elastic behavior, polymeric strands must be free to move in the first place, therefore the polymer must be amorphous and above its glass transition temperature. Thereby, in the simplest form, if an elastomer with a glass transition temperature (T_g) within a range of interest –typically at room temperature or slightly above– is first deformed and then cooled below T_g, segmental motion of the polymeric chains stops, and covalent crosslinking nodes cannot pull the polymer back to its original shape. Raising the temperature back above T_g allows the covalent crosslinking nodes to do their job.

Those principles have been implemented with a wide range of polymers, and combinations thereof in blends and in layers, utilizing for the shape memory effect glass transitions, but also crystallization phenomena.[31,32,33] SMPs include polyacrylate co-polymers,[34] segmented polyurethanes,[35,36] and polyurethane ionomers,[37] poly(ether ether ketone) ionomers,[38] epoxy based polymers,[39] thio-ene based polymers,[40] crosslinked polycyclooctene,[41] polynorbornene,[42] crosslinked ethylene-vinyl acetate copolymers,[43] and various styrene-based polymers.[44]

Perhaps the ultimate refinement in terms of weight reduction in SMM may involve porous polymers. A special class of materials in that category are classified as aerogels and are prepared by drying wet-gels under conditions that preserve the volume of the gel into the final dry object. That process typically involves converting the pore filling liquid into a supercritical fluid (SCF) that is vented of as a gas. In turn, wet-gels are

prepared via a sol-gel process that involves solution polymerization of suitable multifunctional monomers in a suitable solvent.[45,46] For this, covalent crosslinking, *in principle similar to what makes polymers elastomeric*, renders the growing polymer insoluble in the polymerization medium, and induces phase-separation of colloidal polymeric nanoparticles that bear active functional groups on their surface. Moving around randomly, eventually, those polymeric nanoparticles find one another, and get linked via reaction of their surface functional groups into a 3D network that comprises the skeletal framework of the aerogel. By this discussion so far, it may be perceived that shape memory aerogels are mere SMPs in aerogel form. In reality, however, there are conflicting requirements between those two classes of materials. For shape memory elastomers the polymeric strands between crosslinking nodes are typically long by aerogel standards, and if that chemistry is transplanted directly into aerogel synthesis, one will face the fact that longer tethers increase the solubility of the developing polymer. In turn, that causes accumulation of a secondary polymeric layer on the surface of the primary network via reaction of soluble oligomers in the pores with the active functional groups on the nanoparticles.[47,48,49] Upon de-swelling during drying, that continuous secondary layer of polymer pulls the particle network together causing collapse into a more or less dense plastic. Clearly, there is a need for a fine balance between the factors that render a polymer superelastic, and at the same time sufficiently insoluble and able to form a sturdy aerogel skeletal framework. The unsatisfied quest for that balance is what has rendered shape memory aerogels elusive. A closer look at superelasticity and aerogels is therefore in order.

Superelastic aerogels have been described mostly with silica or silica-organic hybrids.[50,51,52,53] The phenomenon has been associated invariably with a spring-back effect

after compression – *not* tension. We are aware of only one recent example of thiol-ene based aerogels that went through temperature cycles, and showed size fixing upon cooling, and recovery upon heating.[54] Again, those materials were tested only under compression. However, folding/unfolding and other complicated deformations typically associated with the shape memory effect require rubber-like superelasticity under tension. In that context, there are numerous literature reports about flexible polymeric aerogels, most notably polyimides,[55] and certain isocyanate-derived aerogels based on polyureas[56] and polyurethanes[49,57] that could be bent by 180^{o}, but rubber-like elasticity is still lacking: only a small fraction, if any, of that deformation could be recovered after stress was removed. Nevertheless, there is a particular class of isocyanate-derived polymers, polyisocyanurates (PIRs), which warrants special attention. PIRs come from trimerization of isocyanates and, because of their high thermal stability and low flammability, are pursued as insulation foams, coatings and adhesives.[58,59,60,61] On the down side though, PIRs are friable – they can be easily crumbled. To overcome that issue, commercial PIRs are urethane-modified polymers made by mixing an excess of a diisocyanate with a diol and a suitable catalyst. Reaction of the diisocyanate both with itself and the diol yields isocyanurate rings linked by urethane tethers. In those poly(isocyanurate-urethane) polymers (PIR-PUR), isocyanurate rings play the role of covalent nodes. PIR-PURs are no longer friable, and in many cases elastomeric.[62,63]

Along the molecular design principles of PIR-PUR, Scheme 1 shows the monomers and the reaction pathway employed in this study towards shape memory aerogels. For closer control of the properties of the polymer we opted against simultaneous formation of the isocyanurate rings and the polyurethane tethers. Instead, the isocyanurate crosslinking

nodes were introduced separately as part of the monomer, by using a commercial triisocyanate derivative of aliphatic hexamethylene diisocyanate (N3300A – see Scheme 1), which combines the rigidity of the isocyanurate ring with the flexibility of the $–(CH_2)_6–$ tethers. The diols were variable-length derivatives of ethylene glycol (EG), and were chosen over, for example, hydrocarbon alternatives, because of the possibility for H-bonding with the urethane groups of neighboring polymeric branches. Chances for H-bonding, which could be enhanced with longer diols, would reduce molecular slippage and macroscopic creep, thus favoring elastic over plastic behavior. On the other hand, though, longer diols would enhance segmental motion of inter-nodal tethers, which could be desirable in terms of lowering glass transition temperatures into a useful range, but they could also increase plasticity. Furthermore, it was also understood that increasing the length of the diol would necessarily increase the solubility of the developing polymer, which would increase the particle size, consequently would decrease surface areas, and would compromise thermal conductivity. However, such a departure from typical aerogel properties was deemed acceptable given our objective towards low-density shape-memory materials rather than more conventional aerogel applications (e.g., in thermal insulation). In practice, particle sizes, and secondary polymer accumulation on the primary network were controlled not only via the chemical identity of the diol, but also via the sol concentration, and via the gelation solvent, which was varied from pure acetonitrile to a 1:1 v/v mixture of acetonitrile/acetone.

Materials are described in terms of their chemical composition, micromorphology and thermomechanical properties. The shape memory effect was quantified with several figures of merit that include the shape fixity ratio, the strain recovery ratio, the strain

recovery rate and the fill factor. Varying the alcohol affected the glass transition temperature, which, in the case of TEG translated into shape-recovery activated at room temperature. That accounts for the most dramatic demonstration of the shape memory effect in terms of potential applications in deployable panels and biomimetic devices.

2. RESULTS AND DISCUSSION

2.1. SYNTHESIS AND CHEMICAL IDENTIFICATION OF POLYISOCYANURATE AEROGELS

The reaction of Scheme 1B was implemented according to the protocol of Scheme 2A. The urethane formation was catalyzed by dibutyltin dilaurate (DBTDL) in a 1:120 mol/mol ratio relative to N3300A, and gelation took place at room temperature. Monomers were used at their stoichiometric amounts (triisocyanate:diol = 2:3 mol/mol). Wet-gels were aged up to 16 h to ensure complete reaction and were dried to aerogels by extracting the pore-filling solvent with liquid CO_2, which, at the end, was converted to a supercritical fluid (SCF) and was vented off as a gas. Sols were prepared in acetonitrile:acetone mixtures from 50:50 v/v to pure CH_3CN. The total monomer concentration was varied between 15% and 25% w/w. The ranges of the solvent ratio and the monomer concentration were based on screening experiments with TEG-based PIR-PUR aerogels, in which we looked for low-density materials demonstrating room-temperature rubber-like superelasticity similar to that of alloys,[21] as shown in Figure 1. Such TEG-based samples either above the selected concentration range, or prepared in sols consisting of more than 50% v/v acetone seemed to collapse into dense “plastics.” Below the selected concentration range, if sols could still form gels, the resulting aerogels did not seem to have the strength to “lift” themselves up

as in Figure 1. Samples prepared in pure acetonitrile did not seem to show optimal performance in terms of their recovery time (Figure 1). Since those two exploratory variables, monomer concentration and solvent composition, seemed to have a similar effect in terms of their ability to form low-density rubber-like superelastic materials, it was deemed reasonable that their effects were coupled. Thereby, for the purposes of the protocol of Scheme 2A, sample preparation with each diol was guided by response surface methodology implemented with a central composite rotatable design model (CCRD – see Appendix I in the Supporting Information),[64,65,66] in which point selection in the domain of the exploratory variables was carried out using the JMP11 software package,[67] from the perspective of a subsequent quadratic dependence of the derived properties (e.g., density, porosity, modulus etc.) on the exploratory variables.[68]

Individual samples are referred to as **ALC-xx**, according to their diol (ALC) and their position (**-xx**) on the rotatable domain. The design space is summarized in Scheme 2B. The exact formulations are tabulated in Tables S.1 and S.2 of Appendix I in the Supporting Information, along with the phenomenological gelation times. Here, in brief, **ALC-1** / **ALC-10** correspond to the middle V_{CH3CN}/V_{sol_Total} ratio (0.75), and th low/high monomer concentrations, respectively. The central point of the design was repeated twice (**ALC-5** and **ALC-6**). Even numbered **ALC-2**, **ALC-4** and **ALC-8** correspond to higher V_{CH3CN} sols. Odd numbered **ALC-3**, **ALC-7** and **ALC-9** correspond to acetone-rich sols.

The chemical composition of **ALC-xx** was confirmed with solid-state CPMAS ^{13}C and ^{15}N NMR (Figure 2). Insight to non-covalent interactions (H-bonding) was obtained with ATR FTIR and is discussed in Section 2.3.2 below in conjunction with the thermomechanical properties of **ALC-xx**. The $N^{13}\underline{C}O$ and $^{15}\underline{N}CO$ resonances of the

isocyanate (expected at 122 ppm and 28.5 ppm, respectively) were absent from all the ^{13}C and ^{15}N NMR spectra, pointing to complete reaction.

The ^{13}C NMR resonances at 149.8 ppm and 157.2 ppm were assigned to the isocyanurate and the urethane carbonyl (–NH(C=O)O–), respectively. The resonances at 61.8 and 70.6 ppm were assigned to the aliphatic carbons of ALC, and the relative intensity of the two resonances changed from **EG-xx** to **TTEG-xx**, as expected from the number of internal vs. terminal –OCH_2CH_2– groups sandwiched between two urethane groups. The remaining two peaks in the aliphatic region, at 43.0 and 27.7 ppm, were assigned to the –CH_2– groups of N3300A (Scheme 1A). Interestingly, the urethane carbonyl resonance at 157.2 ppm (–NH(C=O)O–) was sharper in **EG-xx** and **DEG-xx**, and became progressively broader in **TEG-xx** and **TTEG-xx**. In the solid-state ^{15}N NMR spectra, the resonance at 138.0 ppm was assigned to the isocyanurate ring, and the one at 80.5 ppm to the urethane nitrogen. No resonance was detected in the 50-60 ppm region that could be assigned to –NH_2 from hydrolysis of unreacted –NCO.[56] Just like in the solid-state ^{13}C NMR spectra, again, we noted a progressive peak broadening of the –NH(C=O)O– resonance, which became most prevalent in **TTEG-xx**. Peak broadening in both the ^{13}C and ^{15}N NMR spectra of the –NH(C=O)O– group signifies that as the length of ALC increased, urethane groups found themselves in more diverse environments and/or H-bonded.

2.2. GENERAL MATERIAL PROPERTIES, MICROMORPHOLOGY, AND THE GROWTH MECHANISM OF ALC-XX FROM AN EXPLORATORY VARIABLE PERSPECTIVE

Relevant material properties of ALC-xx are summarized in Table S.3 of Appendix II in the Supporting Information. Here, in graph form, Figure 3 compares shrinkage, bulk

densities and porosities of all **ALC-xx** as a function of their position in the domain of the exploratory variables (i.e., the sol composition). For quick reference, that domain is reproduced as a separate frame in Figure 3. Most **ALC-xx** aerogels shrunk roughly 20% to 25% in linear dimensions relative to the molds. Samples that stand out are all **TTEG-xx** aerogels, except **TTEG-2** and **TTEG-4** (pointed at by gray arrows), and **TEG-7**, **TEG-9** and **TEG-10** (pointed at by blue arrows). **TTEG-2** and **TTEG-4** shrunk less (29% and 31%, respectively) than the other **TTEG-xx** (40%-50%); **TEG-7**, **TEG-9** and **TEG-10** shrunk more than the other **TEG-xx** samples, in fact in the **TTEG-xx** range (40%-50%). Importantly, *all* shrinkage in *all* samples was observed *exclusively* during drying: even the collapsed samples of Figure 3 (i.e., those that shrunk excessively), showed no shrinkage during solvent exchange, suggesting that: (a) all four polymers were swollen in their wet-gel state; and, (b) no major reorganization of the nanostructure took place during solvent exchanges.[69] High shrinkages were accompanied by high bulk densities (ρ_b) –in some cases >1.0 g cm^{-3}– and low porosities (Π): in most collapsed samples Π<10% v/v.[70] At any rate, the vast majority of **EG-xx**, **DEG-xx** and **TEG-xx** were low-density materials (ρ_b<0.5 g cm^{-3}) with high porosities (mostly 70%-80% v/v). Within their respective ranges, ρ_b and Π followed the general upwards and downwards trends expected by increasing the sol-concentration. Two notable exceptions were **EG-1** and **DEG-1** (pointed with color-coded arrows): although their densities/porosities were not excessive (high/low, respectively), yet those two samples did stand out with densities disproportionally higher, and porosities disproportionally lower than those of the rest of the **EG-xx** and **DEG-xx**. Those two samples were at the lower end of the isocyanate concentration range, and upon closer examination they appeared chalky, could not be machined for mechanical testing, and by

looking back at the gelation process it was noticed that the reaction products looked more like loose precipitates (flocks) rather than colloidal gels.

Overall, considering all information above together, longer TTEG generally caused excessive shrinkage, which, in two cases, **TTEG-2** and **TTEG-4**, could be controlled via the two exploratory variables, namely by keeping the TTEG concentration low, in combination with CH_3CN-rich sols. Similarly, the three **TEG-xx** samples that shrunk excessively (**TEG-7**, **TEG-9** and **TEG-10**) were among those from high TEG concentration sols, in combination with acetone-rich solvent. Clearly, as it has been alluded to already from the preliminary runs (Section 2.1), the effects of the monomer concentration and the solvent composition were coupled.

Excluding only **EG-1** and **DEG-1** (i.e., the two samples that seemingly came from flocks), quadratic fitting of ρ_b to monomer concentration (X_1) and solvent ratio (X_2) according to Eq 1 gave good correlations for all four **ALC-xx**, as shown in

$$\rho_b = A(X_1)^2 + B(X_2)^2 + C(X_1)(X_2) + D(X_1) + E(X_2) + F \quad (1)$$

Figure 4 ($0.917 \leq R^2 \leq 0.945$). Coefficients A-F are cited in Table S.4 of the Supporting Information. It is noteworthy that despite the sudden onset of excessive shrinkage in many samples, density still varied smoothly with X_1 and X_2 in all four **ALC-xx** systems. That finding, together with the fact that shrinkage was observed always at the drying stage, signify that all **ALC-xx** sols followed similar gelation processes, and the resulting aerogels shared some key microscopic/network characteristics, irrespective of their macroscopic appearance (collapsed or otherwise).

The micromorphology of **ALC-xx** was investigated with SEM (Figure 5). All non-collapsed samples consisted of networks of large micron-size spherical particles (see **xx**=2

column of Figure 5). The contact area around the interparticle neck-zones of **EG-xx** was narrow. The particle size first increased in **DEG-xx** relative to **EG-xx**, and then decreased (in **TEG-xx** and **TTEG-xx**), while the interparticle neck-zones became wider, in essence fusing particles together. The two **TTEG-xx** samples that did not collapse (**TTEG-2** and **TTEG-4**), and the three **TEG-xx** samples that *did* collapse (**TEG-7**, **TEG-9** and **TEG-10**) became the experimental and conceptual link between the nanostructures of collapsed and non-collapsed samples. Non-collapsed **TTEG-2** consisted of smaller particles than the other **ALC-2** samples, with enhanced merging at the necks. Non-collapsed **TTEG-4** seemed to consist of even smaller particles shrouded by a layer of polymer thicker than the particles themselves. Importantly, the latter was also the common appearance of all **TEG-xx** samples that *did* collapse (see for example **TEG-7** in Figure 5, as well as **TEG-9** and **TEG-10** in Figure S.3 of the Supporting Information). To recast and summarize, remnants of particles were still discernible in all collapsed samples, but they were smaller and coated with a thick layer of polymer.

Albeit at different length scales (about 100× smaller than what we are dealing with here), particle fusion at higher sol concentrations, just like what we have been able to visualize in Figure 5, has been inferred previously with numerous other polymeric aerogels by comparing particle sizes calculated based on small angle x-ray scattering and gas sorption data.[47,48,49] A universally consistent hypothesis that explains both the previous systems, and the morphological evolution noted in Figure 5 involves formation of a primary network of connected spherical particles, followed by accumulation of a secondary polymer layer, preferably at the points of negative curvature – the interparticle necks. That secondary accumulation of polymer takes place via reaction of soluble oligomers, or yet

unreacted monomer remaining in the pores of the primary network with functional groups on the surface of the particles of the primary network. Clearly, that monomer/oligomer-to-network growth mechanism depends on how fast the primary network is formed, hence on the monomer concentration, and the solubility of the developing polymer. The solubility of the developing polymer depends on the solvent system, and the freedom for segmental motion of the polymer chains. In **ALC-xx** the relevant polymeric segments are the $–(CH_2)_6$-NH(CO)-$(OCH_2CH_2)_n$-O(CO)NH-$(CH_2)_6–$ tethers ($1 \leq n \leq 4$) connecting the isocyanurate nodes, and consist of two fixed-length aliphatic moieties ($–(CH_2)_6–$), and one variable-length ether moiety sandwiched in between. The longer the tether, the more soluble the developing polymer, hence the primary network consisted of smaller particles and secondary polymer accumulation was enhanced. Similarly, secondary polymer accumulation was enhanced with sols richer in stronger H-bonding acetone, which favors solubilization of the developing polymer.[56,71] Now, it was also observed that the more secondary polymer accumulation the higher the chances for excessive shrinkage. Given that *all* samples, no exceptions, shrank only during drying, it is reasonable that de-swelling of particles was uniform, and preserved the morphology and porous structure of the particle network. On the other hand, de-swelling of the polymeric layer from secondary accumulation pulled the particle network together causing collapse. Thereby, success in the synthesis of porous PIR-PUR networks is predicated upon the strength of the primary particle network to support itself and resist stresses developing by de-swelling of the secondary polymer layer. Overall, a viable aerogel network requires synthetic parameters that reach a balance between particle size and thickness of the polymeric layer from secondary accumulation.

2.3. THERMOMECHANICAL CHARACTERIZATION

That was carried out with emphasis on data related to shape memory effects.

2.3.1. Glass Transitions. They were determined with temperature scans using dynamic mechanical analysis (DMA) in a tensile test configuration as described in Experimental. Only lower-density, non-collapsed samples were considered. That excludes **EG-1**, **DEG-1**, **TEG-7**, **TEG-9**, **TEG-10**, and all **TTEG-xx** samples except **TTEG-2** and **TTEG-4**. Typical DMA data are exemplified with **TEG-8** in Figure 6A. At lower temperatures all materials were stiff with elastic moduli, *G´*, about 10 times higher than the loss moduli, *G´´*. As temperature increased, both *G´*and *G´´*started decreasing, crossed one another twice, and eventually got again stabilized at higher temperatures. The final values of both *G´*and *G´´* were about 1000 times lower than their respective low-temperature values, but again G´ was approximately 10 times higher than G´´. Results from repetitive scans of the same samples were practically identical. The glass transition temperatures reported, T_g, are the maxima of tan δ (=G´´/G´). T_g values varied randomly by a few degrees within each **ALC-xx**. As shown in Figure 6B, the average T_g values of the four **ALC-xx** followed the order: $(T_g)_{\mathbf{EG\text{-}xx}} > (T_g)_{\mathbf{DEG\text{-}xx}} > (T_g)_{\mathbf{TEG\text{-}xx}} > (T_g)_{\mathbf{TTEG\text{-}xx}}$, and were spaced approximately 10-20 ^oC apart from one another (for the primary data refer to Table S.5 in the Supporting Information). The glass transition zones were generally narrow. For instance, all full widths at half maxima (FWHM – Table S.5) of all tan δ plots for all **ALC-xx** were in the range of 12.0-17.7 ^oC. As the onset of segmental motion in polymers is typically considered the maximum in the G´´curve (indicated with an arrow in Figure 6A). Those maxima were generally 10-13 ^oC lower than the tan δ maxima (see Table S.5 and Figure S.8 in the Supporting Information), and may be considered either as the upper

temperature limits for fixing the shape of the polymer, or loosely as the onset of shape recovery.

2.3.2. The Elastic Properties of ALC-XX Under Tension: Strain Recovery, Creep and Stress Relaxation as a Function of T_g. As a preamble to the shape memory effect, this Section investigates the elastic properties of **ALC-xx** relative to T_g, confirms that **ALC-xx** can store and keep energy (essential for shape recovery), and explores whether they can do that repetitively. This Section offers also an insight to the molecular rearrangements associated with settling after the first stretching cycle, and in some cases some minor creep afterwards. Those results become important in rationalizing differences in shape recovery rates amongst the various **ALC-xx**. For those purposes, two randomly selected samples, **DEG-4** and **TEG-8**, were tested under tension at three different temperatures, T_g+40 ^oC, T_g and T_g–40 ^oC. That range ensures conditions from well above to well below the glass transition zone (see previous Section). Fresh, as-prepared samples were loaded and unloaded five times with constant force ramp rates to pre-determined strain values; at the end of the fifth loading cycle, samples were step-reloaded to the last strain value, which was maintained while the stress was monitored as a function of time.[72] The ultimate strains at each temperature were set just below the respective failure (snapping) points, and were chosen (based on preliminary runs) in a way that would accommodate all five cycles (i.e., accounting for creep). The behavior of both **DEG-4** and **TEG-8** was very similar in all aspects. The results with **TEG-8** are shown in Figure 7 (for the results with **DEG-4** see Figure S.9 of Appendix VII in the Supporting Information). Referring to **TEG-8** and Figure 7, at both T_g and T_g+40 ^oC (40 ^oC and 80 ^oC, respectively), samples were essentially linearly elastic. Overall, at T_g, samples were about twice as stiff

as at T_g+40 °C. At both temperatures, samples became stiffer at the second loading cycle and beyond (the stress-strain slope increased). Beyond the second cycle, stress-strain curves were superimposable at T_g+40 °C. At T_g, we noticed a small drift towards larger strains with repetitive cycling (yellow arrow pointing to the right) indicating a small amount of creep. Below the glass transition range (T_g–40 °C = 0 °C), samples were much stiffer (notice the narrow strain range), and repetitive stretching led to accumulation of unrecoverable strains. At T_g+40 °C samples could store and keep >98% of the energy spent for stretching (last frame of Figure 7). That energy was available for recovery of the original dimensions after stress was released. Energy was progressively lost from the stretched state as the temperature was decreased: already at T_g, **TEG-8** lost about 9% of the energy stored. Below the glass transition range (again at T_g–40 °C), the energy lost was about 65% and kept on increasing even after 20 min of constant strain. Energy loss notwithstanding, stress relaxation was fast at or above T_g, and much slower below the glass transition zone (note the different time scales in the last frame of Figure 7).

There are two possible contributors to settling after the first stretching cycle at T_g and T_g+40 °C, or the subsequent creep at T_g: heating, stretching or both. An insight was obtained with ATR FTIR of several random **ALC-xx** samples. Spectra of a representative sample (**TEG-2**) are shown in Figure 8 (for the others refer to Appendix V in the Supporting Information). Data relevant to this discussion are summarized in Table 1. All spectra were dominated by the isocyanurate carbonyl stretch near 1680 cm^{-1}. The 2300−2000 cm^{-1} region was clean of any unreacted N=C=O stretch in agreement with the solid-state NMR data (Figure 2). The free urethane carbonyl stretch was observed at 1729 cm^{-1} as a shoulder to the intense isocyanurate absorption. Possible carbonyl absorptions of

H-bonded urethane would appear at lower energies, but they were masked by the intense isocyanurate absorption. The N−H bending coupled to C−N stretching gave an absorption at 1529 cm^{-1}.[73] The absorptions at 1240 cm^{-1}, 1129 cm^{-1} and 1049 cm^{-1} were attributed to the ethylene glycol and urethane asymmetric and symmetric C−O−C stretches.[74,75] Using flat baselines from 3050 to 3800 cm^{-1}, the N−H stretch region of all the **ALC-xx** tested was deconvoluted into three absorptions (Figure 8B): one in the 3423-3545 cm^{-1} range (free NH);[76,77] a second one, typically the most intense absorption, in the 3331-3341 cm^{-1} range (NH-bonded to carbonyl: NH···O=C);[77,78] and, a third weaker absorption in the 3204-3234 cm^{-1} range assigned to NH···$O(CH_2)_2$ (NH stretch, H-bonded to glycol groups).[77,79,80] Following the same trend with the progressive broadening of the –NH(C=O)O– resonance in the ^{13}C NMR spectra and the –NH(C=O)O– resonance in the ^{15}N NMR spectra, it is noted that by going from **DEG-2** to **TEG-2** to **TTEG-2**, the absorption intensity ratio of [free NH] : [NH···O=C] : [NH···$O(CH_2)_2$] moved from 4.6/4.4/1.0 to 2.2/7.3/0.5 to 2.2/6.7/1.1 respectively, showing, albeit only qualitatively,[81] an increase of H-bonded NH at the expense of free NH as the length of the ALC increased.

Now, as demonstrated in Figure 8C, a heating cycle above T_g followed by cooling back to room temperature increased the fraction of H-bonded NH. As summarized in Table 1, the new intensity ratio [free NH] : [NH···O=C] : [NH···$O(CH_2)_2$] moved in favor of NH···O=C, at the expense of free NH, becoming 1.6/7.1/1.3, 0.8/8.4/0.8, and, 0.0/8.2/1.8, in **DEG-2**, **TEG-2** and **TTEG-2**, respectively. Next, we investigated the effect of heating above T_g, stretching at that temperature and cooling back to room temperature (Figure 6D). That cycle had a similar effect to just heating-and-cooling; the difference was that a higher portion of free NH would survive the cycle as the ALC became longer (i.e., from DEG to

TTEG). The ratio of [free NH] : [NH···O=C] : [NH···O$(CH_2)_2$] for the three **DEG-2**, **TEG-2** and **TTEG-2** moved to 0.8/7.4/1.8, 1.3/7.7/1.0, and 1.1/7.6/1.3, respectively (Table 1). Similar trends were observed for **DEG-4** and **TEG-8** (data also included in Table 1). In summary, ATR FTIR data have shown that as-prepared **ALC-xx** were in a metastable state. Both heating and stretching were responsible for settling at energy minima that maximized H-bonding interactions. That provides a satisfactory reason for the stiffness increase noted during the first cycle of tensile testing, and the small amount of creep afterwards.

2.3.3. The Shape-Memory Effect (SME). The SME of ALC-xx was demonstrated as shown in Figure 9 with a panel similar to the one used in Figure 1 (**TEG-8**). The strain imposed during bending in Figure 1 was about 25% (calculated from the radius of curvature, *R*, and the thickness of the specimen, *d*, via d/2R). In order to force strains closer to the ultimate strain of that kind of samples (about 60% - see Figure 7), the sample was folded to the tighter radius of curvature as shown in Figure 9. Thus, first, the panel was heated in an oven at T_g+40 ^oC; then it was folded quickly into the spiral form of Figure 9, and that shape was fixed by dipping the folded object in liquid N_2. As the spiral form warmed up to ambient temperature, it unfolded to its original shape.

The SME was quantified formally for all non-collapsed **DEG-xx**, **TEG-xx** samples as well as **TTEG-2** and **TTEG-4** via three individual figures of merit (the strain fixity, the strain recovery, and the strain recovery rate), and a cumulative one (the fill factor). Those figures of merit were calculated from tensile testing data derived from five temperature-stretch-relaxation cycles as demonstrated in Figure 10 (for clarity, the 3D graph is shown from two perspectives).[82]

All first cycles started with fresh, as-prepared samples. In Stage 1 samples were first equilibrated for 5 min at their deformation temperatures ($T_d = T_g + 10$ °C), and then were stretched at 1N min^{-1} near to their stretch limit (typically around 60% strain). In Stage 2 (blue line), stress was kept constant at the maximum value attained in Stage 1, and samples were cooled at 5 °C min^{-1} to their fixation temperature (T_f, well below T_g), where they were allowed to equilibrate for 5 min. In Stage 3, the tensile force was decreased to 0.01 N (i.e. stress was practically removed), samples were allowed to relax (fix) isothermally at T_f for 15 min, and the strain was recorded for the duration. Finally, in Stage 4, strain was recorded while samples were heated at 1 °C min^{-1} (red lines) to their recovery temperatures ($T_r = T_d = T_g + 10$ °C). Cycle 2 and subsequent cycles started after an isothermal hold at T_d for 15 min. As expected from the stress-strain curves of Figure 7, all four stages of the thermal cycle curves coincided almost precisely in cycle 2 and above, pointing to a robust SME.

In order to calculate the SME figures of merit, the thermal cycles of Figure 10 were transformed and projected to selected faces of the 3D representations, as follows. First, since the temperature was cycled at fixed rates, each point along the 3D curve is uniquely defined by time. Figures 11A and 11B are such unfolded-in-time projections of the 3D curves to the strain-temperature (bottom) plane of Figure 10A, or equivalently, to the rear plane of Figure 10B. Figure 11A shows the strain along a random temperature cycle (after the first), while Figure 11B shows the strain during the first two cycles. Figure 11C is the direct projection (no time unfolding) from the perspective of Figure 10B of one full random cycle to the strain-temperature (rear) plane. All figures of merit, of all samples over all

cycles are summarized in Table S.6 of Appendix VIII in the Supporting Information. In graph form, results from the first and fifth cycles are shown in Figure 12.

The strain fixity ratio, $R_f(N)$, quantifies creep during Stage 2 (i.e., during cooling under constant stress), and was calculated for each cycle, N, from the data like those of Figure 11A via Eq 2. (The definition of the two strain values, ε_u and ε_m, are given directly

$$R_f(N) = \frac{\varepsilon_u(N)}{\varepsilon_m(N)} \times 100 \quad (2)$$

in Figure 11A). In agreement with Figure 7, whereas above T_g there is virtually no creep, by and large strain fixity in all cycles, including the first one, was always >98% (Table S.6.1).

The strain recovery ratio, $R_r(N)$, quantifies fatigue from repetitive cycling and, just like $R_f(N)$, it was also calculated from the data of Figure 11A using Eq 3. Reflecting

$$R_r(N) = \frac{\varepsilon_m(N) - \varepsilon_p(N)}{\varepsilon_m(N)} \times 100 \quad (3)$$

the increase in stiffness observed after the first cycle, all strain recovery values started lower in the first cycle (80-90%), increasing and stabilizing thereafter to values >98%. (The increase of $R_r(N)$ beyond the first cycle is already evident from the data shown in Figure 12, but for the near-stabilization just after $N \geq 2$, refer to Table S.6.2.)

The strain recovery rate, $R_t(N)$, is an index introduced in this study in order to quantify and compare the relative speed of strain recovery at the heating Stage 4 among different samples and cycles. $R_t(N)$ is defined via Eq 4 as the maximum slope of the strain

$$R_t(N) = \max\left[-\frac{dStrain}{dt}\right] \quad (4)$$

vs. time curve during heating in Stage 4 (refer to the red line in Figure 11B). Since the strain recovery of Stage 4 did not take place at the natural warm-up rate of the material, but instead it was driven by the imposed heating rate, it was deemed necessary to repeat the experiment at different heating rates (using fresh samples each time), and observe the effect on the rate of recovery (Figure 13). Thus, it is noted that during all cycles, $R_t(N)$ followed a near-linear relationship with the heating rate up to 5 $^oC\ min^{-1}$; therefore, different $R_t(N)$ values reflected steeper recovery curves, or equivalently more narrow temperature windows of recovery. The obvious place to look for supporting evidence for that conclusion was the width of the tan δ plots, but we were unable to find any meaningful correlation between $R_t(N)$ (from Table S.6.3) and the FWHM of tan δ (from Table S.5). Thereby, we concluded that the stretched, frozen starting point of the shape recovery (Stage 4) represented a different state of **ALC-xx** from the as-prepared samples. According to Table 1, that state was most probably characterized by an enhanced amount of H-bonding relative to the innate (as prepared) state of **ALC-xx**. In that regard, it is worth nothing that the highest recovery rate was observed with **DEG-4**, which, based on the IR data of Table 1, did not show any free NH after one heating-stretching cycle.

Finally, the fill factor, *FF(N)*, has been proposed as a combined index of performance,[83] and was calculated from the ratio of the shaded S-shaped area to the total area of the "box" shown in Figure 11C. Obviously, calculation of that ratio is sensitive to the upper and lower temperature limits. As a conservative upper limit we took the maximum temperature for all experiments, T_g+10 ^oC (against the recommended T_g+20 ^oC). The selection of the lower limit, namely the onset of recovery (Stage 4), was based on $R_t(N)$ as follows: first, we noted the temperature of the maximum slope (Eq. 4) of the

corresponding Figure 11B of every **ALC-xx** in every cycle; then we located the temperature at the foot of Stage 4 where the recovery rate was at just the 3% of the maximum rate. That temperature was set as the onset of recovery in every Figure 11C. By its construction, *FF(N)* combines contributions from all three $R_f(N)$, $R_r(N)$, $R_t(N)$, and was also monitored and recorded for all samples during all five cycles. Fill factors (Figure 12, Table S.6.4) started lower in the first cycle, but generally no lower than 0.5 (except for **TTEG-4**, where $FF(1)$=0.4). After samples were broken-in in their first cycles, all fill factors were over 0.60, most over 0.65, and in some cases reached 0.70. Those fill factors are in the range for high-speed elastomers and are considered high.[83,84]

Overall, the strategy of using poly(isocyanutate-urethane) aerogels as lightweight alternative to shape memory polymers has been fruitful, leading to materials showing a robust shape memory effect. According to Figure 9, **ALC-xx** can very well serve as deployable panels in applications where weight is at a premium, e.g., as mirrors or antennas in space. Figure 14 shows that **ALC-xx** can also be molded into complex shapes and programmed to perform more advanced functions mimicking, for example, the complicated muscle coordination of a human hand holding a pen. The slow recovery reported in Figure 14 should not be considered as a deterrent. In practice, fast recovery will be driven by heating with a thin wire resistor embedded with an object.

3. CONCLUSION

As a polymeric class, polyisocyanurates have received a low level of attention as base-materials for polymeric aerogels. As shown here though, the isocyanurate ring can be an effective crosslinking node for imparting both rubber-like elasticity and insolubility of

a developing polyurethane network. Both are necessary conditions for the shape-memory effect, and the synthesis of polymeric aerogels, respectively. Given the specific triisocyanurate node used in this work (a hexamethylene diisocyanate derivative), longer diols (selected from the ethylene glycol family), and solvents with enhanced H-bonding ability (like acetone) lead to extensive shrinkage and dense polymers, thereby they were not suitable for shape memory aerogel synthesis. Once the correct conditions were identified with the help of design-of-experiments statistical methods, poly(isocyanurate-urethane) aerogels showed a robust shape memory effect with high fixity and recovery ratios and fill factors. Since aerogels are low-density materials, large-scale applications of shape memory polymers, as in deployable panels and biomimetic devices, are becoming material-efficient, and within reach. Owing to the necessary compromise between conflicting requirements for rubber-like superelasticity and particle network formation, the aerogel framework of **ACL-xx** consisted of large particles (by aerogel standards). As represented in the Introduction, aerogels with nanostructures consisting of large particles may not be suitable for typical aerogel applications like in thermal insulation. Nevertheless, preliminary results show that the room temperature thermal conductivity of several **ALC-xx** selected randomly was in the 0.052±0.005 W m^{-1} K^{-1} range, namely similar to several commercial thermal insulators like glass or rock wool. Interestingly, filling the pores of **ALC-xx** with silica aerogel (0.015 W m^{-1} K^{-1}) caused a drop of the thermal conductivity to around 0.027 W m^{-1} K^{-1}, namely within a range accessible mainly by aerogels. The properties of those composites are under further investigation.

4. EXPERIMENTAL

4.1. MATERIALS

All reagents and solvents were used as received unless noted otherwise. The isocyanurate node (N3300A) was obtained courtesy of Covestro LLC (Pittsburg, PA) under the trade name Desmodur N3300A. Diols (ALC): ethylene glycol (EG), diethylene glycol (DEG), triethylene glycol (TEG), tetraethylene glycol (TTEG); the catalyst: dibutyltin dilaurate (DBTDL); and, solvents: anhydrous acetonitrile and anhydrous acetone were purchased from Sigma-Aldrich. Siphon-grade CO_2 was purchased from Ozark Gas Co.

4.2. SYNTHESIS OF SHAPE MEMORY POLY(ISOCYANURATE-URETHANE) AEROGELS

In a typical process, N3300A as received (Desmodur N3300A, 0.504 g, 1.00 mmol) and the respective diol (EG, DEG, TEG and TTEG, 1.50 mmol) were dissolved in an anhydrous acetonitrile/acetone mixture according to a central composite rotatory design (CCRD) model (Appendix I in Supporting Information). The solution was stirred in a three-neck round-bottom flask at 23 °C under N_2 for 10 min, and DBTDL (5 μL) was added. The resulting sol was stirred for another 5 min and was poured into molds. Smaller rectangular specimens for dynamic mechanical analysis were cut from cylindrical samples prepared using plastic syringes as molds (All Plastic Norm-Ject Syringes, 20 mL, Fisher Scientific Catalogue No. 14-817-32, 2.53 cm inner diameter). Larger rectangular samples (e.g., Figures 1 and 9) were prepared using plastic containers (Style Selections 16”×12.75” Plastic Multi-Use Insert Drawer Organizer, Model No. 39001, Lowe’s Item No. 105922). Molds for bionic hands (Figure 14) were prepared via a 3-stage process: first the negative

of a volunteer's hand was reproduced into Alja-Safe (Crystalline Silica-Free Alginate for Molding Body Parts);[85] plaster (DAP 4-lb Carton Plaster of Paris Model 10318, Lowe's Item No. 41323) was cast into the alginate mold in order to produce the exact (positive) replica of the hand; finally, the plaster mold was used to make the final mold using AeroMarine Products AM 128 Silicone Mold Making Rubber RTV.[86] Molds were sealed with Parafilm^{TM} and were kept at room temperature for gelation. The gelation time varied from 7 min to about 3h 40 min depending on the chemical identity of the alcohol, the monomer concentration and the fraction of CH_3CN in the solvent system. Gels were aged for 24 h in their molds at room temperature. Subsequently, gels were removed from the molds, washed with acetone (4×8h, using 4× the volume of the gel each time), and were dried with CO_2 taken out as a supercritical fluid (SCF). Samples are referred to as **ALC-xx** where **ALC** stands for the abbreviation of the diol (Scheme 1), and **xx** denotes the position in the domain of the independent variables domain (Scheme 2B).

4.3. METHODS

4.3.1. Drying. Drying of wet-gels was carried out in an autoclave (SPIDRY Jumbo Supercritical Point Dryer, SPI Supplies, Inc. West Chester, PA, or a Spe-edSFE system, Applied Separations, Allentown, PA). Samples were loaded into the autoclave at room temperature, and were covered with acetone. The pressure vessel was closed and liquid CO_2 was allowed in at room temperature. Acetone was drained out from the pressure vessel, while more liquid CO_2 was allowed in. Samples were kept under liquid CO_2 for one hour. Then liquid CO_2 was drained out while more liquid CO_2 was allowed in. The cycle was repeated several times until all acetone had been extracted out of the pores of the

samples. Subsequently, the temperature of the autoclave was raised to 40 ºC and that condition was maintained for two hours. Finally, supercritical fluid (SCF) CO_2 was vented off as a gas.

4.3.2. Chemical Characterization. Solid-state CPMAS ^{13}C-NMR spectra were obtained with samples cut into small pieces on a Bruker Avance III 400 MHz spectrometer with a carbon frequency of 100 MHz, using a 7 mm Bruker MAS probe at a magic angle spinning rate of 5 kHz, with broadband proton suppression, and the CP TOSS pulse sequence. The Total Suppression of Spinning Sidebands (TOSS) pulse sequence was applied by using a series of four properly timed 180º pulses on the carbon channel at different points of a cycle before the acquisition of the FID, after an initial excitation with a 90º pulse on the proton channel. The 90º excitation pulse on the proton and the 180º excitation pulse on carbon were set to 4.2 µs and 10 µs, respectively. A contact time of 2 ms was used for cross polarization. Solid-state ^{13}C NMR spectra were referenced externally to glycine (carbonyl carbon at 176.03 ppm). Chemical shifts are reported versus TMS (0 ppm). Solid-state CPMAS ^{15}N-NMR spectra were also obtained on the same Bruker Avance III 400 MHz Spectrometer with a nitrogen frequency of 40.557 MHz , using a 7 mm Bruker MAS probe with broadband proton suppression and magic angle spinning rate of 5 kHz. For cross polarization, a 90º proton excitation pulse was set to 4.2 µs with 2 ms contact time. Chemical shifts are reported versus liquid ammonia (0 ppm) and were externally referenced to glycine (amine nitrogen at 33.40 ppm). In all solid-state NMR experiments the relaxation delay was set at 5 s.

Attenuated total reflectance (ATR) FTIR spectroscopy was carried out with a Nicolet-FTIR spectrometer Model 750, equipped with a ATR accessory Model 0012-

3XXT. Samples were cut to the size of the ATR crystal (ZnSe, rectangular, 20 mm × 50 mm) and ATR-FTIR spectra were obtained by pressing them against the crystal with the ATR unit's pressure device (gripper). Maximum throughput of the infrared beam to the detector was achieved via optical alignment that was performed with no sample on the crystal. Data were collected at an incident beam angle of 45^{o}, over 32 scans with a resolution of 2 cm^{-1}. In the ATR mode, the penetration depth (pd), and thereby the effective path length (=number of reflections × dp) of the infrared beam is directly proportional to the wavelength. Thereby, an ATR correction was applied to the raw data by multiplying the spectra with a wavelength-dependent factor (roughly $\lambda/5$) that adjusts the relative peak intensities. In order to evaluate H-bonding, the ν(N-H) bands were deconvoluted into three Gaussian-shaped peaks. Peak curve-fitting was performed using the Origin 8.5 software package.

4.3.3. Physical Characterization. Bulk densities (ρ_b) were calculated from the weight and the physical dimensions of the samples. Skeletal densities (ρ_s) were determined with helium pycnometry using a Micromeritics AccuPyc II 1340 instrument.

4.3.4. Structural Characterization. That was carried out using Scanning electron microscopy (SEM) with Au-coated samples on a Hitachi Model S-4700 field-emission microscope.

4.3.5. Thermomechanical Characterization. That was carried out in the tension mode with a TA Instruments Q800 Dynamic Mechanical Analyzer (DMA) equipped with a tension clamp (TA Instruments part No. 984016.901). All specimens for testing had a rectangular geometry (length: 20 mm; width: 15 mm; thickness: 3-4 mm) in the spirit of ASTM D790-10[87] and ASTM D4065;[88] they were cut off with a knife under N_2 in a glove

box, from larger cylindrical samples dipped in liquid N_2. In order to ensure uniform thickness, the surface of all rectangular pieces was smoothened, while still frozen, with a 3 M sand paper (320 grit, part No. 98401). In general, all samples were placed in the load cell at room temperature. The exact length of all samples was measured by the instrument under a small tensile force (0.01 N) that prevents bending. The temperature was stepped to the initial testing temperature, and samples were equilibrated at that temperature for 5 min.

Glass transition temperatures (T_g) were extracted from the viscoelastic properties of the samples, which were measured by applying a continuous sinusoidal oscillation (1 Hz) with a strain amplitude equal to 0.3%, while the temperature was ramped from -150 ^oC to 150 ^oC at 3 ^oC min^{-1}.

Strain recovery (creep) and stress relaxation experiments were carried out at three different temperatures (T_g + 40 ^oC, T_g, and T_g - 40 ^oC) with two samples selected among those with the highest fill factors (**DEG-4** and **TEG-8**). For this, each sample was first stepped, and then equilibrated at the particular temperature for 5 minutes. Subsequently, samples were stretched with a small tensile force (0.01 N), and the length of the sample was measured by the instrument and stored. Each strain recovery cycle begun with a deformation stage wherein the sample was stretched at a constant force rate of 1N min^{-1} up to a final strain, and then the force was released again at 1N min^{-1}. At T_g and T_g+40 ^oC, the final strain was about 50% (i.e., near the sample break point); at T_g–40 ^oC, the final strain was determined by the compliance of the instrument (18 N) and was about 2-4% for **DEG-4** and 0.1% for **TEG-8**. That stress-release cycle was repeated at each temperature five times. After the end of the fifth cycle, the sample was step-stretched to the final strain

reached at the fifth cycle, and that strain was maintained for 20 min while the residual force with which the sample pulls the clamps together was recorded as a function of time.

Shape memory-related properties (strain fixity, strain recovery, strain recovery rates and fill factors) were studied in the controlled force mode as follows: samples were first stepped, and then equilibrated at their deformation temperature ($T_d = T_g + 10$ °C) for 5 min. Subsequently, samples were stretched with a small tensile force (0.01 N), and the length of the sample was measured by the instrument and was stored. Next, specimens were stretched at a constant force rate of 1N min^{-1} up to a little below their break point (typically around 60% strain), and then they were cooled, while under the final stress, at 5 °C min^{-1} to their fixation temperature ($T_f << T_g$). At that point (T_f), samples were equilibrated for 5 min, and the tensile force was reduced to 0.01 N. Samples were allowed to relax (fix) for 15 min (always at T_f), while strain was recorded. Finally, samples were heated at 1 °C min^{-1} to their recovery temperature ($T_r = T_d$) while strain was still recorded. (As a control, a sample was also heated at 3 °C min^{-1} as well as at 5 °C min^{-1}.) Samples were held at T_d of 15 min and the cycle was repeated. Five such cycles were run successively for each sample, and data were analyzed for the fixation and recovery properties.

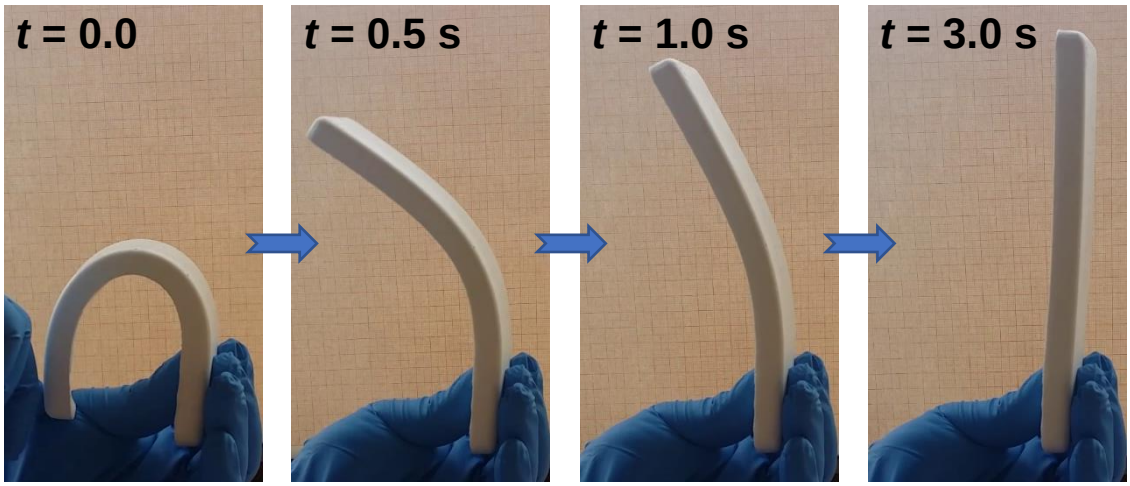

Figure 1. Demonstration of room-temperature superelasticity with a **TEG-8** sample (2´´×8´´, ρ_b= 0.41±0.02g cm^{-3}, Π=67±1 % v/v). Photographs are selected frames from Movie S.1 shown in the Supporting Information.

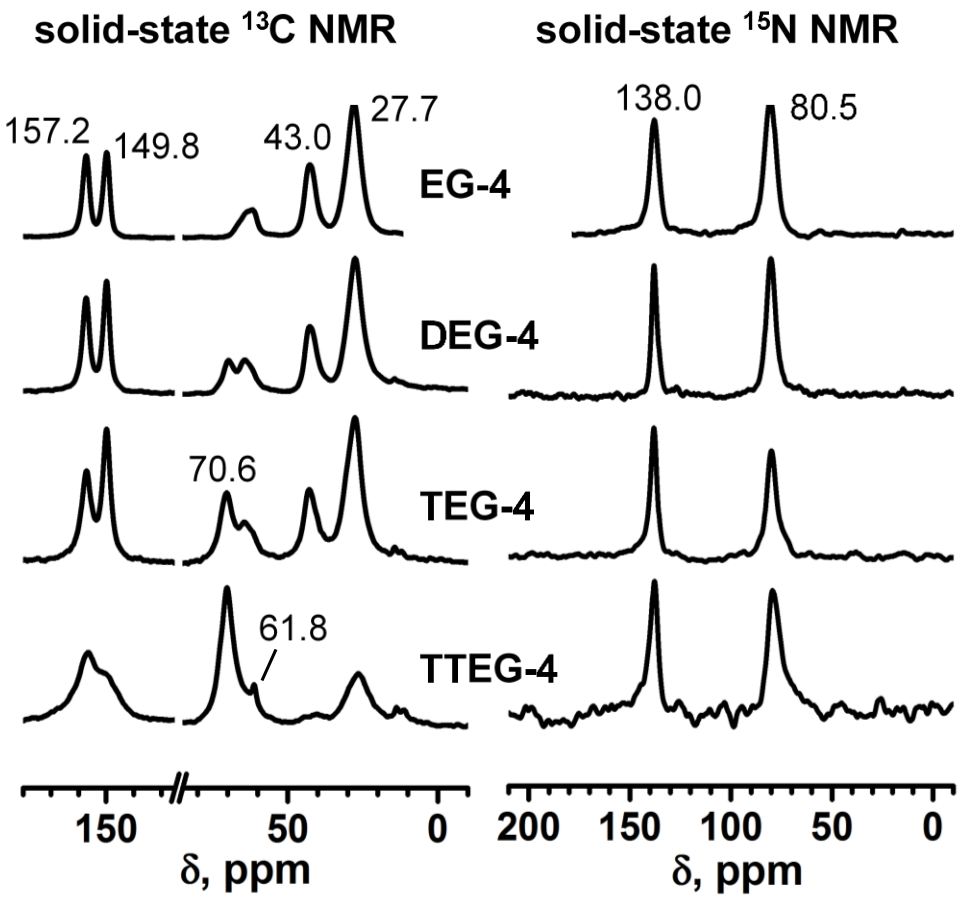

Figure 2. Solid-state CPMAS ^{13}C and ^{15}N NMR of samples as indicated.

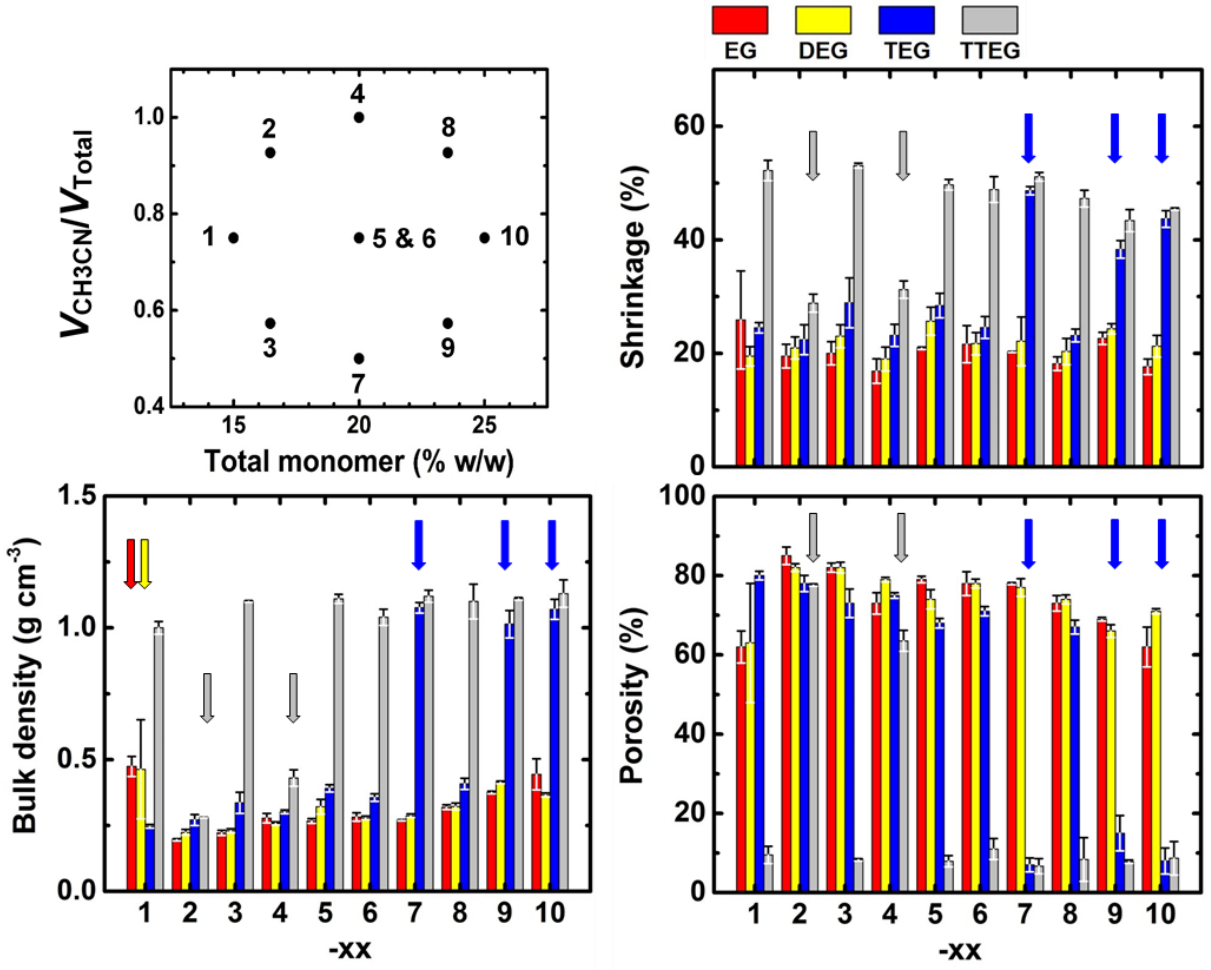

Figure 3. Shrinkage, bulk density and porosity data for all **ALC-xx** samples in the domain of the two exploratory variables (total monomer concentration and solvent ratio). Data were taken from Table S.3 of the Supporting Information. Color-coded arrows point at samples that break the respective "trends'" sort-of-speak and are discussed in the text.

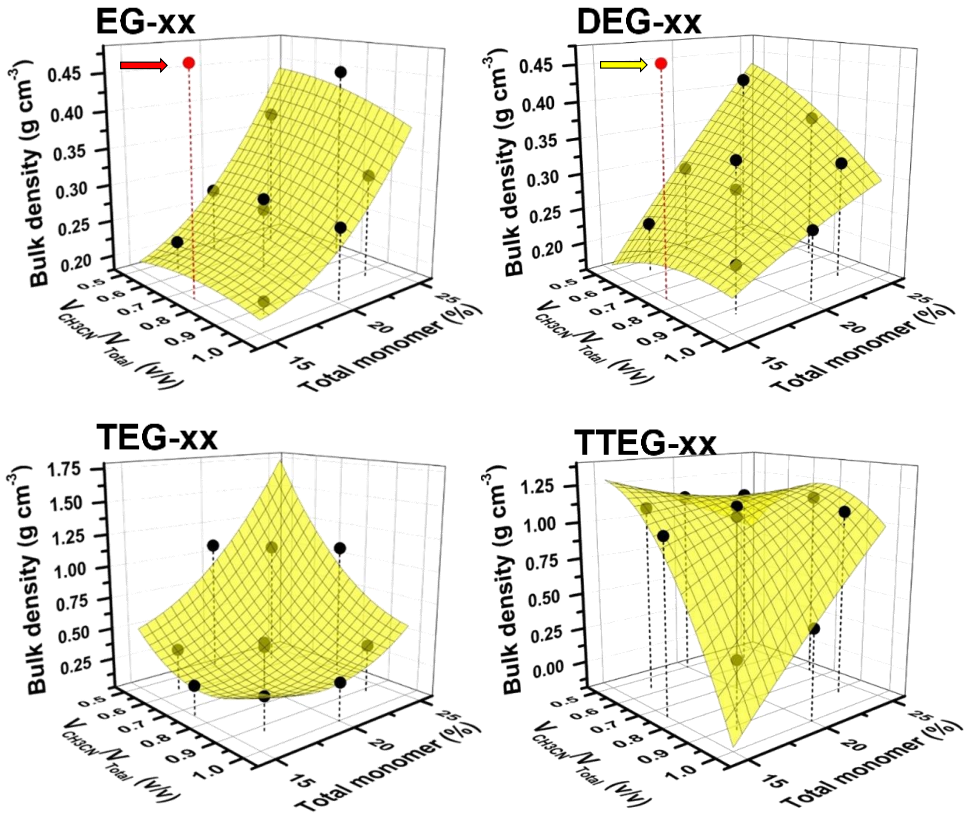

Figure 4. Bulk density data for all **ALC-xx** fitted to the two exploratory variables (monomer concentration and solvent ratio) according to the quadratic model of Eq 1. (Color-coded arrows point at two samples, **EG-1** and **DEG**-2 that could not be fitted by the model. For the coefficients of Eq 1 in all four **ALC-xx** refer to Table S.4 in the Supporting Information.

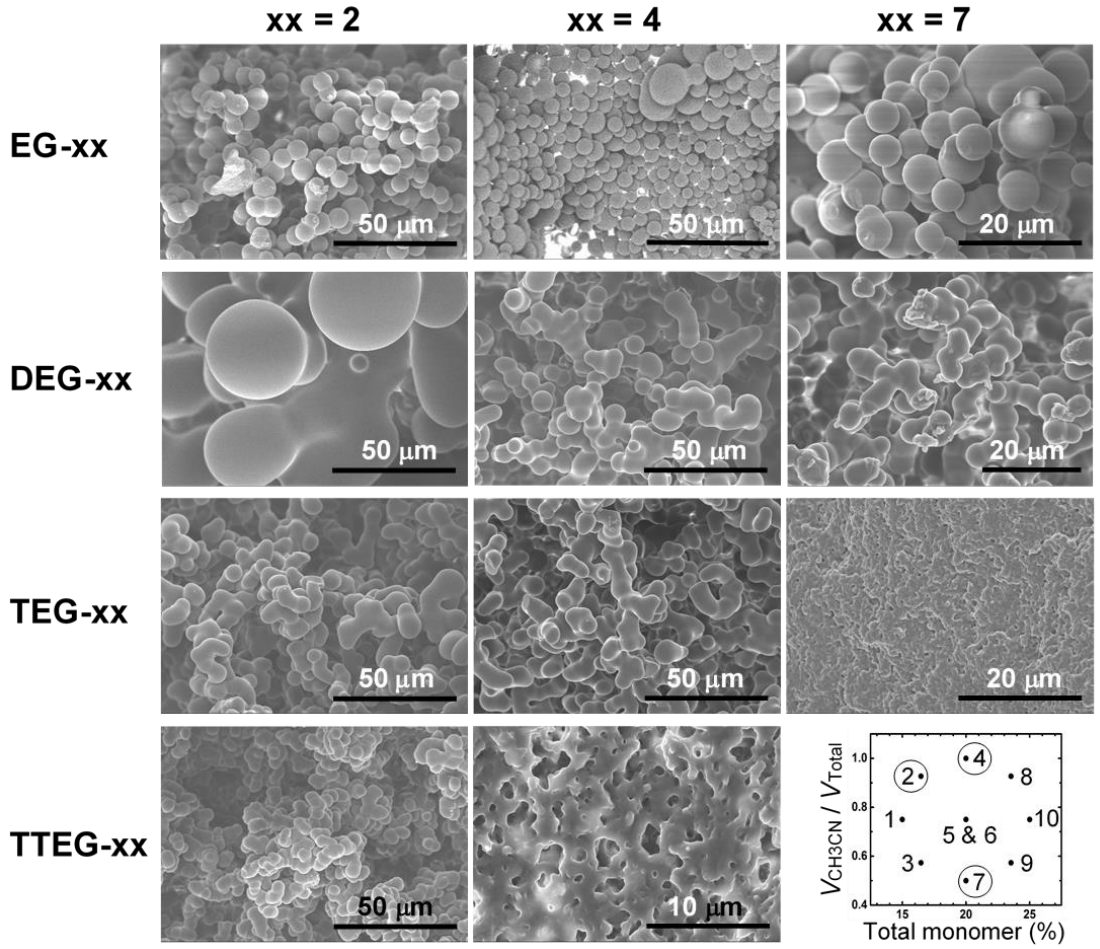

Figure 5. SEM of specific **ALC-xx** samples selected from the domain of the exploratory variable (see lower right frame) for the discussion of the growth mechanism of the solid framework (SEMs of all **EG-xx**, **DEG-xx** and **TEG-xx** samples are shown in Appendix IV of the Supporting Information).

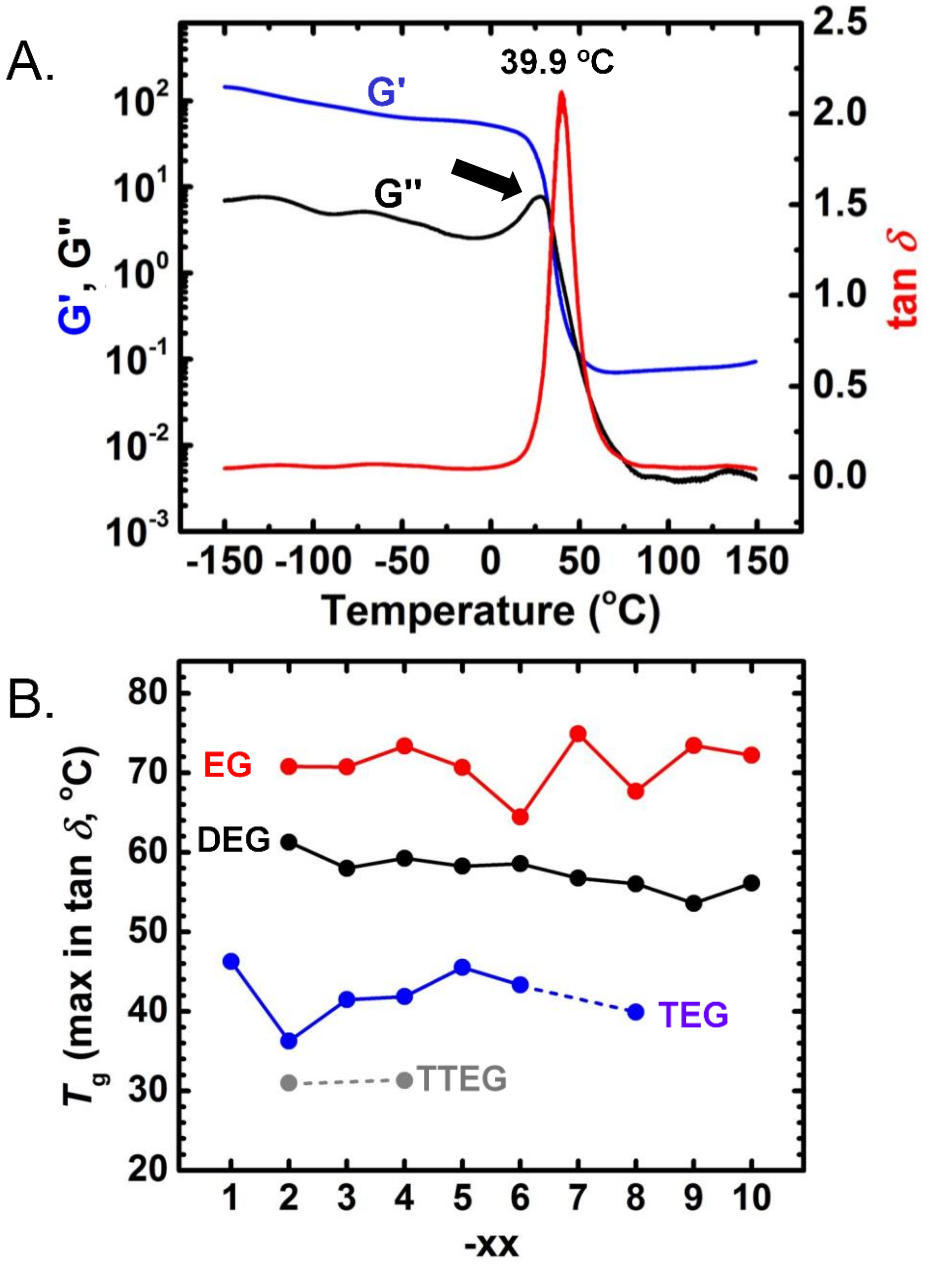

Figure 6. (a). Storage (G´) and loss (G´´) moduli and tan δ (=G´´/G´) curves of a representative sample (**TEG-8**) as a function of temperature. Arrow points to the maximum in the G´´ curve (see text). (b). Glass transition temperatures (T_g as maxima in tan δ) for all non-collapsed **ALC-xx** (Data from Table S.5 in the Supporting Information).

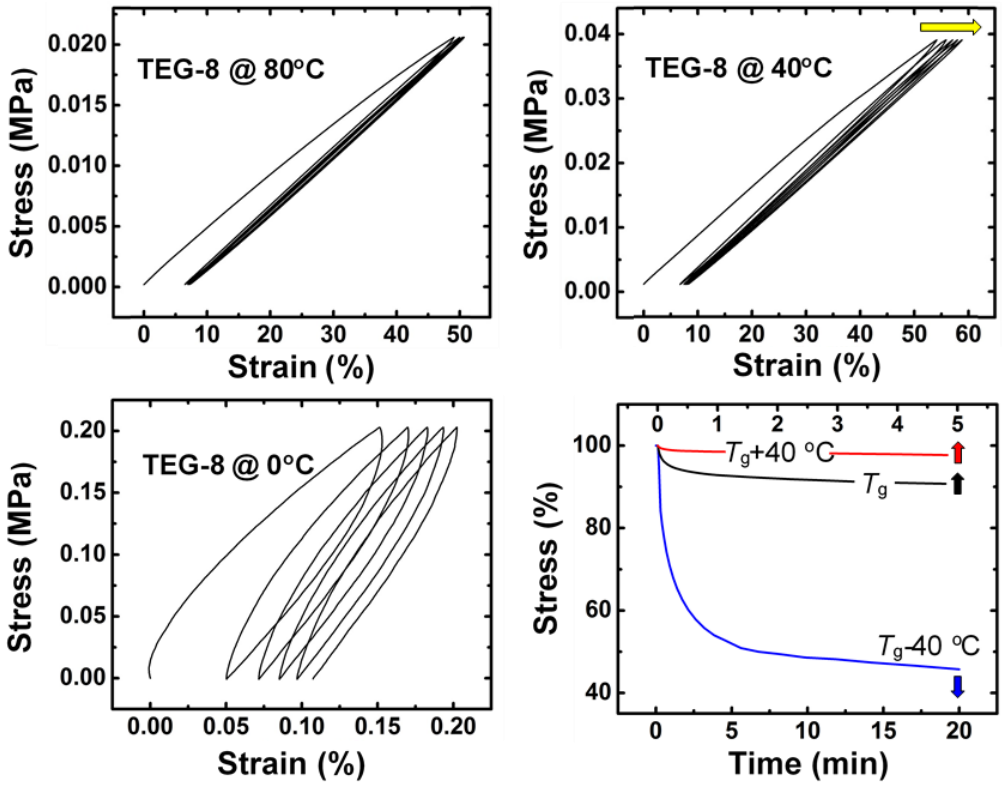

Figure 7. Five consecutive cycle tensile testing of three **TEG-8** samples (one for each frame) at T_g+40 °C (80 °C), T_g (40 °C) and T_g-40 °C (0 °C). Samples were stretched with a constant force rate of 1 N min^{-1}. Maximum strains at T_g and T_g+40 °C were set near the failure point of the sample. The maximum strain at T_g-40 °C was set by the compliance of the instrument (18 N). Yellow arrow indicates creep. Last frame: Stress relaxation run after at the end of the fifth cycle of each frame.

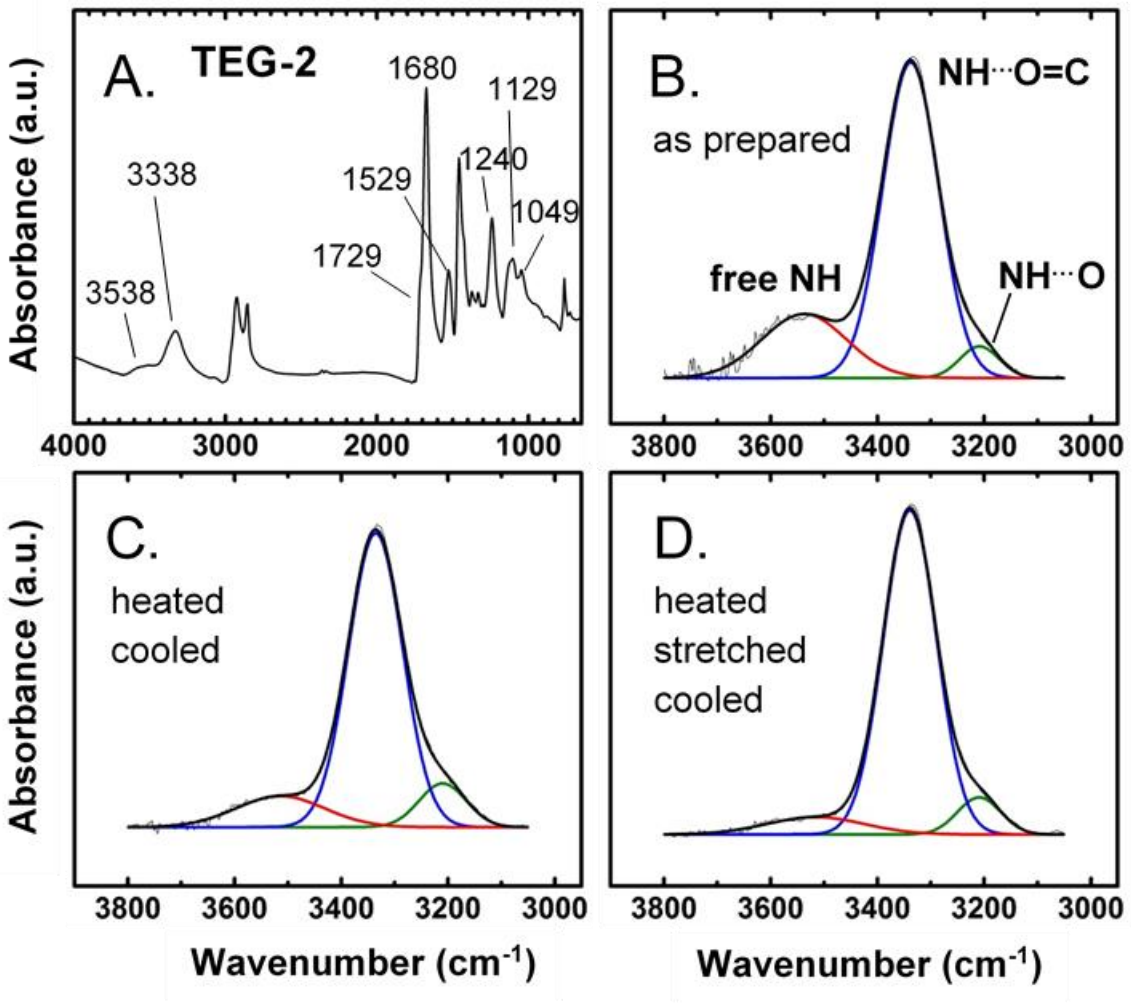

Figure 8. Room-temperature ATR-FTIR spectra of ALC-xx taken under different conditions. (a). The entire spectrum of a representative as-prepared TEG-2 sample. (b). The 3000-3800 cm-1 range of frame A, deconvoluted for H-bonding. (c). The same sample as in A and B, heated at Tg+10 ^{o}C for 15 min, then cooled back to room temperature. (d). The same sample as in A-C, heated again at Tg+10 ^{o}C for 15 min, stretched to about 60% strain, then the stretching force was released, and the sample was let cool back to room temperature (Similar spectra for DEG-2, DEG-4, TEG-2, TEG-8 and TTEG-2 are shown in Appendix V of the Supporting Information. H-bonding data for all samples are summarized in Table 1).

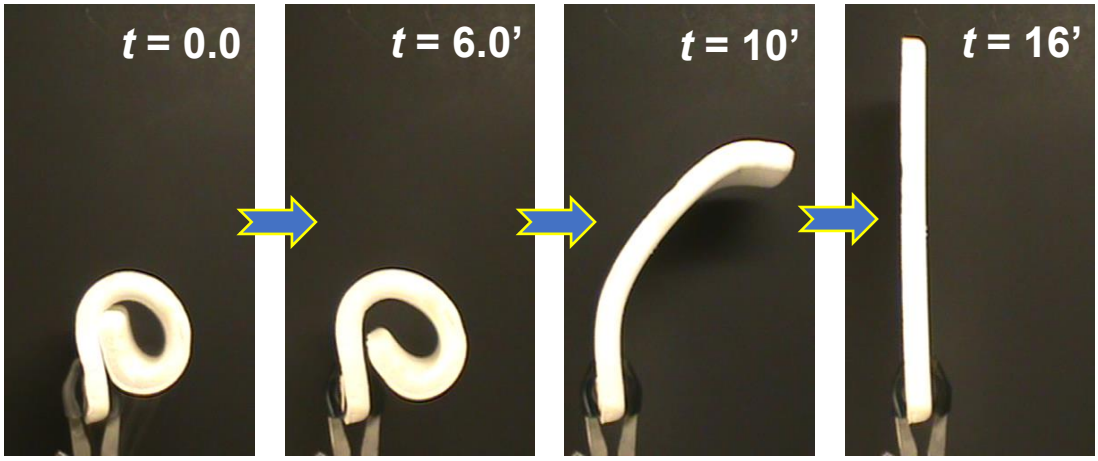

Figure 9. A deployable, shape-memory aerogel panel similar to that in Figure 1 (**TEG-8**). The permanent shape was flat. The sample (2´´×8´´) was heated up above Tg, folded as shown in the first frame, and dipped in liquid N2. The unfolding to the original shape as the sample returned to room temperature is shown in Movie S.2 of the Supporting Information. Selected frames from that movie are shown here.

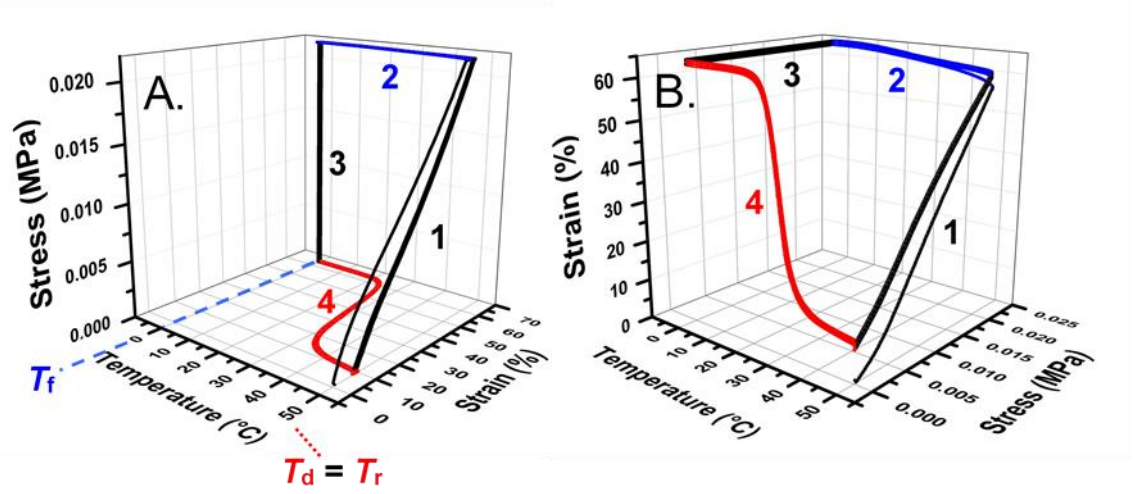

Figure 10. A 3D representation from two different perspectives of a representative temperature cycle experiment aiming at quantifying the figures of merit for the shape memory effect. Data shown are for **TEG-8**. All experiments were performed starting with as-prepared samples, cycled 5 times between a deformation (and recovery) temperature T_d (T_r), and a fixing temperature (T_f). The different stages of the experiment (marked with numbers) are explained in the text.

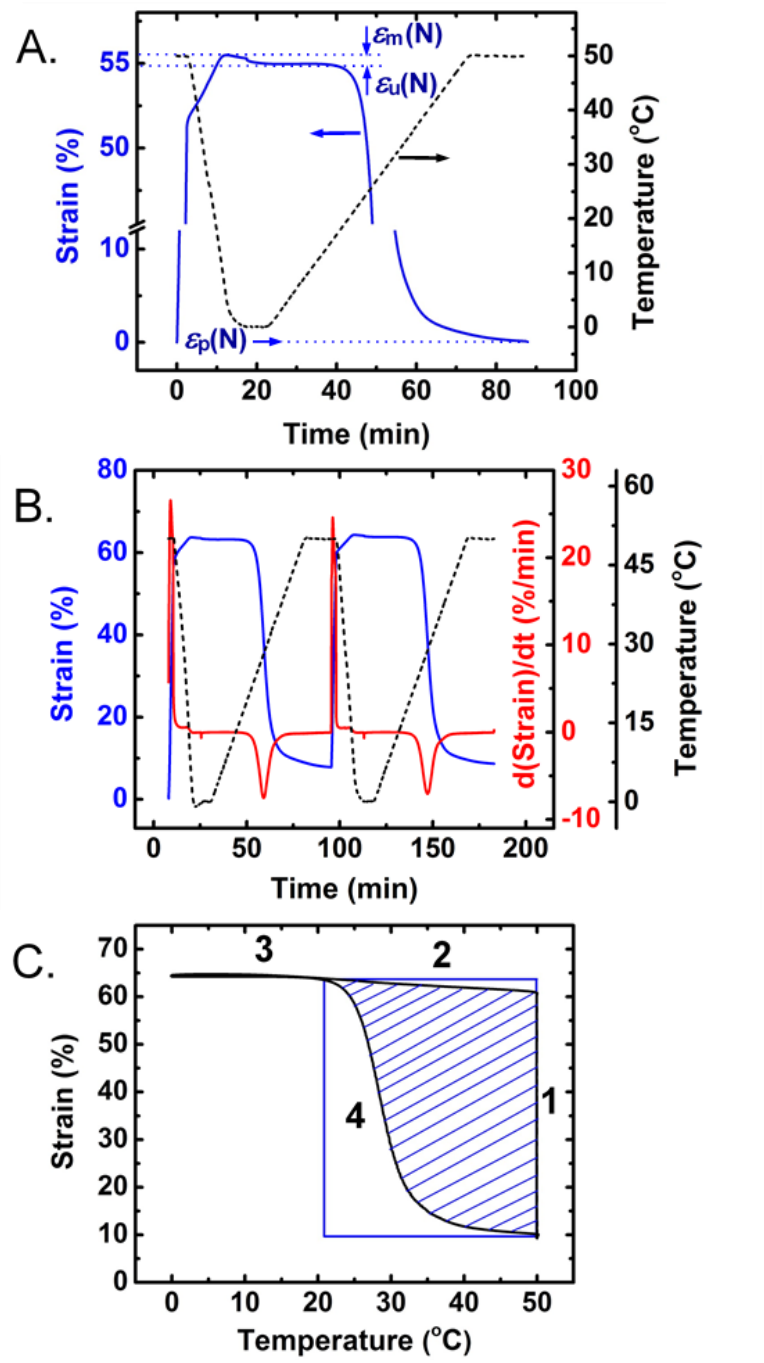

Figure 11. Projections of the entire 3D representation of Figure 10 to different planes, in order to calculate the figures of merit of the shape memory effect. (a). Projection to the Strain-Temperature plane followed by unfolding Temperature into Time. (Temperature vs. time is also included as a dotted line. Strains ε_m, ε_u and ε_p are used in Eq.s 2 and 3 and are defined within this frame.) (b). Plotting same as frame A. This frame also includes (red line) a plot of the first derivative of Strain over Time. (c). Straight projection of the curve to the Strain vs. Temperature plane. Numbers 1-4 refer to the four stages of the experiment as shown in Figure 10.

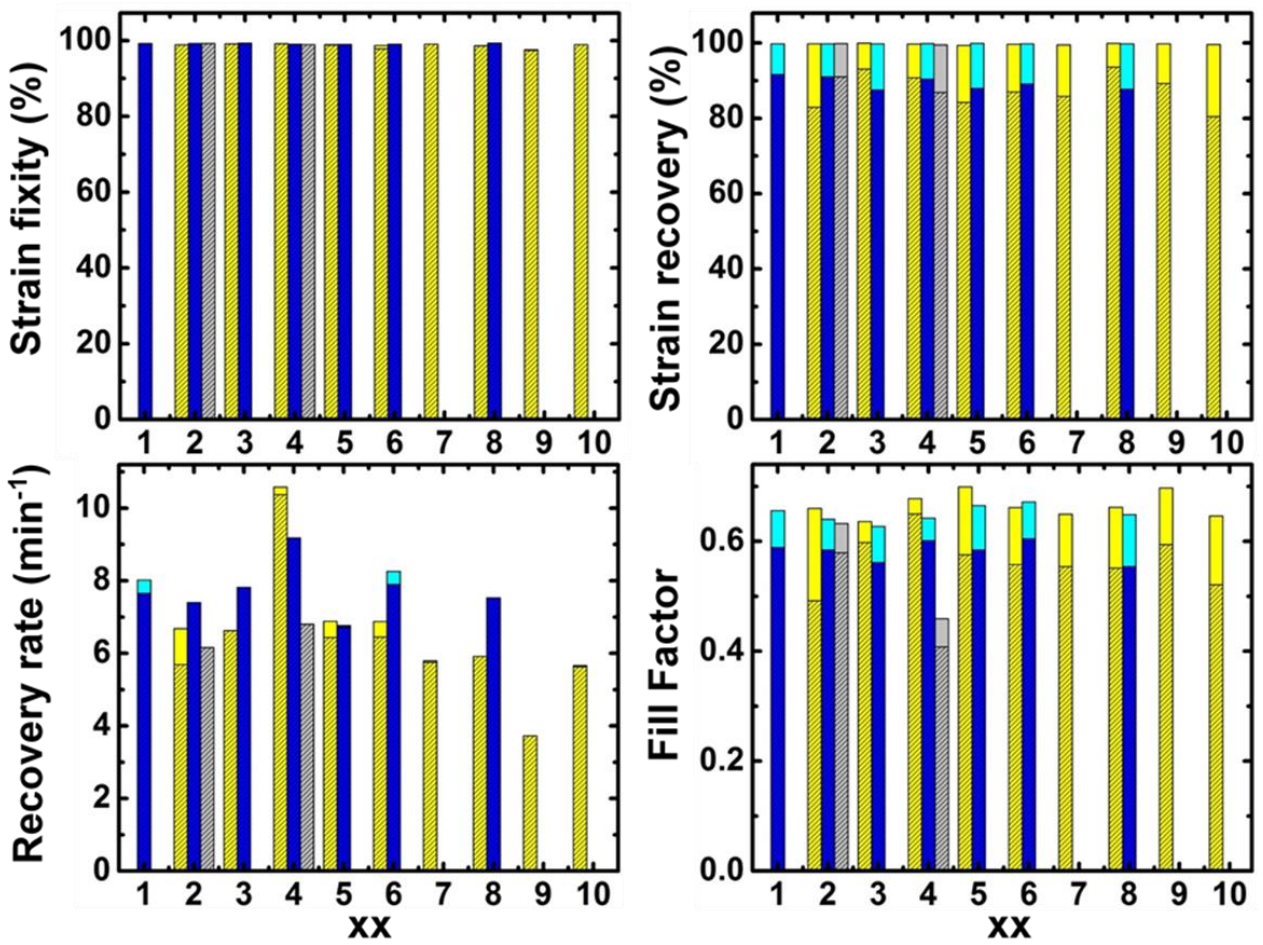

Figure 12. Figures of merit extracted from the data of Figure 11 as described in the text. Color-coding: Yellow: **DEG-xx**; Blue: **TEG-xx**; Gray: **TTEG-xx** (just two samples). Dark or shaded colors: first-cycle data; Lighter colors: fifth-cycle data (All original data for all samples and all cycles are summarized in Table S.6 of Appendix VIII in the Supporting Information).

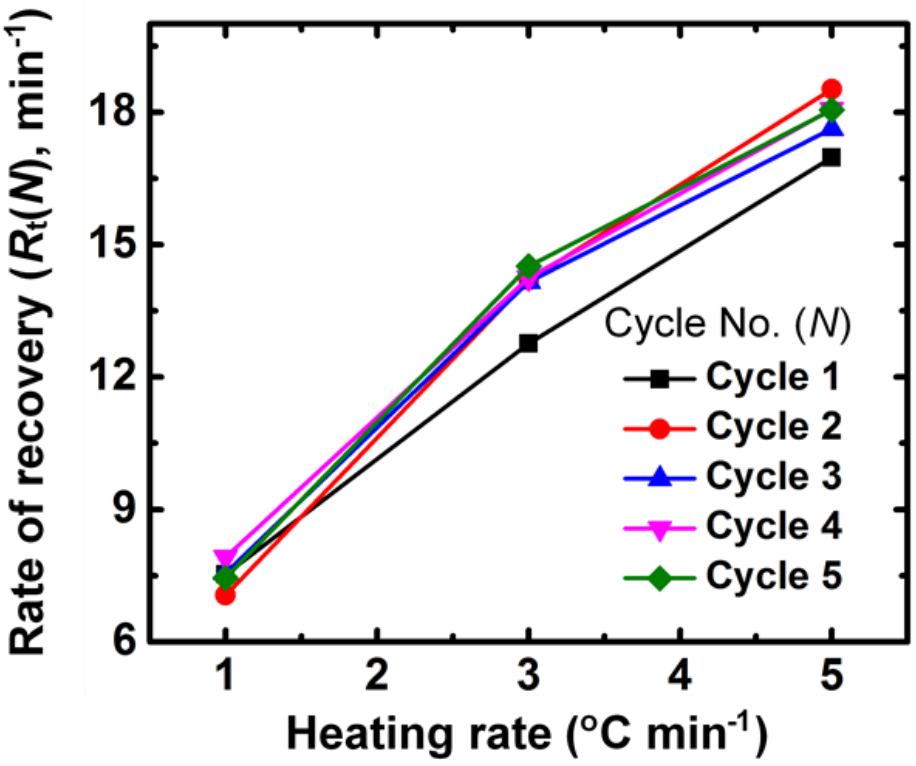

Figure 13. Strain recovery rates, $R_t(N)$, demonstrated with three fresh **TEG-8** samples cycled five times ($1 \leq N \leq 5$) using different heating rates during Stage 4 (i.e., during heating from T_f to T_d - refer to Figure 10, and Figure 11C).

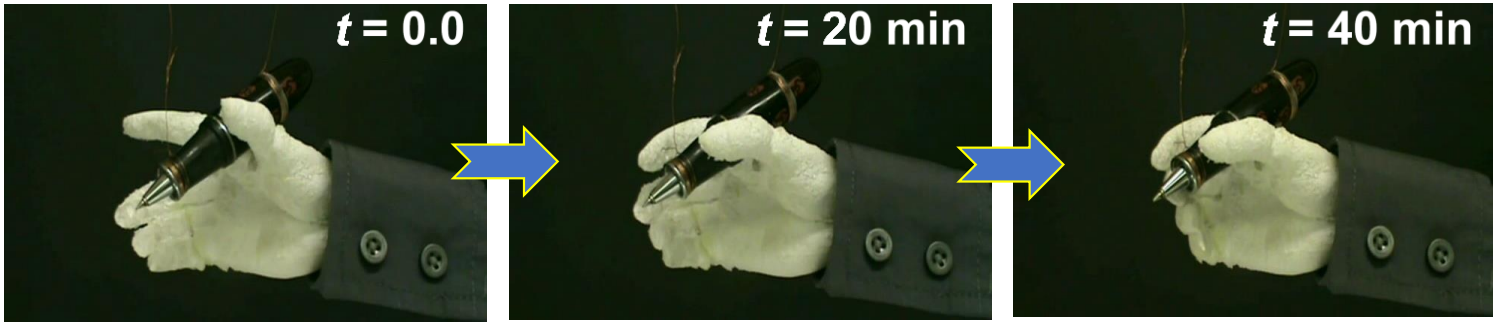

Figure 14. A bionic hand based on a shape-memory polyurethane aerogel (**TEG-8**). In its permanent shape (last frame to the right) the "hand" had been programmed to hold a pen. Frames are taken from Movie S.3 of the Supporting Information. All other conditions identical to those of Figure 9.

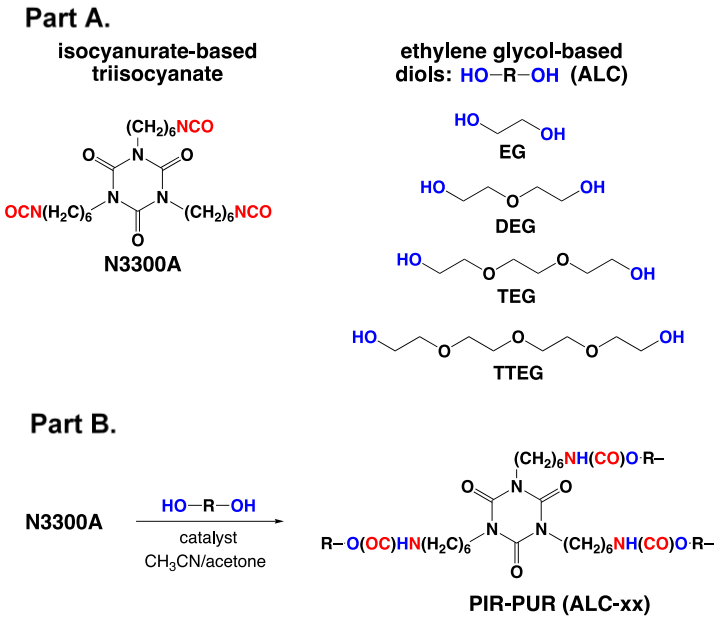

Scheme 1. (a) Reagents (triisocyanate, ethylene glycol-based diols). (b) Reaction pathway to isocyanurate crosslinking nodes linked with urethane tethers (PIR-PUR).

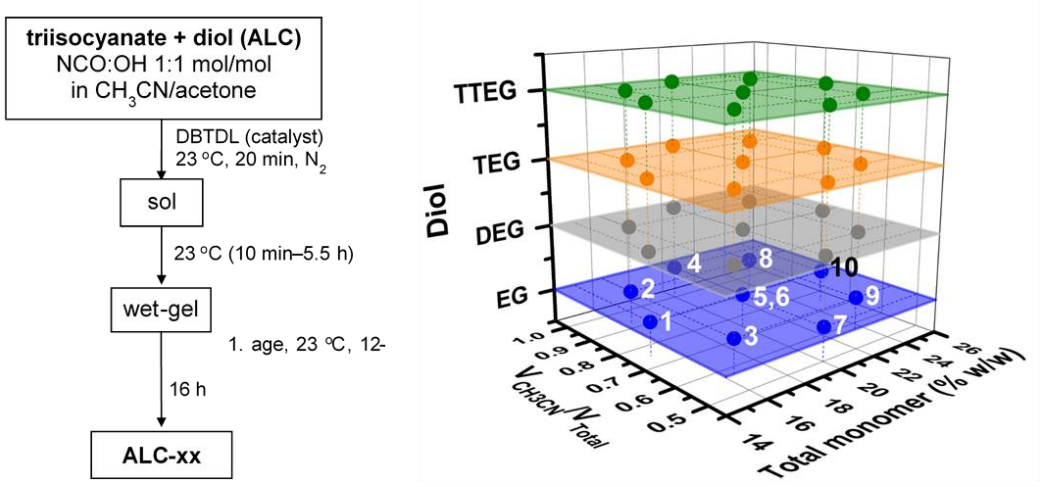

Scheme 2. (a) Synthetic protocol of PIR-PUR aerogels (ALC-xx). (b) ALC-xx formulation according to a central composite rotatable design model (CCRD); Independent (exploratory) variables: volume fraction of CH_3CN in the sol ($0.5 \leq V_{CH3CN}/V_{Total} \leq 1.0$), and total monomer concentration in the sol (15% w/w ≤ Total monomer ≤ 25% w/w).

Table 1. Integrated ratios of Free and H-bonded NH stretching of samples as shown.[a]

Sample	**Conditions**	**[free NH]**	**[NH···O=C]**	**[NH···O(CH$_2$)$_2$]**
		3423-3545 cm^{-1}	3331-3341 cm^{-1}	3204-3234 cm^{-1}
DEG-2	as prepared	4.6	4.4	1.0
	heated-cooled [b]	1.6	7.1	1.3
	heated-stretched-cooled [c]	0.8	7.4	1.8
DEG-4	as prepared	5.5	1.9	1.7
	heated-cooled [b]	1.2	7.6	1.3
	heated-stretched-cooled [c]	0.0	8.6	1.4
TEG-2	as prepared	2.2	7.3	0.5
	heated-cooled [b]	0.8	8.4	0.8
	heated-stretched-cooled [c]	1.3	7.7	1.0
TEG-8	as prepared	2.4	6.6	1.0
	heated-cooled [b]	1.0	7.3	1.7
	heated-stretched-cooled [c]	1.7	6.8	1.5
TTEG-2	as prepared	2.2	6.7	1.1
	heated-cooled [b]	0.0	8.2	1.8
	heated-stretched-cooled [c]	1.1	7.6	1.3

[a] All spectra were taken at room temperature. Data from spectra shown in Figure 8 and Figures S.4-S.7 in the Supporting Information. [b] Heated at T_g+40 ^{o}C, cooled to room temperature. [c] Heated at T_g+40 ^{o}C, stretched at that temperature, left to relax and cooled back to room temperature.

ACKNOWLEDGEMENTS

We thank the Army Research Office for financial support under Award Number W911NF-14-1-0369. We also thank BASF Polyurethanes GmbH for partial support and for suggesting ethylene glycol derivatives. We also thank Covestro LLC (formerly Bayer Corporation U.S.A.) for the generous supply of Desmodur N3300A, and the Materials Research Center of the Missouri University of Science and Technology for support with materials characterization.

REFERENCES

1. Koerner, H.; Price, G.; Pearce, N. A.; Alexander, M.; Vaia, R. A. Remotely Actuated Polymer Nanocomposites—Stress-Recovery of Carbon-Nanotube-Filled Thermoplastic Elastomers. *Nature Materials* **2004**, *3*, 115-120.

2. Lendlein, A.; Jiang, H. Y.; Junger, O.; Langer, R. Light-Induced Shape-Memory Polymers. *Nature* **2005**, *434*, 879-882.

3. Choi, W.; Lahiri, I.; Seelaboyina, R.; Kang, Y. S. Synthesis of Graphene and its Applications: A Review. *Crit. Rev. Solid State Mater. Sci*. **2010**, *35*, 52-71.

4. Kim, H.; Abdala, A. A.; Macosko, C. W. Graphene/Polymer Nanocomposites. *Macromolecules* **2010**, *43*, 6515-6530.

5. Chen, S. J.; Hu, J. L.; Chen, S. G. Studies of The Moisture-Sensitive Shape Memory Effect of Pyridine-Containing Polyurethanes. *Polym. Int.* **2012**, *61*, 314-320.

6. Saunders, J. H.; Frisch, K. C. Polyurethane Chemistry and Technology I. Chemistry. Interscience Publishers: New York, 1962.

7. Sokolowski, W. M.; Tan, S. C. Advanced Self-Deployable Structures for Space Applications. *J. Spacecr. Rockets* **2007**, *44*, 750-754.

8. Metzger, M. F.; Wilson, T. S.; Schumann, D.; Matthews, D. L.; Maitland, D. J. Mechanical Properties of Mechanical Actuator for Treating Ischemic Stroke. *Biomed. Microdevices* **2002**, *4*, 89−96.

9. Daniels, A. U.; Chang, M. K.; Andriano, K. P.; Heller, J. Mechanical Properties of Biodegradable Polymers and Composites Proposed for Internal Fixation of Bone. *J. Appl. Biomater.* **1990**, *1*, 57−78.

10. Lendlein, A.; Langer, R. Biodegradable, Elastic Shape-Memory Polymers for Potential Biomedical Applications. *Science* **2002**, *296*, 1673−1676.

11. Metcalfe, A.; Desfaits, A.; Salazkin, I.; Yahia, L. H.; Sokolowski, W. M.; Raymond, J. Cold Hibernated Elastic Memory Foams for Endovascular Interventions. *Biomaterials* **2003**, *24*, 491−497.

12. Gonzalez-Garcia, Y.; Mol, J. M. C.; Muselle, T.; De Graeve, I.; Van Assche, G.; Scheltjens, G.; Van Mele, B.; Terryn, H. A Combined Mechanical, Microscopic and Local Electrochemical Evaluation of Self-Healing Properties of Shape-Memory Polyurethane Coatings. *Electrochim. Acta* **2011**, *56*, 9619-9626.

13. Hood, P. J.; Garrigan, S.; Auffinger, F. Method of Making and Using Shape Memory Polymer Patches. U.S. Patent No. 7981229 B2, 2011.

14. Sahoo, N. G.; Jung, Y. C.; Goo, N. S.; Cho, J. W. Conducting Shape Memory Polyurethane-Polypyrrole Composites for An Electroactive Actuator. *Macromol. Mater. Eng.* **2005**, *290*, 1049-1055.

15. Hu, J. L.; Meng, H. P.; Li, G. Q.; Ibekwe, S. I. A Review of Stimuli-Responsive Polymers for Smart Textile Applications. *Smart Mater. Struct.* **2012**, *21*, 053001, doi:10.1088/0964-1726/21/5/053001.

16. Mock, C. C. Assembly for Delayed Lowering of a Raised Toilet Seat. U.S. Patent No. 8359677 B1, 2013.

17. Kikutani, T.; Kondo, S.; Hayashi, S.; Sugihara, K.; Haguri, T.; Akimoto, K. Grip Member, Toothbrush Using The Grip Member and Western Tableware Using The Grip Member. U.S. Patent No. 6173477, 2001.

18. Ölander, A. An Electrochemical Investigation of Solid Cadmium-Gold Alloys. *J. Am. Chem. Soc.* **1932**, *54*, 3819–3833.

19. Buehler, W. J.; Gilfrich, J. W.; Wiley, R. C. Effects of Low-Temperature Phase Changes on The Mechanical Properties of Alloys Near Composition TiNi. *J. Appl. Phys.* **1963**, *34*, 1475–1477.

20. Wang, F. E.; Buehler, W. J.; Pickart, S. J. Crystal Structure and a Unique Martensitic Transition of TiNi. *J. Appl. Phys.* **1965**, *36*, 3232–3239.

21. For an example of superelasticity see: https://www.youtube.com/watch?v=1rrPv5AlVXg.

22. Duerig, T. W.; Pelton, A. R. Ti-Ni Shape Memory Alloys. In *Materials Properties Handbook: Titanium Alloys*; Welsch, G., Boyer, R., Collings E. W., Eds.; American Society for Metals, 1994; pp. 1994 1035–1048.

23. Vernon, L. B.; Vernon, H. M. Producing Molded Articles such as Dentures from Thermoplastic Synthetic Resins. U.S. Patent No. 2234993, 1941.

24. Rainer, W. C.; Redding, E. M.; Hitov, J. J.; Sloan, A. W.; Stewart, W. D. Heat-Shrinkable Polyethylene. U.S. Patent No. 3144398, 1964.

25. Perrone, R. J. Heat-shrinkable Articles Made from Silicone Rubber–Polyethylene Compositions. U.S. Patent No. 3326869, 1967.

26. Wray, C.; P. E. Elastic Memory Articles. U.S. Patent No. GB1075704, 1967.

27. Hayashi, S.; Shirai, Y. Development of Polymeric Shape Memory Material. *Mitsubishi Technical Bulletin 184*, Dec. **1988**.

28. Hayashi, S.; Tobushi, H.; Kojima, S. Mechanical Properties of Shape Memory Polymer of Polyurethane Series. *JSME Inernational Journal Series I* **1992**, *35*, 206–302.

29. Hayashi, S. Properties and Applications of Polyurethane-Series Shape Memory Polymer. *International Progress in Urethanes* **1993**, *6*, 90–115.

30. “Rubber-like elasticity” sometimes is also referred to as a “memory effect,” which might become a source of confusion, particularly with respect to SMPs. Used in this context, “memory effect” has nothing to do with shape recovery triggered by an external stimulus.

31. Berg, G. J.; McBride, M. K.; Wang, C.; Bowman, C. N. New Directions in the Chemistry of Shape Memory Polymers. *Polymer* **2014**, *55*, 5849-5872.

32. Hager, M. D.; Bode, S.; Weber, C.; Schubert, U. S. Shape Memory Polymers: Past, Present and Future Developments. *Progress in Polymer Science* **2015**, *49*, 3-33.

33. Behl, M.; Razzaq, M. Y.; Lendlein, A. Multifunctional Shape-Memory Polymers. *Adv. Mater.* **2010**, *22*, 3388-3410.

34. Kagami, Y.; Gong J. P.; Osada, Y. Shape Memory Behaviors of Crosslinked Copolymers Containing Stearyl Acrylate. *Macromol. Rapid Commun.* **1996**, *17*, 539-543.

35. Hu, J. L.; Mondal, S. Structural Characterization and Mass Transfer Properties of Segmented Polyurethane: Influence of Block Length of Hydrophilic Segments. *Polym. International* **2005**, *54*, 764-771.

36. Pilate, F.; Mincheva, R.; Winter, J. D.; Gerbaux, P.; Wu, L.; Todd, R.; Raquez, J. M.; Dubois, P. Design of Multistimuli-Responsive Shape-Memory Polymer Materials by Reactive Extrusion. *Chem. Mater.* **2014**, *26*, 5860-5867.

37. Zhu, Y.; Hu, J.; Yeung, K. W.; Choi, K. F.; Liu, Y Q.; Liem, H. M. Effect of Cationic Group Content on Shape Memory Effect in Segmented Polyurethane Cationomer. *J. Appl. Polym. Sci.* **2007**, *103*, 545-556.

38. Shi, Y.; Yoonessi, M.; Weiss, R. A. High Temperature Shape Memory Polymers. *Macromolecules* **2013**, *46*, 4160-4167.

39. Xie, T.; Rousseau, I. A. Facile Tailoring of Thermal Transition Temperatures of Epoxy Shape Memory Polymers. *Polymer* **2009**, *50*, 1852-1856.

40. Nair, D. P.; Cramer, N. B.; Scott, T. F.; Bowman, C. N.; Shandas, R. Photopolymerized Thiol-Ene Systems as Shape Memory Polymers. *Polymer* **2010**, *51*, 4383-4389.

41. Liu, C. D.; Chun, S. B.; Mather, P. T.; Zheng, L.; Haley, E. H.; Coughlin, E. B. Chemically Cross-Linked Polycyclooctene: Synthesis, Characterization, and Shape Memory Behavior. *Macromolecules* **2002**, *35*, 9868-9874.

42. Sakurai, K.; Kashiwagi, T.; Takahashi, T. Crystal Structure Of Polynorbornene. *J. Appl. Polym. Sci.* **1993**, *47*, 937-940.

43. Li, F. K.; Zhu, W.; Zhang, X.; Zhao, C. T.; Xu, M. Shape Memory Effect of Ethylene–Vinyl Acetate Copolymers. *J. Appl. Polym. Sci.* **1999**, *71*, 1063-1070.

44. Sakurai, K.; Tanaka, H.; Ogawa, N.; Takahashi, T. Shape-Memorizable Styrene-Butadiene Block Copolymer. I. Thermal And Mechanical Behaviors and Structural Change with Deformation. *J. Macromol. Sci. Part B* **1997**, *36*, 703-716.

45. Pierre, A. C.; Pajonk, G. M. Chemistry of Aerogels and Their Applications. *Chem. Rev.* **2002**, *102*, 4243-4265.

46. Morris, C. A.; Anderson, M. L.; Stroud, R. M.; Merzbacher, C. I.; Rolison, D. R. Silica Sol as A Nanoglue: Flexible Synthesis of Composite Aerogels. *Science* **1999**, *284*, 622-624.

47. Chidambareswarapattar, C.; McCarver, P. M.; Luo, H.; Lu, H.; Sotiriou-Leventis, C.; Leventis, N. Fractal Multiscale Nanoporous Polyurethanes: Flexible to Extremely Rigid Aerogels from Multifunctional Small Molecules. *Chem. Mater*. **2013**, *25*, 3205-3224.

48. Chidambareswarapattar, C.; Xu, L.; Sotiriou-leventis, C.; Leventis, N. Robust Monolithic Multiscale Nanoporous Polyimides and Conversion to Isomorphic Carbons. *RSC Adv.* **2013**, *3*, 26459-26469.

49. Bang, A.; Buback, C.; Sotiriou-Leventis, C.; Leventis, N. Flexible Aerogels from Hyperbranched Polyurethanes: Probing The Role of Molecular Rigidity with Poly(Urethane Acrylates) Versus Poly(Urethane Norbornenes). *Chem. Mater*. **2014**, *26*, 6979−6993.

50. Kucheyev, S. O.; Stadermann, M.; Shin, S. J.; Satcher Jr., J. H.; Gammon, S. A.; Letts, S. A.; van Buuren, T.; Hamza, A. V. Super-Compressibility of Ultralow-Density Nanoporous Silica. *Adv. Mater.* **2012**, *24*, 776-780.

51. Hayase, G.; Kanamori, K.; Nakanishi, K. New Flexible Aerogels and Xerogels Derived from Methyltrimethoxysilane/Dimethyldimethoxysilane co-Precursors. *J. Mater. Chem.* **2011**, *21***,** 17077-17079.

52. Hayase, G.; Kanamori, K.; Hasegawa, G.; Maeno, A.; Kaji, H.; Nakanishi, K. A Superamphiphobic Macroporous Silicone Monolith with Marshmallow-like Flexibility. *Angew. Chem. Int. Ed.* **2013**, *52*, 10788-10791.

53. Kanamori, K.; Aizawa, M.; Nakanishi, K.; Hanada, T. New Transparent Methylsilsesquioxne Aerogels and Xerogels with Improved Mechanical Properties. *Adv. Mater.* **2007**, *19*, 1589-1593.

54. Michal, B. T.; Brenn, W. A.; Nguyen, B. N.; McCorkle, L. S.; Meador, M. A. B.; Rowan, S. J. Thermoresponsive Shape-Memory Aerogels from Thiol-Ene Networks. *Chem. Mater.* **2016**, *28*, 2341-2347.

55. Meador, M. A. B.; Malow, E. J.; Silva, R.; Wright, S.; Quade, D.; Vivod, S. L.; Guo, H.; Guo, J.; Cakmak, M. Mechanically Strong, Flexible Polyimide Aerogels Cross-Linked with Aromatic Triamine. *ACS Appl. Mater. Interfaces* **2012**, *4*, 536-544.

56. Leventis, N.; Chidambareswarapattar, C.; Bang, A.; Sotiriou- Leventis, C. Cocoon-in-Web-like Superhydrophobic Aerogels from Hydrophilic Polyurea and Use in Environmental Remediation. *ACS Appl. Mater. Interfaces* **2014**, *6*, 6872−6882.

57. Chidambareswarapattar, C.; McCarver, P. M.; Luo, H.; Lu, H.; Sotiriou Leventis, C.; Leventis, N. Fractal Multiscale Nanoporous Polyurethanes: Flexible to Extremely Rigid Aerogels from Multifunctional Small Molecules. *Chem. Mater.* **2013**, *25*, 3205-3224.

58. Skowronski, M. J. Isocyanurate Foam The Role of the Isocyanate. *Annual Technical Conference* **1977**, *23*, 167-170.

59. Kordomenos, P. I.; Kresta, J. E.; Frisch, K. C. Thermal Stability of Isocyanate-Based Polymers. 2. Kinetics of Thermal Dissociation of Model Urethane, Oxazolidone, and Isocyanurate Block Copolymers. *Macromolecules* **1987**, *20*, 2077-2083.

60. Modesti, M.; Simioni, F.; Checchin, M.; Pielichowski, J.; Prociak, A. Thermal Stability and Fire Performance of Modified Polyisocyanurate Foams. *Cellular Polymers* **1999**, *18*, 329-342.

61. Petunova, M. D.; Luchkina, L. V.; Askadskii, A. A.; Kovriga, O. V. Synthesis and Properties of Poyisocyanurate Networks Based on 2,4-Toluene Diisocyanate and Poly(oxytetramethylene) Glycol. *Polymer Science, Ser. A* **2009**, *51*, 542-549.

62. Liszkowska, J.; Czuprynski, B.; Paciorek-Sadowska, J. Thermal Proporties of Polyurethane-Polyisocyanurate (PUR-PIR) Foams Modified with Tris(5-hydroxypentyl) Citrate. *J. Adv. Chem. Eng.* **2016**, *6*, 1000148.

63. Polyurethane and Polyiso: the Difference? PIMA Technical Bulletin #202. http://c.ymcdn.com/sites/www.polyiso.org/resource/resmgr/technical_bulletins/tb202_jun30.pdf (01-18-2017).

64. Maleki, H.; Durães, L.; Portugal, A. Development of Mechanically Strong Ambient Pressure Dried Silica Aerogels with Optimized Properties. *J. Phys. Chem. C* **2015**, *119*, 7689-7703.

65. Montgomery, D. C. Design and Analysis of Experiments, 6th ed.; John Wiley & Sons: New York, U.S.A., **2006**.

66. Goupy, J.; Creighton, L. Introduction to Design of Experiments with JMP Examples, 3rd ed; SAS Institute Inc.: Cary, NC, U.S.A., **2007**.

67. SAS Institute Inc. 2013.Using JMP 11. Cary, NC: SAS Institute Inc.: http://www.jmp.com/en_us/offers/free-trial.html?utm_source=google&utm_campaign=td70114000002KZJq&utm_medium=cpc&utm_term=sas%20jmp (01-25-2017).

68. It is noted that in our case (2 exploratory variables) the total number of samples required by the CCRD model (9 plus one repeat at the center) is equal to what would have been required by a fully factorial design (FFD) model using two exploratory variables at three levels each. The difference between FFD and CCRD is that in the latter all peripheral points are equidistant from the center point of the domain.

69. Mohite, D. P.; Mahadik-Khanolkar, S.; Luo, H.; Lu, H.; Sotiriou-Leventis, C.; Leventis, C. Polydicyclopentadiene Aerogels Grafted with PMMA: II. Nanoscopic Characterization and Origin of Macroscopic Deformation. *Soft Mat.* **2013**, *9*, 1531-1539.

70. Porosities, Π, were calculated via $\Pi=(\rho_s-\rho_b)/\rho_s$, whereas skeletal densities –ρ_s, included in Table S.3– were for all **ALC-xx** in the 1.2-1.3 g cm^{-3} range, and did not vary in any systematic fashion within each ALC.

71. It is noted that this description is still just a first-order approximation: The issue of what combination of ALC, ALC concentration and solvent is appropriate in order to minimize shrinkage and prevent collapse is convoluted further with the fact that longer ALC are expected to promote H-bonding between the –(OCH_2CH_2)– and the –NH(CO)– groups (see Section 2.3.2), which reduces segmental motion of the polymeric chains.

72. Tcharkhtchi, A.; Abdallah-Elhirtsi, S.; Ebrahimi, K.; Fitoussi, J.; Shirinbayan, M.; Farzaneh, S. Some New Concepts of Shape Memory Effect of polymers. *Polymer* **2014**, *6*, 1144-1163.

73. Silverstein, R. M.; Bassler, G. C.; Morrill, T. C. Spectroscopic Identification of Organic Compounds, Fifth Edition. John Wiley & Sons, Inc. New York, 1991, pp 122-123.

74. Silverstein, R. M.; Bassler, G. C.; Morrill, T. C. Spectroscopic Identification of Organic Compounds, Fifth Edition. John Wiley & Sons, Inc. New York, 1991, pp 112,120.

75. McCarthy, S. J.; Meijs, G. F.; Mitchell, N.; Gunatillake, P. A.; Heath, G.; Brandwood, A.; Schindhelm, K. In-vivo Degradation of Polyurethanes: Transmission-FTIR Microscopic Characterization of Polyurethanes Sectioned by Cryomicrotomy. *Biomaterials* **1997**, *18*, 1387−1409.

76. Sung, C. S.; Schneider, N. S. Temperature Dependence of Hydrogen Bonding in Toluene Diisocyanate Based Polyurethanes. *Macromolecules* **1977**, *10*, 452-458.

77. Teo, L.-S.; Chen, C.-Y.; Kuo, J.-F. Fourier Transform Infrared Spectroscopy Study on Effects of Temperature on Hydrogen Bonding in Amine-Containing Polyurethanes and Poly(urethane-urea)s. *Macromolecules* **1997**, *30*, 1793-1799.

78. Saito, Y.; Nansai, S.; Kinoshita, S. Structural Studies on Polyurethane Fibers. I. Crystal and Molecular Structures of Aliphatic Polyurethanes from Hexamethylene Diisocyanate and Some Linear Glycols. *Polym. J.* **1972**, *3*, 113−121.

79. Christenson, C. P.; Harthcock, M. A.; Meadows, M. D.; Spell, H. L.; Howard, W. L.; Creswick, M. W.; Guerra, R. E.; Turner, R. B. Model MDI/butanediol Polyurethanes: Molecular Structure, Morphology, Physical and Mechanical Properties. J. *Polym. Sci. Part B: Polym. Phys.* **1986**, *24*, 1401-1439.

80. Lee, H. S.; Wang, Y. K.; MacKnight, W. J.; Hsu, S. L. Spectroscopic Analysis of Phase-Separation Kinetics in Model Polyurethanes. *Macromolecules* **1988**, *21*, 270-273.

81. It is noted that the extinction coefficient of free NH is about 3 times lower than that of H-bonded N-H.[75]

82. Lendlein, A.; Kelch, S. Shape-Memory Polymers. *Angew. Chem. Int. Ed.* **2002**, *41*, 2034-2057.

83. Liu, C.; Qinb, H.; Mather, P. T. Review of Progress in Shape-Memory Polymers. *J. Mater. Chem.* **2007**, *17*, 1543–1558.

84. Liu, C.; Chun, S. B.; Mather, P. T.; Zheng, L.; Haley, E. H.; Coughlin, E. B. Chemically Crosslinked Polycyclooctene: Synthesis, Characterization, and Shape Memory Behavior. *Macromolecules* **2002**, *35*, 9868-9874.

85. http://www.reynoldsam.com/product/alja-safe/?gclid=CNaw_ciyw8kCFZI8gQod3JAGFQ.

86. http://www.aeromarineproducts.com/128-hgal-lp.html?gclid=CIHDjfm22ckCFQEcaQodUvsNyg.

87. Standard Test Methods for Flexural Properties of Unreinforced and Reinforced Plastics and Electrical Insulating Materials: http://www.astm.org/DATABASE.CART/HISTORICAL/D790-10.htm.

88. Standard Practice for Plastics: Dynamic Mechanical Properties: Determination and Report of Procedures: http://www.astm.org/Standards/D4065.htm.

SUPPORTING INFORMATION

Appendix I: Design, formulation and gelation times of **ALC-xx**.

Appendix II: General material properties of **ALC-xx**.

Appendix III: Fitting bulk densities of **ALC-xx** to system variables.

Appendix IV: SEM of all **ALC-xx**.

Appendix V: ATR FTIR of **DEG-2**, **DEG-4**, **TEG-8** and **TTEG-2**.

Appendix VI: Glass transition data.

Appendix VII: Tensile testing and stress relaxation of **DEG-4**.

Appendix VIII: Figures of merit for the SME of all **ALC-xx**.

Movie S.1: Demonstration of superelasticity (separate file).

Movie S.2: Demonstration of a deployable panel (separate file).

Movie S.3: Demonstration of a bionic hand (separate file).

Appendix I: Design, formulation and gelation times of **ALC-xx**.

ALC-xx preparation via a Central Composite Rotatable Design (CCRD) model

The independent (exploratory) variables (otherwise also referred to as factors, f) were the total weight percent monomers (N3300A + alcohol) in the sol (X_1), and the fraction of acetonitrile in the solvent system (X_2). (In other words, in the design of **ALC-xx**, f=2.) Each factor was varied at three levels between two extremes that were identified with preliminary scouting experiments based on TEG-derived aerogels. Thus, the total monomer concentration was bracketed between 15% and 25% w/w, and the fraction of acetonitrile was varied from 0.500 to 1.000.

A central composite rotatable design model contains factorial points (dark circles) along with center points and is reinforced with a group of star points (Scheme S.1). Always a central composite design includes twice as many star points as factors (four in our case), and those star points are set at the extreme values (low and high) for each factor in the design. Center points are created by setting all factors at their midpoints. In normalized form, center points fall at the zero level. Thereby, since all points are disposed symmetrically with respect to the experimental center, the design is referred to as "central." Since the variance of any predicted response depends on the distance from the center of design space, this rotatable design provides equal precision in all directions.

In total, this design consists of 2^f factorial points (shown as dark circles in Scheme S.1), 2f axial (star) points and N_0 central points as replicates. Then, the total number of design points, N of a CCRD is determined by: $N = 2^f + 2f + N_0$.

Now, each factorial point is offset by ±1 unit from the coordinates of the central point of the design, and the star points are placed at a distance of $|\alpha| > 1$ from the center of

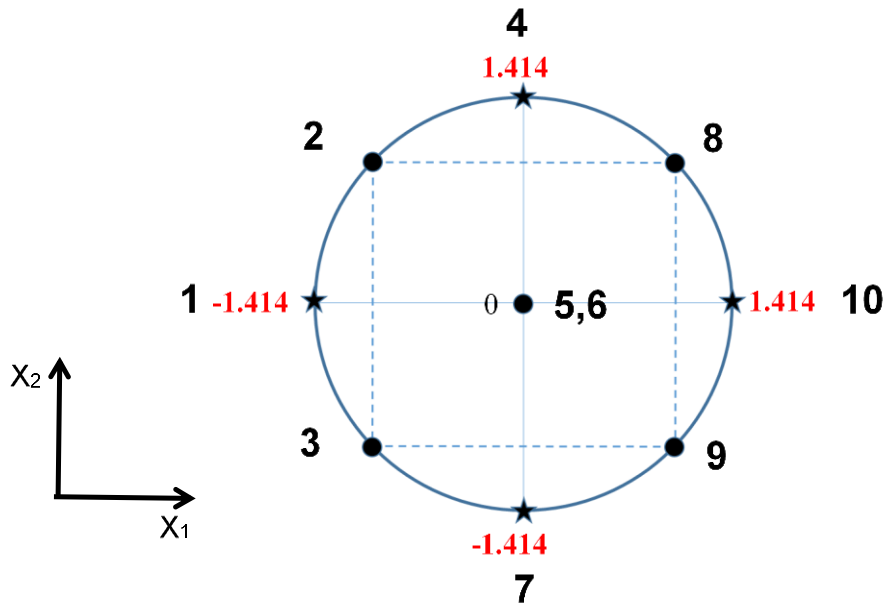

Scheme S.1. Central Composite Rotatable Design Model showing factorial points (dark circles: 2,3,8,9), center points (one, plus one duplicate: 5,6) and star points (1,4,7,10). The latter stand at the experimental extremes. Numbers in bold face red: orthogonalized design points.

the design and in such a way that all the factorial and star points lie on a circle with radius α. To maintain rotatability, the value of α depends on the number of experimental runs in the factorial portion of the central composite design:

$$\alpha = [\text{number of factorial runs}]^{1/4}$$

Here, the factorial is a full factorial with f factors, thus:

$$\alpha=[2^f]^{1/4}$$

Table S.1 gives the values of the normalized variables X_1 and X_2, as well as their translation to the **ALC-xx** system. (For the values of **xx** refer to Scheme S.1.) It is noted that although the required calculations are straightforward and can be carried out by hand easily, nevertheless the placement of the points was done using the JMP11 software package (SAS Institute Inc. 2013. Using JMP 11. Cary, NC: SAS Institute Inc.).

Table S.1. Experimental factors and levels in the central composite design for **ALC-xx.**

factors	unit	factor levels (values)				
		axial points		center point	star points (α = 1.414)[1]	
		-1	1	0	-α	α
[monomer] (X_1)	% w/w	16.46	23.54	20.00	15	25
V_{CH3CN}/V_{Total} (X_2)	mL/mL	0.574	0.927	0.750	0.500	1.000

[1] At the experimental extremes

Table S.2. Formulations of **EG-xx** based on Scheme S.1 and Table S.1, and corresponding gelation times. [a]

DOE No. (-xx)	total monomer (% w/w)	$\frac{V_{CH3CN}}{V_{Total}}$	Alcohol [b]				Desmodur N3300A [c]				CH_3CN		Acetone		Gelation time (min)
			mass (g)	volume (mL)	mmol	C (M)	mass (g)	volume (mL)	mmol	C (M)	mass (g)	volume (mL)	mass (g)	volume (mL)	
EG-xx															
1	15	0.750	0.093	0.0837	1.50	0.3117	0.504	0.4308	1.00	0.2078	2.538	3.2289	0.846	1.0695	46
2	16.46	0.927	0.093	0.0837	1.50	0.3435	0.504	0.4308	1.00	0.2290	2.808	3.5731	0.221	0.2796	35
3		0.574	0.093	0.0837	1.50	0.3442	0.504	0.4308	1.00	0.2294	1.736	2.2086	1.294	1.6355	34
4	20	1.000	0.093	0.0837	1.50	0.4222	0.504	0.4308	1.00	0.2814	2.388	3.0387	0.000	0.0000	15
5		0.750	0.093	0.0837	1.50	0.4227	0.504	0.4308	1.00	0.2818	1.791	2.2790	0.597	0.7549	10
6		0.750	0.093	0.0837	1.50	0.4227	0.504	0.4308	1.00	0.2818	1.791	2.2790	0.597	0.7549	7
7		0.500	0.093	0.0837	1.50	0.4233	0.504	0.4308	1.00	0.2822	1.194	1.5194	1.194	1.5097	26
8	23.54	0.927	0.093	0.0837	1.50	0.5031	0.504	0.4308	1.00	0.3354	1.798	2.2879	0.142	0.1790	8
9		0.574	0.093	0.0837	1.50	0.5041	0.504	0.4308	1.00	0.3360	1.112	1.4142	0.828	1.0472	15
10	25	0.500	0.093	0.0837	1.50	0.5377	0.504	0.4308	1.00	0.3584	1.343	1.7093	0.448	0.5662	16

[a] Catalyst 5 μL in all formulations. [b] Volumes of the alcohols were calculated based on their densities: **EG**: 1.113 g cm^{-3}; **DEG**: 1.118 g cm^{-3}; **TEG**: 1.100 g cm^{-3}; **TTEG**: 1.125 g cm^{-3}. [c] The volume of **N3300A** was calculated based on its density (1.170 g cm^{-3}) provided by the supplier.

Table S.2. Formulations of **DEG-xx** based on Scheme S.1 and Table S.1, and corresponding gelation times [a] (Continued).

DOE No. (-xx)	total monomer (% w/w)	$\frac{V_{CH3CN}}{V_{Total}}$	Alcohol [b]				Desmodur N3300A [c]				CH_3CN		Acetone		Gelation time (min)
			mass (g)	volume (mL)	mmol	C (M)	mass (g)	volume (mL)	mmol	C (M)	mass (g)	volume (mL)	mass (g)	volume (mL)	
DEG-xx															
1	15	0.750	0.159	0.1424	1.50	0.2805	0.504	0.4308	1.00	0.1870	2.819	3.5862	0.940	1.1878	143
2	16.46	0.927	0.159	0.1424	1.50	0.3091	0.504	0.4308	1.00	0.2061	3.119	3.9685	0.246	0.3105	124
3		0.574	0.159	0.1424	1.50	0.3097	0.504	0.4308	1.00	0.2065	1.928	2.4530	1.437	1.8164	103
4	20	1.000	0.159	0.1424	1.50	0.3799	0.504	0.4308	1.00	0.2533	2.653	3.3750	0.000	0.0000	39
5		0.750	0.159	0.1424	1.50	0.3804	0.504	0.4308	1.00	0.2536	1.990	2.5312	0.663	0.8384	53
6		0.750	0.159	0.1424	1.50	0.3804	0.504	0.4308	1.00	0.2536	1.990	2.5312	0.663	0.8384	53
7		0.500	0.159	0.1424	1.50	0.3810	0.504	0.4308	1.00	0.2540	1.326	1.6875	1.326	1.6768	77
8	23.54	0.927	0.159	0.1424	1.50	0.4528	0.504	0.4308	1.00	0.3018	1.997	2.5410	0.157	0.1988	25
9		0.574	0.159	0.1424	1.50	0.4536	0.504	0.4308	1.00	0.3024	1.235	1.5707	0.920	1.1631	51
10	25	0.500	0.159	0.1424	1.50	0.4838	0.504	0.4308	1.00	0.3225	1.492	1.8984	0.497	0.6288	35

[a] Catalyst 5 μL in all formulations. [b] Volumes of the alcohols were calculated based on their densities: **EG**: 1.113 g cm^{-3}; **DEG**: 1.118 g cm^{-3}; **TEG**: 1.100 g cm^{-3}; **TTEG**: 1.125 g cm^{-3}. [c] The volume of **N3300A** was calculated based on its density (1.170 g cm^{-3}) provided by the supplier.

Table S.2. Formulations of **TEG-xx** based on Scheme S.1 and Table S.1, and corresponding gelation times [a] (Continued).

DOE No. (-xx)	total monomer (% w/w)	$\frac{V_{CH3CN}}{V_{Total}}$	Alcohol [b]				Desmodur N3300A [c]				CH_3CN		Acetone		Gelation time (min)
			mass (g)	volume (mL)	mmol	C (M)	mass (g)	volume (mL)	mmol	C (M)	mass (g)	volume (mL)	mass (g)	volume (mL)	
TEG-xx															
1	15	0.750	0.225	0.2045	1.50	0.2548	0.504	0.4308	1.00	0.1699	3.100	3.9435	1.033	1.3062	78
2	16.46	0.927	0.225	0.2045	1.50	0.2811	0.504	0.4308	1.00	0.1874	3.430	4.3639	0.270	0.3415	71
3		0.574	0.225	0.2045	1.50	0.2811	0.504	0.4308	1.00	0.1874	2.120	2.6974	1.580	1.9974	76
4	20	1.000	0.225	0.2045	1.50	0.3452	0.504	0.4308	1.00	0.2301	2.917	3.7112	0.000	0.0000	40
5		0.750	0.225	0.2045	1.50	0.3460	0.504	0.4308	1.00	0.2307	2.188	2.7834	0.729	0.9219	54
6		0.750	0.225	0.2045	1.50	0.3460	0.504	0.4308	1.00	0.2307	2.188	2.7834	0.729	0.9219	49
7		0.500	0.225	0.2045	1.50	0.3460	0.504	0.4308	1.00	0.2307	1.459	1.8556	1.459	1.8439	50
8	23.54	0.927	0.225	0.2045	1.50	0.4115	0.504	0.4308	1.00	0.2743	2.196	2.7942	0.173	0.2187	37
9		0.574	0.225	0.2045	1.50	0.4115	0.504	0.4308	1.00	0.2743	1.358	1.7272	1.012	1.2790	48
10	25	0.500	0.225	0.2045	1.50	0.4379	0.504	0.4308	1.00	0.2919	1.641	2.0876	0.547	0.6915	25

[a] Catalyst 5 μL in all formulations. [b] Volumes of the alcohols were calculated based on their densities: **EG**: 1.113 g cm^{-3}; **DEG**: 1.118 g cm^{-3}; **TEG**: 1.100 g cm^{-3}; **TTEG**: 1.125 g cm^{-3}. [c] The volume of **N3300A** was calculated based on its density (1.170 g cm^{-3}) provided by the supplier.

Table S.2. Formulations of **TTEG-xx** based on Scheme S.1 and Table S.1, and corresponding gelation times [a] (Continued).

DOE No. (-xx)	total monomer (% w/w)	$\frac{V_{CH3CN}}{V_{Total}}$	Alcohol [b]				Desmodur N3300A [c]				CH_3CN		Acetone		Gelation time (min)
			mass (g)	volume (mL)	mmol	C (M)	mass (g)	volume (mL)	mmol	C (M)	mass (g)	volume (mL)	mass (g)	volume (mL)	
TTEG-xx															
1	15	0.750	0.291	0.2589	1.5	0.2441	0.504	0.4308	1.00	0.1627	3.168	4.3008	1.127	1.4245	125
2	16.46	0.927	0.291	0.2589	1.5	0.2577	0.504	0.4308	1.00	0.1718	3.741	4.7594	0.294	0.3724	134
3		0.574	0.291	0.2589	1.5	0.2577	0.504	0.4308	1.00	0.1718	2.312	2.9419	1.732	2.1784	217
4	20	1.000	0.291	0.2589	1.5	0.3167	0.504	0.4308	1.00	0.2111	3.181	4.0475	0.000	0.0000	114
5		0.750	0.291	0.2589	1.5	0.3171	0.504	0.4308	1.00	0.2114	2.386	3.0356	0.795	1.0055	114
6		0.750	0.291	0.2589	1.5	0.3171	0.504	0.4308	1.00	0.2114	2.386	3.0356	0.795	1.0055	125
7		0.500	0.291	0.2589	1.5	0.3175	0.504	0.4308	1.00	0.2117	1.591	2.0238	1.591	2.0110	142
8	23.54	0.927	0.291	0.2589	1.5	0.3773	0.504	0.4308	1.00	0.2516	2.395	3.0474	0.189	0.2385	60
9		0.574	0.291	0.2589	1.5	0.3780	0.504	0.4308	1.00	0.3056	0.934	1.8837	1.103	1.3949	50
10	25	0.500	0.291	0.2589	1.5	0.4032	0.504	0.4308	1.00	0.2688	1.790	2.2767	0.596	0.7541	55

[a] Catalyst 5 μL in all formulations. [b] Volumes of the alcohols were calculated based on their densities: EG: 1.113 g cm^{-3}; DEG: 1.118 g cm^{-3}; TEG: 1.100 g cm^{-3}; TTEG: 1.125 g cm^{-3}. [c] The volume of N3300A was calculated based on its density (1.170 g cm^{-3}) provided by the supplier.

Appendix II: General material properties of **ALC-xx**.

Table S.3. General material characterization data for all **ALC-xx** aerogels.

DOE No. (-xx)	total monomer (% w/w)	$\frac{V_{CH3CN}}{(V_{CH3CN} + V_{Acetone})}$	linear shrinkage [a,b] (%)	bulk density [a] (ρ_b, g cm^{-3})	skeletal density [c] (ρ_s, g cm^{-3})	Porosity (Π % void space)
EG-xx						
1	15.00	0.750	25.89 ± 8.65	0.474 ± 0.038	1.248 ± 0.028	62.02 ± 4.03
2	16.46	0.927	19.52 ± 2.09	0.196 ± 0.004	1.267 ± 0.021	84.53 ± 2.19
3	16.46	0.574	20.01 ± 2.04	0.222 ± 0.010	1.255 ± 0.008	82.31 ± 1.15
4	20.00	1.000	16.88 ± 2.16	0.278 ± 0.018	1.020 ± 0.017	72.75 ± 2.71
5	20.00	0.750	20.91 ± 0.21	0.267 ± 0.009	1.252 ± 0.004	78.67 ± 0.83
6	20.00	0.750	21.62 ± 3.27	0.282 ± 0.016	1.255 ± 0.027	77.53 ± 3.01
7	20.00	0.500	20.25 ± 0.10	0.270 ± 0.002	1.223 ± 0.002	77.92 ± 0.26
8	23.54	0.927	18.18 ± 1.20	0.320 ± 0.009	1.166 ± 0.017	72.56 ± 1.96
9	23.54	0.574	22.63 ± 1.08	0.375 ± 0.005	1.199 ± 0.002	68.72 ± 0.46
10	25.00	0.750	17.62 ± 1.38	0.444 ± 0.059	1.178 ± 0.003	62.31 ± 5.02
DEG-xx						
1	15.00	0.750	19.50 ± 1.70	0.463 ± 0.188	1.249 ± 0.006	62.93 ± 15.06
2	16.46	0.927	20.94 ± 1.95	0.224 ± 0.011	1.236 ± 0.004	81.88 ± 0.98
3	16.46	0.574	23.01 ± 2.03	0.230 ± 0.008	1.279 ± 0.012	82.02 ± 1.37
4	20.00	1.000	19.01 ± 2.09	0.258 ± 0.006	1.233 ± 0.003	79.08 ± 0.58
5	20.00	0.750	25.67 ± 2.46	0.321 ± 0.028	1.224 ± 0.008	73.77 ± 2.43
6	20.00	0.750	21.70 ± 1.96	0.279 ± 0.007	1.295 ± 0.010	78.46 ± 1.12
7	20.00	0.500	22.12 ± 4.30	0.287 ± 0.007	1.237 ± 0.021	76.80 ± 2.21
8	23.54	0.927	20.34 ± 2.31	0.322 ± 0.013	1.228 ± 0.004	73.78 ± 1.13
9	23.54	0.574	24.32 ± 0.90	0.414 ± 0.005	1.224 ± 0.016	66.18 ± 1.62
10	25.00	0.750	21.26 ± 1.93	0.366 ± 0.008	1.250 ± 0.002	70.72 ± 0.67

[a] Average of 5 samples. [b] Shrinkage = 100 × (mold diameter – sample diameter)/(mold diameter). [c] Single sample, average of 50 measurements.

Table S.3. General material characterization data for all **ALC-xx** aerogels (Continued).

DOE No. (-xx)	total monomer (% w/w)	$\frac{V_{CH3CN}}{(V_{CH3CN} + V_{Acetone})}$	linear shrinkage[a,b] (%)	bulk density [a] (ρ_b, g cm^{-3})	skeletal density [c] (ρ_s, g cm^{-3})	Porosity (Π % void space)
TEG-xx						
1	15.00	0.750	24.51 ± 0.90	0.247 ± 0.007	1.225 ± 0.009	79.84 ± 1.10
2	16.46	0.927	22.42 ± 2.64	0.271 ± 0.021	1.228 ± 0.011	77.93 ± 2.05
3	16.46	0.574	28.91 ± 4.39	0.336 ± 0.040	1.267 ± 0.018	73.48 ± 3.62
4	20.00	1.000	23.16 ± 1.95	0.302 ± 0.007	1.222 ± 0.004	75.29 ± 0.70
5	20.00	0.750	28.41 ± 2.16	0.391 ± 0.014	1.208 ± 0.003	67.63 ± 1.20
6	20.00	0.750	24.56 ± 1.92	0.356 ± 0.014	1.216 ± 0.002	70.72 ± 1.17
7	20.00	0.500	48.67 ± 0.72	1.076 ± 0.020	1.151 ± 0.003	6.52 ± 1.76
8	23.54	0.927	23.15 ± 1.13	0.408 ± 0.021	1.227 ± 0.003	66.75 ± 1.74
9	23.54	0.574	38.32 ± 1.55	1.014 ± 0.052	1.195 ± 0.012	15.15 ± 4.47
10	25.00	0.750	43.69 ± 1.47	1.070 ± 0.038	1.159 ± 0.002	7.68 ± 3.28
TTEG-xx						
`1	15.00	0.750	52.21 ± 1.80	1.001 ± 0.024	1.106 ± 0.003	9.49 ± 2.19
2	16.46	0.927	28.84 ± 1.58	0.279 ± 0.001	1.247 ± 0.003	77.63 ± 0.31
3	16.46	0.574	53.09 ± 0.44	1.103 ± 0.003	1.203 ± 0.002	8.31 ± 0.30
4	20.00	1.000	31.24 ± 1.52	0.430 ± 0.031	1.179 ± 0.003	63.53 ± 2.65
5	20.00	0.750	49.71 ± 0.95	1.113 ± 0.017	1.209 ± 0.001	7.94 ± 1.41
6	20.00	0.750	48.87 ± 2.28	1.043 ± 0.031	1.172 ± 0.001	11.01 ± 2.65
7	20.00	0.500	51.11 ± 0.75	1.119 ± 0.023	1.199 ± 0.002	6.67 ± 1.93
8	23.54	0.927	47.27 ± 1.46	1.096 ± 0.066	1.196 ± 0.001	8.36 ± 5.52
9	23.54	0.574	43.40 ± 1.95	1.108 ± 0.005	1.202 ± 0.002	7.82 ± 0.45
10	25.00	0.750	45.43 ± 0.21	1.126 ± 0.052	1.233 ± 0.002	8.68 ± 4.22

[a] Average of 5 samples. [b] Shrinkage = 100 × (mold diameter – sample diameter)/(mold diameter). [c] Single sample, average of 50 measurements.

Appendix III: Fitting bulk densities of **ALC-xx** to system variables.

Table S.4. Coefficients of quadratic fitting of the bulk densities (ρ_b) of all **ALC-xx** to total monomer concentration (X_1) and solvent composition (X_2) according to: [a] $\rho_b = A(X_1)^2 + B(X_2)^2 + C(X_1)(X_2) + D(X_1) + E(X_2) + F$.

ALC-xx	A	B	C	D	E	F	R^2
EG-xx (without **EG-1**)	-0.1792	0.0016	-0.0116	0.4523	-0.0331	0.2378	0.945
DEG-xx (without **DEG-1**)	-0.2919	-0.0002	-0.0344	1.0273	0.0527	-0.7561	0.925
TEG-xx	3.7349	0.0081	-0.2167	-2.5213	-0.0910	1.9986	0.917
TTEG-xx	-5.0311	-0.0010	0.3253	-0.2374	-0.1678	2.9717	0.935

[a] Fitting was carried out with orthogonalized variables. Orthogonalization minimizes correlation between terms. The orthogonal transforms of the two variables are given by: 1. $X_1 = \frac{(total\ monomer - 20)}{5}$, 2. $X_2 = \frac{(solvent\ fraction - 0.750)}{0.250}$.

The experimental and the computed response values of ρ_b were analyzed statistically via analysis of variance (ANOVA) at a confidence level of P = 0.05 or 95%. The quality of the fitting of ρ_b by the quadratic model equation was expressed by the coefficient of determination (R^2), and its statistical significance was checked by Fishers test value (F-value).

Appendix IV: SEM of all **ALC-xx**.

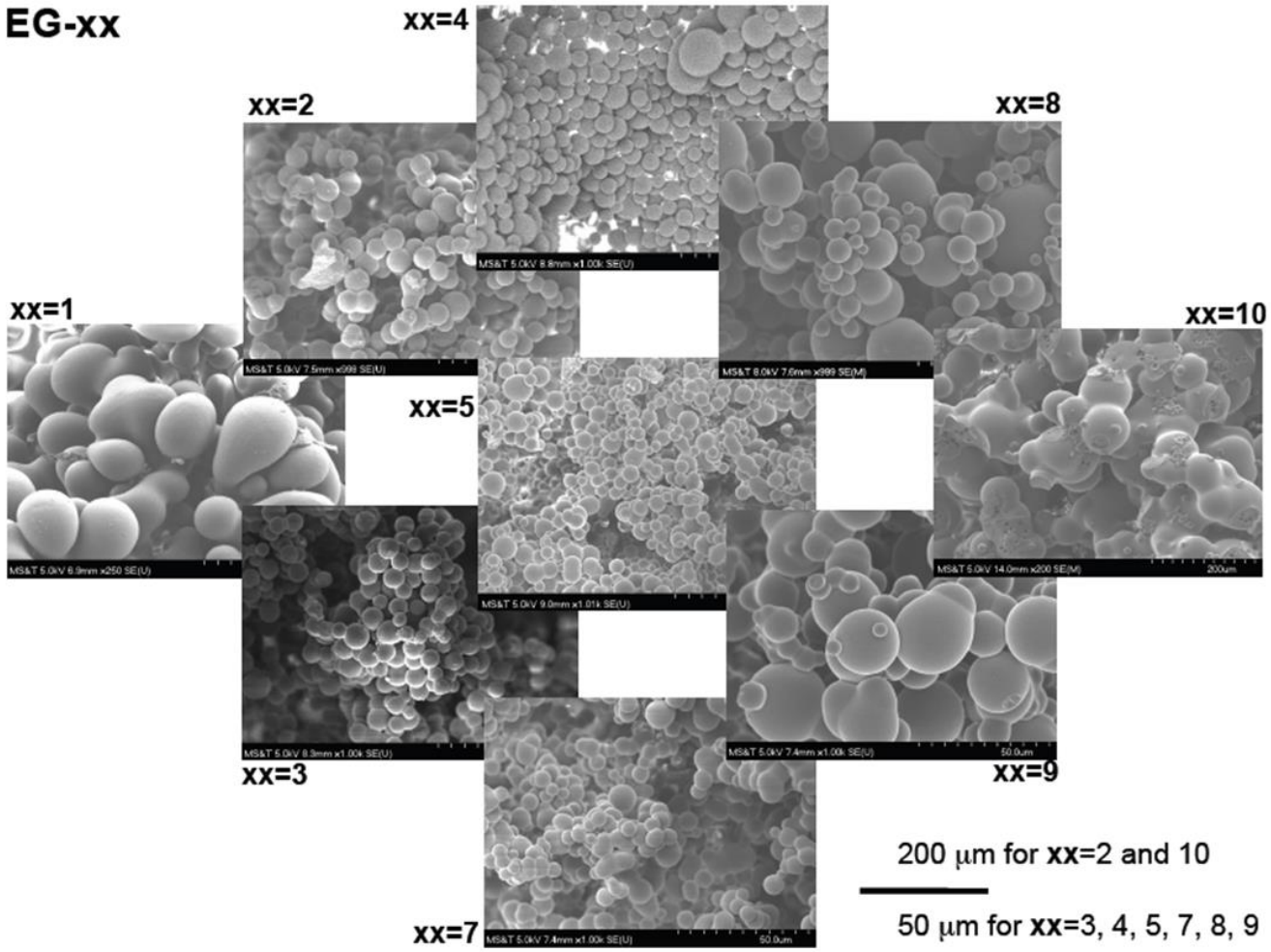

Figure S.1. SEM of all EG-xx.

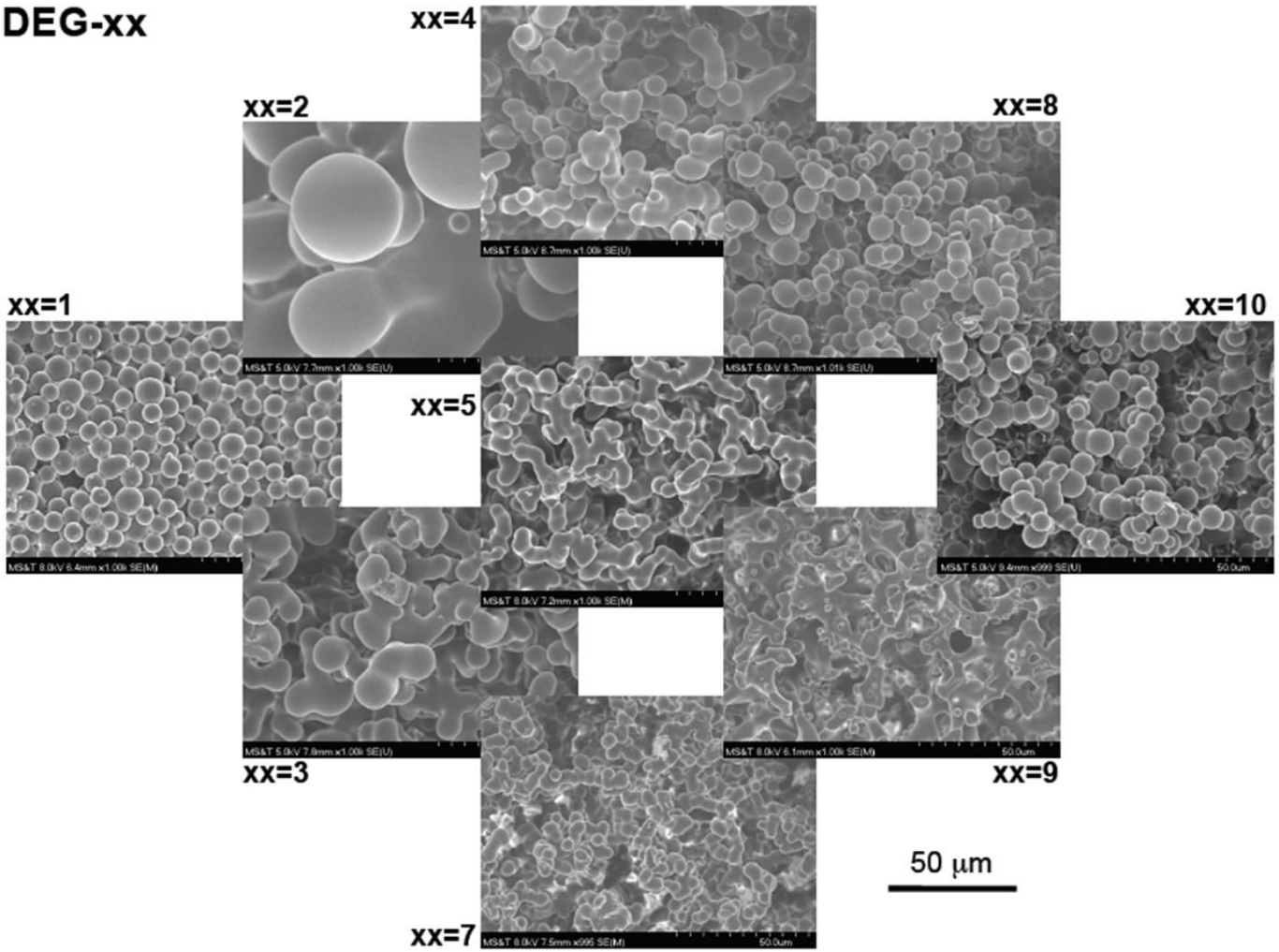

Figure S.2. SEM of all DEG-xx.

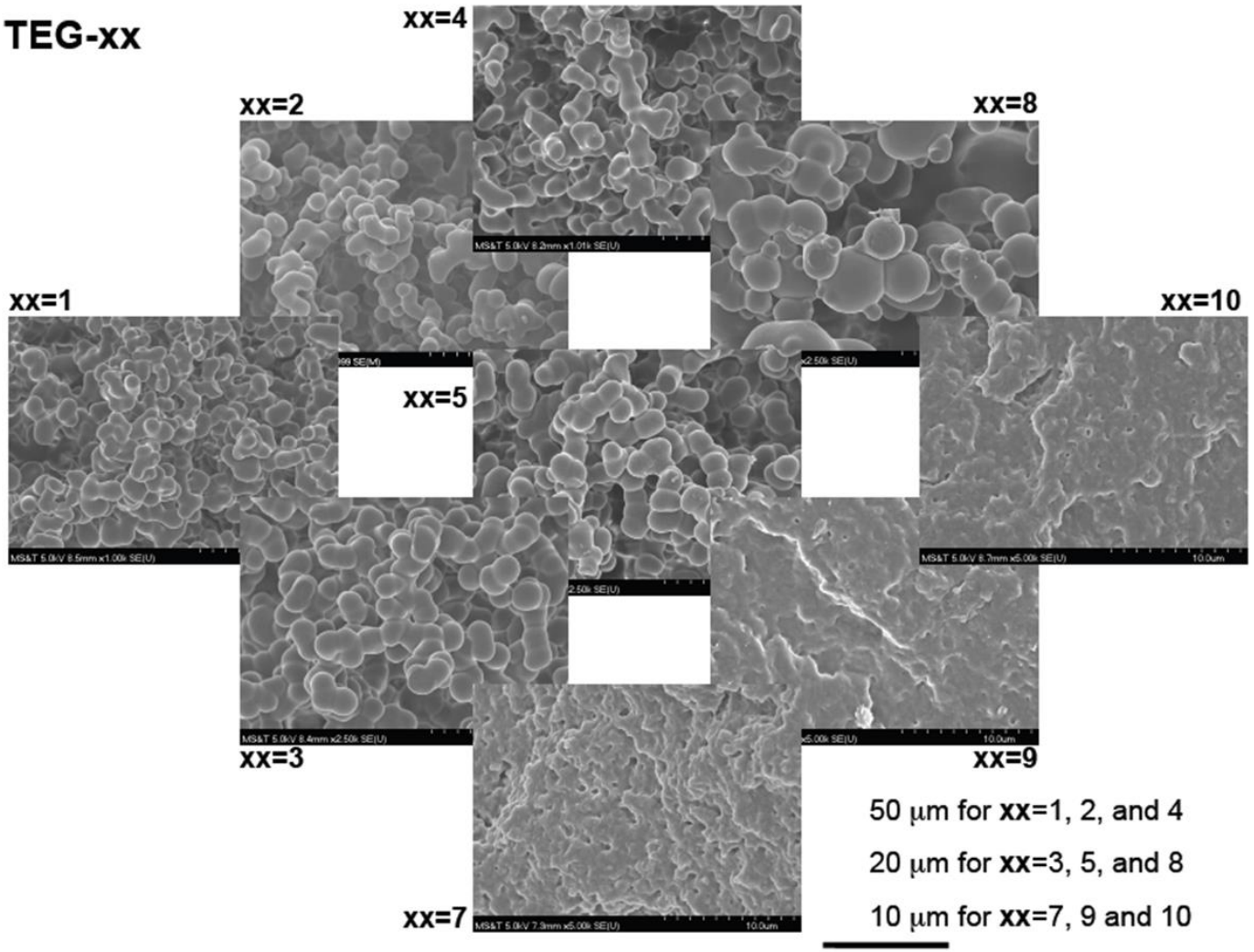

Figure S.3. SEM of all TEG-xx.

Appendix V: ATR FTIR of **DEG-2**, **DEG-4**, **TEG-2**, **TEG-8** and **TTEG-2**.

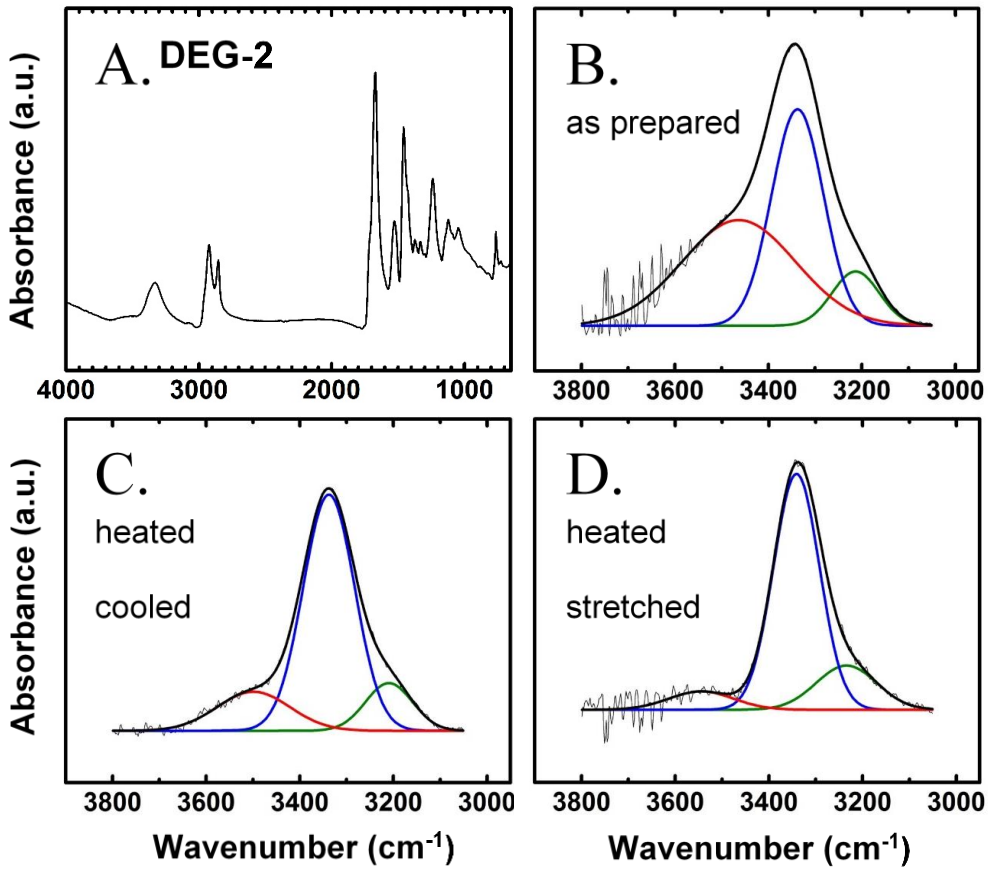

Figure S.4. Room-temperature ATR-FTIR spectra of **DEG-2** taken under different conditions. (a). The entire spectrum. (b). The 3000-3800 cm^{-1} range of frame A, deconvoluted for H-bonding. (c). The same sample as in A and B, heated at T_g+10 ^oC for 15 min, then cooled back to room temperature. (d). The same sample as in A-C, heated again at T_g+10 ^oC for 15 min, stretched to about 60% strain, then the stretching force was released, and the sample was cooled back to room temperature.

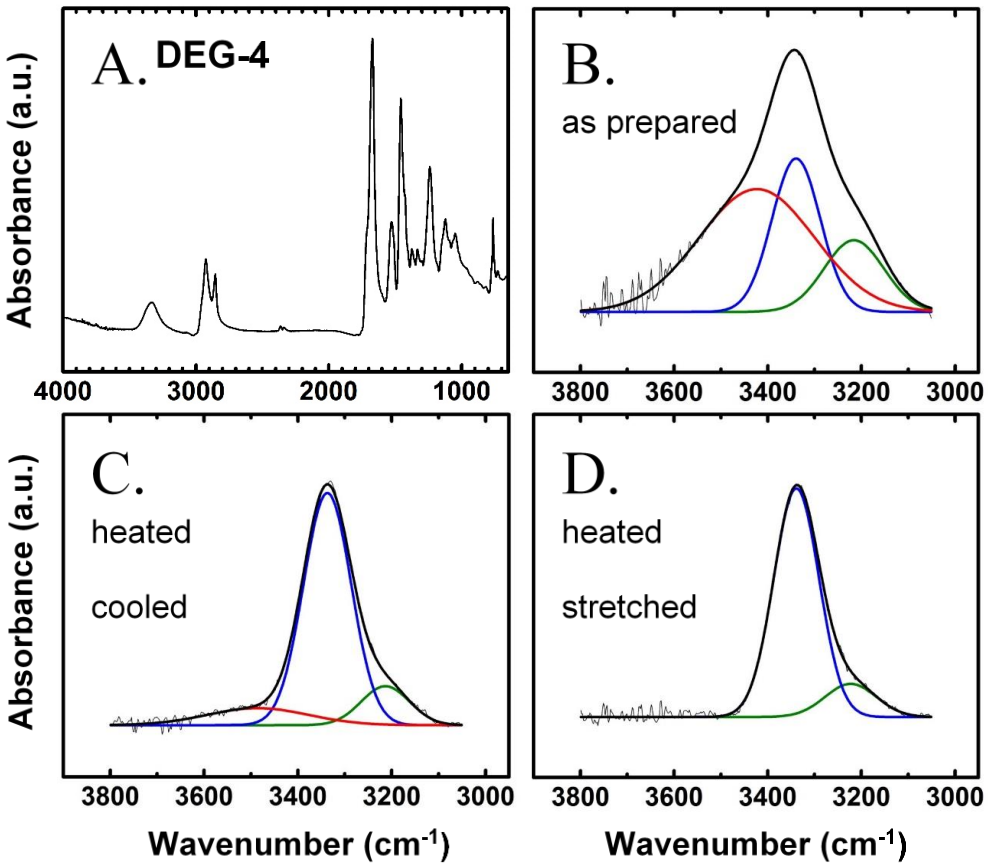

Figure S.5. Room-temperature ATR-FTIR spectra of **DEG-4** taken under different conditions. (a). The entire spectrum. (b). The 3000-3800 cm^{-1} range of frame A, deconvoluted for H-bonding. (c). The same sample as in A and B, heated at T_g+10 ºC for 15 min, then cooled back to room temperature. (d). The same sample as in A-C, heated again at T_g+10 ºC for 15 min, stretched to about 60% strain, then the stretching force was released, and the sample was cooled back to room temperature.

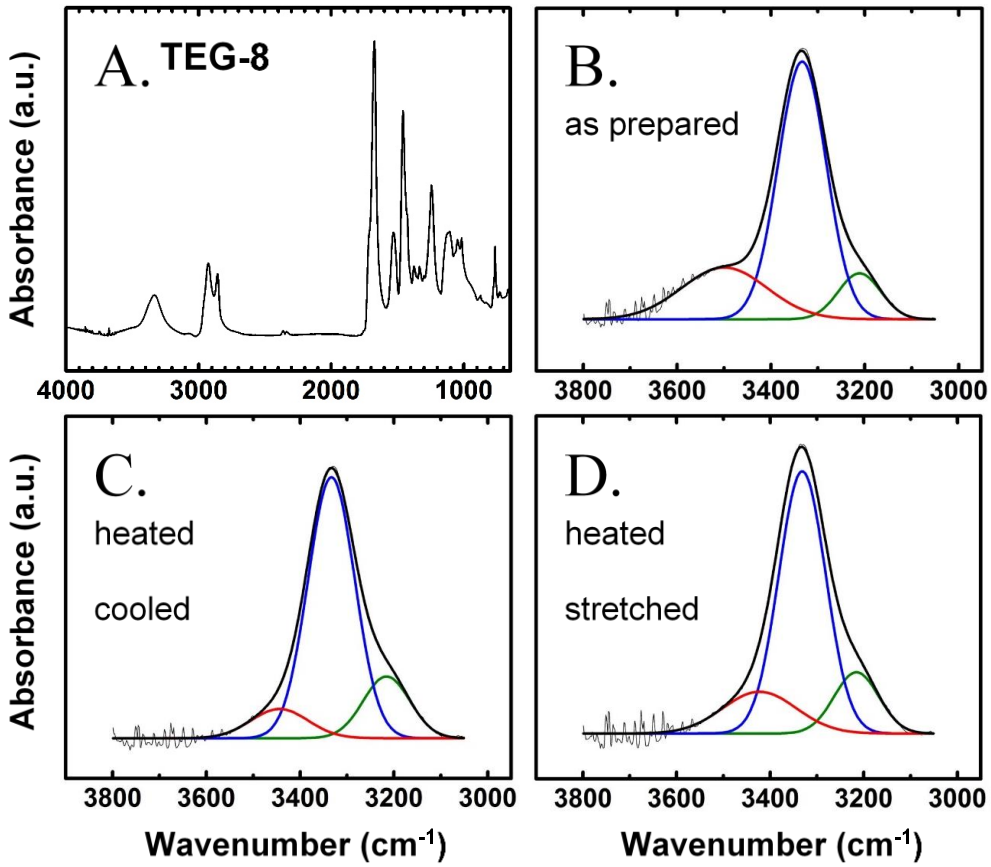

Figure S.6. Room-temperature ATR-FTIR spectra of **TEG-8** taken under different conditions. (a). The entire spectrum. (b). The 3000-3800 cm^{-1} range of frame A, deconvoluted for H-bonding. (c). The same sample as in A and B, heated at T_g+10 ^oC for 15 min, then cooled back to room temperature. (d). The same sample as in A-C, heated again at T_g+10 ^oC for 15 min, stretched to about 60% strain, then the stretching force was released and the sample was cooled back to room temperature.

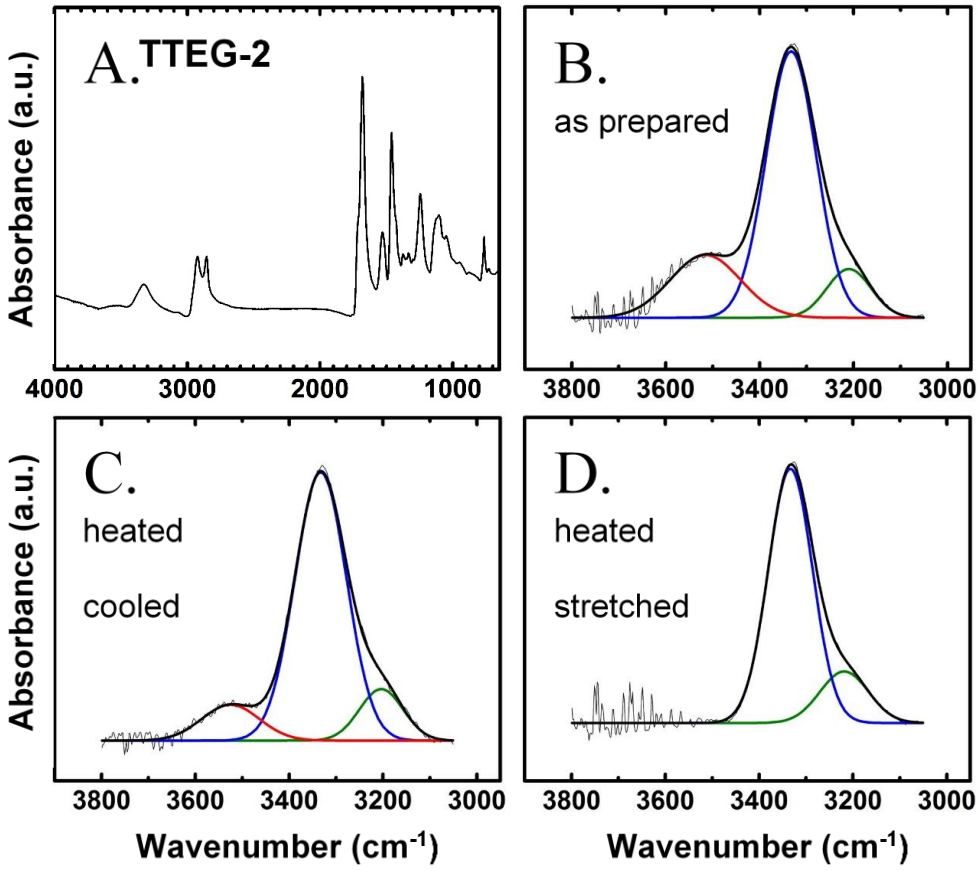

Figure S.7. Room-temperature ATR-FTIR spectra of **TTEG-2** taken under different conditions. (a). The entire spectrum. (b). The 3000-3800 cm^{-1} range of frame A, deconvoluted for H-bonding. (c). The same sample as in A and B, heated at T_g+10 ^oC for 15 min, then cooled back to room temperature. (d). The same sample as in A-C, heated again at T_g+10 ^oC for 15 min, stretched to about 60% strain, then the stretching force was released, and the sample was cooled back to room temperature.

Appendix VI: Glass transition data.

Table S.5. Glass transition data for all non-collapsed **ALC-xx** samples. All values are temperatures in ºC. T_g values are the maxima in the tan δ plots.

-xx	EG-xx			DEG-xx			TEG-xx			TTEG-xx		
	T_g	tan δ FWHM	max G"	T_g	tan δ FWHM	max G´	T_g	tan δ FWHM	max G"	T_g	tan δ FWHM	max G"
1	-	-	-	-	-	-	46.3	14.9	33.3	-	-	-
2	70.8	13.4	63.6	61.3	12.4	51.9	36.3	14.9	27.4	31.0	15.1	17.3
3	70.7	13.0	63.3	58.0	14.2	46.2	41.5	14.9	30.9	-	-	-
4	73.4	12.4	64.8	59.3	13.3	47.6	41.9	17.6	23.3	31.3	14.9	19.9
5	70.7	12.8	62.3	58.3	12.0	48.1	45.5	14.9	32.8	-	-	-
6	64.4	14.1	56.0	58.6	13.3	46.4	43.3	17.7	27.5	-	-	-
7	74.9	16.1	63.9	56.7	12.6	51.1	-	-	-	-	-	-
8	67.7	16.2	53.4	56.0	16.8	47.2	39.9	15.0	28.0	-	-	-
9	73.4	14.6	46.3	53.6	15.9	41.3	-	-	-	-	-	-
10	72.2	15.4	53.3	56.1	12.8	47.1	-	-	-	-	-	-

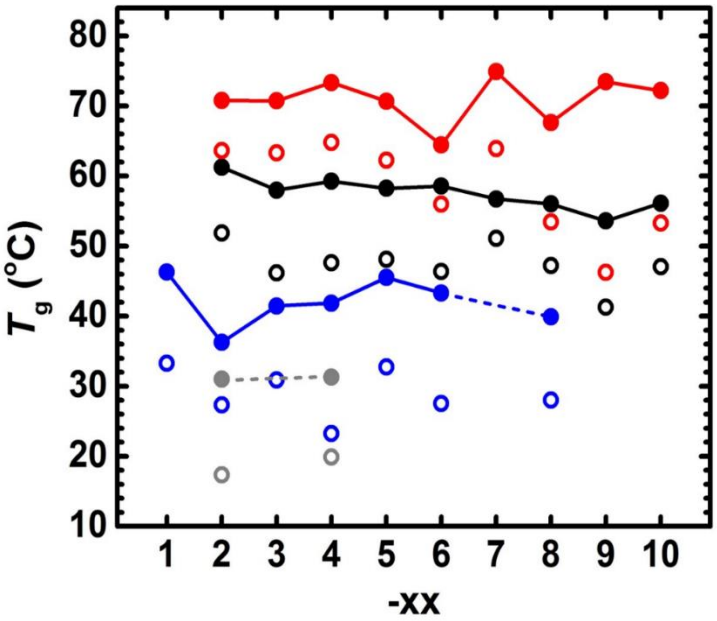

Figure S.8. Data from Table S.5. Closed circles: Glass transition temperatures (Tg) of all non-collapsed ALC-xx samples as a function of xx. Open Circles: maxima in the G´´plots (considered as the point where the polymer starts to soften). Red: EG-xx; Black: DEG-xx; Blue: TEG-xx; and, Gray: TTEG-xx.

Appendix VII: Tensile testing and stress relaxation of **DEG-4**.

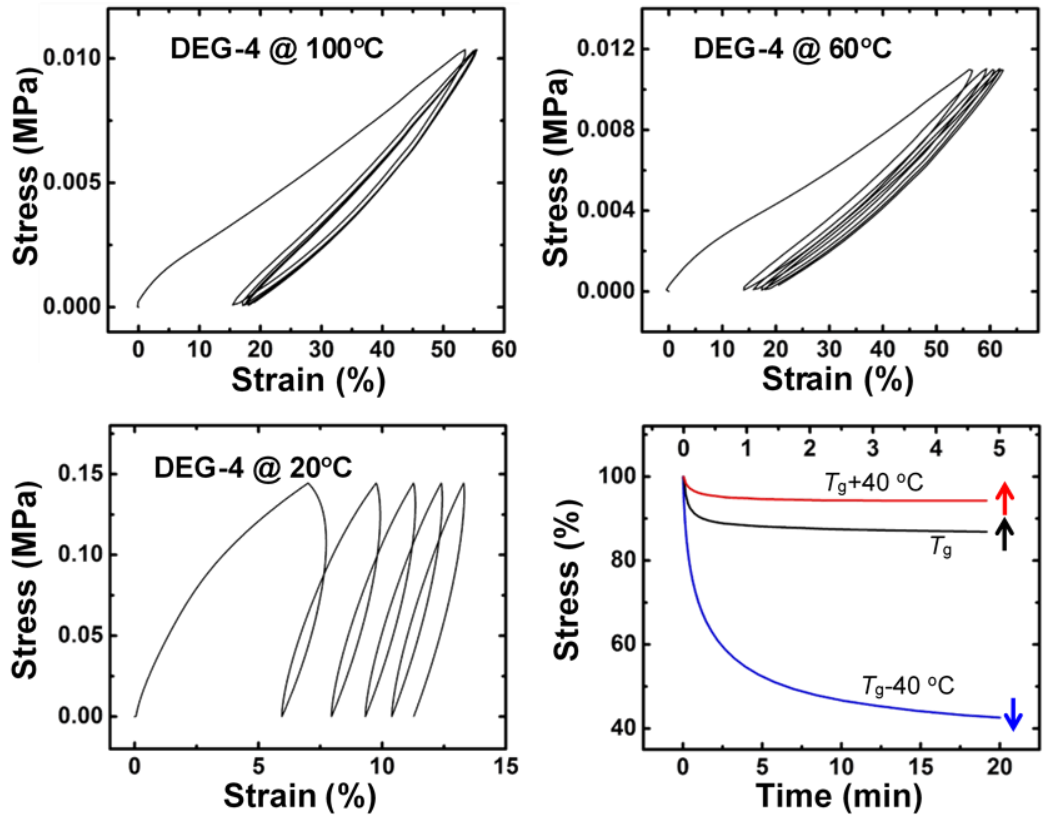

Figure S.9. Five-cycle tensile testing of three **DEG-4** samples (one for each frame) at T_g+40 °C (100 °C), T_g (60 °C) and T_g-40 °C (20 °C). Samples were stretched with a constant force rate of 1 N min^{-1}. Maximum strains at T_g and T_g+40 °C were set near the failure point of the sample. The maximum strain at T_g-40 °C was set by the compliance of the instrument (18 N). Last frame: Stress relaxation run after at the end of the fifth cycle of each frame.

Appendix VIII: Figures of merit for the SME of all **ALC-xx** (Only non-collapsed samples were tested).

Table S.6.1. Strain fixity (Rf) of all ALC-xx as shown (Temperature was cycled for five times in combination with tensile testing).

DOE No. (-xx)	total monomer (% w/w)	$\frac{V_{CH3CN}}{V_{Total}}$	Strain fixity, R_f (%)				
			Temperature cycle No.				
			1	2	3	4	5
DEG-xx							
2	16.46	0.927	98.9	98.8	98.5	98.8	98.8
3	16.46	0.574	99.1	99.0	99.0	98.9	99.0
4	20.00	1.000	99.1	99.1	99.4	99.4	98.9
5	20.00	0.750	98.8	98.8	98.8	98.8	98.9
6	20.00	0.750	97.8	98.7	98.7	98.6	98.7
7	20.00	0.500	99.0	99.1	99.0	99.1	98.9
8	23.54	0.927	98.5	98.6	98.6	98.6	98.6
9	23.54	0.574	97.4	97.5	97.5	97.5	97.5
10	25.00	0.750	98.9	98.7	98.7	98.6	98.6
TEG-xx							
1	15.00	0.750	99.2	99.1	99.1	99.1	99.2
2	16.46	0.927	99.2	99.1	99.1	99.1	99.2
3	16.46	0.574	99.3	99.1	99.2	99.5	99.3
4	20.00	1.000	99.0	98.9	98.9	98.9	98.9
5	20.00	0.750	99.0	98.8	98.8	98.8	98.8
6	20.00	0.750	99.0	98.8	98.8	98.8	98.8
8	23.54	0.927	99.3	99.1	99.1	99.1	99.1
TTEG-xx							
2	16.46	0.927	99.2	99.1	99.1	99.1	99.1
4	20.00	1.000	98.9	98.8	98.8	98.8	98.9

Table S.6.2. Strain recovery (R_r) of all **ALC-xx** as shown (Temperature was cycled for five times in combination with tensile testing).

DOE No. (-xx)	total monomer (% w/w)	$\frac{V_{CH3CN}}{V_{Total}}$	Strain recovery, R_r (%)				
			Temperature cycle No.				
			1	2	3	4	5
DEG-xx							
2	16.46	0.927	82.9	96.9	98.9	99.3	99.8
3	16.46	0.574	93.0	99.0	99.5	99.8	99.9
4	20.00	1.000	90.8	98.5	99.3	99.6	99.7
5	20.00	0.750	84.2	97.2	98.5	98.9	99.3
6	20.00	0.750	87.0	97.5	99.1	99.6	99.6
7	20.00	0.500	85.8	96.7	98.6	99.1	99.5
8	23.54	0.927	93.6	99.0	99.3	99.7	99.9
9	23.54	0.574	89.2	98.6	99.1	100.0	99.8
10	25.00	0.750	80.5	95.3	97.4	97.7	99.6
TEG-xx							
1	15.00	0.750	91.6	98.7	99.3	99.6	99.8
2	16.46	0.927	91.0	98.5	99.4	99.6	99.8
3	16.46	0.574	87.5	99.0	99.4	99.6	99.8
4	20.00	1.000	90.4	98.2	99.4	99.7	99.8
5	20.00	0.750	87.9	98.2	99.0	99.0	99.9
6	20.00	0.750	89.1	98.9	99.7	99.6	99.8
8	23.54	0.927	87.7	98.5	99.4	99.6	99.8
TTEG-xx							
2	16.46	0.927	91.0	99.3	99.7	99.8	99.8
4	20.00	1.000	86.9	98.2	99.0	99.1	99.5

Table S.6.3. Strain recovery rate (R_t) of all **ALC-xx** as shown (Temperature was cycled for five times in combination with tensile testing).

DOE No. (-xx)	total monomer (% w/w)	$\frac{V_{CH3CN}}{V_{Total}}$	Strain recovery rate, R_t (min^{-1})				
			Temperature cycle No.				
			1	2	3	4	5
DEG-xx							
2	16.46	0.927	5.69	5.86	5.70	5.78	6.68
3	16.46	0.574	6.62	6.44	6.49	6.49	6.40
4	20.00	1.000	10.37	10.58	10.69	10.88	10.58
5	20.00	0.750	6.44	6.76	6.59	6.83	6.89
6	20.00	0.750	6.45	6.51	7.04	6.70	6.87
7	20.00	0.500	5.75	5.74	5.79	5.97	5.79
8	23.54	0.927	5.92	5.53	5.82	5.21	5.70
9	23.54	0.574	3.72	3.64	3.57	3.67	3.70
10	25.00	0.750	5.63	5.82	5.85	5.89	5.67
TEG-xx							
1	15.00	0.750	7.65	7.99	7.61	8.10	8.02
2	16.46	0.927	7.40	7.43	7.45	7.60	7.26
3	16.46	0.574	7.82	7.73	7.60	7.55	7.48
4	20.00	1.000	9.18	8.96	9.35	8.78	8.52
5	20.00	0.750	6.73	6.82	6.79	6.73	6.76
6	20.00	0.750	7.90	8.15	7.63	8.10	8.25
8	23.54	0.927	7.53	7.06	7.56	7.92	7.45
TTEG-xx							
2	16.46	0.927	6.16	6.35	6.05	6.01	6.05
4	20.00	1.000	7.80	7.48	6.97	6.62	6.80

Table S.6.4. Fill Factor (*FF*) of all **ALC-xx** as shown (Temperature was cycled for five times in combination with tensile testing).

DOE No. (-xx)	total monomer (% w/w)	$\frac{V_{CH3CN}}{V_{Total}}$	Fill Factor (FF)				
			Temperature cycle No.				
			1	2	3	4	5
DEG-xx							
2	16.46	0.927	0.492	0.628	0.636	0.641	0.660
3	16.46	0.574	0.598	0.629	0.672	0.656	0.636
4	20.00	1.000	0.650	0.691	0.715	0.698	0.678
5	20.00	0.750	0.575	0.680	0.652	0.668	0.699
6	20.00	0.750	0.558	0.662	0.670	0.656	0.661
7	20.00	0.500	0.554	0.616	0.621	0.657	0.649
8	23.54	0.927	0.551	0.601	0.641	0.643	0.662
9	23.54	0.574	0.594	0.684	0.649	0.696	0.697
10	25.00	0.750	0.521	0.630	0.608	0.607	0.646
TEG-xx							
1	15.00	0.750	0.589	0.617	0.623	0.663	0.656
2	16.46	0.927	0.584	0.616	0.610	0.639	0.640
3	16.46	0.574	0.561	0.625	0.618	0.649	0.627
4	20.00	1.000	0.601	0.655	0.650	0.665	0.642
5	20.00	0.750	0.584	0.640	0.654	0.647	0.665
6	20.00	0.750	0.605	0.666	0.664	0.654	0.672
8	23.54	0.927	0.554	0.627	0.653	0.684	0.648
TTEG-xx							
2	16.46	0.927	0.579	0.655	0.647	0.637	0.633
4	20.00	1.000	0.408	0.500	0.460	0.460	0.459

II. NANOSTRUCTURE-DEPENDENT THERMODYNAMIC-KINETIC CORRELATION OF THE SHAPE RECOVERY RATE AND THE YOUNG'S MODULUS IN SHAPE-MEMORY POLMER AEROGELS

Suraj Donthula[1], Chandana Mandal[1], James Schisler,[#,1] Theodora Leventis,[#,1] Mary Ann B. Meador[*,2] Chariklia Sotiriou-Leventis[*,1] and Nicholas Leventis[*,1]

[1] Department of Chemistry, Missouri University of Science and Technology, Rolla, MO 65409, U.S.A.

[2] Materials and Structures Division, Mailstop 49-3, NASA Glenn Research Center, Cleveland OH 44135, U.S.A. [#]Summer student via the ARO High School Student Apprenticeship Program. [*]Correspondence: Tel.: 573-341-4391 (NL) 573-341-4353 (CSL) 216-433-3221 (MABM). E-mail: leventis@mst.edu, cslevent@mst.edu, maryann.meador@nasa.gov

Submitted for publication in *Applied Materials and Interfaces*

ABSTRACT

Thermodynamic-kinetic relationships are not uncommon, but rigorous correlations are rare. Based on the parabolic free energy profiles of elastic deformation, a generalized Marcus-type thermodynamic-kinetic relationship was identified between the shape recovery rate, $R_t(N)$, and the elastic modulus, E, in superelastic poly(isocyanurate-urethane) shape memory aerogels. The latter were prepared with mixtures of diethylene, triethylene and tetraethylene glycol, and an aliphatic triisocyanate. Synthetic parameters were varied systematically using a statistical design-of-experiments approach. Microstructures obtained in each formulation could be put into two groups, one consisting of micron-size particles connected with large necks, and a second one classified as

bicontinuous. The two types of microstructure could be explained consistently by spinodal decomposition involving early versus late phase separation relative to the gel point. Irrespective of microstructure, all samples showed a shape memory effect with shape fixity and shape recovery ratios close to 100%. Larger variations (0.35-0.71) in the overall figure of merit, the fill factor, were traced to a variability in the shape recovery rates, $R_t(N)$, which in turn were related to the microstructure. Materials with bicontinuous microstructures were stiffer and showed slower recovery rates. Thereby, using the elastic modulus, E, as a proxy for microstructure, the correlation of $R_t(N)$ with E was traced to a relationship between the activation barrier for shape recovery, $\Delta A^{\#}$, and the specific energy of deformation, (reorganization energy, λ), which in turn is proportional to the elastic modulus. Data were fitted well (R^2=0.92) by the derived equations. The inverse correlation between $R_t(N)$ and the elastic modulus, E, provides a means for qualitative predictability of the shape recovery rates, the fill factors, and the overall quality of the shape memory effect.

TOC Graphic

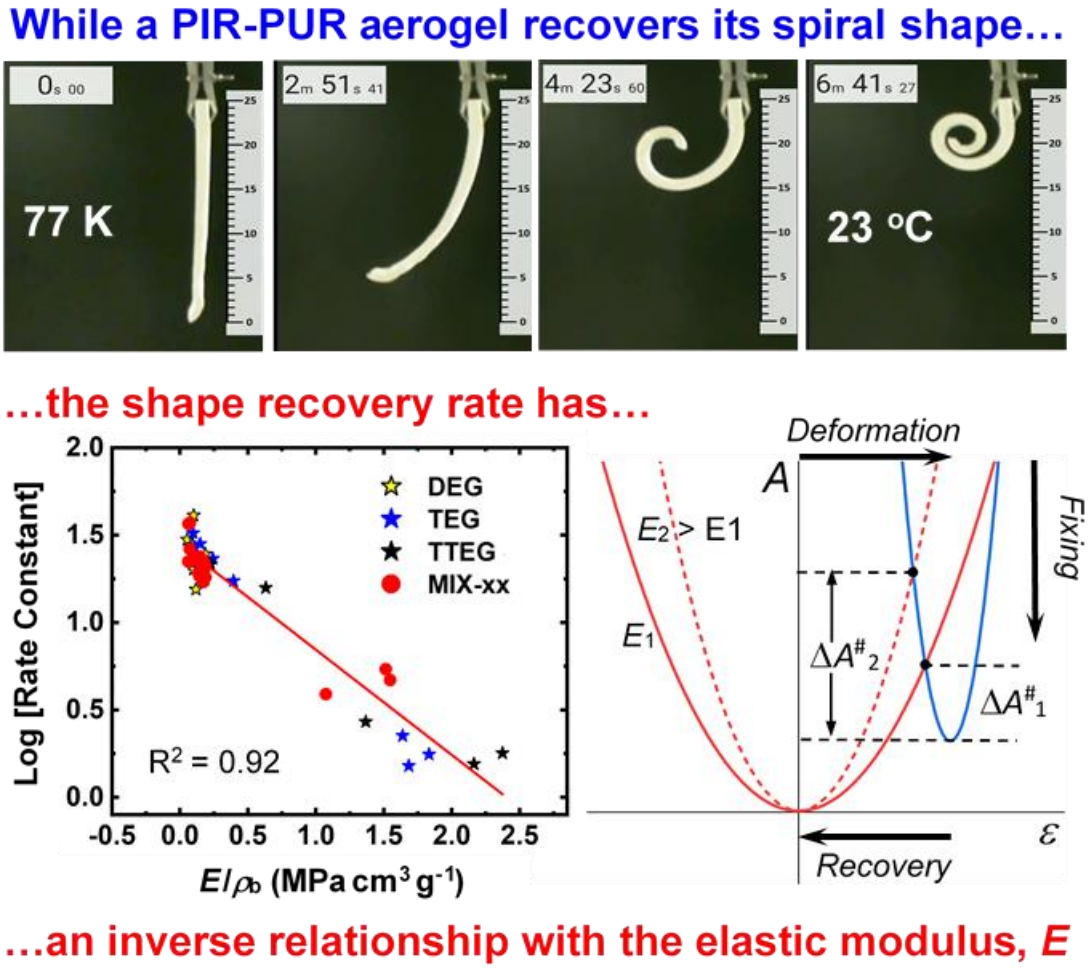

1. INTRODUCTION

Shape memory materials (SMM) remember their permanent shape and return to it from a temporary deformation after they are triggered with a specific stimulus,[1] usually a temperature change.[2] The first SMMs were certain Au-Cd alloys (1930s).[3] Shape memory polymers (SMP)[4,5,6] followed soon thereafter (1940s).[7] Commercial SMP products were already available (e.g., heat shrinking tubing) before systematic studies were initiated in

the 1990s in order to find practical solutions to some of the issues associated with shape memory alloys,[8,9,10] such as high density, low tolerance for high strains, and high cost.[11] SMP have potential as deployable and adaptive structures or in various medical applications. SMP aerogels, in particular, may have potential as lightweight deployable or adaptive antenna substrates, especially due to their very low dielectric constants, approaching 1 as the density decreases.[12] Polymer aerogel antennas have been demonstrated to have higher gain and wider bandwidth with up to 80% weight savings over conventional antenna substrates.[13]

The ultimate refinement in terms of weight savings in SMP can be realized with porous polymers, a special class of which is polymeric aerogels. Aerogels in general are highly porous, low-density solids obtained by drying wet-gels under conditions that preserve their volume into the final dry artifact.[14] Typically, those conditions involve exchange of the pore-filling solvent with a supercritical fluid (e.g., SCF CO_2) that is vented off like a gas. The first shape-memory aerogels (2016) were based on thiol-ene polymers.[15] However, not all SMP can be made into shape memory polymeric aerogels.[16] A necessary condition for SMPs is that they have to be elastomers.[1] However, the requirements that render polymers elastomeric typically increase the solubility of the polymer and render phase separation of what will become the skeletal framework of a wet-gel, and eventually of an aerogel, difficult. Recently, the interplay of those factors was balanced with certain aliphatic poly(isocyanurate-urethane) (PIR-PUR) skeletal frameworks obtained from a hexamethylene diisocyanate trimer (N3300A), and four short diols derived from ethylene glycol (ethylene glycol itself, as well as di-, tri- and tetra-ethylene glycol). The triisocyanate core introduced rigid isocyanurate crosslinking nodes (netpoints) that would

pull the network back together after deformation. Increasing the internodal flexibility with longer diols yielded PIR-PUR aerogels with near-ambient glass transition temperatures (T_g), but also increased the percentage of samples that would undergo unacceptable high shrinkage, resulting to low-porosity materials resembling dense plastics. Deformation of those PIR-PUR aerogels above their T_g's, followed by fixing the temporary shape at temperatures well below T_g, and re-heating back above T_g resulted in a robust shape-memory effect that was used to demonstrate possible applications in diverse areas ranging from space exploration (e.g., deployable panels) to biomedicine (e.g., biomimetic body parts – a human hand-like object performing a function).[16]

This report stems from our efforts to probe further the properties of that class of shape-memory PIR-PUR aerogels by employing *mixtures* of the same glycol-derived short diols used previously (Scheme 1A). The ratio of diols and the sol concentration were varied systematically with a statistical experimental design methodology. The new materials showed again a robust shape memory effect with high figures of merit as their single-diol counterparts.[16] However, they also possessed some additional characteristics that shifted our attention and became the focal point of this study. Specifically, at first, interplay of gelation kinetics (controlled primarily by the total monomer concentration) and the solubility of the developing polymer (that depended on the specific mixture of diols) "froze" and locked-in-space bicontinuous microstructures at their early stages of phase separation. During thermomechanical characterization of the shape memory effect of those bicontinuous microstructures, we noticed a profound inverse relationship between the elastic modulus and the shape recovery rate (a thermodynamic and a kinetic quantity, respectively): bicontinuous microstructures were associated with order-of-magnitude

higher Young's moduli and 3-5 times slower shape recovery rates than samples in which spinodal microstructures had time to undergo coarsening and spheroidization. Eventually, it was discovered that this inverse relationship extends over and encompasses not only the PIR-PUR samples of this study, but also the single-diol PIR-PUR aerogels of our previous study.[16] We are not aware of any prior reports of such phenomena in shape-memory polymers, and the reason they were overlooked in our previous single-diol study was that high-modulus samples had undergone significant shrinkage, and became almost fully dense. Since the focus of that study was on aerogels, the thermomechanical properties of denser samples were not investigated in detail. In contrast, here, bicontinuous structures are higher in modulus without having become fully dense, rendering the said inverse relationship between shape recovery rate and elastic modulus quite pronounced.

Empirical thermodynamic-kinetic relationships are not uncommon. Consider for example the Hammond postulate,[17] the Hammett linear free energy relationships,[18] the concept of kinetic acidity,[19] as well as relationships between kinetic and equilibrium swelling of gels.[20] Albeit unrelated, closer to this work is the fact that the stress relaxation of short-fiber reinforced polymers slows down as the content of fibers, and therefore the elastic modulus, increases.[21] On the other hand, rigorous thermodynamic-kinetic correlations are rare. A notable exception is the Marcus theory as it applies to electron,[22] H^+, H^-,[23] and CH_3 transfer.[24] In a generalized analogy to the Marcus equation, the cause of the thermodynamic-kinetic relationship reported here lies with the properties of crossing parabolic free energy profiles.

2. RESULTS AND DISCUSSION

2.1. SYNTHESIS OF MIXED-ALCOHOL PIR-PUR AEROGELS (MIX-XX)

Aliphatic N3300A triisocyanate was put to react with the stoichiometric amount of a mixture of DEG, TEG, and TTEG (triisocyanate:total diol = 2:3 mol/mol). Polymerization took place at room temperature in a acetonitrile/acetone mixture, and was catalyzed with dibutyltin dilaurate in a 1:120 mol/mol ratio with respect to N3300A (Scheme 1B). Polyurethane wet-gels were aged for 24 h (unoptimized), solvent-exchanged with acetone, and were dried in an autoclave with liquid CO_2 that was converted to a supercritical fluid (SCF), and was vented off like a gas according to standard procedures (see Experimental).

Based on previous results,[16] the study was carried out as a central composite face-centered experimental design,[25] with three exploratory variables: (a) the total monomer concentration, (b) the mole fraction of DEG (the most rigid diol), and (c) the mole fraction of TTEG (the most flexible diol), letting TEG act as a filler. The V_{CH3CN}/V_{Total} ratio was fixed at 0.875 throughout, because screening runs indicated that using pure acetonitrile produced materials with slower elastic recovery, while including a small amount of acetone (<25 %) solved this problem. On the other hand, higher amounts of acetone caused the materials to collapse to dense plastics on drying. Each of the three exploratory variables was set at a low, an intermediate, and a high value. For the purposes of the ensuing discussion the low total monomer concentration level is referred to as Level 1, the intermediate level as Level 2 and the high level as Level 3. The design space is shown in Figure 1. Individual samples are referred to as **MIX-xx**. "**MIX**" emphasizes that samples were based on mixtures of diols, and "**-xx**" is the run number, indicating the position of

each material in the design space (Figure 1). The total model consisted of 15 points; the central point (**MIX-10**) was repeated three times (samples: **MIX-11** to **MIX-13**). The exact formulations of all samples are tabulated in Table S.1 of Appendix I in Supporting Information along with the respective phenomenological gelation times (i.e., the time it took each sol to stop flowing).

2.2. CHEMICAL CHARACTERIZATION OF MIXED-ALCOHOL PIR-PUR AEROGELS

Thermogravimetric analysis (TGA, Figure S.1 in Appendix II of the Supporting Information) showed no mass loss up to about 200 ^{o}C by any other **MIX-xx** except **MIX-17**, indicating absence of residual processing solvents in the samples. **MIX-17** lost progressively up to 2% w/w by 150 ^{o}C. The chemical composition of all **MIX-xx** was probed with solid-state CPMASS ^{13}C and ^{15}N NMR, CHN elemental analysis and ATR-FTIR.

Representative ^{13}C and ^{15}N NMR spectra are shown in Figure 2 using three samples across a diagonal of the design space (Figure 1): **MIX-1** –> **MIX-12** –> **MIX-16**. Those samples were selected in order to probe: (a) the invariance of the chemical composition with monomer concentration (Level 1 to Level 3); (b) the invariance of the chemical composition with microstructure (note in particular **MIX-16** and the discussion in Section 2.3); (c) the complete incorporation of the monomers in the polymeric network (the diagonal was selected so that irrespective of the diols, samples contain the same ratio of near-urethane group versus internal CH_2 groups); and, (d) possible end-groups (via ^{15}N), which, in conjunction with CHN analysis, is useful information related to the growth mechanism, and thereby the **MIX-xx** micromorphology (Section 2.3).

In ^{13}C NMR, the urethane carbonyl resonance was found at 156.7 ppm. The peak at 149.2 ppm corresponded to the isocyanurate carbonyls of N3300A.[26] The resonance at 63.9 ppm was assigned to the methylene carbons near the urethane linkages, i.e., –NH(CO)-O$\underline{C}H_2$–. The internal methylene groups of DEG, TEG and TTEG gave a more intense resonance at 70.0 ppm. Peaks in the 26-43 ppm range came from the –$(CH_2)_6$– groups of the triisocyanate. As mentioned above, the three samples were chosen so that the number of carbons, and therefore the relative intensity of near-urethane group carbons (–NH(CO)-O$\underline{C}H_2$–) vs. the total internal –O$\underline{C}H_2\underline{C}H_2$O– resonances was the same; consequently, the three spectra look very similar, supporting that the three diols were incorporated in the prescribed amounts. Finally, the integrated relative intensities of the total –CH_2– groups of the triisocyanate (26-43 ppm) vs. the total –CH_2– groups of the glycols (60-80 ppm) were in close agreement with the expected formulations of the corresponding **MIX-xx**.

Turning to ^{15}N NMR, all spectra showed only two resonances: at 136.7 ppm and 78.8 ppm, corresponding to the isocyanurate, and the urethane –$\underline{N}$H(CO)-O– nitrogens, respectively. No resonances of any dangling terminal -NH_2 groups were detectable (expected in the range of 40-50 ppm.[27]). In all, both ^{13}C and ^{15}N NMR behaved as if we were dealing with infinite polymer networks.

Both experimental and theoretical CHN elemental analysis data are cited in Table S.2 of Appendix I in Supporting Information. Theoretical (expected) amounts of CHN were calculated assuming: (a) infinite networks; (b) full incorporation of the triisocyanate and diols into the aerogel skeletal framework; and, (c) random binding of the triisocyanate with the three diols. Half of each interconnecting diol was assigned to one isocyanurate core and

the other half to the second isocyanurate core at its other end. The agreement between the theoretical and experimental values was remarkable, in particular considering the fact that we were dealing with as-prepared materials, whose further 'purification' (in the classical preparative chemistry context) was impossible. The CHN analysis results, together with the solid-state NMR data, support the infinite network hypothesis, which in turn suggests that all urethanes of this study were relatively soluble: oligomers stayed in solution for a relatively long period before phase separation, which allowed them either to grow in size to the point that end groups were undetectable, or, more probably, to react with end-groups of other nearby oligomers.

ATR-FTIR spectra were obtained for three representative samples, **MIX-4** from concentration Level 1, **MIX-9** from Level 2, and **MIX-16** from Level 3. All three samples behaved similarly. Representative data are shown with **MIX-9** in Figure 3. Data for the other two samples are shown in Figures S.2 and S.3 of Appendix III in Supporting Information. Figure 3A shows the full spectrum of **MIX-9**; Figure 3B is a magnified version of the NH-stretch region of Figure 3A; Figure 3C shows the NH region after heating at T_g + 40 ^oC and cooling back to room temperature; and, Figure 3D shows again the NH stretch region after heating at T_g + 40 ^oC, stretching near the ultimate break-point, letting strain relax, and cooling back to room temperature. In all spectra, the most intense absorption was the isocyanurate carbonyl stretch at 1676 cm^{-1}. The free urethane carbonyl stretch appeared as a 1729 cm^{-1} shoulder of the isocyanurate C=O stretch. H-bonded urethane carbonyl stretches were expected at lower energies, that is underneath the isocyanurate stretch, and thereby could not be observed. Turning to the urethane C-NH functionality, the N-H bending coupled to the C-N stretch gave a medium-size absorption

at 1525 cm^{-1}. A broad absorption extending from about 3000 cm^{-1} to almost 3500 cm^{-1} was assigned to the N-H stretch. In all spectra, that broad absorption was deconvoluted and was fitted with five Gaussian curves. In contrast to the corresponding single-diol polyurethanes,[16] no free N-H (expected in the range of 3423-3545 cm^{-1}) was detected in any spectrum.[28,29] In all spectra, three of the five Gaussians were in the 3059-3251 cm^{-1} range, thereby they were assigned to stretching of N-H that was H-bonded to glycol units ($NH\cdots O(CH_2)_2$).[30,31,32] The two remaining Gaussians were in the 3333-3397 cm^{-1} range, and they were assigned to stretching of N–H, H-bonded to carbonyls ($NH\cdots O=C$).[29,30] The total integrated area of $NH\cdots O(CH_2)_2$ ranged from 1.50× to 1.68× that of $NH\cdots O=C$. By heating at T_g + 40 ^oC, the total area of $NH\cdots O(CH_2)_2$ increased slightly at the expense of $NH\cdots O=C$. Taking **MIX-9** as an example, the relative ratio of the five fitting Gaussian curves in as-prepared samples was (5:18:38):(33:6), and after heating changed to (5:18:44):(29:5). Those changes were not considered significant. (Parentheses group the three peaks corresponding to $NH\cdots O(CH_2)_2$, and the two peaks corresponding to $NH\cdots O=C$.) Adding a stretching step (Figure 3D), left the peak balance practically unaffected: (5:16:41):(32:6). (The results for **MIX-4** and **MIX-16** from Figures S.2 and S.3 were (starting from as-prepared samples): (5:15:42):(32:5) / (5:20:42):(27:5) / (5:15:45):(30:5), and (5:13:42):(35:5) / (5:16:42):(31:6) / (5:16:42):(31:6), respectively.) Overall, all ATR-FTIR data suggest that in contract to the corresponding single-diol PIR-PUR aerogels,[16] as-prepared **MIX-xx** were already strongly H-bonded. No free NH was detected. Heating and stretching did not cause any additional settling attributable to more favorable H-bonding interactions.

2.3. MICROMORPHOLOGY AND THE GROWTH PROCESS

Microscopically (SEM, Figure 4), all samples except **MIX-17** consist of a solid framework interpenetrating with void space. **MIX-17** looked like a dense plastic. Microstructures could be put in two groups: The first group consisted of random distributions of fused micron-sized particles, and included all samples at concentration Levels 1 and 2 (15% and 20% w/w, respectively), and sample **MIX-15** from Level 3 (monomer concentration at 25% w/w). Generally, the size of the connecting interparticle necks was on the same order as the particles themselves. Only in **MIX-15** at Level 3, necks were clearly smaller than the particles. The particle size decreased as the monomer concentration increased from 15% to 25% following effectively a direct relationship with gelation times (Table S.1); therefore particle growth was related to gelation kinetics. The second group of samples (surrounded by a red dashed line in Figure 4) included the remaining three non-collapsed samples at Level 3, **MIX-14**, **MIX-16** and **MIX-18**, showing a very different microstructure consisting of bicontinuous networks of about same-size interconnected strings and interconnected voids. The width of those strings and voids was one order-of-magnitude smaller than the diameter of their closest relative: **MIX-15** at Level 3. Strings, for example, were only 0.4-0.6 μm wide and completely featureless at all magnifications. That morphology is expected from spinodal decomposition that involves a late phase separation taking place close to the gelation point, which in turn "freezes" those networks in space.[33,34,35] That interpretation is consistent with: (a) the fact that those bicontinuous microstructures were observed from sols richer in longer TEG and TTEG, whose developing polymers were expected to be more soluble; and, (b) the fact that they were observed only in samples from higher concentration sols (Level 3) that gelled

faster. In that context, noting that all samples at concentration Level 3 gelled within a narrow time-interval (60 ± 10 min - see Table S.1), sample **MIX-15**, which was based on a high-DEG formulation, would be expected to phase-separate earlier; thereby, by the more-or-less common gel-point of all samples at Level 3, its bicontinuous network would have time to coarsen into spheroidal domains – hence its particulate morphology. At the other extreme, **MIX-17** did not use any DEG, and it is suggested that gelation may have never taken place at all (i.e., what was perceived as a gel may have been a very viscous polymeric solution). In that regard, the polymeric domains of the bicontinuous network had time to coalesce during aging and contract into a dense plastic upon drying. Extrapolating conceptually from those growth processes at Level 3, the morphology of all samples at Levels 1 and 2 may have been the result of an evolution along a similar path whereas slower reactions, due to lower monomer concentrations, delayed gelation, giving time for further spheroidization and formation of larger particles. That interpretation is also consistent with the larger particles observed in DEG-richer **MIX-2** and **MIX-3** (within Level 1): earlier phase separation expected in those sols allowed more time for coarsening and formation of larger spheroidal domains. Although nucleation-and-growth could not be ruled out from the outset, eventually that gelation mechanism was deemed unlikely given the fact that such a process would be expected to be initiated by aggregation of small oligomers; in that case we should have been able to detect some end-group effects in the CHN elemental analysis data,[36] or "see" dangling terminal $-NH_2$ groups in the solid-state ^{15}N NMR spectra,[27] neither of which was the case with any sample, as discussed in Section 2.2 above. At any rate, irrespective of the growth mechanism, the fact is that we distinguish two well-defined micromorphologies, and as it will become apparent below, morphology

correlates with several material properties of interest ranging from shrinkage, to stiffness, to the shape recovery rate.

2.4. BULK MATERIAL PROPERTIES

All relevant data are included in Table S.3 of Appendix IV in Supporting Information. Skeletal densities, ρ_s, (via He pycnometry) were all in a narrow range (1.19-1.22 g cm^{-3}). Bulk densities, ρ_b, were calculated from the sample weight and physical dimensions and increased from 0.25 g cm^{-3} (monomer concentration at Level 1) to 0.53 g cm^{-3} (Level 3). Percent porosities were calculated via $\Pi=100\times(\rho_s - \rho_b)/\rho_s$ and they varied in the 56-79% v/v range. Densified **MIX-17** felt far outside those ranges (ρ_b = 1.17 g cm^{-3} and Π=3% v/v).

Bulk densities, not including **MIX-17**, were plotted versus the exploratory variables (Figure 5) and were fitted with a quadratic model (Eq 1) where non-significant terms (i.e., those with null-hypothesis probability values P>0.1) were eliminated stepwise until all remaining terms had P<0.1 (In Eq 1, X_1, X_2, X_3 stand for the exploratory variables (Figure 1); for the coefficients A-J of all fitted properties refer to Table S.4 of Appendix V in Supporting Information.) Figure 5 shows that for higher mol fractions of TTEG, the bulk-density surfaces at monomer concentrations 20% and 25% deviated upwards relative to the 15% samples; albeit unbiased by high-density **MIX-17**, that deviation was steeper at the 25% concentration level. Bulk densities are not only a function of the sol concentration, but also of shrinkage.

$$\text{Property} = A(X_1)^2 + B(X_2)^2 + C(X_3)^2 + D(X_1)(X_2) + E(X_1)(X_3) + F(X_2)(X_3) + G(X_1) + H(X_2) + I(X_3) + J \quad (1)$$

Shrinkage took place during drying and varied from 24% to 31% in linear dimensions, except for **MIX-17** that shrunk 45.3% (Table S.3). Quadratic fitting of shrinkage as a function of the exploratory variables (Figure 6, not including **MIX-17**) emphasizes that at Levels 1 and 2, shrinkage did not vary much with composition, however, at Level 3 shrinkage increased sharply as the mol fractions of longer diols, TTEG and TEG, increased. Higher shrinkage is what drove densities disproportionally higher at the high-TTEG end of concentration Level 3 (25%) in Figure 5. Interestingly, while the shrinkage of spheroidal **MIX-15** at concentration Level 3 did not fall far off the shrinkage of the rest of the samples (i.e., at Levels 1 and 2), the subsequent sharp increase of that surface tracked the transition from the spheroidal to the bicontinuous micromorphology of Figure 4, which, as discussed in Section 2.3 above, comprises a balance of early versus late spinodal decomposition and gelation.

2.5. THERMAL CHARACTERIZATION

2.5.1. Glass Transitions. Glass transition temperatures, T_g, were measured with a Dynamic Mechanical Analyzer (DMA) in the tension mode as described in Experimental Section. Samples were subjected to a small-amplitude strain oscillation at 1 Hz and the temperature was ramped from well below (-50 ^oC) to well above (150 ^oC) the expected glass transition range. The typical literature-suggested ramp rate that was tried here first too was 3 ^oC min^{-1}.[37] Initially samples were stiff, but as temperature neared the glass transition range, both the storage (E') and loss moduli (E'') started to decrease, crossing each other along the way twice, and eventually leveling off at values about 1000× lower that those they started from. Typical data are shown in Figure 7A. Glass transition

temperatures (T_g) are reported as the maxima of tan δ (=E"/E') – refer to Table S.5 of Appendix VI in the Supporting Information. The local maxima in the E" curves (pointed at with an arrow in Figure 7A) are included in Table S.5 and can be considered as the onset of the glass transition range. Those maxima were 12-20 ^{o}C lower than the maxima in tan δ.

It has been cautioned, that T_g values of porous polymers obtained with DMA may be overestimated,[38] because a combination of low thermal conductivities, and relatively fast heating rates, may not allow samples to reach thermal equilibrium with the driving stimulus (temperature). Thermal conductivity values, $k_{thermal}$, of all **MIX-xx** were measured at 37.5 ^{o}C in the spirit of ASTM C518-17 using the hot plate method (see Experimental),[39] and were found in the range of 45-100 mW m^{-1} K^{-1} (refer to Table S.6 of Appendix VII in Supporting Information). In turn, those $k_{thermal}$ values were used in order to calculate the time needed for typical samples employed in the DMA experiments (5-6 mm thick) to reach thermal equilibrium. For this, it is noted that $k_{thermal}$ can be expressed (Eq 2) as the product of bulk density, ρ_b, the heat capacity under constant pressure, c_P, and the thermal

$$k = \rho_b \times c_P \times D_{thermal} \quad (2)$$

diffusivity, $D_{thermal}$, of the samples.[32] The c_P values of **MIX-xx** were calculated as weighted averages of the c_P values of the pure-diol PIR-PURs we published recently.[16] All relevant values ($k_{thermal}$, ρ_b, c_P, $D_{thermal}$) are included in Table S.6. $D_{thermal}$ varied in the range of 0.05-0.15 mm^2 s^{-1}. Mathematically, the heat transfer problem across our samples is analogous to conducting thin-layer-cell voltammetry, and it has an exact solution.[33] Nevertheless, a good estimate of the time, τ, required for a heat wave to reach the center of the DMA specimens (2.5-3.0 mm below its surface) can be obtained by introducing the

relevant values in the statistical Einstein-Smoluchowski root mean square displacement equation (Eq 3), and by setting $\langle x^2 \rangle = [(\text{sample thickness})/2]^2$. Time τ was calculated on the order of 52 ± 12 s. Since in the DMA experiment, heat is supplied continuously, the

$$\langle x^2 \rangle = 2 \times D_{\text{thermal}} \times \tau \quad (3)$$

time required to reach thermal equilibrium should be somewhat shorter than that estimate, thereby the calculated τ-range is considered as an upper limit for thermal equilibration. Consistently with those calculations, using temperature ramps of 5, 3, 1 and 0.5 ^{o}C min^{-1}, we see (Figure 7B) that the T_g values at first decreased sharply (at heating rates between 5 and 3 ^{o}C min^{-1}), and then practically leveled off for heating at about 1 ^{o}C min^{-1}. The latter was the heating rate used in all subsequent thermomechanical experiments.

With that heating rate (black bars in Figure 7B), T_g varied narrowly over the **MIX-xx** domain (30-42 ^{o}C). Those T_g values were fitted with a quadratic model (Figure S.4 in Appendix VI of the Supporting Information) and the surfaces were compared with the expected surface calculated by considering T_g of **MIX-xx** as weighted averages of the T_g values of the single-diol PIR-PURs.[16] The experimental surfaces of **MIX-xx** were significantly lower than the expected one, which, in combination with their curvature, points to interactions between mixed diols that evidently modified the molecular arrangement found in the pure systems. That conclusion agrees with the ATR-IR data, which showed no free NH in **MIX-xx**, in contrast to their pure-diol analogues.

2.5.2. Thermomechanical Behavior and the Shape Memory Effect (SME).

Thermomechanical properties were characterized under tension using a DMA in the same configuration as for measuring T_gs. Fresh as-prepared samples were cut into the same geometric sizes used for the determination of T_g (see Experimental), they were placed in

the tension fixture of the DMA, and were subjected to five temperature and stress/relaxation cycles as shown in 3D format from two different perspectives in Figure 8.[1] In Step 1, samples were heated up to their deformation temperature ($T_d = T_g + 10\ ^oC$) and were equilibrated for 5 min. Then, they were stretched at 1N min^{-1} to strain values near the maximum strain of each sample (pre-determined with other samples). Maximum stains were typically around 60%, but for bicontinuous samples at concentration Level 3 (**MIX-14**, **MIX-16**, **MIX-18**), they were found as low as 20%. In Step 2, stress was maintained at the maximum value applied in Step 1, and the temperature was decreased at 5 $^oC\ min^{-1}$ to the fixation temperature ($T_f = T_g - 40\ ^oC$). Once at T_f, samples were equilibrated for 5 min. Strain was monitored continuously throughout Step 2. In Step 3, while the temperature was maintained at T_f, the applied stress was removed suddenly (decreased to 0.01 N), and samples were allowed to fix their shape for 15 min under continuous strain monitoring. Typically, only a very small change in the sample dimensions (contraction) occurred during that time. In the final Step 4, the temperature was increased at 1 $^oC\ min^{-1}$ to the recovery temperature (T_r), which was set equal to the initial deformation temperature (i.e., $T_r = T_d = T_g + 10\ ^oC$). Again, strain was recorded continuously. Samples were held at T_r for 15 min and the sequence of Steps 1-4 was repeated. According to Figure 8, all samples showed relaxation phenomena during the first thermomechanical cycle. Similar relaxation in the pure-diol PIR-PUR analogues was accompanied by a disappearance of free NH and an increase in H-bonding NH. Here, **MIX-xx** did not show any free NH, including the as-prepared samples, therefore relaxation was attributed to other (non H-bonding) non-covalent interactions. After the first cycle, the thermomechanical profile kept on tracing

itself, suggesting a robust SME that was quantified and related to the nanostructure as described below.

The elastic moduli, *E*, of all **MIX-xx** at T_g + 10 ^oC were calculated from the stress-strain curves of Step 1 of each cycle. Primary data are given in Table S.7 of Appendix VIII in Supporting Information. Figure 9A shows the results from cycles 1 and 5 in bar-graph format. In general, samples became less stiff after the first thermal cycle, except bicontinuous **MIX-14**, **MIX-16** and **MIX-18** at Level 3, which become somewhat stiffer. *E* increased with density from Level 1 to Level 3, as expected,[42] however, that increase was not smooth. The *E* values started off quite low at Levels 1 and 2 (below 0.1 MPa), and jumped up by almost a 10-fold at Level 3. That jump though was observed only in bicontinuous **MIX-14**, **MIX-16** and **MIX-18**. The *E* value of shperoidal **MIX-15** at Level 3 followed the smooth trend set by Levels 1 and 2. It is self-evident that in porous materials stiffness is related to the amount of the material at the interconnects of the building blocks; if those building blocks are particles, stiffness depends on the size and shape of the particle interfaces.[43] All other things being equal, the material in bicontinuous microstructures is more evenly distributed along the network and thereby are stiffer.[35,44] Now, Figure 9B shows the response surfaces of *E* at cycle 5 with respect to the exploratory variables. At Levels 1 and 2, the secondary dependence of *E* on the relative diol ratio, was counterbalanced by the increase in density, and thereby generalizations in that respect were difficult. However, the overall similarity of the surfaces in Figures 9B with those of shrinkage in Figure 6 is raher striking, and links two basic material properties so far, shrinkage with modulus, to micromorphology.

The shape memory effect suggested by thermomechanical cycling (Figure 8) is demonstrated in Figure 10 with **MIX-14** cast into a spiral permament shape using a mold as shown. The spiral artifact was stretched flat at T_g+40 ^oC, and while stretched it was dipped in liquid nitrogen. Then it was clamped upside-down, and it was let to thaw back to room temperature. The snapshots of Figure 10 were taken from a movie that is included as Supporting Information. Clearly, the elastic energy stored in the sample during stretching was enough to lift the sample weight and bring it back to its original shape. The shape memory ability of all **MIX-xx** was evaluated via an overall figure of merit that is referred to as Fill Factor, $FF(N)$, whereas N is the thermomechanical cycle number ($1 \leq N \leq 5$).[45] $FF(N)$ was calculated graphically from the ratio of the shaded area underneath the S-shaped curve of Figure 11A to the total area of the box around the S-curve, as shown. The S-curve is the projection of a 3D thermomechanical cycle (Figure 8) on the strain-temperature plane, and includes all information about a sample's ability to fix and recover its shape, as well as how fast it does so, i.e., how steep is the S-shaped curve. By definition, $FF(N)$ depends on the selection of the high and low temperature limits. As the lower limit (i.e., the onset of recovery) we considered the temperature at which the slope of the recovery curve was at 3% of its maximum slope at the inflection point. As the upper temperature limit we chose a more conservative $T_r = T_g + 10$ ^oC rather than the reported $T_g + 20$ ^oC.[45] All $FF(N)$ data are given in Table S.8 of Appendix VIII in Supporting Information. Figure 11B shows and compares in bar-graph format all $FF(1)$ and $FF(5)$ values. Throughout, $FF(2) \approx FF(5)$, consistent the settling noted after the first thermomechanical cycle in Figure 8. Post-settling, $FF(N>1)$ reached values as high as 0.7, which are considered high.[45,46] Upon closer inspection of Figure 11B, we see a general downward trend in the $FF(5)$ values

from Level 1 to Level 2. That trend, however, was interrupted, and in some cases it was reversed, at Level 3. For additional insight, $FF(N)$ was deconvoluted to its three contributing figures of merit: the strain fixity ratio ($R_f(N)$), the strain recovery ratio ($R_r(N)$) and the strain recovery rate ($R_t(N)$). $R_f(N)$ and $R_r(N)$ were calculated from strain vs. time plots (e.g., Figure 12A), which were constructed by first projecting the 3D curves of Figure 8 on the strain-temperature plain (just like for constructing Figure 11A), followed by unfolding that projection in time. The last operation was based on the fact that temperature was varied at a controlled rate, thereby it was uniquely defined at every point in time. $R_t(N)$ was calculated from the derivative of the strain vs. time curves as shown in Figure 12B. All data for $R_f(N)$, $R_r(N)$ and $R_t(N)$ are given in Tables S.9 – S.11 of Appendix VIII in Supporting Information.

The strain fixity ratio, $R_f(N)$, describes how well a sample can retain its temporary (stretched) shape at a temperature sufficiently lower than T_g under stress-free-conditions. $R_f(N)$ was calculated for each cycle, N, via Eq 4, from the ratio of the equilibrium strain at the low- temperature, stress-free condition, $\varepsilon_u(N)$, to the maximum strain, $\varepsilon_m(N)$, at which

$$R_f(N) = \frac{\varepsilon_u(N)}{\varepsilon_m(N)} \times 100 \quad (4)$$

the sample was stretched at the deformation temperature, T_d, in the beginning (Step 1) of the cycle – see Figure 12A. By definition, $R_f(N)$ expresses the total creep during Steps 2 and 3 of every cycle, that is (a) under stress during cooling, (b) under stress during the first 5-min stay at T_f, and (c) under a stress-free condition during the subsequent 15-min stay at T_f. $R_f(N)$ values were always, including cycle 1, greater than 97% (Figure 13A). Even collapsed **MIX-17** showed $R_f(N)$>94%. It is concluded that strain fixity did not have a significant contribution in the differentiation among the $FF(N)$ values.

The strain recovery ratio, $R_r(N)$, reports the ability of a sample heated back up to T_r (=T_d) to recover its starting shape in a particular stress-cool-heat cycle, N. Referring again to Figure 12A, $R_r(N)$ values were calculated via Eq 5 as the ratio of the recovered strain to the maximum strain the sample was stretched at the beginning of the cycle. The recovered

$$R_r(N) = \frac{\varepsilon_m(N) - \varepsilon_p(N)}{\varepsilon_m(N)} \times 100 \quad (5)$$

strain in a cycle N was the difference between the residual strain after the full cycle, $\varepsilon_p(N)$, and the maximum strain, $\varepsilon_m(N)$, the sample was stretched at in Step 1 of that cycle. Comparing $R_r(N)$ values among cycles gives a measure of fatigue. As shown in Figure 13B, all $R_r(N)$ values started off lower in the first cycle (79-91%), increasing afterwards to ≥99.5% for all samples except **MIX-18** that settled at 98.1%. The increase of $R_r(N)$ after the first cycle was consistent with settling noted above. Overall, all **MIX-xx** demonstrated excellent shape recovery, but again, just like with $R_f(N)$, the $R_r(N)$ ratio did not make a meaningful contribution to the differentiation noted among the $FF(N)$ values in Figure 11B.

Finally, $R_t(N)$ is a measure of the speed with which strain recovers back during the final heating stage of a thermomechanical cycle (Step 4). $R_t(N)$ was introduced[16] as a means to quantify the fact that the area underneath the S-shaped curve of Figure 11A, and thereby $FF(N)$, depend on the curve steepness. Referring to Figure 12B, $R_t(N)$ values for each cycle were caluclated via Eq 6 from the slopes at the inflection points of the recovery curves. Because strain recovery was driven by the heating rate, sufficient low heating rates

$$R_t(N) = \max\left[-\frac{dStrain}{dt}\right] \quad (6)$$

would ensure quasi thermal equilibrium conditions, and thereby slopes would represent an innate property of the material rather than the imposed driving force (temperature ramp).

The heating rate in use in all experiments was 1 ^{o}C min^{-1}, stemming from the measurements of the glass transition temperatures, as discussed in Section 2.5.1. $R_t(N)$ data are presented in bar-graph format in Figure 14 for the first and fifth cycles of all **MIX-xx**. $R_t(N)$ values varied from 2 min^{-1} to 10 min^{-1}. With obvious "outliers" **MIX-2** and **MIX-5**, on average $R_t(N)$ showed a slight increase with density from Levels 1 to 2, and that trend was followed by spheroidal **MIX-15** at Level 3.[47] That trend is reminiscent of a rate law like $R_t(N) = k_{rate}$ ρ_b. But obviously, even to put it generously, that law is very weak, as it is violated in a major fashion by bicontinuous materials **MIX-14**, **MIX-16** and **MIX-18**, which showed just the opposite relationship: their $R_t(N)$ values were 3-5 times *lower* than the values of all other samples in this study. In the context of this discussion then, an all-sample inclusive rate law would have a rate constant, k_{rate}, dependent on micromorphology. The latter, however, is difficult to express in numbers in order to enter it in any form of quantification. In this context, two properties that can be expressed quantitatively, shrinkage and elastic modulus, have shown clear correlations with micromorphology, and thereby can be used as *proxies* for the latter. We see no obvious quantitative relationship between $R_t(N)$ and shrinkage. On the other hand, the relationship between $R_t(N)$ and E can be expressed quantitatively.

The elastic modulus, E, a measure of stiffness, is a thermodynamic quantity that is proportional to the work needed to carry out a certain amount of deformation (see below). The recovery rate is a kinetic quantity, and at first glance there is no obvious reason why it has to be related to the elastic modulus. However, even just a cursory comparison of Figures 14 and 9A reveals a quite pronounced inverse relationship between $R_t(N)$ and E, especially at Level 3, suggesting that stiffer samples (that require more energy for

deformation) should be also associated with higher activation barriers for shape recovery. An apparently similar kinetic-thermodynamic phenomenon has been debated frequently in the literature, and concerns short fiber reinforced polymers, which, evidently, undergo slower isothermal stress relaxation as the amount of fibers increases (and thereby the composite becomes stiffer).[21,48,49,50] That phenomenon has been attributed either to covalent bond formation between fibers and the polymer, or to interfacial phenomena whereas fibers slow the movement of polymeric chains in their vicinity, or to the effect of the viscoelastic properties of the polymer on the shear stress transfer to fibers.[21] None of those processes apply in our case.

Elastic deformation has a parabolic mass-specific free energy profile, A (Eq 7).

$$A = \frac{E}{2r_b}e^2 \tag{7}$$

The "width" "width" of the parabola is related inversely to the elastic modulus, E (Scheme 2). Stiffer materials ($E_2 > E_1$) have narrower specific energy profiles, (e.g., dashed red line in Scheme 2). According to our thermomechanial protocol (Figure 8), stretching a sample (at T_d) to ε_m increases the specific free energy of the material by $\lambda = (E/2\rho_b)\varepsilon_m^2$ (that is $\lambda = A$ at ε_m – Scheme 2). No covalent or non-covalent bonds are broken during that deformation. Elastic deformation involves only entropic work.[1,51] Thereby, the reorganization energy λ is purely entropic, and equal to $-T_d\Delta S$. From the two expressions for λ it is derived that $\Delta S = -E\varepsilon_m^2/2T_d\rho_b$. Freezing the stretched sample to T_f (= T_g – 40 ^oC), creates a much stiffer material (by approximately 1000 times – see Figure 7A), with a much narrower energy profile than that of the original state at T_d (refer to the blue parabola in Scheme 2). The bottom of that profile is by $(T_f - T_d)\Delta S$ lower than the reorganization

energy λ expended to stretch the sample to ε_m. Thereby, $\Delta A = l - (T_f - T_d)\Delta S$. According to Scheme 2, just by considering the shape of the parabolic profiles, the activation barrier for shape recovery, $\Delta A^{\#}$, is higher for a stiffer material (that is, for $E_2 > E_1$, crossing point 2 is higher than point 1), thus justifying slower recovery rates for stiffer materials.

Quantitatively, the energy barrier for strain recovery, $\Delta A^{\#}$ (Scheme 2), is calculated based on the equations of crossing parabolas. In the most general case $\Delta A^{\#}$ is given by Eq 8, which was derived (see Appendix IX in Supporting Information) by normalizing the

$$\Delta A^{\#} = \frac{2l}{(1-\varepsilon)^2}\left[\sqrt{\varepsilon} - \sqrt{1 - \frac{\Delta A(1-\varepsilon)}{2l}}\right]^2 \tag{8}$$

density-specific elastic moduli (E/ρ_b) to their highest value, namely the modulus of the fixed sample (blue parabola in Scheme 2). ε stands for the normalized density-specific modulus; in turn, $\lambda = \varepsilon\varepsilon_m^2/2$, and ΔS is given by $\Delta S = -\varepsilon\varepsilon_m^2/2T_d$. If the moduli of the red and blue energy profiles were equal, then the activation barrier would be given by the typical Marcus equation (Eq 9), and λ would be given, as discussed above, by $\lambda = (E/2\rho_b)\varepsilon_m^2$.

$$\Delta A^{\#} = \frac{(\Delta A - l)^2}{4l} \tag{9}$$

After the appropriate substitutions, and considering the fact that $\varepsilon \approx 0.001$, the general case of Eq 8 takes the form of Eq 10.

$$\Delta A^{\#} = \varepsilon e_m^2\left(1 - \frac{T_f}{2T_d}\right) \tag{10}$$

Assuming an exponential relationship between the activation barriers for shape recovery and the corresponding rate constants (k_{rate}), Eq 10 yields Eq 11 (see Appendix IX), where C is the pre-exponential factor. The temperature T in the denominator is the

$$Logk_{rate} = LogC - \frac{\varepsilon e_m^2}{2.303RT}\left(1 - \frac{T_f}{2T_d}\right) \quad (11)$$

temperature at the inflection points in Figure 12B (i.e., where the derivative is calculated at); those T are very close to the glass transition temperatures – see Table S.12 of Appendix VIII in Supporting Information. (Similar expressions –see Eq.s S.4 and S.6 in Appendix IX– were derived from the Marcus expression of Eq 9 above.) Substituting $k_{rate} = R_t(N)/\rho_b$, Eq 11 yields Eq 12. Figure 15 confirms the linear relationship between Log $R_t(5)/\rho_b$ and

$$Log\frac{R_t(N)}{r_b} = LogC - \frac{\varepsilon e_m^2}{2.303RT}\left(1 - \frac{T_f}{2T_d}\right) \quad (12)$$

E/ρ_b (data from Tables S.12 of Appendix VIII in the Supporting Information). It is noted that in addition to the data from **MIX-xx**, Figure 15 also includes the relevant data for all samples with porosities >10% from our previous work on shape memory PIR-PUR aerogels based on pure DEG, TEG and TTEG diols.[16] As mentioned in the Introduction, since the focus of that study was on aerogels, the thermomechanical properties of denser samples were not investigated in detail. Clearly, in terms of the shape memory effect, slow recovery rates are associated with stiffer materials. In turn, a broader generalization can be made by cross-referencing Figure 4 with the SEMs of the samples from pure-diols:[16] significantly stiffer samples are related to bicontinuous micromorphologies, including those in samples that appear partially collapsed, yet with porosities ≥10 %.

3. CONCLUSION

In summary, PIR-PUR aerogels were prepared with mixed ethylene glycol-derived diols and an aliphatic triisocyanate. Synthetic parameters were varied systematically using a statistical design-of-experiments approach. The chemical composition of each sample reflected its formulation, as designed. Microstructures could be put in two groups, one consisting of micron-size particles connected with large necks, and a second one classified as bicontinuous. The two groups could be explained consistently by a gelation mechanism involving spinodal decomposition and early versus late phase separation relative to the gel point. Irrespective of microstructure, all samples showed a robust shape memory effect with shape fixity and shape recovery ratios close to 100%. The overall figure of merit, the fill factor, was found in the range of 0.35-0.71; that variability was related, at least partly, to the shape recovery rates, $R_t(N)$, which in turn were related to the micromorphology. Materials with bicontinuous micromorphologies were stiffer and showed slower recovery rates. The inverse correlation between $R_t(N)$ and the elastic modulus, E, provides a means for a qualitative predictability of the shape recovery rates, thereby the fill factor, and in turn the overall quality of the shape memory effect. That predictability can be summarized as follows: bicontinuous microstructures are stiffer and recover their shape more slowly. Quantitatively, the correlation of $R_t(N)$ and E (Eq. 12) was traced to a linear correlation of the activation barrier for shape recovery and the elastic modulus (Eq 10). The elastic modulus is proportional to the specific work done for a certain amount of deformation (that is the integral underneath the stress-strain curve). Thereby, Eq. 10 represents a rigorous thermodynamic-kinetic correlation, analogous to the Marcus expression for electron transfer reactions.

4. EXPERIMENTAL

4.1. MATERIALS

All reagents and solvents were used as received unless noted otherwise. The triisocyanate (N3300A) was obtained courtesy of Covestro LLC (Pittsburg, PA) under the trade name Desmodur N3300A. Diols (ALC): diethylene glycol (DEG), triethylene glycol (TEG), tetraethylene glycol (TTEG); the catalyst: dibutyltin dilaurate (DBTDL); and, solvents: anhydrous acetonitrile and anhydrous acetone were purchased from Sigma-Aldrich. Siphon-grade CO_2 was purchased from Ozark Gas Co.

4.2. SYNTHESIS OF SHAPE MEMORY POLY(URETHANE-ISOCYANURATE) AEROGELS

In a typical process, exemplified with **MIX-10**, N3300A as-received (Desmodur N3300A, 0.338 g, 0.67 mmol) and the suitable amounts of diols (DEG, 0.027 g, 0.25 mmol; TEG, 0.075 g, 0.50 mmol; TTEG, 0.049 g, 0.25 mmol) were dissolved in an anhydrous acetonitrile/acetone (87.5/12.5) mixture. All formulations (Table S.1 in Supporting Information) were selected according to a central composite face-centered design (CCFD) model (see Figure 1),[52,53] using the JMP11 software package.[54,55] The solution was stirred in a three-neck round-bottom flask at 23 °C under N_2 for 10 min, and DBTDL (3.35 μL) was added. The resulting sol was stirred for another 5 min and was poured into suitable molds. Smaller rectangular specimens for dynamic mechanical analysis were cut from cylindrical samples prepared using plastic syringes as molds (All Plastic Norm-Ject Syringes, 20 mL, Fisher Scientific Catalogue No. 14-817-32, 2.53 cm inner diameter). Larger rectangular samples suitable for ATR-IR and thermal conductivity measurements

were prepared using plastic containers (Style Selections 16”×12.75” Plastic Multi-Use Insert Drawer Organizer, Model No. 39001, Lowe’s Item No. 105922). An aluminum mold for casting gels in the form of a spiral (Figure 10) was fabricated from an aluminum block using a waterjet. After casting the sol, molds were sealed with Parafilm^{TM} and were kept at room temperature for gelation. The gelation time varied from 50 min to about 2 h 50 min depending on the ratio of alcohols and the monomer concentration (Table S.1). Gels were aged for 24 h in their molds at room temperature. Subsequently, gels were removed from the molds, washed with acetone (4×, 8h each time, using 4× the volume of the gel each time), and were dried with CO_2 taken out as a supercritical fluid (SCF). Samples are referred to as **MIX-xx** where **xx** denotes the position in the domain of the independent variables (Figure 1).

4.3. METHODS

4.3.1. Drying. Drying of wet-gels was carried out in an autoclave (Spe-edSFE system, Applied system, Applied Separations, Allentown, PA). Wet-gels were loaded into the autoclave at room temperature and were covered with acetone. The pressure vessel was closed, and liquid CO_2 was allowed in at room temperature. Acetone was drained out from the pressure vessel, while more liquid CO_2 was allowed in. When no more acetone was coming out of the autoclave, samples were kept under liquid CO_2 for half an hour. Then liquid CO_2 was drained out while more liquid CO_2 was allowed in. The cycle was repeated several times until all acetone had been extracted out of the pores of the gels. Subsequently, the temperature of the autoclave was raised to 40 ^{o}C, and that condition was maintained for two hours. Finally, supercritical fluid (SCF) CO_2 was vented off as a gas.

4.3.2. Chemical Characterization. Solid-state CPMAS ^{13}C-NMR spectra were obtained with samples cut into small pieces on a Bruker Avance III 400 MHz spectrometer with a carbon frequency of 100 MHz, using a 7 mm Bruker MAS probe at a magic angle spinning rate of 5 kHz, with broadband proton suppression, and the CP TOSS pulse sequence. The Total Suppression of Spinning Sidebands (TOSS) pulse sequence was applied by using a series of four properly timed 180º pulses on the carbon channel at different points of a cycle before the acquisition of the FID, after an initial excitation with a 90º pulse on the proton channel. The 90º excitation pulse on the proton and the 180º excitation pulse on carbon were set to 4.2 µs and 10 µs, respectively. A contact time of 2 ms was used for cross polarization. Solid-state ^{13}C NMR spectra were referenced externally to glycine (carbonyl carbon at 176.03 ppm). Chemical shifts are reported versus TMS (0 ppm). Solid-state CPMAS ^{15}N-NMR spectra were also obtained on the same Bruker Avance III 400 MHz Spectrometer with a nitrogen frequency of 40.557 MHz, using a 7 mm Bruker MAS probe with broadband proton suppression and magic angle spinning at 5 kHz. For cross polarization, a 90º proton excitation pulse was set to 4.2 µs with 2 ms contact time. Chemical shifts were externally referenced to glycine (amine nitrogen at 33.40 ppm), and are reported versus liquid ammonia (0 ppm). In all solid-state NMR experiments, the relaxation delay was set at 5 s.

Attenuated total reflectance (ATR) FTIR spectroscopy was carried out with a Nicolet-FTIR spectrometer Model 750, equipped with an ATR accessory Model 0012-3XXT. Samples were cut to the size of the ATR crystal (ZnSe, rectangular, 20 mm × 50 mm) and ATR-FTIR spectra were obtained by pressing them against the crystal with the ATR unit's pressure device (gripper). Maximum throughput of the infrared beam to the

detector was achieved via optical alignment that was performed with no sample on the crystal. Data were collected at an incident beam angle of 45^{o}, over 32 scans with a resolution of 2 cm^{-1}. In the ATR mode, the penetration depth (pd), and thereby the effective path length (=number of reflections × dp) of the infrared beam is directly proportional to the wavelength. Thereby, an ATR correction was applied to the raw data by multiplying the spectra with a wavelength-dependent factor (roughly $\lambda/5$) that adjusted the relative peak intensities. In order to evaluate H-bonding, the ν(N-H) bands were deconvoluted into five Gaussian-shaped peaks. Peak curve-fitting was performed using the Origin 8.5 software package.

CHN elemental analysis was conducted with an Exeter Analytical Model CE440 Elemental Analyzer, calibrated with acetanilide, urea, and glycine. All calibration standards and **MIX-xx** samples were run three times and results (Table S.2) are given as averages.

4.3.3 Physical Characterization. Bulk densities (ρ_b) were calculated from the weight and the physical dimensions of the samples. Skeletal densities (ρ_s) were determined with helium pycnometry using a Micromeritics AccuPyc II 1340 instrument.

4.3.4. Structural Characterization. That was carried out using Scanning electron microscopy (SEM) with Au/Pd (60/40) coated samples on a Hitachi Model S-4700 field-emission microscope.

4.3.5. Thermal Characterization. Thermogravimetric analysis (TGA) was conducted under O_2 with a TA Instruments Model TGA Q50 thermogravimetric analyzer, using a heating rate of 10 °C min^{-1}.

Modulated Differential Scanning Calorimetry (MDSC) was conducted under N_2 with a TA Instruments Differential Scanning Calorimeter Model Q2000. Heat capacities, c_p, at 23 ^oC of samples (2–5 mg), were measured using the MDSC method and calibrated against a sapphire standard and run from 0 ^oC to 30 ^oC at 0.5 ^oC min^{-1} in the modulated T4P mode, using 100 s as the modulation period and 0.13 ^oC as the modulation amplitude. Raw c_p data were multiplied with a correction factor (0.795 ± 0.052) based on measuring the heat capacities of a rutile and of a corundum sample just before running the shape memory aerogel samples and taking the ratios with the corresponding literature values for heat capacities.

The thermal conductivity of aerogel samples was measured according to ASTM Standard No. C177 (Standard Test Method for Steady-State Heat Flux Measurements and Thermal Transmission Properties by Means of the Guarded Hot Plate Apparatus) using a thermal conductivity analyzer consisting of a 4´´×4´´ aluminum block heated from the inside with three cartridge heaters (No. 3618K26, McMaster-Carr), and the temperature on the upper surface was maintained at 37.5 ^oC using a temperature controller (Part No. CN7833, Omega Engineering, INC.). The temperature-controlled surface of the aluminum block was covered with aerogel sample. Subsequently, a 4´´×4´´×0.5´´ reference sample (NIST standard SRM 1453, Expanded Polystyrene Board – closed cell),[47] with two thermocouples attached near the centers of the two opposite faces, was placed over the aerogel sample. An aluminum bucket with crushed ice was supported by two screw-jacks (Product No. 11210-08, Ace Glass INC.) on two opposite sides, and was placed on top of the reference sample in such a way that the entire top (4´´×4´´) surface of the reference sample was in contact with the base surface of the ice bucket. To ensure good contact

between the ice-cold bucket and the NIST standard, the height of the screw-jacks was adjusted based on the thickness of the aerogel sample (thickness minus 5%). A fourth thermocouple was also placed deep in the crushed ice to monitor its temperature. A 4-channel handheld data logger thermometer (Part No. HH378, Omega Engineering, INC.) was used to record the temperature at the four different places in the setup, as just described: at the bottom of the sample, at the top of the sample, at the top of the reference sample, and in the ice water. Once the setup was thermally equilibrated (about an hour), the readings of the four thermocouples were recorded six times in 15 minute intervals. The thermal conductivity was calculated based on the fact that the same amount of heat flows through both the sample and the reference sample. The apparatus was calibrated with (a) a second 4´´×4´´×0.5´´ piece of the NIST standard run as an unknown; and, (b) several 4´´×4´´×0.4´´ pieces of commercially available Aspen Aerogel blankets. Because the aerogel samples were not applied as single monoliths, but rather as two pieces tightly fit side-by-side, the apparatus was also calibrated with two NIST standard samples (10.2×10.2×1.3 cm and 10.2×7.6×1.3 cm) fitted likewise, side-by-side. That arrangement made no statistically significant difference. All calibration and crosscheck data are provided along with the thermal conductivity data of all **MIX-xx** in Table S.6 of Appendix VII in Supporting Information.

4.3.6. Thermomechanical Characterization. That was carried out in the tension mode with a TA Instruments Q800 Dynamic Mechanical Analyzer (DMA) equipped with a tension clamp (TA Instruments Part No. 984016.901). All specimens for testing had a rectangular geometry (length: 20 mm; width: 15 mm; thickness: 5-6 mm) in the spirit of ASTM D790-10,[57] and ASTM D4065;[58] they were cut off with a knife under N_2 in a glove

box, from larger cylindrical samples dipped in liquid N_2. In order to ensure uniform thickness, the surface of all rectangular pieces was smoothened, while still frozen, with a 3 M sand paper (320 grit, part No. 98401). In general, all samples were clamped to the tension fixture at room temperature. The exact length of all samples was measured by the instrument under a small tensile force (0.01 N) that prevents bending. The temperature was stepped to the initial testing temperature, and samples were equilibrated at that temperature for 5 min.

Glass transition temperatures (T_g) were extracted from the viscoelastic properties of the samples, which were determined by applying a continuous sinusoidal oscillation (1 Hz) with a strain amplitude equal to 0.3%, while the temperature was ramped from -50 ^oC to 150 ^oC at 3 ^oC min^{-1}. As a control, two other fresh samples of each formulation were also tested under the same parameters, while the temperature was ramped from -50 ^oC to 150 ^oC at 1.0 and 0.5 ^oC min^{-1}. **MIX-3**, **MIX-4**, **MIX-14**, and **MIX-18** were also tested at a temperature ramp of 5 ^oC min^{-1}.

Shape memory-related properties (strain fixity, strain recovery, strain recovery rates and fill factors) and elastic moduli were studied in the controlled force mode as follows: samples were first stepped, and then equilibrated at their deformation temperature ($T_d = T_g + 10$ ^oC) for 5 min. Subsequently, samples were stretched with a small tensile force (0.01 N), and the length of the sample was measured by the instrument and was stored. Next, specimens were stretched at a constant force rate of 1N min^{-1} up to a little below their break point (typically around 60% strain), and then they were cooled, while under the final stress, at 5 ^oC min^{-1} to their fixation temperature ($T_f << T_g$). At that point (T_f), samples were equilibrated for 5 min, and the tensile force was reduced to 0.01 N. Samples were allowed

to relax (fix) for 15 min (always at T_f), while strain was recorded. Finally, samples were heated at 1 ^oC min^{-1} to their recovery temperature (T_r=T_d) while strain was still recorded. Samples were held at T_d for 15 min and the cycle was repeated. Five such cycles were run successively for each sample, and data were analyzed for their fixation and recovery properties as described in Section 2.5.2.

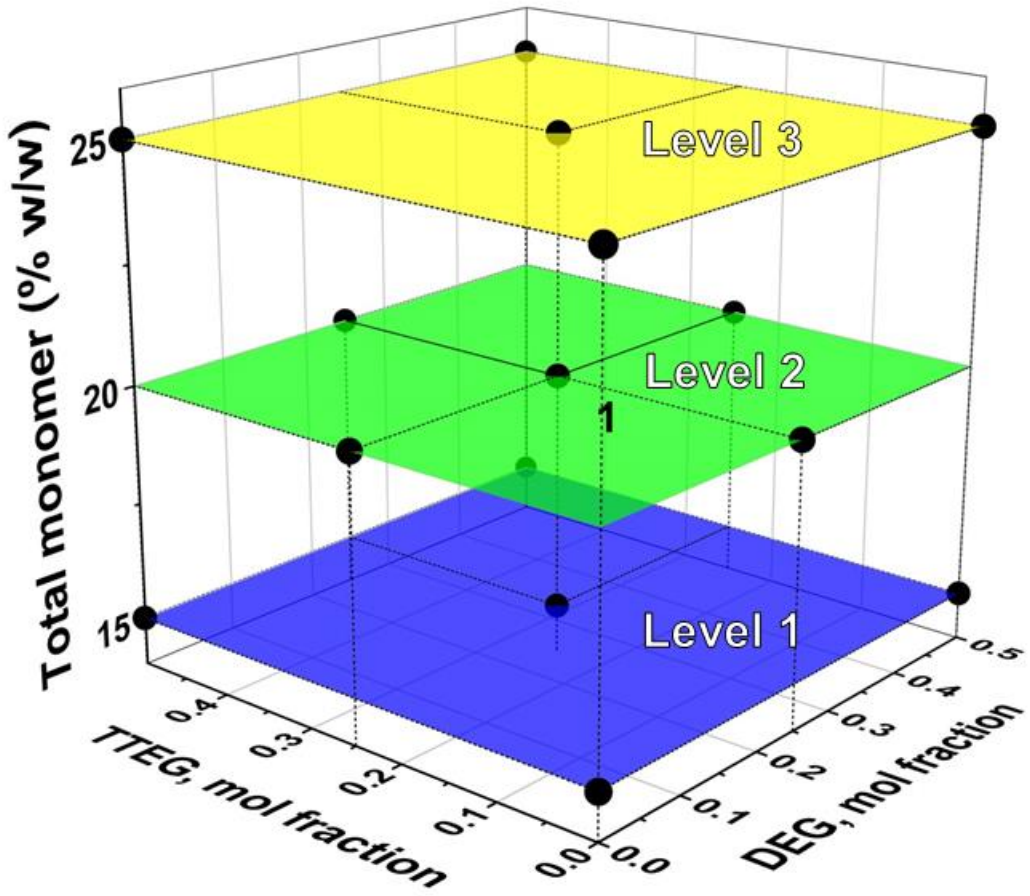

Figure 1. **MIX-xx** formulations according to a central composite face-centered design model, with independent variables the mol fractions of DEG and TTEG, and the total monomer concentration. The model includes 18 samples, at three monomer concentration levels. **MIX-11** to **MIX-13** were repeats of the central point **MIX-10**.

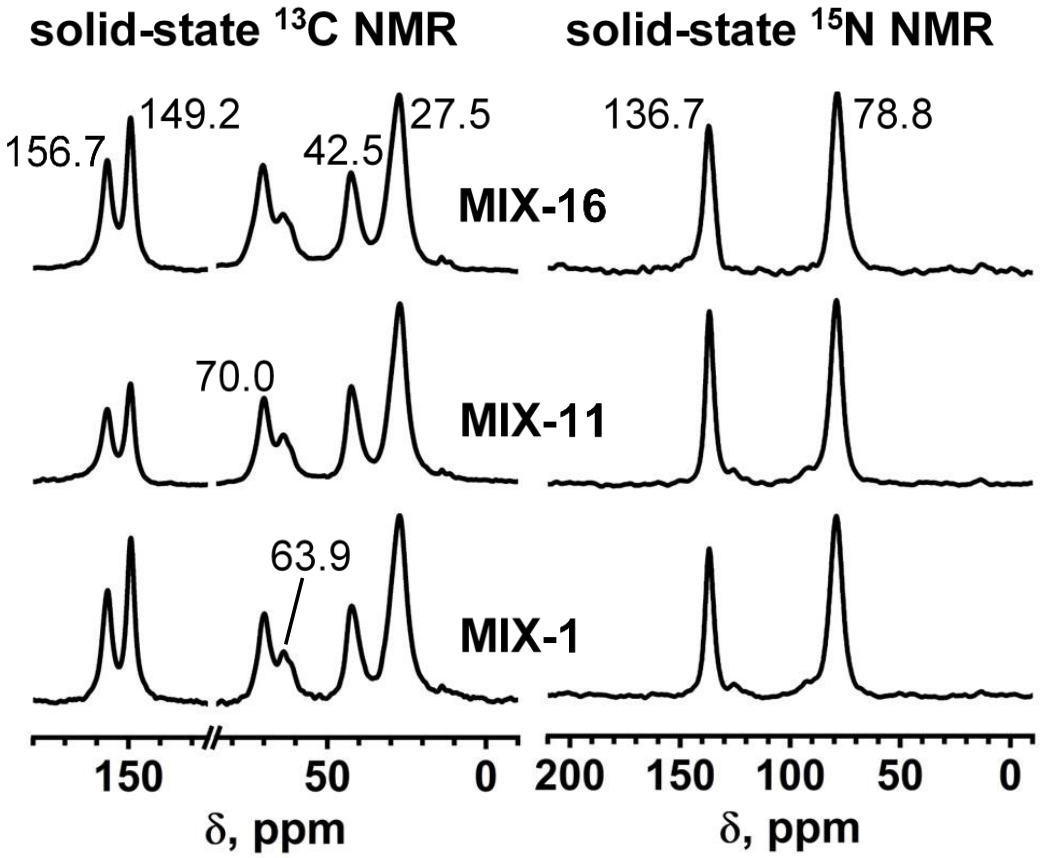

Figure 2. Representative solid-state CPMAS ^{13}C and ^{15}N NMR of **MIX-xx** aerogels as indicated.

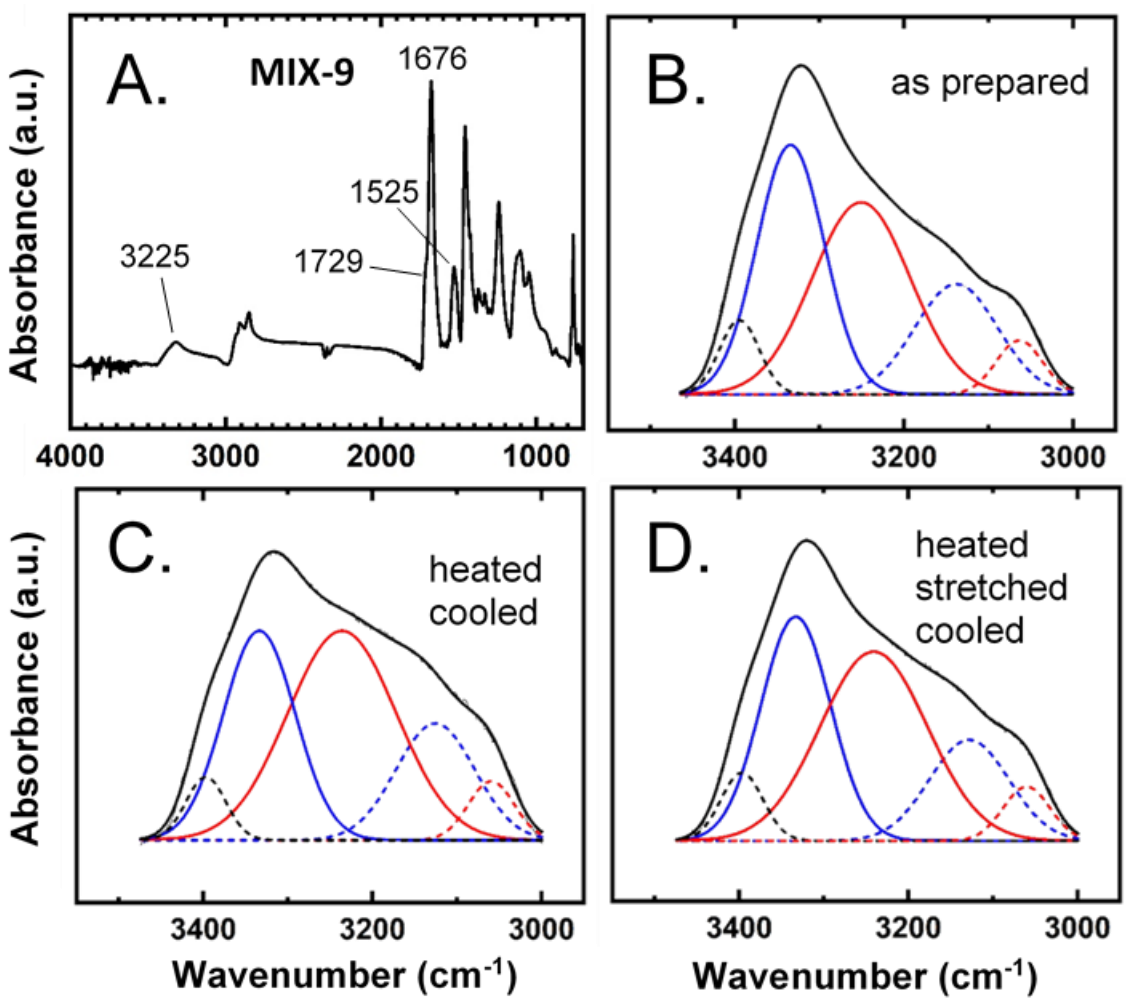

Figure 3. Representative room-temperature ATR-FTIR spectra of **MIX-xx** under different conditions, exemplified with **MIX-9**. (a) The entire spectrum. (b) The 3000-3470 cm^{-1} range of frame A, deconvoluted for H-bonding. (c) The same sample as in A and B, after heating at T_g+40 ^oC for 15 min, and cooling back to room temperature. (d) The same sample as in A-C, heated again at T_g+40 ^oC for 15 min, stretched to about 60% strain, followed by stress release, and cooling back to room temperature.

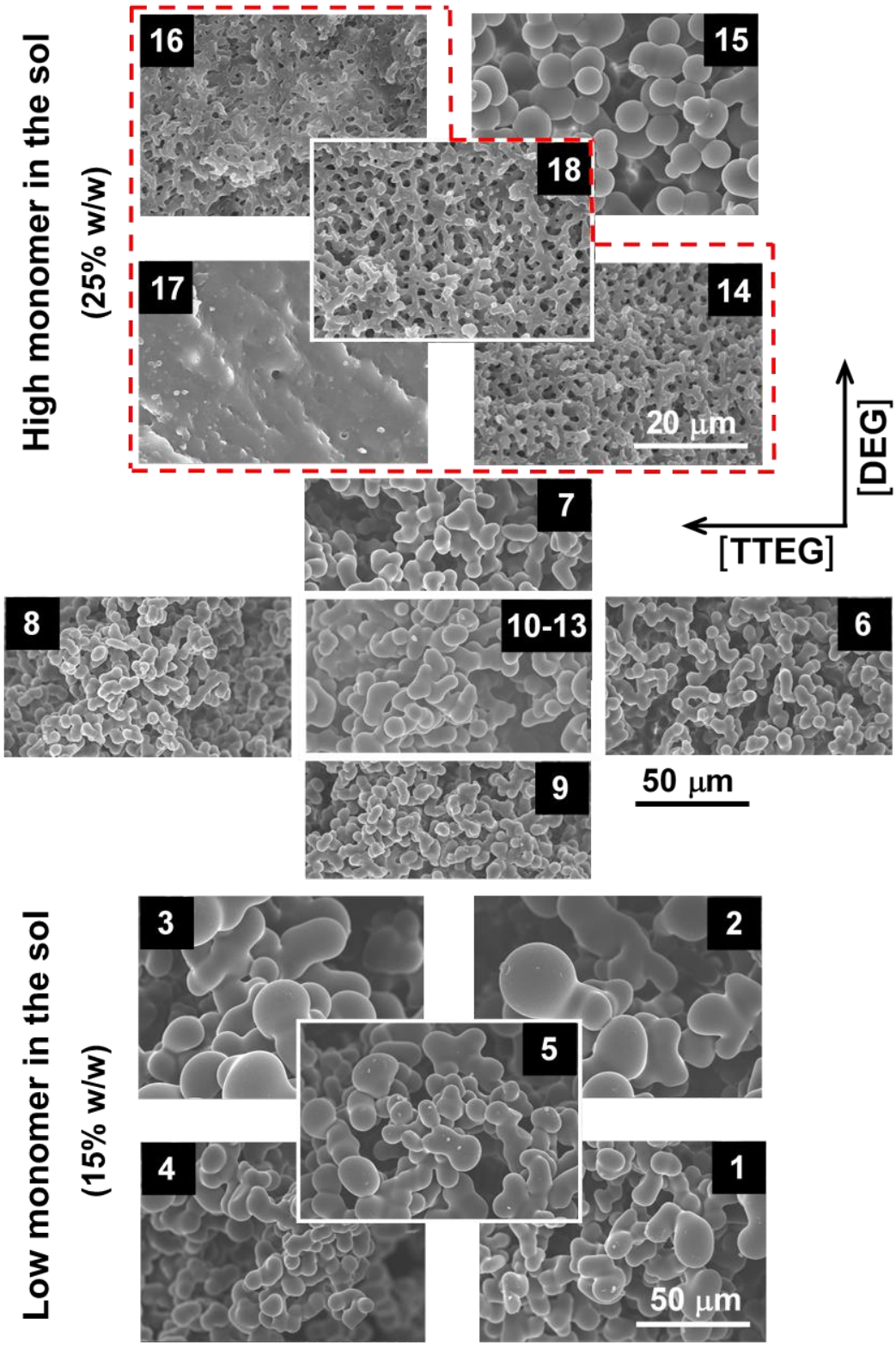

Figure 4. Scanning electron micrographs (SEM) of all **MIX-xx** (refer to Figure 1).

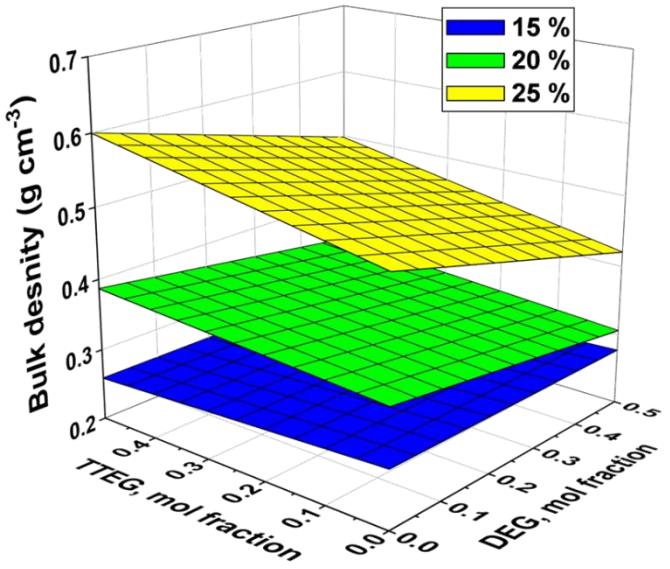

Figure 5. Fitting bulk density data (not including **MIX-17**) to the three exploratory variables according to Eq 1. Color-coding corresponds to the three monomer concentration levels (Figure 1). Primary data and the coefficients of the fitting equations are given in the Supporting Information.

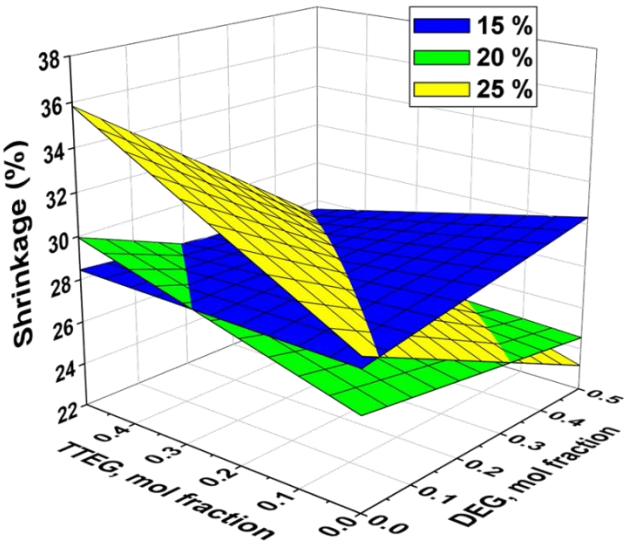

Figure 6. Fitting shrinkage data (not including **MIX-17**) to the three exploratory variables according to Eq 1. Color-coding corresponds to the three monomer concentration levels (Figure 1). Primary data and the coefficients of the fitting equations are given in the Supporting Information.

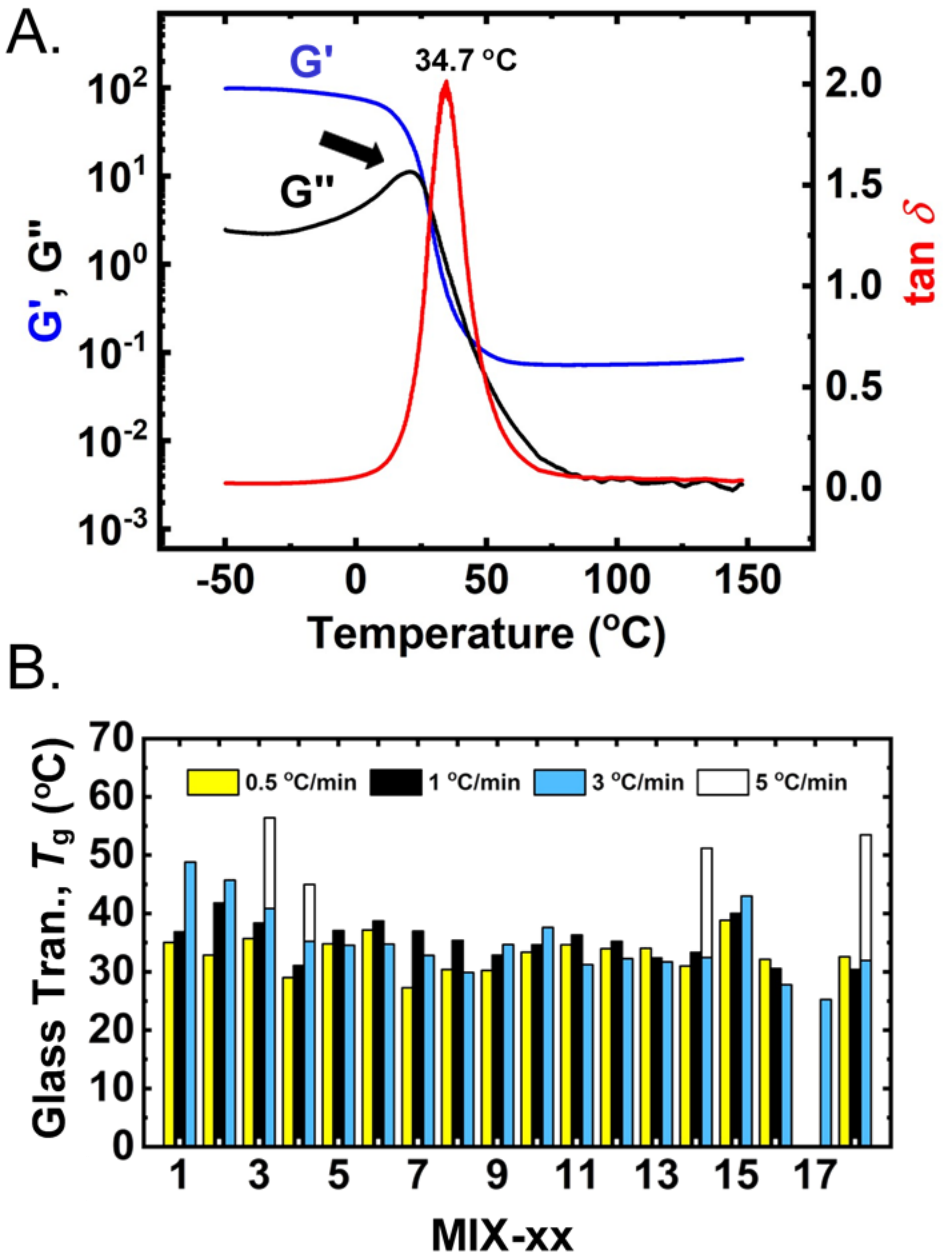

Figure 7. (a) Storage (G´) and loss (G´´) moduli and tan δ (=G´´/G´) curves of a representative sample (**MIX-9**) as a function of a temperature sweep at 3 °C min^{-1}. Arrow points to the maximum of the G´´ curve (see text). (b) Glass transition temperatures (T_g as maxima in tan δ) for all non-collapsed **MIX-xx** at four different temperature sweep rates as indicated (Data from Table S.5 of Appendix VI in Supporting Information. For fitting, see Figure S.4 in the same Appendix).

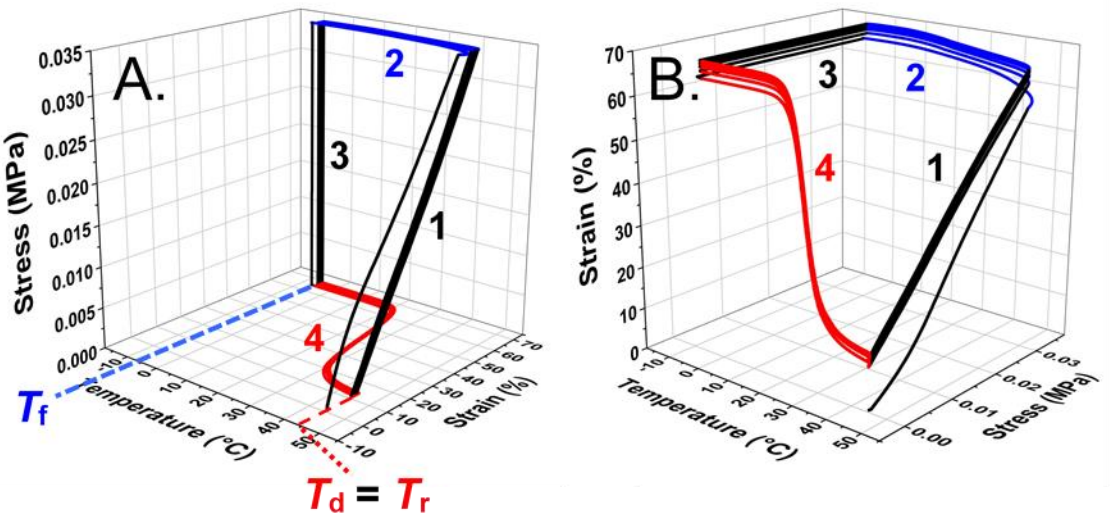

Figure 8. Representative thermomechanical characterization data of **MIX-xx** in 3D format from two different perspectives using **MIX-9** as an example. The graph includes all 5 successive temperature cycles from a deformation (T_d) to a fixing temperature (T_f) and back to a recovery temperature ($T_r = T_d$), as indicated. Numbers within the frame indicate the four successive steps of the experiment (see text).

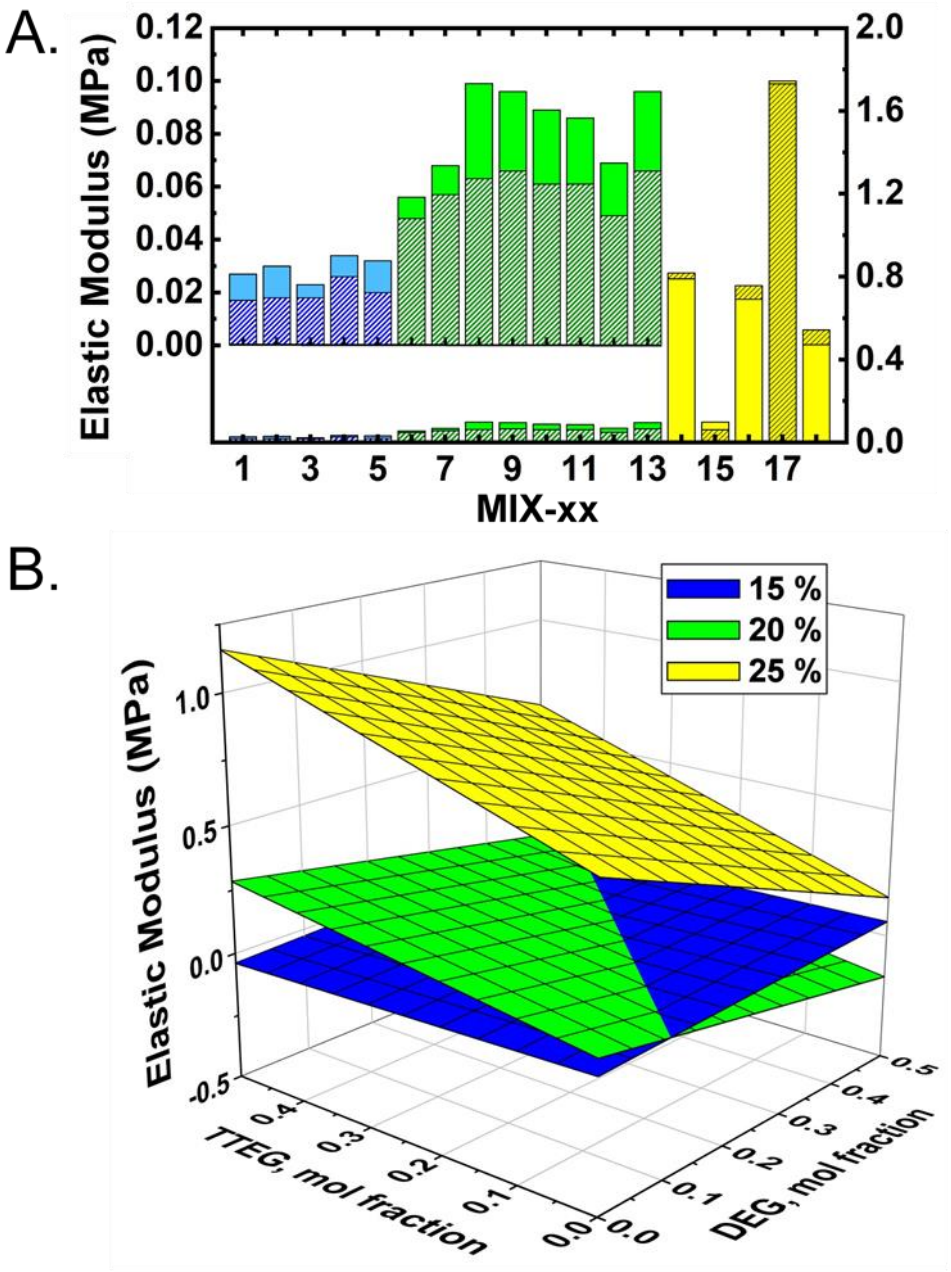

Figure 9. (a) Elastic moduli, *E*, obtained from the initial slopes of the stress-strain curves of Step 1 in cycles 1 and 5 (clear and shaded areas, respectively) of data like those shown in Figure 8. (b) Elastic moduli from cycle 5 fitted to the three exploratory variables according to Eq 1. Color-coding corresponds to the three monomer concentration levels (Figure 1). For the coefficients of the fitting equations, see Table S.4 in Appendix V of the Supporting Information.

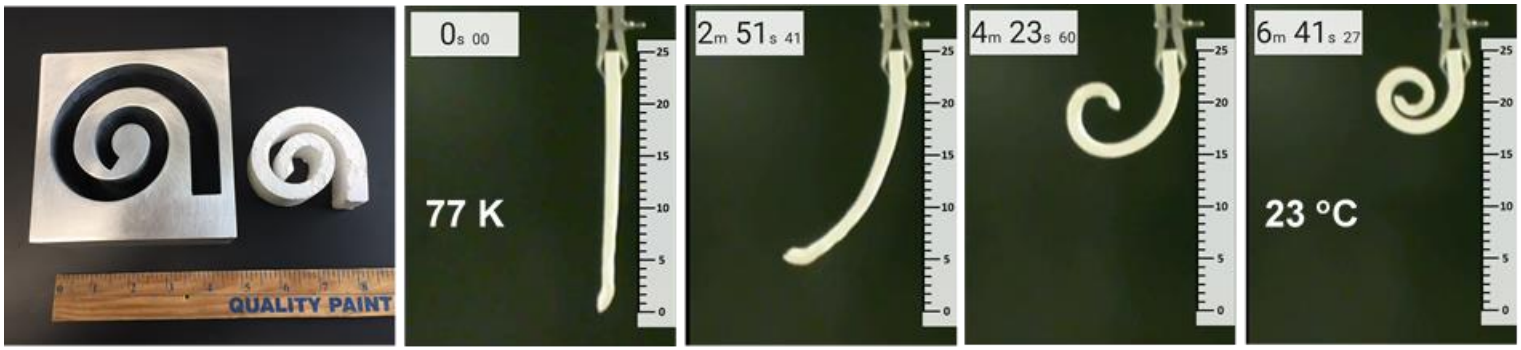

Figure 10. A **MIX-14** aerogel ($T_g \approx 32$ °C) cast in a spiral permanent shape using the mold shown in the left-most frame. The sample was heated at T_g+40 °C, and was stretched flat. While stretched, the sample was dipped in liquid N_2 fixing that shape. Then the sample was suspended vertically. As the sample thawed back to room temperature, it lifted its weight and recovered its form. The successive frames have been taken from the movie given in Supporting Information.

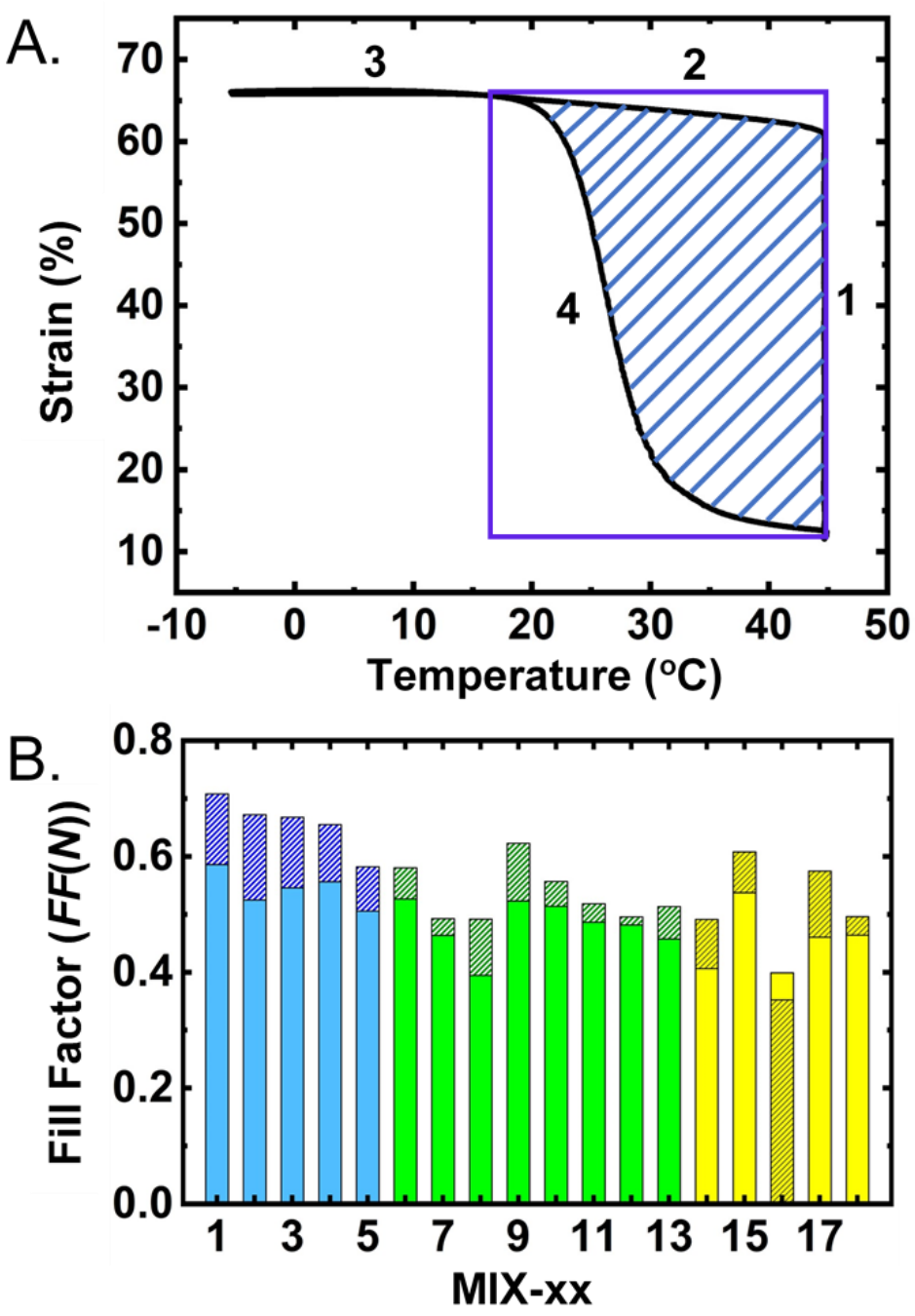

Figure 11. (a) A representative direct projection to the strain/temperature plane of a random cycle of the entire 3D representations like that of Figure 8. Numbers 1-4 refer to the four stages of the experiment as indicated in Figure 8. Fill factors (*FF*(*N*)) for all samples in all cycles, *N*, were calculated from the ratios of the shaded areas over the entire areas of the surrounding squares and are provided in Table S.8 of the Supporting Information. (b) *FF*(*N*) values for cycles *N*=1 (clear colored bars) and *N*=5 (shaded colored bars). Color-coding corresponds to the three monomer concentration levels (Figure 1).

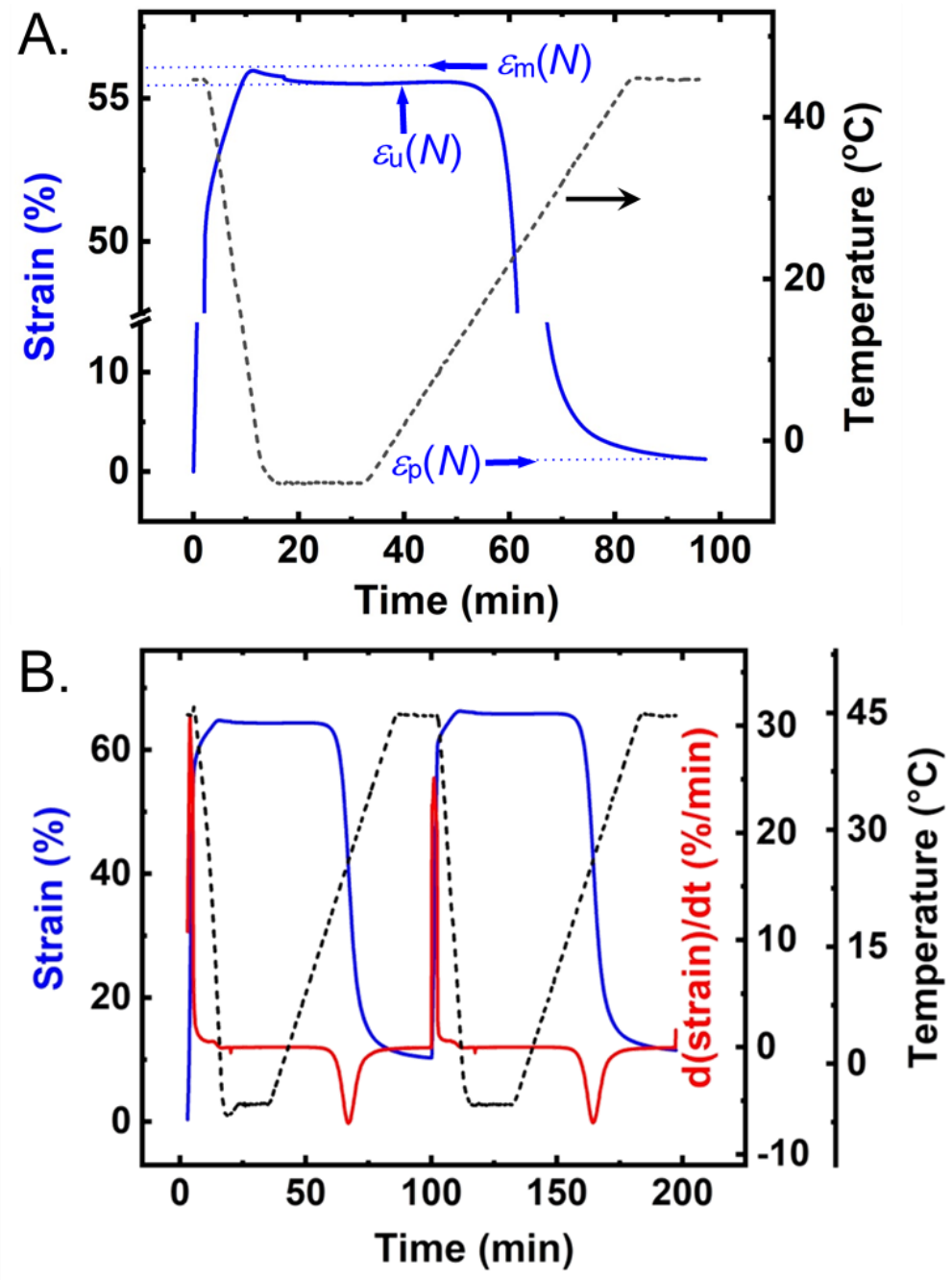

Figure 12. Representative data for the calculation of $R_f(N)$, $R_r(N)$ and $R_t(N)$: Projections of a 3D plot like that in Figure 8 on the strain-temperature plain, followed by unfolding temperature into time. (a) A single temperature cycle magnified appropriately; temperature is included as a dotted line. Strains ε_m, ε_u and ε_p, marked within the frame, were used for the calculation of $R_f(N)$ and $R_r(N)$, according to Eq.s 4 and 5. (b) Several cycles like that of frame A, including the first derivative of strain vs. time for the calculation of $R_t(N)$, according to Eq 6.

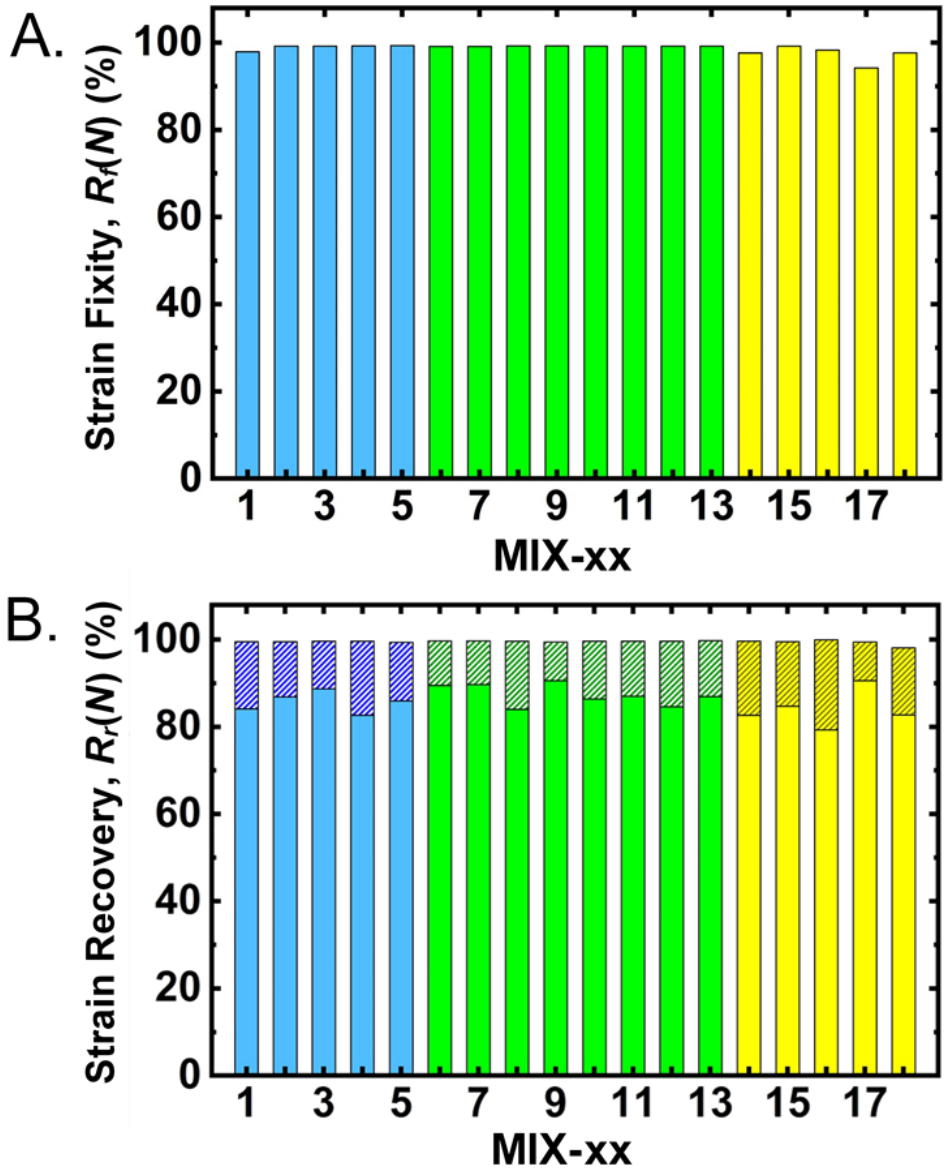

Figure 13. (a) Strain fixity ratios, $R_f(N)$; and, (b) Strain recovery ratios, $R_r(N)$, for all **MIX-xx** aerogels for cycles N=1 (clear colored bars) and N=5 (shaded colored bars). Color-coding corresponds to the three monomer concentration levels (Figure 1).

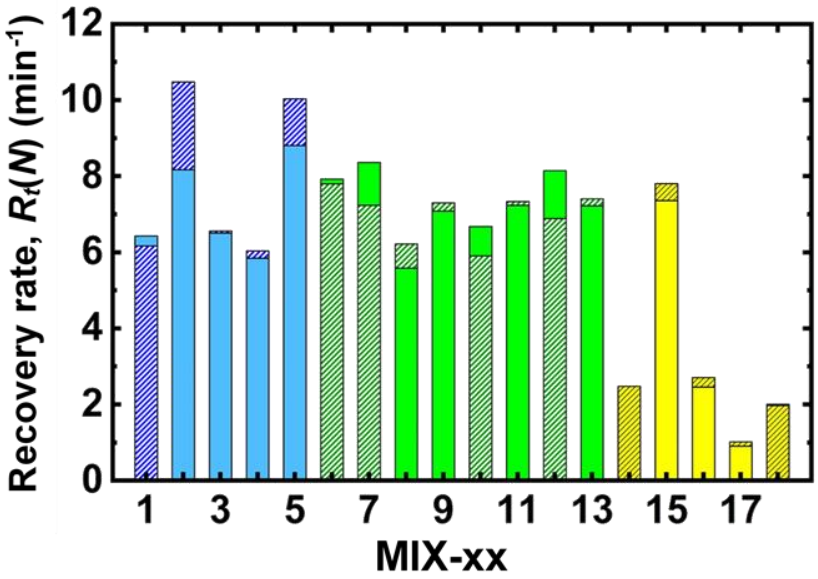

Figure 14. Strain recovery rates, $R_t(N)$ for all **MIX-xx** aerogels for cycles N=1 (clear colored bars) and N=5 (shaded colored bars). Color-coding corresponds to the three monomer concentration levels (Figure 1).

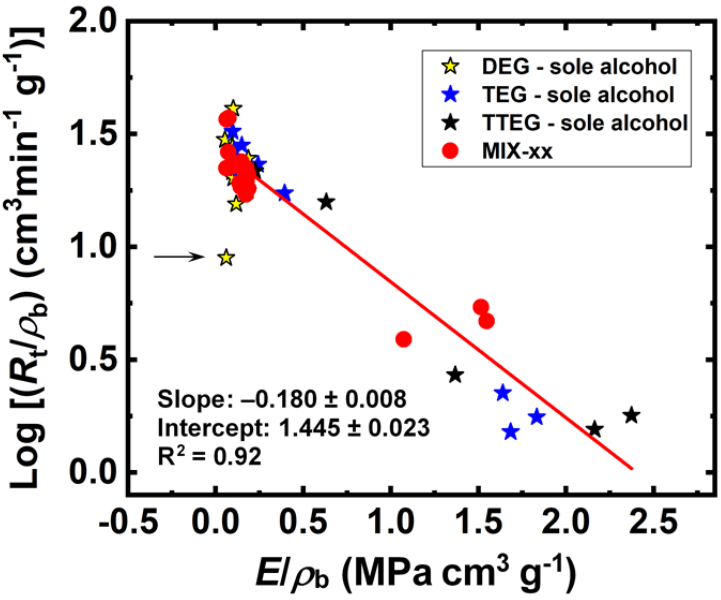

Figure 15. Correlation of Log [$R_t(5)/\rho_b$] and E/ρ_b according to Eq 12. Graph includes data from single-diol PIR-PURs as indicated within the frame.[14] Data were analyzed as follows: first all data were fitted linearly; residuals were calculated; a single data point (shown with an arrow) whose residual was more than 2×sigma from the average was rejected; remaining data were fitted again and key statistical information (slope, intercept, correlation) are shown within the graph.

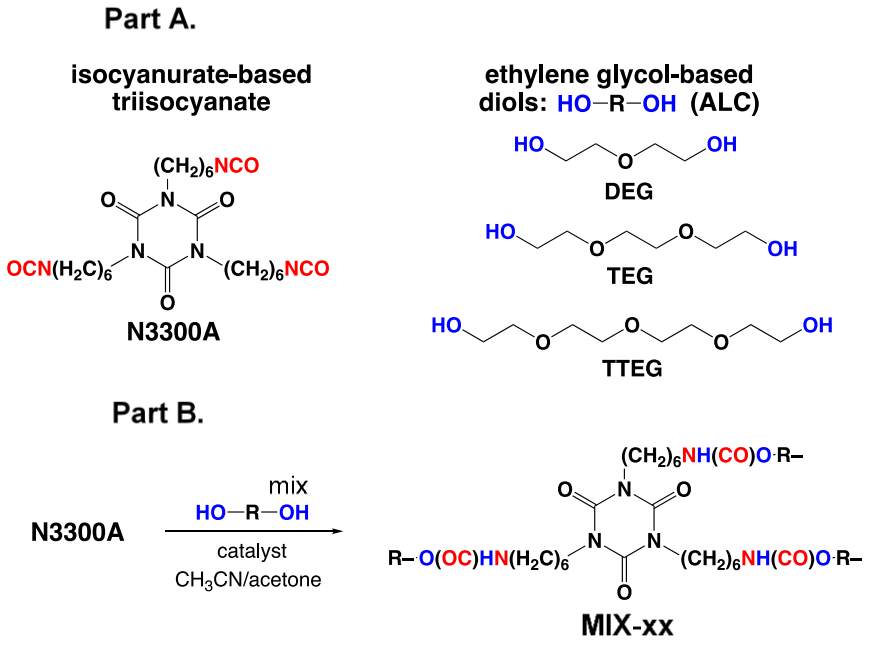

Scheme 1. (a) Reagents (triisocyanate, ethylene glycol-based diols). (b) Reaction of isocyanurate crosslinking nodes with mixtures of the three diols to PIR-PUR aerogels (MIX-xx).

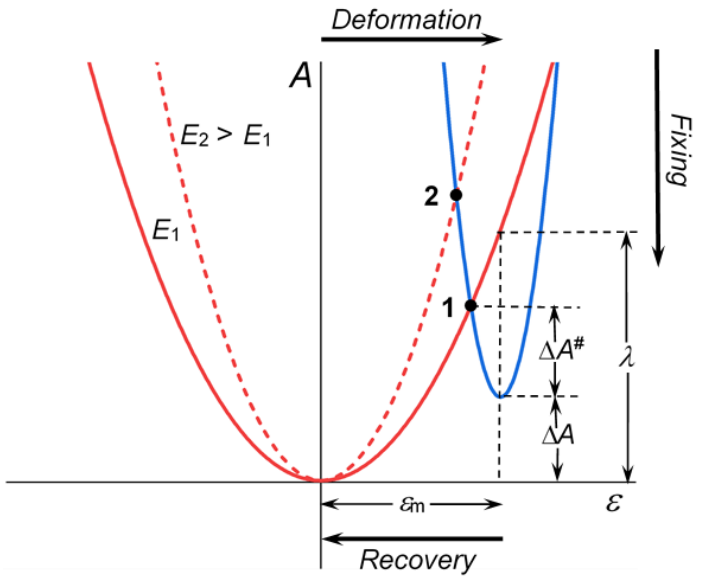

Scheme 2. Helmholtz Free Energy (A) Surfaces Upon Elastic Deformation (ε) at the Deformation Temperature (T_d>T_g, red parabolas) and at the Fixing Temperature (T_f<T_g, blue parabola); E_1, E_2: two possible elastic moduli at T_d.

ACKNOWLEDGEMENT

We thank the Army Research Office for financial support under Award Number W911NF-14-1-0369. We also thank Covestro LLC (formerly Bayer Corp. U.S.A.) for the generous supply of Desmodur N3300A and the Materials Research Center of the Missouri University of Science and Technology for support with materials characterization.

REFERENCES

1. Lendlein, A.; Kelch, S. Shape-Memory Polymers. *Angew. Chem. Int. Ed.* **2002**, *41*, 2034-2057.

2. Saunders, J. H.; Frisch, K. C. Polyurethane Chemistry and Technology I. Chemistry; Interscience Publishers: New York, 1962.

3. Ölander, A. An Electrochemical Investigation of Solid Cadmium-Gold Alloys. *J. Am. Chem. Soc.* **1932**, *54*, 3819−3833.

4. Berg, G. J.; McBride, M. K.; Wang, C.; Bowman, C. N. New Directions in the Chemistry of Shape Memory Polymers. *Polymer* **2014**, *55*, 5849−5872.

5. Hager, M. D.; Bode, S.; Weber, C.; Schubert, U. S. Shape Memory Polymers: Past, Present and Future Developments. *Prog. Polym. Sci.* **2015**, *49-50*, 3−33.

6. Behl, M.; Razzaq, M. Y.; Lendlein, A. Multifunctional Shape-Memory Polymers. *Adv. Mater.* **2010**, *22*, 3388−3410.

7. Vernon, L. B.; Vernon, H. M. Producing Molded Articles such as Dentures from Thermoplastic Synthetic Resins. U.S. Patent No. 2234993, 1941.

8. Hayashi, S.; Shirai, Y. Development of Polymeric Shape Memory Material. Mitsubishi Technical Bulletin 184; Dec 1988.

9. Hayashi, S.; Tobushi, H.; Kojima, S. Mechanical Properties of Shape Memory Polymer of Polyurethane Series. *JSME Int. J., Ser. I* **1992**, *35*, 296−302.

10. Hayashi, S. Properties and Applications of Polyurethane-Series Shape Memory Polymer. *Int. Prog. Urethanes* **1993**, *6*, 90−115.

11. Duerig, T. W.; Pelton, A. R. Ti-Ni Shape Memory Alloys. In Materials Properties Handbook: Titanium Alloys; Welsch, G., Boyer, R., Collings, E. W., Eds.; American Society for Metals, 1994; pp 1035-1048.

12. Meador, M. A. B.; McMillon, E.; Barrios, E.; Mueller, C. H.; Miranda, F. A. Dielectric and Other Properties of Polyimide Aerogels Containing Fluorinated Blocks. *ACS Applied Materials and Interfaces*, **2014**, *6*, 6062‑6068.

13. Meador, M. A. B.; Wright, S.; Sandberg, A.; Nguyen, B. N.; Van Keuls, F. W.; Mueller, C.H.; Rodríguez-Solís, R.; Miranda, F. A. Low Dielectric Polyimide Aerogels as a Substrate for Lightweight Patch Antennas. *ACS Applied Materials and Interfaces*, **2012**, *4*, 6346-6353.

14. Vareda, J. P.; Lamy-Mendes, A.; Durães, L. A Reconsideration on the Definition of the Term Aerogel Based on Current Drying Trends. *Micropor. Mesopor. Mat.* **2018**, *258*, 211-216.

15. Michal, B. T.; Brenn, W. A.; Nguyen, B. N.; McCorkle, L. S.; Meador, M. A. B.; Rowan, S. J. Thermoresponsive Shape-Memory Aerogels from Thiol-Ene Networks. *Chem. Mater.* **2016**, *28*, 2341−2347.

16. Donthula, S.; Mandal, C.; Leventis, T.; Schisler, J.; Saeed, A. M.; Sotiriou-Leventis, C.; Leventis, N. Shape-Memory Poly(isocyanurate-urethane) (PIR-PUR) Aerogels for Deployable Panels and Biomimetic Applications. *Chem. Mater.* **2017**, *29*, 4461-4477.

17. Hammond, G. S. A Correlation of Reaction Rates. *J. Am. Chem. Soc.* **1955**, *77*, 334-338.

18. Jaffé, H. H. A Reexamination of the Hammett Equation. *Chem. Rev.* **1953**, *53*, 191-261.

19. Bordwell, F. G.; Matthews, W. S.; Vanier, N. R. Acidities of Carbon Acids. IV. Kinetic vs. Equilibrium Acidities as Measures of Carbanion Stabilities. The Relative Effects of Phenylthio, Diphenylphosphino, and Phenyl Groups. *J. Am. Chem. Soc.* **1975**, *97*, 442-443.

20. Ofner, III, C. M.; Schott, H. Swelling Studies of Gelatin I: Gelatin Without Additives. *J. Pharmaceutical Sci.* **1986**, *75*, 790-796.

21. Obaid, N.; Kortschot, M. T.; Sain, M. Understanding the Stress Relaxation Behavior of Polymers Reinforced with Short Elastic Fibers. *Materials* **2017**, *10*, 472; doi: 10 3390/ma10050472.

22. Atkins, P.; DePaula. J. Atkins' Physical Chemistry 8th Edition. Oxford University Press: New York, N.Y. 2006, p 897.

23. Kim, D.; Lee, I.-S. H.; Kreevoy, M. M. The Marcus Theory of Reactions of Quinolinium Ions with BH_4^- and OH^-. *J. Am. Chem. Soc.* **1990**, *112*, 1889-1894.

24. Lewis, E. S.; McLaughlin, M. L.; Douglas, T. A. Methyl Transfers. 10. The Marcus Equation Application to Soft Nucleophiles. *J. Am. Chem. Soc.* **1985**, *107*, 6668-6673.

25. Williams, J. C.; Meador, M. A. B.; McCorkle, L.; Mueller, C.; Wilmoth, N. Synthesis and Properties of Step-Growth Polyamide Aerogels Crosslinked with Triacid Chlorides. *Chem. Mater.* **2014**, *26*, 4163-4171.

26. Leventis, N.; Sotiriou-Leventis, C.; Chandrasekaran, N.; Mulik, S.; Larimore, Z. J.; Lu, H.; Churu, G.; Mang, J. T. Multifunctional Polyurea Aerogels from Isocyanates and Water. A Structure-Property Case Study. *Chem. Mater.* **2010**, *22*, 6692-6710.

27. Leventis, N.; Chidambareswarapattar, C.; Bang, A.; Sotiriou-Leventis, C. Cocoon-in-Web-like Superhydrophobic Aerogels from Hydrophilic Polyurea and Use in Environmental Remediation. *ACS Appl. Mater. Interfaces* **2014**, *6*, 6872-6882.

28. Sung, C. S.; Schneider, N. S. Temperature Dependence of Hydrogen Bonding in Toluene Diisocyanate Based Polyurethanes. *Macromolecules* **1977**, *10*, 452−458.

29. Teo, L.-S.; Chen, C.-Y.; Kuo, J.-F. Fourier Transform Infrared Spectroscopy Study on Effects of Temperature on Hydrogen Bonding in Amine-Containing Polyurethanes and Poly(urethane-urea)s. *Macromolecules* **1997**, *30*, 1793−1799.

30. Saito, Y.; Nansai, S.; Kinoshita, S. Structural Studies on Polyurethane Fibers. I. Crystal and Molecular Structures of Aliphatic Polyurethanes from Hexamethylene Diisocyanate and Some Linear Glycols. *Polym. J.* **1972**, *3*, 113−121.

31. Christenson, C. P.; Harthcock, M. A.; Meadows, M. D.; Spell, H. L.; Howard, W. L.; Creswick, M. W.; Guerra, R. E.; Turner, R. B. Model MDI/butanediol Polyurethanes: Molecular Structure, Morphology, Physical and Mechanical Properties. *J. Polym. Sci., Part B: Polym. Phys.* **1986**, *24*, 1401−1439.

32. Lee, H. S.; Wang, Y. K.; MacKnight, W. J.; Hsu, S. L. Spectroscopic Analysis of Phase-Separation Kinetics in Model Polyurethanes. *Macromolecules* **1988**, *21*, 270−273.

33. Nakanishi, K.; Tanaka, N. Sol-Gel with Phase Separation. Hierarchically Porous Materials Opimized for High-Performance Liquid Chromatography Separations. *Acc. Chem. Res.* **2007**, *40*, 863-873.

34. Nakanishi, K. Pore Structure Control of Silica Gels Based on Phase Separation. *J. Porous Mater.* **1997**, *4*, 67-112.

35. Kanamori, K.; Nakanishi, K.; Hanada, T. Rigid Macroporous Poly(divinylbenzene) Monoliths with a Well-Defined Bicontinuous Morphology Prepared by Living Radical Polymerization. *Adv. Mater.* **2006**, *18*, 2407-2411.

36. For a quantitative end-groups analysis of star polymers, see Supporting Information of: Leventis, N.; Sotiriou-Leventis, C.; Saeed, A. M.; Donthula, S.; Majedi Far, H.; Rewatkar, P. M.; Kaiser, H.; Robertson, J. D.; Lu, H.; Churu, G. Nanoporous Polyurea from a Triisocyanate and Boric Acid: A Paradigm of a General Reaction Pathway for Isocyanates and Mineral Acids. *Chem. Mater.* **2016**, *28*, 67-78.

37. Xie, T. Tunable Polymer Multi-Shape Memory Effect. *Nature* **2010**, *464*, 267–270.

38. Ross, K. A.; Campanella, O. H.; Okos, M. R. The Effects of Porosity on Glass Transition Measurement. *Int. J. Food Properties* **2002**, *5*, 611-628.

39. Standard Test Method for Steady-State Thermal Transmission Properties by Means of the Heat Flow Meter Apparatus. ASTM Int. C518-15 (2016).

40. Bird, R. B.; Stewart, W. E.; Lightfoot, E. N. *Transport Phenomena, 2nd Edition*. John Wiley & Sons Inc., New York, N.Y. 2001, Chapter 9, p 268.

41. Bard, A. J.; Faulkner, L. R. Electrochemical Methods, Fundamentals and Applications Second Edition, John Wiley & Sons, New York, N.Y. 2001, Chapter 11.7.1, p. 452.

42. Ashby, M. F. The Properties of Foams and Lattices. *Philos.Trans. R. Soc., A* **2006**, *364*, 15−30.

43. See for example: Mulik, S.; Sotiriou-Leventis, C.; Churu, G.; Lu, H.; Leventis, N. Cross-linking 3D Assemblies of Nanoparticles into Mechanically Strong Aerogels by Surface-Initiated Free-Radical Polymerization. *Chem. Mater.* **2008**, *20*, 5035-5046.

44. Klemmer, H.F.M.; Allgaier, J.; Frielinghaus, H.; Holderer, O.; Ohl, M. Influence of the amphiphilicity profile of copolymers on the formation of liquid crystalline mesophases in microemulsions. *Colloid Polym. Sci*. **2017**, *295*, 911-923.

45. Liu, C.; Qin, H.; Mather, P. T. Review of Progress in Shape-Memory Polymers. *J. Mater. Chem.* **2007**, *17*, 1543-1558.

46. Liu, C.; Chun, S. B.; Mather, P. T.; Zheng, L.; Haley, E. H.; Coughlin, E. B. Chemically Crosslinked Polycyclooctene: Synthesis, Characterization, and Shape Memory Behavior. *Macromolecules* **2002**, *35*, 9868−9874.

47. Other minor trends related to the chemical makeup of **MIX-xx** include an increase $R_t(N)$ at Levels 1 and 2 with the amount of more rigid DEG (e.g., **MIX-1** ---> **MIX-2**, or **MIX-9** ---> **MIX-**(**10**-**13**) ---> **MIX-7**). That increase: (a) was moderated by higher TTEG concentrations (e.g., **MIX-4** versus **MIX-3**, or **MIX-6** versus **MIX-7**); and, (b) was magnified if it was accompanied by a decrease in TTEG (**MIX-4** versus **MIX-5**). For constant DEG, $R_t(N)$ increased as TTEG decreased (e.g., **MIX-8** ---> **MIX-**(**10**-**13**) ---> **MIX-6**).

48. Stan, F.; Fetecau, C. Study of Stress Relaxation in Polytetrafluoroethylene Composites by Cylindrical Macroindentation. *Compos. Part B. Eng.* **2013**, *47*, 298-307.

49. Geethamma, V. G.; Pothen, L. A.; Rhao, B.; Neelakantan, N. R.; Thomas, S. Tensile Stress Relaxation of Short-coir-fiber-reinforced Natural Rubber Composites. *J. Appl. Polym. Sci.* **2004**, *94*, 96-104.

50. Suhara, F.; Kutty, S. K.; Nando, G. B. Stress Relaxation of Polyester Fiber-polyurethane Elastomer Composite with Different Interfacial Bonding Agents. *J. Elastom. Plastics* **1998**, *30*, 103-117.

51. Ward, I. M.; Sweeney, J. An Introduction to The Mechanical Properties of Solid Polymers Second Edition. John Wiley & Sons, Ltd. West Chester, England 2004, Chapter 2, pp 19-30.

52. Maleki, H.; Durães, L.; Portugal, A. Development o Mechanically Strong Ambient Pressure Dried Silica Aerogels with Optimized Properties. *J. Phys. Chem. C* **2015**, *119*, 7689−7703.

53. Montgomery, D. C. Design and Analysis of Experiments, 6th ed.; John Wiley & Sons: New York, 2006.

54. SAS Institute Inc. 2013. Using JMP 11. Cary, NC: SAS Institute Inc.: http://www.jmp.com/en_us/offers/freetrial.html?utm_source=google&utm_campaign=td70114000002KZJq&utm_medium=cpc&utm_term=sas%20jmp.

55. Goupy, J.; Creighton, L. Introduction to Design of Experiments with JMP Examples, 3rd ed; SAS Institute Inc.: Cary, NC, U.S.A., **2007**.

56. Zarr, R. R.; Pintar, A. L. Standard Reference Materials: SRM 1453, Expanded Polystyrene Board, for Thermal conductivity from 281 K to 313K. *NIST Special Publication 260*-175, **2012**. http://dx.doi.org/10.6028/NIST.SP.260-175).

57. Standard Test Methods for Flexural Properties of Unreinforced and Reinforced Plastics and Electrical Insulating Materials. ASTM Int. D790-10: http://www.astm.org/DATABASE.CART/HISTORICAL/D790-10.htm.

58. Standard Practice for Plastics: Dynamic Mechanical Properties: Determination and Report of Procedures. ASTM D4065: http://www.astm.org/Standards/D4065.htm.

SUPPORTING INFORMATION

Appendix I. Formulations, gelation times and CHN elemental analysis data.

Appendix II. Thermogravimetric analysis data (TGA) of all MIX-xx.

Appendix III. Additional ATR-IR data.

Appendix IV. Materials characterization data.

Appendix V. Coefficients for all property fitting equations.

Appendix VI. Glass transition temperature (T_g) data.

Appendix VII. Thermal conductivity data.

Appendix VIII. Thermomechanical data [E, FF(N), R_f(N), R_r(N) and R_t(N)].

Appendix IX. Derivation of $\Delta A^{\#}$ for the shape recovery and the relationship between R_t(N) and the Young's modulus E.

Movie demonstrating the shape memory effect of MIX-xx (Separate File).

Appendix I. Formulations, gelation times and CHN elemental analysis data.[c]

Table S.1.A. Formulations of the MIX-xx samples according to a Central Composite Face Centered design (Table S.1.B), and their gelation times. [a]

xx	Alcohol [b]									Desmodur N3300A [c]			CH_3CN		Acetone		Gelation time
	DEG			TEG			TTEG			mass (g)	volume (mL)	mmol	mass (g)	volume (mL)	mass (g)	volume (mL)	
	mass (g)	volume (mL)	mmol	mass (g)	volume (mL)	mmol	mass (g)	volume (mL)	mmol								
1	0.000	0.000	0.000	0.150	0.137	1.000	0.000	0.000	0.000	0.338	0.289	0.670	2.419	3.078	0.346	0.440	2 h 48’
2	0.053	0.047	0.000	0.075	0.068	1.000	0.000	0.000	0.000	0.338	0.289	0.670	2.310	2.939	0.330	0.420	1 h 32’
3	0.053	0.047	0.000	0.000	0.000	0.750	0.097	0.086	0.250	0.338	0.289	0.670	2.419	3.078	0.346	0.440	2 h 3’
4	0.000	0.000	0.000	0.075	0.068	0.500	0.097	0.086	0.500	0.338	0.289	0.670	2.528	3.216	0.361	0.459	3 h 11’
5	0.027	0.024	0.000	0.075	0.068	0.500	0.049	0.043	0.500	0.338	0.289	0.670	2.419	3.078	0.346	0.440	1 h 50’
6	0.027	0.024	0.250	0.113	0.102	0.750	0.000	0.000	0.000	0.338	0.289	0.670	1.669	2.123	0.238	0.303	1 h 15’
7	0.053	0.047	0.250	0.038	0.034	0.500	0.049	0.043	0.250	0.338	0.289	0.670	1.669	2.123	0.238	0.303	1 h 32’
8	0.027	0.024	0.250	0.038	0.034	0.500	0.097	0.086	0.250	0.338	0.289	0.670	1.746	2.221	0.249	0.317	1 h 27’
9	0.000	0.000	0.250	0.113	0.102	0.500	0.049	0.043	0.250	0.338	0.289	0.670	1.746	2.221	0.249	0.317	1 h 41’
10	0.027	0.024	0.250	0.075	0.068	0.500	0.049	0.043	0.250	0.338	0.289	0.670	1.707	2.172	0.244	0.310	1 h 35’
11	0.027	0.024	0.250	0.075	0.068	0.500	0.049	0.043	0.250	0.338	0.289	0.670	1.707	2.172	0.244	0.310	1 h 52’
12	0.027	0.024	0.250	0.075	0.068	0.500	0.049	0.043	0.250	0.338	0.289	0.670	1.707	2.172	0.244	0.310	1 h 37’
13	0.027	0.024	0.250	0.075	0.068	0.250	0.049	0.043	0.500	0.338	0.289	0.670	1.707	2.172	0.244	0.310	1 h 38’
14	0.000	0.000	0.500	0.150	0.137	0.500	0.000	0.000	0.000	0.338	0.289	0.670	1.281	1.629	0.183	0.233	1 h 2’
15	0.053	0.047	0.500	0.075	0.068	0.500	0.000	0.000	0.000	0.338	0.289	0.670	1.223	1.556	0.175	0.222	53’
16	0.053	0.047	0.500	0.000	0.000	0.250	0.097	0.086	0.250	0.338	0.289	0.670	1.281	1.629	0.183	0.233	49’
17	0.000	0.000	0.500	0.075	0.068	0.000	0.097	0.086	0.500	0.338	0.289	0.670	1.338	1.703	0.191	0.243	1 h 6’
18	0.027	0.024	0.500	0.075	0.068	0.000	0.049	0.043	0.500	0.338	0.289	0.670	1.281	1.629	0.183	0.233	1 h 11’

[a]Catalyst 3.35 μL in all formulations. [b] Volumes of the alcohols were calculated based on their densities: DEG: 1.118 g cm^{-3}; TEG: 1.100 g cm^{-3}; TTEG: 1.125 g cm^{-3}. [c] The volume of N3300A was calculated based on its density (1.170 g cm^{-3}) provided by the supplier.

Table S.1.B. Experimental factors (exploratory variables), and levels according to a Central Composite Face Centered Design (CCFD) for MIX-xx.

factors	unit	factor levels (values)				
		axial points		center point	star points (α = 1)[1]	
		-1	1	0	-α	α
mole fraction of TTEG (X_1)	mol/mol	0.0	0.5	0.25	0.0	0.5
mole fraction of DEG (X_2)	mol/mol	0.0	0.5	0.25	0.0	0.5
[monomer] (X_3)	% w/w	15	25	20	15	25

[1] Equidistant points, with distance $|\alpha|=1$, from the center of the design space. The placement of the points design points in the orthogonal space together with their actual values (in parentheses), are shown in Scheme S.1 below. For the normalizing transforms of X_1-X_3 see Appendix V.

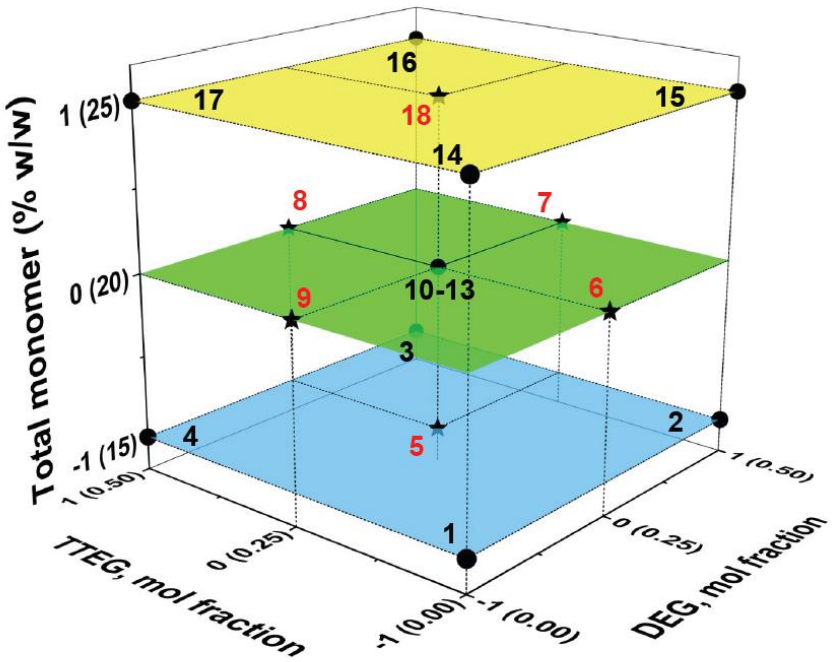

Scheme S.1. Central Composite Face Centered Design Model showing factorial points (dark circles: 1,2,3,4,14,15,16,17), center points (one, plus three duplicates: 10,11,12,13) and star points (5,6,7,8,9,18). Star points are those at the centers of each face of the factorial space, and are denoted with numbers in bold face red.

Table S.2. CHN Elemental analysis data of all MIX-xx. [a]

Sample I.D.	%C		%H		%N	
	Experimental	**Theoretical**	**Experimental**	**Theoretical**	**Experimental**	**Theoretical**
Calibration standards						
Acetanilide	71.08 ± 0.01	71.09	6.70 ± 0.02	6.71	10.33 ± 0.04	10.36
Glycine	32.06 ± 0.13	32.00	6.81 ± 0.03	6.71	18.51 ± 0.04	18.66
Urea	19.90 ± 0.03	20.00	6.73 ± 0.11	6.71	46.19 ± 0.12	46.65
Aerogels						
MIX-1	54.63 ± 0.12	54.31	8.05 ± 0.03	7.87	11.77 ± 0.07	11.51
MIX-2	54.85 ± 0.12	54.30	8.14 ± 0.03	7.81	12.15 ± 0.05	12.06
MIX-3	54.48 ± 0.10	54.31	8.27 ± 0.09	7.87	11.72 ± 0.12	11.51
MIX-4	54.40 ± 0.08	54.32	8.06 ± 0.03	7.93	11.25 ± 0.06	11.02
MIX-5	54.92 ± 0.03	54.31	8.42 ± 0.04	7.87	11.75 ± 0.02	11.51
MIX-6	54.37 ± 0.06	54.30	7.99 ± 0.02	7.84	11.81 ± 0.04	11.78
MIX-7	54.41 ± 0.09	54.30	8.18 ± 0.04	7.84	11.82 ± 0.03	11.78
MIX-8	54.52 ± 0.10	54.31	8.00 ± 0.02	7.90	11.31 ± 0.07	11.26
MIX-9	54.32 ± 0.13	54.31	8.01 ± 0.12	7.90	11.39 ± 0.06	11.26
MIX-10	54.89 ± 0.12	54.31	8.47 ± 0.03	7.87	11.69 ± 0.05	11.51
MIX-11	54.91 ± 0.10	54.31	8.48 ± 0.03	7.87	11.64 ± 0.06	11.51
MIX-12	54.74 ± 0.06	54.31	8.19 ± 0.01	7.87	11.63 ± 0.03	11.51
MIX-13	54.61 ± 0.08	54.31	8.04 ± 0.01	7.87	11.63 ± 0.04	11.51
MIX-14	54.41 ± 0.14	54.31	8.05 ± 0.05	7.87	11.54 ± 0.05	11.51
MIX-15	54.82 ± 0.08	54.30	8.18 ± 0.03	7.81	12.09 ± 0.04	12.06
MIX-16	54.32 ± 0.08	54.31	8.07 ± 0.16	7.87	11.69 ± 0.03	11.51
MIX-17	54.75 ± 0.03	54.32	8.11 ± 0.01	7.93	11.16 ± 0.01	11.02
MIX-18	54.31 ± 0.01	54.31	8.22 ± 0.01	7.87	11.42 ± 0.04	11.51

[a] All experimental values are averages of three runs. Errors are standard deviations.

Appendix II. Thermogravimetric analysis data (TGA) of all MIX-xx.

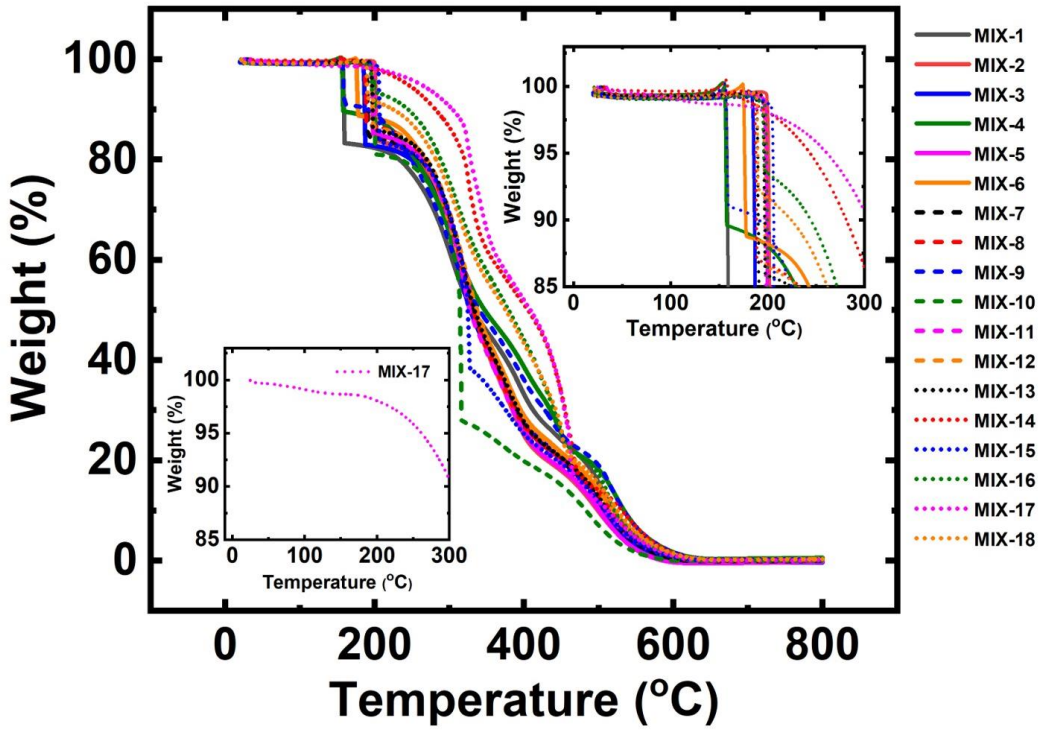

Figure S.1. Thermogravimetric analysis (TGA) data of all **MIX-xx** under N_2 at 10 ^oC min^{-1}.

Appendix III. Additional ATR-IR data.

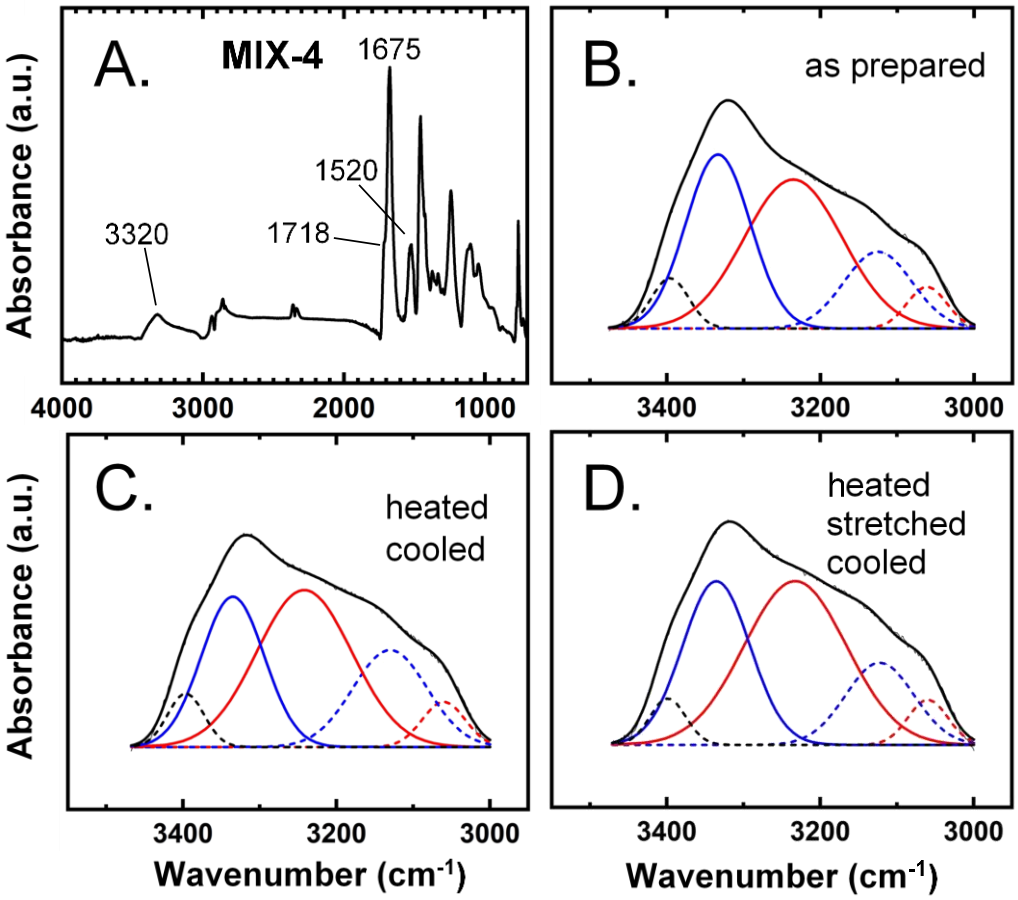

Figure S.2. Room-temperature ATR-FTIR spectra of MIX-4. (a). The entire spectrum. (b). The 3000-3470 cm^{-1} range of frame A, deconvoluted for H-bonding. (c). Same sample as in A and B, heated at T_g+40 ^oC for 15 min, then cooled back to room temperature. (d). Same sample as in A-C, heated again at T_g+40 ^oC for 15 min, stretched to about 60% strain, then stress was released, and the sample was cooled back to room temperature.

Analysis of deconvoluted spectra in frames B-D:

B			C			D	
Wavenumber (cm^{-1})	**Integration (%)**		**Wavenumber (cm^{-1})**	**Integration (%)**		**Wavenumber (cm^{-1})**	**Integration (%)**
3061	5		3060	5		3060	5
3125	15		3130	20		3122	15
3236	42		3242	42		3233	45
3333	32		3335	27		3335	30
3396	5		3396	5		3399	5

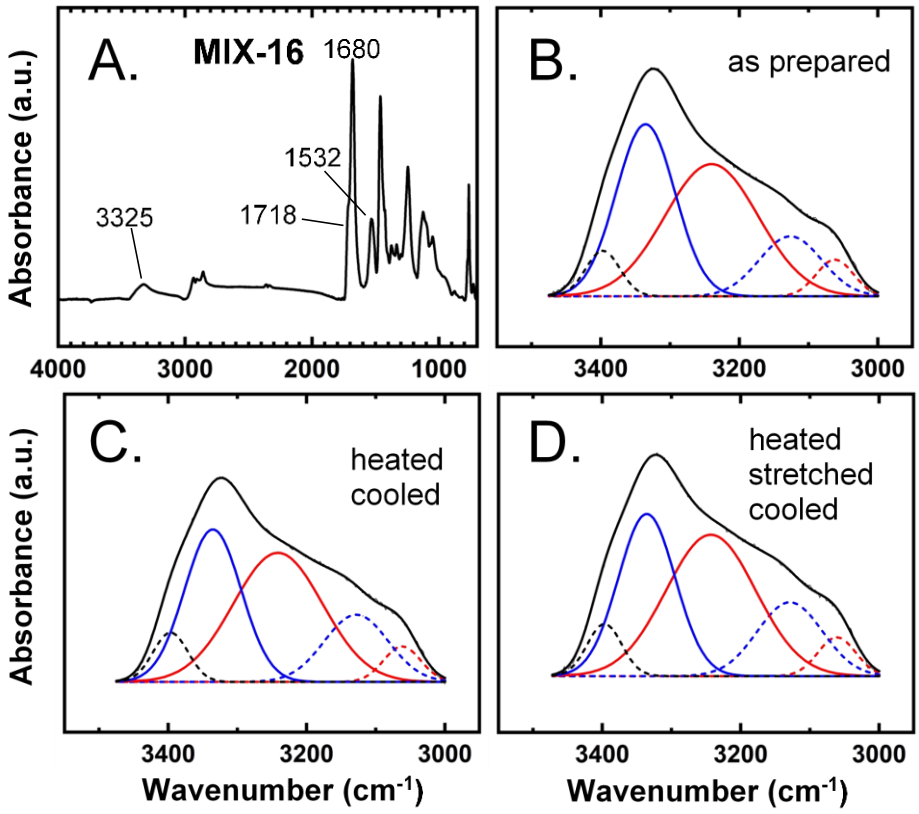

Figure S.3. Room-temperature ATR-FTIR spectra of MIX-16. (a). The entire spectrum. (b). The 3000-3470 cm^{-1} range of frame A, deconvoluted for H-bonding. (c). Same sample as in A and B, heated at T_g+40 ^oC for 15 min, then cooled back to room temperature. (d). Same sample as in A-C, heated again at T_g+40 ^oC for 15 min, stretched to about 60% strain, then stress was released, and the sample was cooled back to room temperature.

Analysis of deconvoluted spectra in frames B-D:

B			C			D	
Wavenumber (cm^{-1})	**Integration (%)**		**Wavenumber (cm^{-1})**	**Integration (%)**		**Wavenumber (cm^{-1})**	**Integration (%)**
3062	5		3062	5		3061	5
3126	13		3128	16		3129	16
3240	42		3241	42		3243	42
3335	35		3336	31		3336	31
3397	5		3397	6		3397	6

Appendix IV. Materials characterization data.

Table S.3. Materials characterization data of all MIX-xx Aerogels.

Sample I.D.	DEG, mol/mol	TEG, mol/mol	TTEG, mol/mol	total monomer (% w/w)	linear shrinkage [a,b] (%)	bulk density [a] (ρ_b, g cm^{-3})	skeletal density [c] (ρ_s, g cm^{-3})	Porosity (Π, % void space)
MIX-1	0.00	1.00	0.00	15	28.11 ± 0.46	0.276 ± 0.014	1.198 ± 0.004	76.96 ± 1.24
MIX-2	0.50	0.50	0.00	15	30.53 ± 0.76	0.285 ± 0.031	1.218 ± 0.002	76.60 ± 2.55
MIX-3	0.50	0.00	0.50	15	27.28 ± 0.76	0.249 ± 0.006	1.206 ± 0.004	79.35 ± 0.65
MIX-4	0.00	0.50	0.50	15	28.44 ± 0.35	0.265 ± 0.006	1.187 ± 0.003	77.67 ± 0.60
MIX-5	0.25	0.50	0.25	15	28.61 ± 0.84	0.269 ± 0.001	1.210 ± 0.005	77.77 ± 0.53
MIX-6	0.25	0.75	0.00	20	24.42 ± 0.22	0.327 ± 0.002	1.213 ± 0.003	73.04 ± 0.35
MIX-7	0.50	0.25	0.25	20	24.86 ± 0.41	0.324 ± 0.019	1.204 ± 0.002	73.09 ± 1.59
MIX-8	0.25	0.25	0.50	20	27.44 ± 0.97	0.364 ± 0.014	1.197 ± 0.003	69.59 ± 1.21
MIX-9	0.00	0.75	0.25	20	27.94 ± 1.18	0.371 ± 0.016	1.207 ± 0.004	69.26 ± 1.39
MIX-10	0.25	0.50	0.25	20	25.08 ± 0.71	0.326 ± 0.003	1.217 ± 0.004	73.21 ± 0.48
MIX-11	0.25	0.50	0.25	20	27.44 ± 0.54	0.354 ± 0.010	1.196 ± 0.002	70.40 ± 0.86
MIX-12	0.25	0.50	0.25	20	27.47 ± 0.46	0.359 ± 0.012	1.191 ± 0.002	69.86 ± 1.03
MIX-13	0.25	0.50	0.25	20	26.97 ± 0.72	0.354 ± 0.006	1.224 ± 0.005	71.08 ± 0.70
MIX-14	0.00	1.00	0.00	25	29.03 ± 0.65	0.529 ± 0.009	1.206 ± 0.002	56.14 ± 0.77
MIX-15	0.50	0.50	0.00	25	23.33 ± 0.08	0.423 ± 0.010	1.204 ± 0.001	64.87 ± 0.84
MIX-16	0.50	0.00	0.50	25	27.42 ± 0.87	0.500 ± 0.018	1.192 ± 0.002	58.05 ± 1.52
MIX-17	0.00	0.50	0.50	25	45.31 ± 0.35	1.172 ± 0.018	1.205 ± 0.002	2.74 ± 1.50
MIX-18	0.25	0.50	0.25	25	27.89 ± 0.46	0.506 ± 0.006	1.195 ± 0.001	57.66 ± 0.51

[a] Average of 5 samples. [b] Shrinkage = 100 × (mold diameter – sample diameter)/(mold diameter). [c] Single sample, average of 50 measurements.

Appendix V. Coefficients for all property fitting equations.

Table S.4. Coefficients of the fitting equations of various properties of all MIX-xx aerogels (excluding MIX-17) to TTEG mole fraction (X_1), DEG mole fraction (X_2) and total monomer concentration (X_3) according to: *Property* = $A(X_1)^2 + B(X_2)^2 + C(X_3)^2 + D(X_1)(X_2) + E(X_1)(X_3) + F(X_2)(X_3) + G(X_1) + H(X_2) + I(X_3) + J$.

Property	A	B	C	D	E	F	G	H	I	J	R^2
Bulk density (ρ_b)	-	-	0.0430	-	0.0246	-0.0251	0.0139	-0.0262	0.1216	0.3474	0.9920
Shrinkage	-	-	2.1913	-0.7856	1.7234	-1.9179	1.0979	-1.5929	0.0507	26.4539	0.8851
Recovery rate ($R_t(N)$)	-	-	-1.3350	-1.1147	-	-	-1.0702	1.0294	-2.1793	7.0096	0.8393
Elastic Modulus	-	-	0.2862	-	0.1302	-0.1457	0.1075	-0.1189	0.3252	0.0588	0.9047
Glass transition (T_g) - 3 ºC/min	-	3.8319	-	-	-	-	-4.3983	1.2085	-4.3023	33.0137	0.7241
Glass transition (T_g) - 1 ºC/min	1.9908	-	-1.3292	-	-	-	-2.4046	2.8275	-1.9604	34.8261	0.8806

[a] Fitting was carried out with orthogonalized variables. The normalizing transforms of the three variables are given by: 1. $X_1 = \frac{(\boldsymbol{TTEG\ mole\ fraction - 0.25})}{\boldsymbol{0.25}}$ ($0 \leq$ TTEG mol fraction ≤ 0). 2. $X_2 = \frac{(\boldsymbol{DEG\ mole\ fraction - 0.25})}{\boldsymbol{0.25}}$ ($0 \leq$ DEG mol fraction ≤ 0.5). 3. $X_3 = \frac{(\boldsymbol{total\ monomer - 20})}{\boldsymbol{5}}$ (15% w/w $\leq$ [total monomer] $\leq$ 25% w/w). The experimental and the computed response values of all properties were analyzed statistically via analysis of variance (ANOVA). Coefficients A-J with a probability value for the null hypothesis of $P \leq 0.1$ were considered statistically significant and were retained.

Appendix VI. Glass transition temperature (T_g) data.

Table S.5. Glass transition temperatures (T_g) of all MIX-xx aerogels as a function of the heating rate. All values are temperatures in ^oC. T_g values are the maxima in the tan δ plots.

Sample I.D.	Heating rate							
	0.5 ^{o}C/min		1.0 ^{o}C/min		3.0 ^{o}C/min		5.0 ^{o}C/min	
	T_g	max G"	T_g	max G"	T_g	max G"	T_g	max G"
MIX-1	35.03	23.24	36.88	25.56	48.81	33.83		
MIX-2	32.89	41.38	41.81	32.35	45.72	29.83		
MIX-3	35.72	25.85	38.39	28.84	40.88	22.97	56.44	37.61
MIX-4	29.04	18.80	31.10	21.44	35.25	21.59	44.99	29.42
MIX-5	34.83	23.87	37.07	27.28	34.58	20.20		
MIX-6	37.18	25.27	38.72	29.56	34.77	20.84		
MIX-7	27.27	37.37	36.98	27.85	32.84	21.15		
MIX-8	30.43	19.72	35.42	21.52	29.92	14.11		
MIX-9	30.25	19.03	32.87	23.72	34.71	20.70		
MIX-10	33.39	22.68	34.67	23.35	37.61	22.67		
MIX-11	34.64	23.27	36.30	25.66	31.25	17.56		
MIX-12	33.97	23.74	35.24	25.94	32.28	18.82		
MIX-13	34.04	23.61	32.39	22.71	31.73	17.69		
MIX-14	31.03	18.11	33.34	23.54	32.48	14.52	51.22	37.41
MIX-15	38.86	30.28	40.04	31.62	43.01	26.68		
MIX-16	32.16	19.52	33.54	24.27	27.82	7.78		
MIX-17					25.27	-15.12		
MIX-18	32.61	19.31	30.43	18.70	31.97	18.60	53.51	39.37

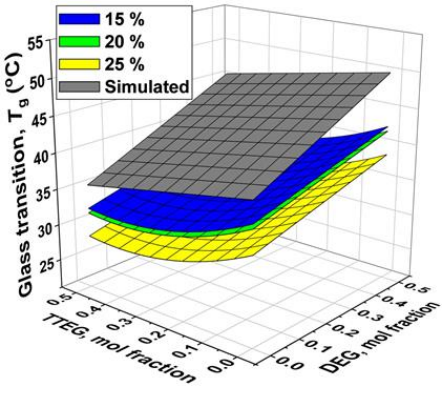

Figure S.4. Quadratic fitting of Tg data at 1 ^{o}C min-1 (Table S.5) to the three exploratory variables. Color-coding: monomer concentration levels. For the fitting parameters refer to Table S.4. Gray plane: calculated Tg's as weighted averages of the Tg's of aerogels from the pure diols.

Appendix VII. Thermal conductivity data.

Table S.6. Thermal conductivity, thermal diffusivity and estimated thermal equilibration times of all MIX-xx.

Sample I.D.	sample thickness (d, mm)	bulk density [a] (ρ_b, g cm^{-3})	total thermal conductivity, k [b] (mW m^{-1} K^{-1})	heat capacity, c_p [c] (J g^{-1} K^{-1})	thermal diffusivity, $D_{thermal}$ [d] (mm^2/sec)	time (τ, sec) [e]
MIX-1	6.12	0.288 ± 0.003	45.2 ± 1.9	1.711 ± 0.074	0.092 ± 0.006	51
MIX-2	6.04	0.237 ± 0.024	50.5 ± 2.3	1.622 ± 0.047	0.131 ± 0.015	35
MIX-3	6.24	0.258 ± 0.008	63.3 ± 2.8	1.686 ± 0.057	0.146 ± 0.009	33
MIX-4	6.11	0.292 ± 0.007	39.1 ± 1.7	1.775 ± 0.061	0.075 ± 0.005	62
MIX-5	5.54	0.263 ± 0.008	46.1 ± 1.9	1.699 ± 0.047	0.103 ± 0.006	37
MIX-6	6.15	0.357 ± 0.009	51.5 ± 2.4	1.667 ± 0.057	0.087 ± 0.005	55
MIX-7	5.96	0.323 ± 0.009	46.7 ± 1.9	1.654 ± 0.042	0.087 ± 0.005	51
MIX-8	6.31	0.417 ± 0.012	58.0 ± 2.6	1.731 ± 0.054	0.080 ± 0.005	62
MIX-9	5.32	0.389 ± 0.009	45.0 ± 2.2	1.743 ± 0.061	0.066 ± 0.004	53
MIX-10	5.65	0.353 ± 0.001	51.3 ± 2.1	1.699 ± 0.047	0.086 ± 0.004	47
MIX-14	6.05	0.631 ± 0.030	99.6 ± 7.1	1.711 ± 0.074	0.092 ± 0.009	50
MIX-15	6.42	0.448 ± 0.001	59.5 ± 2.7	1.622 ± 0.047	0.082 ± 0.004	63
MIX-16	5.63	0.519 ± 0.020	44.8 ± 2.3	1.686 ± 0.057	0.051 ± 0.004	77
MIX-18	5.76	0.606 ± 0.005	72.6 ± 4.2	1.699 ± 0.047	0.071 ± 0.005	59

[a] Two samples were prepared and average of those two samples was calculated. [b] Two such samples were placed side by side and thermal conductivity was measured. [c] Weighted mole fraction average using heat capacities of individual diol aerogels (SMPAs). c_p of DEG - SMPA = 1.533 ± 0.059 J g^{-1} K^{-1}, TEG - SMPA = 1.711 ± 0.074 J g^{-1} K^{-1}, TTEG - SMPA = 1.839 ± 0.097 J g^{-1} K^{-1}. [d] Thermal diffusivity, $D_{thermal} = k/(\rho_b \times c_p)$. [e] Calculated from $(d/2)^2 = 2 \times D_{thermal} \times \tau$.

Standards	Expected thermal conductivity, k (mW m^{-1} K^{-1})	Measured thermal conductivity, k (mW m^{-1} K^{-1})
NIST standard SRM 1453	34.3	34.9 ± 1.3
NIST standard SRM 1453 (as two pieces side-by-side)	34.3	34.7 ± 1.1
Aspen Spaceloft Subsea – 10mm [a]	14.5	14.2 ± 0.5
Aspen – Cryogel – 10mm [a]	17.0	16.2 ± 0.6
Aspen – Cryogel Z – 5mm [a]	17.0	18.3 ± 0.8
Aspen – Pyrogel XT–E – 10mm [a]	21.0	19.4 ± 0.6

[a] http://www.aerogel.com/products-and-solutions/all-insulation-products/.

Appendix VIII. Thermomechanical data [E, $FF(N)$, $R_f(N)$, $R_r(N)$ and $R_t(N)$].

Table S.7. Elastic moduli, E, of MIX-xx calculated from the slopes of the stress-strain curves of Step 1 of every thermomechanical cycle (N=1 to N=5) (Temperature was cycled from T_d to T_r through T_f for five times in combination with tensile testing).

Sample I.D.	DEG, mol/mol	TEG, mol/mol	TTEG, mol/mol	total monomer (% w/w)	Elastic Modulus, E (MPa)				
					Temperature cycle No., N				
					1	2	3	4	5
MIX-1	0.00	1.00	0.00	15	0.027	0.017	0.017	0.017	0.017
MIX-2	0.50	0.50	0.00	15	0.030	0.018	0.017	0.018	0.018
MIX-3	0.50	0.00	0.50	15	0.023	0.019	0.018	0.018	0.018
MIX-4	0.00	0.50	0.50	15	0.034	0.027	0.026	0.026	0.026
MIX-5	0.25	0.50	0.25	15	0.032	0.022	0.021	0.02	0.020
MIX-6	0.25	0.75	0.00	20	0.056	0.048	0.048	0.048	0.048
MIX-7	0.50	0.25	0.25	20	0.068	0.055	0.055	0.055	0.057
MIX-8	0.25	0.25	0.50	20	0.099	0.064	0.063	0.064	0.063
MIX-9	0.00	0.75	0.25	20	0.096	0.069	0.067	0.067	0.066
MIX-10	0.25	0.50	0.25	20	0.089	0.062	0.062	0.061	0.061
MIX-11	0.25	0.50	0.25	20	0.086	0.063	0.062	0.061	0.061
MIX-12	0.25	0.50	0.25	20	0.069	0.050	0.050	0.050	0.049
MIX-13	0.25	0.50	0.25	20	0.096	0.069	0.069	0.068	0.066
MIX-14	0.00	1.00	0.00	25	0.790	0.796	0.794	0.789	0.818
MIX-15	0.50	0.50	0.00	25	0.099	0.067	0.063	0.061	0.061
MIX-16	0.50	0.00	0.50	25	0.692	0.758	0.769	0.783	0.757
MIX-17	0.00	0.50	0.50	25	1.745	1.761	1.790	1.774	1.731
MIX-18	0.25	0.50	0.25	25	0.472	0.548	0.547	0.545	0.543

Table S.8. Fill factors ($FF(N)$) of all MIX-xx aerogels as shown (Temperature was cycled from T_d to T_r through T_f for five times in combination with tensile testing).

Sample I.D.	DEG, mol/mol	TEG, mol/mol	TTEG, mol/mol	total monomer (% w/w)	Fill Factor ($FF(N)$)				
					Temperature cycle No., N				
					1	2	3	4	5
MIX-1	0.00	1.00	0.00	15	0.59	0.67	0.66	0.68	0.71
MIX-2	0.50	0.50	0.00	15	0.53	0.65	0.62	0.68	0.67
MIX-3	0.50	0.00	0.50	15	0.55	0.62	0.63	0.61	0.67
MIX-4	0.00	0.50	0.50	15	0.56	0.65	0.64	0.65	0.66
MIX-5	0.25	0.50	0.25	15	0.51	0.56	0.56	0.56	0.58
MIX-6	0.25	0.75	0.00	20	0.53	0.56	0.57	0.57	0.58
MIX-7	0.50	0.25	0.25	20	0.46	0.54	0.50	0.50	0.49
MIX-8	0.25	0.25	0.50	20	0.40	0.46	0.47	0.47	0.49
MIX-9	0.00	0.75	0.25	20	0.52	0.59	0.59	0.60	0.62
MIX-10	0.25	0.50	0.25	20	0.51	0.55	0.56	0.58	0.56
MIX-11	0.25	0.50	0.25	20	0.49	0.52	0.51	0.56	0.52
MIX-12	0.25	0.50	0.25	20	0.48	0.53	0.53	0.53	0.50
MIX-13	0.25	0.50	0.25	20	0.46	0.52	0.54	0.51	0.51
MIX-14	0.00	1.00	0.00	25	0.41	0.50	0.49	0.48	0.49
MIX-15	0.50	0.50	0.00	25	0.54	0.58	0.65	0.61	0.61
MIX-16	0.50	0.00	0.50	25	0.40	0.39	0.38	0.35	0.35
MIX-17	0.00	0.50	0.50	25	0.46	0.50	0.52	0.52	0.58
MIX-18	0.25	0.50	0.25	25	0.46	0.53	0.52	0.54	0.50

Table S.9. Shape fixity ratios ($R_f(N)$) of all MIX-xx aerogels as shown (Temperature was cycled from T_d to T_r through T_f for five times in combination with tensile testing).

Sample I.D.	DEG, mol/mol	TEG, mol/mol	TTEG, mol/mol	total monomer (% w/w)	Strain fixity, $R_f(N)$ (%)				
					Temperature cycle No., N				
					1	2	3	4	5
MIX-1	0.00	1.00	0.00	15	97.9	97.9	95.4	96.2	96.5
MIX-2	0.50	0.50	0.00	15	99.2	99.2	99.2	99.2	99.2
MIX-3	0.50	0.00	0.50	15	99.2	99.2	99.1	99.1	99.1
MIX-4	0.00	0.50	0.50	15	99.3	99.2	99.2	99.2	99.2
MIX-5	0.25	0.50	0.25	15	99.3	99.3	99.2	99.2	99.2
MIX-6	0.25	0.75	0.00	20	99.2	99.1	99.1	99.1	99.1
MIX-7	0.50	0.25	0.25	20	99.1	99.0	99.0	99.0	99.0
MIX-8	0.25	0.25	0.50	20	99.3	99.2	99.2	99.2	99.2
MIX-9	0.00	0.75	0.25	20	99.3	99.2	99.2	99.2	99.2
MIX-10	0.25	0.50	0.25	20	99.2	99.1	99.1	99.1	99.1
MIX-11	0.25	0.50	0.25	20	99.2	99.1	99.1	99.1	99.1
MIX-12	0.25	0.50	0.25	20	99.2	99.1	99.1	99.1	99.1
MIX-13	0.25	0.50	0.25	20	99.2	99.1	99.1	99.1	99.1
MIX-14	0.00	1.00	0.00	25	97.6	97.5	97.6	97.7	97.7
MIX-15	0.50	0.50	0.00	25	99.2	99.1	99.1	99.1	99.1
MIX-16	0.50	0.00	0.50	25	98.3	97.8	97.7	97.8	97.8
MIX-17	0.00	0.50	0.50	25	94.2	93.7	94.8	94.0	94.2
MIX-18	0.25	0.50	0.25	25	97.7	97.2	97.2	97.2	97.2

Table S.10. Shape recovery ratios ($R_r(N)$) of all MIX-xx aerogels as shown (Temperature was cycled from T_d to T_r through T_f for five times in combination with tensile testing).

Sample I.D.	DEG, mol/mol	TEG, mol/mol	TTEG, mol/mol	total monomer (% w/w)	Strain recovery, $R_r(N)$ (%)				
					Temperature cycle No., N				
					1	2	3	4	5
MIX-1	0.00	1.00	0.00	15	84.1	97.7	99.0	99.4	99.5
MIX-2	0.50	0.50	0.00	15	86.9	96.8	98.6	99.7	99.5
MIX-3	0.50	0.00	0.50	15	88.7	98.2	99.4	99.6	99.7
MIX-4	0.00	0.50	0.50	15	82.7	97.8	99.6	99.5	99.6
MIX-5	0.25	0.50	0.25	15	86.0	96.2	98.5	98.9	99.4
MIX-6	0.25	0.75	0.00	20	89.5	98.7	99.4	99.6	99.7
MIX-7	0.50	0.25	0.25	20	89.7	98.9	99.4	99.6	99.7
MIX-8	0.25	0.25	0.50	20	84.0	97.5	98.9	99.4	99.6
MIX-9	0.00	0.75	0.25	20	90.6	97.8	98.5	98.5	99.5
MIX-10	0.25	0.50	0.25	20	86.4	97.3	99.1	99.5	99.6
MIX-11	0.25	0.50	0.25	20	87.0	98.1	99.1	99.5	99.7
MIX-12	0.25	0.50	0.25	20	84.6	98.1	99.6	99.5	99.6
MIX-13	0.25	0.50	0.25	20	86.9	97.6	99.1	99.3	99.8
MIX-14	0.00	1.00	0.00	25	82.7	97.8	99.6	99.5	99.6
MIX-15	0.50	0.50	0.00	25	84.7	97.1	98.7	99.4	99.5
MIX-16	0.50	0.00	0.50	25	79.3	98.1	99.3	99.5	100.0
MIX-17	0.00	0.50	0.50	25	90.6	97.8	98.5	98.5	99.5
MIX-18	0.25	0.50	0.25	25	82.7	97.9	97.3	97.8	98.1

Table S.11. Shape recovery rates ($R_t(N)$) of all MIX-xx aerogels as shown (Temperature was cycled from T_d to T_r through T_f for five times in combination with tensile testing).

Sample I.D.	DEG, mol/mol	TEG, mol/mol	TTEG, mol/mol	total monomer (% w/w)	Strain recovery rate, $R_t(N)$ (min^{-1})				
					Temperature cycle No., N				
					1	2	3	4	5
MIX-1	0.00	1.00	0.00	15	6.4	6.3	6.4	6.4	6.2
MIX-2	0.50	0.50	0.00	15	8.2	10.8	9.7	9.4	10.5
MIX-3	0.50	0.00	0.50	15	6.5	7.1	6.9	6.2	6.6
MIX-4	0.00	0.50	0.50	15	5.8	6.0	6.1	6.0	6.0
MIX-5	0.25	0.50	0.25	15	8.8	10.4	9.3	9.6	10.0
MIX-6	0.25	0.75	0.00	20	7.9	7.9	8.3	8.8	7.8
MIX-7	0.50	0.25	0.25	20	8.4	8.0	8.1	7.1	7.2
MIX-8	0.25	0.25	0.50	20	5.6	5.9	6.1	6.1	6.2
MIX-9	0.00	0.75	0.25	20	7.1	7.0	7.2	7.2	7.3
MIX-10	0.25	0.50	0.25	20	6.7	5.7	5.8	5.8	5.9
MIX-11	0.25	0.50	0.25	20	7.2	7.3	7.1	7.6	7.3
MIX-12	0.25	0.50	0.25	20	8.1	7.0	7.1	7.1	6.9
MIX-13	0.25	0.50	0.25	20	7.2	7.3	7.4	7.4	7.4
MIX-14	0.00	1.00	0.00	25	2.5	2.4	2.5	2.4	2.5
MIX-15	0.50	0.50	0.00	25	7.4	7.6	7.6	7.6	7.8
MIX-16	0.50	0.00	0.50	25	2.5	2.6	2.6	2.6	2.7
MIX-17	0.00	0.50	0.50	25	0.9	0.9	1.0	1.0	1.0
MIX-18	0.25	0.50	0.25	25	2.0	2.4	2.3	2.3	2.0

Table S.12. Collection of relevant data for MIX-xx and pure diol PIR-PUR aerogels for plotting Log $R_t(N)$ versus the specific elastic modulus (E/ρ_b) at the 5th cycle.

Sample I.D.	**Strain recovery rate, $R_t(5)$ (min^{-1})**	**Elastic Modulus, E (MPa)**	**Bulk density (ρ_b, g cm^{-3})**	**Temperature at R_t (^oC)**
MIX-1	6.17	0.017	0.276	30.15
MIX-2	10.48	0.018	0.285	32.02
MIX-3	6.56	0.018	0.249	32.76
MIX-4	6.03	0.026	0.265	27.92
MIX-5	10.03	0.020	0.269	26.27
MIX-6	7.80	0.048	0.327	30.97
MIX-7	7.24	0.057	0.324	29.44
MIX-8	6.22	0.063	0.364	30.03
MIX-9	7.30	0.066	0.371	29.65
MIX-10	5.90	0.061	0.326	30.11
MIX-11	7.33	0.061	0.354	35.38
MIX-12	6.89	0.049	0.359	30.13
MIX-13	7.40	0.066	0.354	17.75
MIX-14	2.48	0.818	0.529	30.22
MIX-15	7.81	0.061	0.423	30.15
MIX-16	2.71	0.757	0.500	32.02
MIX-17	1.02	1.731	1.172	32.76
MIX-18	1.97	0.543	0.506	27.92

Table S.12. Collection of relevant data for MIX-xx and pure diol PIR-PUR aerogels for plotting Log $R_t(N)$ versus the specific elastic modulus (E/ρ_b) at the 5th cycle (Continued).

Sample I.D.	Strain recovery rate, $R_t(5)$ (min^{-1})	Elastic Modulus, E (MPa)	Bulk density (ρ_b, g cm^{-3})	Temperature at R_t (ºC)
DEG-2	6.68	0.012	0.224	41.89
DEG-3	6.40	0.022	0.230	40.31
DEG-4	10.58	0.026	0.258	41.04
DEG-5	6.89	0.030	0.321	39.86
DEG-6	6.87	0.052	0.279	41.64
DEG-7	5.79	0.029	0.287	40.73
DEG-8	5.70	0.059	0.322	40.69
DEG-9	3.70	0.025	0.414	40.23
DEG-10	5.67	0.043	0.366	39.30
TEG-1	8.02	0.024	0.247	30.07
TEG-2	7.26	0.029	0.271	31.37
TEG-3	7.48	0.044	0.336	30.02
TEG-4	8.52	0.045	0.302	31.68
TEG-5	6.76	0.154	0.391	30.41
TEG-6	8.25	0.086	0.356	30.67
TEG-7	1.63	1.812	1.076	25.77
TEG-8	7.45	0.065	0.408	28.64
TEG-9	2.28	1.662	1.014	25.86
TEG-10	1.89	1.961	1.070	24.45
TTEG-1	2.71	1.368	1.001	20.47
TTEG-2	6.05	0.063	0.279	19.90
TTEG-4	6.80	0.272	0.430	31.52
TTEG-6	1.87	2.475	1.043	27.65
TTEG-8	1.70	2.371	1.096	24.98

Appendix IX. Derivation of the activation barrier for the shape recovery and the relationship between shape recovery rate and the Young's modulus.

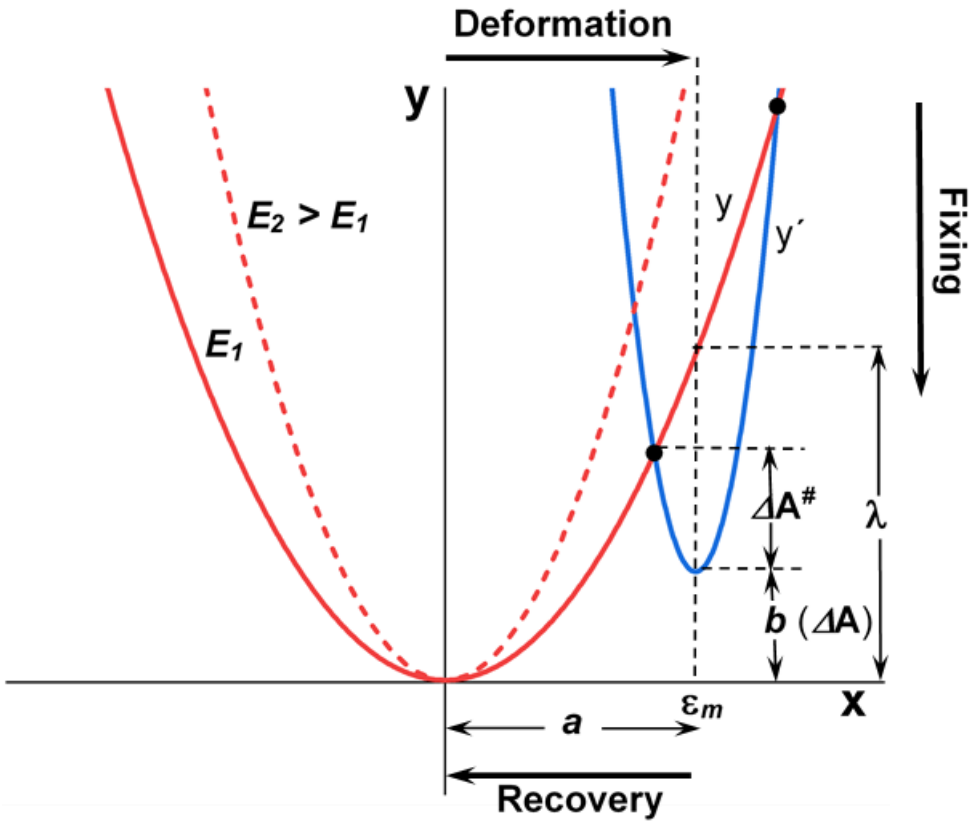

Scheme S.2. The geometry of crossing parabolas (red and blue) with unequal widths. (Note: Higher 'moduli' (e.g., $E_2 > E_1$) give narrower parabolas).

Based on Scheme S.2 above, the equations of the two parabolas are:

$$y = \varepsilon x^2$$

$$(y' - b) = (x - a)^2 \Rightarrow y' = x^2 - 2ax + a^2 + b$$

Whereas 'a' and 'b' are the displacements of the two parabolas in the 'x' and 'y' directions, respectively. Without compromizing generality, the coefficients of the parabolas (describing their widths) are normalized to the narrower parabola of the two. As

shown in Scheme S.2, the y-parabola (solid red) is considered wider than the y´ (blue). In our case, the normalizing factor ε is proportional to the Young's modulus and is on the order of 0.001.

At the two crossing points of the two parabolas (shown with bold dots) y=y´, therefore:

$$(1-\varepsilon)x^2 - 2ax + a^2 + b = 0 \Rightarrow x^2 - \frac{2a}{1-\varepsilon}x + \frac{a^2+b}{1-\varepsilon} = 0$$

At those crossing points, the values of x are given by the roots of the quadratic equation above:

$$x_{@crossings} = \frac{\frac{2a}{1-\varepsilon} \pm \sqrt{\frac{4a^2}{(1-\varepsilon)^2} - 4\frac{a^2+b}{1-\varepsilon}}}{2}$$

The first crossing point is given by:

$$x_{@FIRST\_crossing} = \frac{a}{1-\varepsilon} - \sqrt{\frac{a^2}{(1-\varepsilon)^2} - \frac{a^2+b}{1-\varepsilon}}$$

And the y-value at that crossing point is therefore:

$$y_{@FIRST\_crossing} = \varepsilon (x_{@FIRST\_crossing})^2 =$$

$$= \varepsilon \left[\frac{a^2}{(1-\varepsilon)^2} - 2\frac{a}{1-\varepsilon}\sqrt{\frac{a^2}{(1-\varepsilon)^2} - \frac{a^2+b}{1-\varepsilon}} + \frac{a^2}{(1-\varepsilon)^2} - \frac{a^2+b}{1-\varepsilon} \right] =$$

$$= \varepsilon \left[\frac{2a^2}{(1-\varepsilon)^2} - 2\frac{a}{1-\varepsilon}\sqrt{\frac{a^2}{(1-\varepsilon)^2} - \frac{a^2+b}{1-\varepsilon}} - \frac{a^2+b}{1-\varepsilon} \right] =$$

$$= \frac{\varepsilon a^2}{(1-\varepsilon)^2}\left[2 - 2\sqrt{\frac{(1-\varepsilon)^2}{a^2}\frac{a^2}{(1-\varepsilon)^2} - \frac{(1-\varepsilon)^2}{a^2}\frac{a^2+b}{1-\varepsilon}} - \frac{(1-\varepsilon)^2}{a^2}\frac{a^2+b}{1-\varepsilon} \right] =$$

$$= \frac{\varepsilon a^2}{(1-\varepsilon)^2}\left[2 - 2\sqrt{1-(1-\varepsilon)(1+\frac{b}{a^2})} - (1-\varepsilon)(1+\frac{b}{a^2})\right] =$$

$$= \frac{\varepsilon a^2}{(1-\varepsilon)^2}\left[1 - 2\sqrt{1-(1-\varepsilon)(1+\frac{b}{a^2})} + [1-(1-\varepsilon)(1+\frac{b}{a^2})]\right] =$$

$$= \frac{\varepsilon a^2}{(1-\varepsilon)^2}\left[1 - \sqrt{1-(1-\varepsilon)(1+\frac{b}{a^2})}\right]^2 =$$

$$= \frac{\varepsilon a^2}{(1-\varepsilon)^2}\left[1 - \sqrt{\varepsilon\left[1+\frac{b(\varepsilon-1)}{\varepsilon a^2}\right]}\right]^2$$

To start putting physical meaning into those parabolas, the activation barrier for shape recovery ($\Delta A^{\#}$, refer to Scheme S.2) is given by:

$$\Delta A^{\#} = y_{@FIRST\_crossing} - b = \frac{\varepsilon a^2}{(1-\varepsilon)^2}\left[1 - \sqrt{\varepsilon\left[1+\frac{b(\varepsilon-1)}{\varepsilon a^2}\right]}\right]^2 - b$$

which, after some rearrangement, becomes:

$$\Delta A^{\#} = \frac{\varepsilon a^2}{(1-\varepsilon)^2}\left[\sqrt{\varepsilon} - \sqrt{1-\frac{b(1-\varepsilon)}{\varepsilon a^2}}\right]^2$$

Since the reorganization energy upon stretching at a (= ε_m) is $\lambda = (\varepsilon a^2)/2$, and the thermodynamic driving force for recovery $\Delta A = b$, the last equation becomes:

$$\Delta A^{\#} = \frac{2\lambda}{(1-\varepsilon)^2}\left[\sqrt{\varepsilon} - \sqrt{1-\frac{\Delta A(1-\varepsilon)}{2\lambda}}\right]^2 \qquad (1)$$

MARCUS ANALOGUE:

If the two parabolas have the same modulus, E, thereby the same width, then they are described by:

$$y = \frac{E}{2}x^2$$

$$(y' - b) = \frac{E}{2}(x - a)^2 \Rightarrow y' = \frac{E}{2}x^2 - Eax + \frac{E}{2}a^2 + b$$

By setting y=y´ and after the suitable manipulations, the activation barrier is given by a (much simplified) Marcus-type expression:

$$\Delta A^{\#} = \frac{(\Delta A - \lambda)^2}{4\lambda} \qquad (2)$$

where $\lambda = \frac{E\varepsilon_m^2}{2}$

****

Now, referring to Scheme S.2 the (reorganization) energy expended to stretch the sample to ε_m (= a) is given (in units of specific modulus as a multiple of the lowest specific modulus) by:

$$\lambda = \frac{\varepsilon\varepsilon_m^2}{2}$$

But that stretching energy is purely entropic, thereby:

$$\lambda = -T_d\Delta S$$

Therefore, the entropy change upon stretching (a decrease, that is $\Delta S<0$) is given by:

$$\Delta S = -\frac{\varepsilon\varepsilon_m^2}{2T_d}$$

The settling energy on cooling from T_d to T_f is equal to $(T_f - T_d)\Delta S$. Thereby, from Scheme S.2:

$$\Delta A = l - (T_f - T_d)\Delta S = \frac{\varepsilon e_m^2}{2} - (T_f - T_d)\frac{-\varepsilon e_m^2}{2T_d} =$$

$$= \frac{\varepsilon e_m^2}{2T_d}\left[T_d + T_f - T_d\right] = \frac{\varepsilon e_m^2}{2}\frac{T_f}{T_d}$$

The above expressions are completely general. They apply irrespective to whether the initial and final states have the same or different moduli.

From the last expression and the expression for λ we calculate:

$$\frac{\Delta A}{l} = \frac{T_f}{T_d}$$

Substituting to Eq 1, we get:

$$\Delta A^{\#} = \frac{\varepsilon e_m^2}{(1-\varepsilon)^2}\left[\sqrt{\varepsilon} - \sqrt{1 - \frac{T_f}{2T_d}(1-\varepsilon)}\right]^2$$

$$= \frac{\varepsilon^2 e_m^2}{(1-\varepsilon)^2}\left[1 - \sqrt{\frac{1}{\varepsilon} - \frac{T_f}{2T_d}\left(\frac{1}{\varepsilon} - 1\right)}\right]^2$$

That expression is again completely general. However, here, based on the fact that $\varepsilon \approx 0.001$, $1 - \varepsilon \approx 1$, and $(1/\varepsilon) - 1 \approx 1/\varepsilon$ and the last expression can be simplified into:

$$\Delta A^{\#} = \varepsilon^2 e_m^2\left[1 - \sqrt{\frac{1}{\varepsilon}\left(1 - \frac{T_f}{2T_d}\right)}\right]^2$$

It turns out that for the specific values of ε, T_f (about -10 ^oC) and T_d (about 40 ^oC), the square root above has a numerical value of about 24 (>>1), thereby the last expression is simplified into:

$$\Delta A^{\#} = \varepsilon e_m^2 \left(1 - \frac{T_f}{2T_d}\right) \tag{3}$$

****

MARCUS ANALOGUE:

Here again, the two parabolas have the same modulus. By substituting:

$$\lambda = \frac{\varepsilon e_m^2}{2}$$

and

$$\Delta A - \lambda = \frac{\varepsilon e_m^2}{2}\left(\frac{T_f}{T_d} - 1\right)$$

into Eq 2, we obtain:

$$\Delta A^{\#} = \frac{\varepsilon e_m^2}{8}\left(\frac{T_f}{T_d} - 1\right)^2$$

whereas now ε is the exact specific modulus, E/ρ_b; E: moduli (MPa) of the unstretched samples.

$$\Delta A^{\#} = \frac{E}{\rho_b}\frac{e_m^2}{8}\left(\frac{T_f}{T_d} - 1\right)^2 \tag{4}$$

****

In both equations 3 and 4, the activation barrier, $\Delta A^{\#}$, is related linearly to the modulus of the initial (unstretched) state.

Since rate constants, k, are related to activation barriers exponentially:

$$k_{rate} = Ce^{-\frac{\Delta A^{\#}}{RT}}$$ where C is the pre-exponential factor.

Inserting $\Delta A^{\#}$ from equation 3, we obtain:

$$Logk_{rate} = LogC - \frac{\varepsilon e_m^2}{2.303RT}\left(1 - \frac{T_f}{2T_d}\right) \quad (5)$$

Inserting $\Delta A^{\#}$ from equation 4 we obtain:

$$Logk_{rate} = LogC - \frac{1}{2.303}\frac{E}{r_b}\frac{e_m^2}{8RT}\left(\frac{T_f}{T_d} - 1\right)^2 \quad (6)$$

In either case (equations 5 or 6) Log k_{rate} depends linearly on the specific modulus (generalized or otherwise) of the initial (unstretched) state, which is what was found experimentally (Figure 15 of the main article).

III. EXPLOSIVE VERSUS THERMITE BEHAVIOR IN IRON(0) AEROGELS INFILTRATED WITH PERCHLORATES

Nicholas Leventis[*,1], Suraj Donthula[1], Chandana Mandal[1], Michael S. Ding[*,2] and Chariklia Sotiriou-Leventis[*,1]

[1] Department of Chemistry, Missouri University of Science and Technology, Rolla, MO 65409, U.S.A. leventis@mst.edu; cslevent@mst.edu

[2] Electrochemistry Branch, Army Research Laboratory, 2800 Powder Mill Road, Adelphi, MD 20783, U.S.A. michael.s.ding.civ@mail.mil

Published in *Chemistry of Materials* **2015**, *27*, 8126-8137

ABSTRACT

Monolithic nanoporous iron was prepared via carbothermal reduction of interpenetrating networks of polybenzoxazine and iron oxide nanoparticles. Excess carbon was burned off at 600 ^{o}C in air, and oxides produced from partial oxidation of the Fe(0) network were reduced back to Fe(0) with H_2 at different temperatures (**temp**) ranging from 300 ^{o}C to 1300 ^{o}C. Samples were carbon-free, for **temp**>400 ^{o}C also oxide-free, and are referred to according to the final H_2-reduction temperature as **Fe-temp**. **Fe-temp** monoliths were infiltrated with perchlorates, dried exhaustively and were ignited with a flame in open air. Most experimentation was conducted with $LiClO_4$. Depending on **temp**, monoliths fizzled out (≤400 ^{o}C), exploded violently (500 ^{o}C to 900 ^{o}C) or behaved as thermites (≥950 ^{o}C). Samples sealed in evacuated tubes did not explode, while if sealed under N_2 the explosive effect was intensified. Thus, explosive behavior was attributed to rapid heating and expansion of gas filling nanoporous space. However, although that condition was

necessary for explosive behavior, it was not sufficient. Based on SEM, particle sizes via N_2 sorption, electrical conductivity measurements and mechanical strength data under quasi-static compression, it was concluded that the boundaries between the three types of behavior after ignition were associated with: (a) mild sintering (fizzling/explosive boundary at around 500 ^oC); and, (b) melting-like fusion of skeletal nanoparticles (explosive/thermite boundary at around 950 ^oC). Overall, mechanically weaker networks fizzled out; too strong behaved as thermites; networks of intermediate strength exploded. For thermite behavior in particular, other factors may be also at play, such as a combination of reduced porosity, a sub-stoichiometric amount of $LiClO_4$ and a slower heat release rate. The latter was supported by TGA data in O_2 and was attributed to a slower rate of oxidation of progressively thicker nanostructures as the H_2-reduction temperature increased.

TOC Graphic

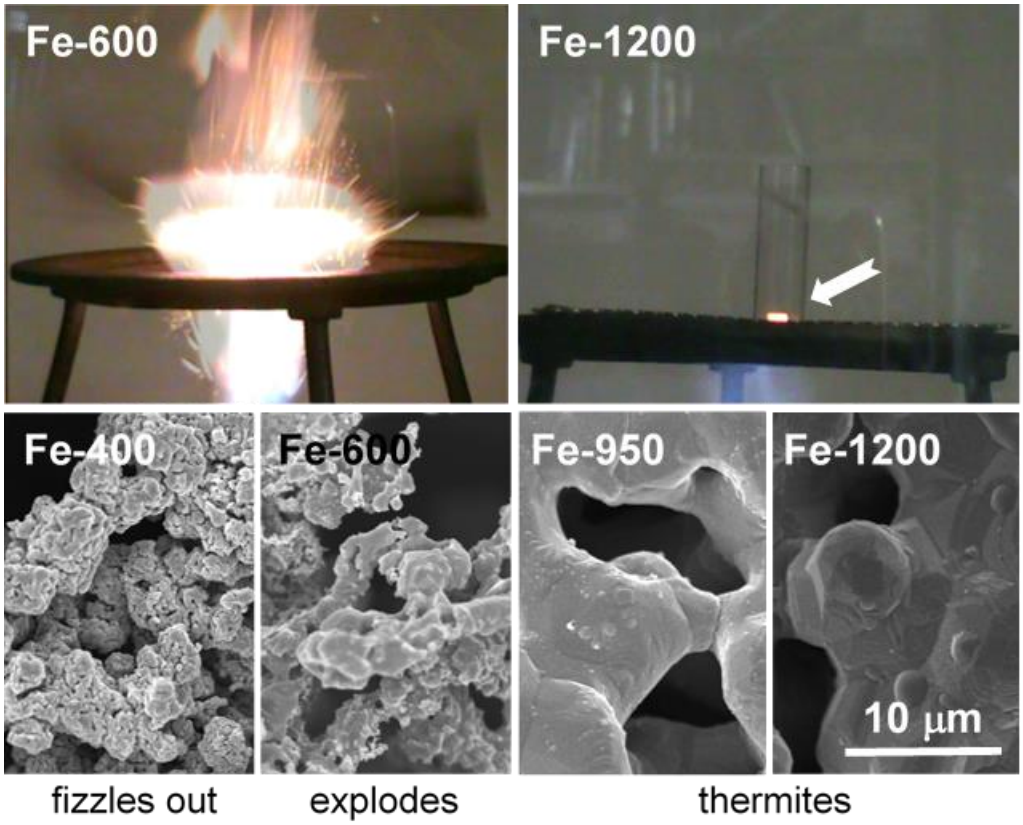

1. INTRODUCTION

Thermites produce intense heat via solid-state reactions.[1] Here we explore the factors controlling an unusual type of explosive behavior whereas a solid-state reaction does not produce gasses, instead provides the heat for rapid expansion of gas filling open nanoporous space. This line of research was motivated by the quest for an alternative nanostructured heat source to activate thermal batteries.[2] In the so-called pressed pellet technology, the heat source is commonly a mixture of micron-sized metallic iron and $KClO_4$.[3,4] That technology works sufficiently well as a heat source, but lack of mechanical integrity renders pressed heat pellets difficult to handle in a battery assembly, the ability to

reduce their thickness is limited, and therefore efficient materials utilization is practically impossible. Alternatively, thin-film thermites, such as "NanoFoil," are based on alternating layers of Al/Ni, each a few dozen of nanometers thick.[5] Ignition is started in a way that the combustion front moves parallel to the Al/Ni layers. Although NanoFoil moves the technology in the right direction in terms of fast rise, high volumetric power density, more flexible form-factor, greater mechanical strength, and better production efficiency, yet there are drawbacks. For instance, bimetallic nano-layered materials are still not flexible enough for thin-film thermal battery applications and their manufacturing process (physical vapor sputtering) is too expensive.

Clearly, there are visible benefits from combining the monolithicity and intrinsic nano-sizing of NanoFoil with the high energy content of the Fe/perchlorate chemistry of pressed pellets. Hence, materials to look for should be based on monolithic bicontinuous iron with interconnected nanopores defined by a sturdy metallic network. The expertise we brought in for this is related to the carbothermal synthesis of metallic nanoporous aerogels (e.g., Fe, Co, Ni, Sn and Cu) from co-gelation of interpenetrating networks of metal oxide and carbonizable resorcinol-formaldehyde (RF) nanoparticles.[6-8] The main, and perhaps only drawback of the iron oxide-RF route for the task at hand was that the resulting Fe(0) aerogels were not monolithic. In fact, Fe(0) aerogels were the only ones in the carbothermal series that were obtained as chunks rather than monoliths.[6,8] At this point, noting that among metallic aerogels, Fe(0) was the hardest to produce in terms of required reduction temperature ($\geq$800 ^{o}C),[8] and reasoning that physical rearrangement (e.g., shrinkage) in the carbonizable RF matrix might have been the cause of disintegration of the Fe(0) monoliths, we decided to use the apparent mechanical strength of nanoporous

carbon from a diverse array of polymeric aerogel precursors as a qualitative indicator for the mechanical integrity of the resulting iron aerogels. *In other words, we sought after a dual role for the carbon aerogel matrix: that of a consumable carbon source for the carbothermal reduction of the oxide, and that of a template.* In recent years, the list of carbonizable polymeric aerogels is getting longer (including polyureas,[9] polyimides,[10] polyacrylonitrile[11]), however, polybenzoxazine (PBO) aerogels stand out not only for their mechanical integrity, but also for their chemical similarity with RF aerogels: they are both phenolic resins,[12-16] hence co-gelation with an iron oxide (FeOx) network should follow similar chemistry with RF. Indeed, interpenetrating PBO-FeOx networks were obtained recently by catalyzing polymerization of a benzoxazine (BO) monomer by the Bronsted acidity of a $[Fe(H_2O)_6]Cl_3$ sol in DMF ($pK_{a,1}$=1.19, $pK_{a,2}$=2.49).[17] Gelation of the $[Fe(H_2O)_6]Cl_3$ sol was carried out by irreversible deprotonation with an epoxide (epichlorohydrin – Scheme 1A).[18-21] Ring-fusion aromatization of the PBO network (at 200 ^oC/air – Scheme 1B) ensured a high carbonization yield.[16] Pyrolysis of aromatized PBO-FeOx networks at 800 ^oC/Ar triggered carbothermal reduction of the FeOx network to monolithic metallic Fe(0).

Since it is virtually impossible to balance precisely the amounts of carbon and FeOx, the resulting Fe(0) monoliths ended up with a small amount of residual carbon (≤5% w/w). For several applications (e.g., in catalysis) that C-impurity would not matter, however, for thermites, in which Fe(0) is ignited in a confined environment, the presence of unreacted carbon would generate hot CO_2 and would be detrimental. Residual carbon was removed oxidatively with a brief treatment at 600 ^oC (20 min) under flowing air. That

step caused partial oxidation of Fe(0) to Fe_2O_3, which was reduced back to Fe(0) under flowing H_2 at the same temperature (600 ^oC).

The resulting nanoporous Fe(0) was carbon-free and monolithic, as designed. Importantly though, it was also noted that the temperature of the final H_2-reduction step had a great effect on the behavior upon ignition. Namely, it was noted that $LiClO_4$-loaded nanoporous Fe(0) monoliths produced at 600 $^oC/H_2$ exploded violently (even though they contained no carbon), while on the other hand if the final H_2-reduction step had been carried out at 1300 $^oC/H_2$, $LiClO_4$-loaded monoliths showed the desirable thermite behavior. All other things being equal, since the unexpected explosive behavior was observed from the higher-porosity (92% v/v) 600 $^oC/H_2$-treated samples, but not from the lower-porosity (50% v/v) 1300 $^oC/H_2$-treated ones, it was attributed to rapid heating and expansion of the pore-filling gas (air).[17] According to this line of reasoning, C-free samples reduced with H_2 at even lower temperatures (i.e., at <600 ^oC) would have higher porosities and should demonstrate even more powerful explosions. As demonstrated herewith though, that turned out to be not true. Thus, we took over and describe a systematic investigation whose goal was to correlate the explosive versus thermite behavior of perchlorate-loaded monolithic nanoporous Fe(0) with the material properties obtained at various final H_2-reduction temperatures. Based on control experiments that include ignition in sealed tubes under vacuum (in which no explosive behavior was observed) and in sealed tubes under N_2 (giving *extremely* powerful explosions), it was confirmed that explosive behavior of perchlorate-loaded Fe(0) aerogels is indeed due to rapid heating and expansion of the pore filling gas. However, although gas (air) filled nanopores is a necessary condition for explosive behavior, it is not sufficient. Based on analysis of the pore structure, the iron

network morphology and the interparticle connectivity, it was concluded that explosive versus thermite behavior is actually controlled by the extent of fusion of skeletal Fe(0) nanoparticles that is brought about by annealing phenomena during H_2-reduction at different temperatures. At first approximation, mechanically weaker networks will fizzle out; too strong will behave as thermites; networks of intermediate strength will explode.

CAUTION: Ignition experiments described herewith are dangerous. Work should be conducted in a fume hood with a protective shield and the sash down. Despite that double protective layer, face protection is highly recommended and ear protection is also advisable for experiments conducted in test tubes sealed under N_2. Emphatically, flame-sealing of test tubes with perchlorate-loaded Fe(0) aerogels inside, either under vacuum or under N_2, should be done by a skilled professional with appropriate face and body protection. We did not have any incidents of tubes exploding at that stage, however, should such an incident were to occur, it could be devastating.

2. RESULTS AND DISCUSSION

2.1. SYNTHESIS OF NANOPOROUS Fe(0) WITH VARIABLE POROSITY

Scheme 2 summarizes the synthetic protocol for Fe(0) aerogels from the PBO-FeOx network to the final product. For details refer to the Experimental Section. After carbothermal reduction, residual carbon was removed with a brief treatment at 600 ^{o}C under flowing air (20 min). Oxides produced from partial oxidation of Fe(0) were reduced back to Fe(0) under flowing H_2 at various temperatures. Samples are referred to as **Fe-temp**, whereas '**temp**' stands for the temperature of the final H_2-reduction step. Photographs in Scheme 2 emphasize the volumetric changes along processing. The

dimensions of the terminal samples decreased as the final H_2-reduction step was carried out from 300 ºC to 1300 ºC (Figure 1).

Preliminary screening of **Fe-temp** was conducted in terms of linear shrinkage, bulk density (ρ_b), skeletal density (ρ_s) and porosity (Π). Results are summarized in Table 1. Linear shrinkage increased monotonically with processing temperature from 53% in **Fe-300** to 77% in **Fe-1300**. The bulk density, however, first decreased between **Fe-300** and **Fe-400** from 0.74 g cm^{-3} to 0.44 g cm^{-3}, and then increased monotonically up to 3.78 g cm^{-3} in **Fe-1300**. As shown in Figure 2A, by ignoring **Fe-300** and **Fe-350** (points in red), Log ρ_b scales linearly with Log (100-% shrinkage) with a slope of $-3.0_7 \pm 0.2_8$, meaning that ρ_b scales linearly with the volume, which in turn points at a constant chemical composition from **Fe-400** to **Fe-1300**.

The skeletal density, ρ_s, of the solid framework of Fe-300 and Fe-350 was lower (4.57 g cm^{-3} and 5.05 g cm^{-3}, respectively) than that of samples Fe-400 and above, in which values were all $\geq$7.3 g cm^{-3} (refer to Table 1).

The fact that skeletal densities of **Fe-400** until **Fe-1300** were somewhat lower than the density of α-Fe (ρ_{Fe}=7.874 g cm^{-3}) could signify either incomplete reduction (i.e., presence of residual Fe_2O_3 at a level of $\leq$9% - by weighted average calculations), or presence of a very small amount of closed porosity along the skeletal framework (calculated at about 3% v/v via $100\times(\rho_s/\rho_{Fe})$). Based on XRD and thermogravimetric analysis data (see Section 2.2), presence of residual oxides at the level calculated here was excluded, leaving open the possibility for some low-level of closed porosity. On the other hand, the percent *open* porosity (Π), calculated via $\Pi=100\times(\rho_s-\rho_b)/\rho_s$, was generally quite high. At first, it increased slightly between **Fe-300** and **Fe-400** and then decreased

monotonically from 94% v/v (**Fe-400**) to 50% v/v (**Fe-1300** - Figure 2B). From **Fe-400** to **Fe-1300**, Π varied linearly versus ρ_b (Figure 2C), as expected from the rearranged relationship $\Pi/100=1-(1/\rho_s)\times\rho_b$, again signifying constant chemical composition, as already suggested by Figure 2A. From the slope of Figure 2C ($-0.130_6\pm0.001_6$ cm^3 g^{-1}) the overall average skeletal density was calculated at $\rho_s=7.6_3\pm0.1_2$ g cm^{-3}.

2.2. CHEMICAL AND THERMOGRAVIMETRIC CHARACTERIZATION OF NANOPOROUS Fe(0) AEROGELS - IMPLICATIONS FOR VARIABLE NETWORK REACTIVITY

The chemical makeup of the crystalline phases of the product from the final H_2-reduction step was investigated with X-ray diffraction. Only α-Fe could be identified above **Fe-400** (Figure 3). On the contrary, **Fe-300** contained only a very small amount of α-Fe, consisting mainly of Fe_2O_3 and Fe_3O_4 (63:37 mol/mol).[22]

All XRD spectra were totally clean of any residual crystalline carbon that might have been expected from the fact that Fe(0) is a known catalyst for low-temperature graphitization of C.[23-25] The absence of residual amorphous carbon was evaluated using thermogravimetric analysis (TGA) in O_2. Under those conditions, samples consisting only of Fe(0) should show a mass increase of 142.98% due to oxidation to Fe_2O_3. (Calculated via: Fe % w/w = % mass increase × $[2\times MW_{Fe}/MW_{Fe2O3}]$, *MW*: molecular weight.) At a heating rate of 10 ^oC min^{-1} (Figure 4A), that mass gain was reached (142.7-144.6%) by samples processed between 500 ^oC and 900 ^oC (solid lines in Figure 4A). Consequently, since all samples went through an identical 600 ^oC/air treatment, it was concluded that no sample contained any residual carbon. Therefore, discrepancies of certain samples from the theoretical level of mass gain should be attributed to other factors. Thus, TGA of **Fe-**

300 and **Fe-350** (dotted lines) showed significant amounts of oxide, consistent with XRD. **Fe-400** showed a mass increase of 141.2% w/w, which was consistent with incomplete reduction and the presence of 1.2% w/w Fe_2O_3 (below the detection limit at the attenuation level of the XRD spectrum of Figure 3). Interestingly, TGA at 10 $^oC\ min^{-1}$ of **Fe-950** and above (dashed lines) behaved as if those samples consisted of a progressively decreasing amount of Fe(0). Reducing the TGA heating rate to 5 $^oC\ min^{-1}$ (Figure 4B) restored a common level for the maximum mass increase at 142.1-142.3% w/w, which corresponds to 99.5-99.6% w/w of Fe(0). Those observations, considered together with the fact that as the final H_2-reduction temperature was increased the onset of oxidation in TGA moved progressively to higher temperatures (from less than 200 ^oC for **Fe-400** to over 600 ^oC for **Fe-1200** and **Fe-1300**, see Figure 4A) point to a kinetic effect in the oxidation of **Fe-temp** by air. That kinetic effect has to be attributed to the network morphology rather than the chemical composition of the samples, which was practically constant for all **Fe-400** and above. We see no reasons why that kinetic effect cannot be generalized to other oxidizing agents (e.g., perchlorates - Section 2.5).

2.3. NANOSCOPIC CHARACTERIZATION OF Fe(0) AEROGELS - THE NETWORK MORPHOLOGY AND THE POROUS STRUCTURE

SEM (Figure 5) shows that all samples consisted of particles. A rather profound increase in feature size is noted at around 950 ^oC. That is, starting from **Fe-950**, samples show clear evidence of massive melting-like fusion of particles along virtual strands of a classic pearl-necklace-like depiction of aerogels.[26] (Samples processed at 1400 ^oC were completely featureless and were not included in any further evaluation.) The sudden feature-size increase at around 950 ^oC coincides with the increased difficulty to oxidize

Fe(0) in TGA at 10 ^{o}C min^{-1} (Figure 4A), thereby the two events are related. Conversely, guided by the TGA-in-O_2 data, a second, albeit less profound, change seems to happen at around 400 ^{o}C. That is, although **Fe-400** was nearly oxide free, it looks more like **Fe-300** and **Fe-350**, which contained substantial amounts of oxides, and less like its chemically equivalent samples from **Fe-500** and above. From **Fe-500** to **Fe-900**, particle size seems to remain constant. The difference of **Fe-300** to **Fe-400** from **Fe-500** to **Fe-900** seems to be some particle coalescence through surface-like fusion (sintering).

A quantitative evaluation of those nanostructures in terms of pore and particle size was obtained with N_2 sorption porosimetry in combination with skeletal density data. Results are included in Table 1. N_2-Sorption porosimetry shows virtually no pores in the 1.7-300 nm range for any sample from **Fe-400** to **Fe-1300**, and therefore all open porosity, Π, was due to larger macropores. Samples **Fe-300** and **Fe-350** did have a low percentage of pores in the 1.7-300 nm range (refer to the $V_{>300\_nm}/V_{Total}$ column in Table 1). Surface areas, β, calculated using the BET equation, were in general low to begin with ($\leq$76 m^2 g^{-1}) and showed an overall downward trend as the processing temperature increased. That downward trend was not linear. We note two sudden drops in the surface area: one 14-fold decrease between **Fe-350** and **Fe-500**, and a second 23-fold drop between **Fe-900** and **Fe-1000**. Between **Fe-500** and **Fe-900**, surface areas remained about constant at around 5 m^2 g^{-1}. The two drops coincided with the temperature ranges of changing behavior in TGA and particle morphology in SEM as discussed above. BET surface areas were utilized to calculate average pore diameters via $4\times V_{Total}/\beta$, as well as particle diameters via $6/(\rho_s\beta)$. (The total specific pore volume was calculated via $V_{Total}=(1/\rho_b)-(1/\rho_s)$ – all values are included in Table 1.) Thus, each fast drop in β was reflected on a rapid increase in pore

and particle size. Figure 6 shows the particle size as a function of processing temperature. The step-increase in particle size in the 900-1000 ^{o}C range coincides with the melting-like fusion of particles observed in SEM, and the step-increase in the 300-500 ^{o}C range is consistent with surface-fusion of smaller particles as again noted qualitatively in SEM. Sintering and melting-like fusion render interparticle necks wider. Quantitative evidence for the latter was obtained from the elastic properties and the electrical conductivity of the network as a function of the processing temperature. Owing to instrumental constrains, reported elastic properties capture changes along melting-like fusion, while electrical conductivity captures changes along sintering at lower temperatures. From that perspective the two sets of data are complementary.

2.4. SINTERING AS A FUNCTION OF PROCESSING TEMPERATURE VIA MECHANICAL STRENGTH AND BULK ELECTRICAL CONDUCTIVITY DATA

The mechanical properties of **Fe-temp** were probed with quasi-static compression using either an Instron machine, or for weaker samples (those processed at lower final H_2-reduction temperatures) a Dynamic Mechanical Analyzer. As noted by the overall stress-strain curves (Figure 7A), samples could accommodate large deformations, showing short linear elastic ranges (Figure 7B) followed by yield behavior and inelastic hardening reminiscent of ductile aerogels (polymeric[27,28] and polymer-crosslinked[29,30]), whereas skeletal material is squeezed within the open porosity. The elastic modulus, *E*, was calculated from the slope of the early linear part of the stress-strain curves (Figure 7B). From **Fe-400** to **Fe-900**, *E* was low (in the 4.5-14 kPa range), but increased rapidly between **Fe-900** and **Fe-950** (Figure 7C). That rapid increase in stiffness coincided with the onset

of melting-like fusion observed in SEM, as well as the particle size increase calculated from the N_2 sorption data. From **Fe-950** and above, Log *E* varied about linearly with Log ρ_b (Figure 7D), and the slope (3.6±0.7) was in the range reported for mechanically strong polymer-crosslinked silica aerogels,[30] and other stiff all-polymer aerogels (e.g., certain polyurethanes).[27] The maximum *E* value (370 MPa) was attained by **Fe-1300**. Returning to Figure 7A, we note that as **Fe-temp** become stiffer their ability to carry loads increases, and the yield point (point of departure from the linear elastic behavior) moves to higher stresses.

The electrical conductivity, σ, was measured using a four-point probe (see Experimental). σ increased continuously with the processing temperature (Figure 8A) from 2.14 S m^{-1} in **Fe-300** to 1.59×10^5 S m^{-1} in **Fe-1000**. The latter value was just about two orders of magnitude within the conductivity of bulk iron (10^7 S m^{-1} – shown by a doted horizontal line in Figure 8A). (**Fe-1100** and above were beyond the range of our four-point probe.) The increase of σ with the final H_2-reduction temperature did not take place in a simple fashion. We note two areas of rapid increase: one at around 400 ^oC, i.e., as the material turned from a mixture of Fe(0) and oxides to pure Fe(0), and a second one at around 700-800 ^oC. As a result, σ did not follow a simple relationship with bulk density (Figure 8B), or the particle size (Figure 8C). Specifically, in the 500-800 ^oC range, σ increased by approximately 3-orders of magnitude for a nominal increase in density just by a factor of 1.15×, and for a small increase in particle size (from 151 nm to 194 nm). Beyond that and between **Fe-700** and **Fe-1000**, σ followed an exponential relationship with ρ_b of the type $\sigma = 1.26\times10^4(\rho_b)^{1.55\pm0.12}$ (R^2=0.977). The exponent of ρ_b was equal to that

found for carbon aerogels derived from resorcinol-formaldehyde aerogels (1.5),[31] pointing again, like *E* above, to an aerogel-like skeletal interconnectivity. Overall, the step-wise conductivity increase is consistent with particle sintering, which starts at around 500 ^{o}C and is followed by melting-like fusion in agreement with SEM and N_2 sorption data.

2.5. LOADING WITH PERCHLORATES AND IGNITION

Samples were loaded with perchlorates ($LiClO_4$, $NaClO_4$ or $KClO_4$) by filling the pores with saturated acetone solutions of the salts followed by extensive drying (see Experimental). Owing to its higher solubility in acetone (0.427 mol mol^{-1})[32] and its low melting point (236 ^{o}C), use of $LiClO_4$ would ensure stoichiometric loading of the pores with the salt and wetting of the iron framework well before the ignition point. At the other extreme, $KClO_4$ (m.p.=610 ^{o}C) is practically insoluble in all common solvents, hence the actual loading of the Fe(0) monoliths with that salt was very low. $NaClO_4$ (solubility in acetone: 0.197 mol mol^{-1};[32] m.p.=468 ^{o}C) presents an intermediate situation. Reportedly, the solid-state reaction of Fe(0) and $KClO_4$ yields FeO.[33] The stoichiometric Fe(0):perchlorate mol/mol ratio for that reaction is equal to 4 (eq 1). In addition, ignition of certain samples yielded Fe_3O_4 as well as Fe_2O_3. Should those oxides have come from direct reaction of iron with the perchlorate (eqs 2 and 3), the required amount of the latter should be higher than what is needed for FeO, and the Fe(0):perchlorate mol/mol ratio

$$4\ Fe + LiClO_4 \longrightarrow 4\ FeO + LiCl \quad (1)$$

$$12\ Fe + 4\ LiClO_4 \longrightarrow 4\ Fe_3O_4 + 4\ LiCl \quad (2)$$

$$8\ Fe + 3\ LiClO_4 \longrightarrow 4\ Fe_2O_3 + 3\ LiCl \quad (3)$$

decreases to 3 and 2.7, respectively. The amount of the perchlorate in each sample was quantified gravimetrically (see Table S.1 in the Supporting Information). With the exception of lower-porosity samples (**Fe-900** and above), the amount of $LiClO_4$ was generally sufficient for all three possibilities: the Fe(0):perchlorate mol/mol ratio varied between 1.8 and 3.0, while for **Fe-900** and above it generally fluctuated in the 4-6 range. In the cases of $NaClO_4$ and $KClO_4$, the amount of the salt was always lower than the stoichiometric amount. With $KClO_4$ in particular, the amount of the salt was extremely low (e.g., **Fe-600**:$KClO_4$=162 mol/mol and **Fe-1000**:$KClO_4$=314 mol/mol).

Samples (about 0.2 g) of perchlorate-loaded **Fe-temp** monoliths were placed in open vials and were ignited with a Bunsen burner placed underneath. Most experimentation was conducted with $LiClO_4$. In that regard, selected $LiClO_4$ samples were also ignited in: (a) evacuated flame-sealed glass test tubes; (b) glass test tubes flame-sealed under 1 atm of N_2; and, (c) a bomb-calorimeter (BC) with an electric resistor. Whenever possible (see below), the residue after ignition was collected and was analyzed with XRD. Product distributions, results from quantitative phase analysis and thermochemical calculations are cited in Table S.1. Movies of most samples ignited in the open air, in evaluated tubes and in tubes sealed under N_2 are also provided in Supporting Information. Video frames at the precise moment of ignition from most experiments are shown in Figures 9 and 10.

2.5.1. Ignition of $LiClO_4$-Loaded Samples. In open air Fe-400 (and below) fizzled out; the fireball was confined within the vial (Figure 9 and Movies S.AIR.1 to S.AIR.8). **Fe-500** demonstrated a relatively weak explosive behavior, while ignition of **Fe-600** and **Fe-700** produced violent explosions with extremely bright flashes (Figure 9) and a very loud noise. **Fe-800** also exploded, but the intensity of the phenomenon was

noticeably diminished. The behavior of **Fe-900** to **Fe-1200** could not be characterized as explosive: the "fireball" was getting progressively smaller, yet remained larger than the actual samples. **Fe-1300** simply glowed red. Although explosions of **Fe-600** to **Fe-800** shuttered and destroyed the vials, fragments could still be recovered and residues were analyzed with XRD as mentioned above. **Fe-900** to **Fe-1300** monoliths remained monolithic.

Ignition under vacuum, even of samples that in open-air exploded (i.e., **Fe-500** to **Fe-800**), produced bright optical effects, but no explosions (Figure 9 and Movies S.VAC.1 to S.VAC.5). The sealed glass ampules remained intact and had to be broken in order to recover samples for XRD analysis. On the other hand, ignition in glass ampules sealed under N_2, even of samples that contained significant amounts of oxides (e.g., **Fe-350**), produced extremely violent explosions (Movie S.N2.1). Ampules were pulverized completely, and no fragments could be recovered for product identification.

As shown in Table S.1, whenever ignition was conducted under inert conditions (i.e., under vacuum or in the BC, cases of **Fe-700** and **Fe-800**) the extent of the reaction and the product distribution were similar. The main iron product was FeO (eq 1).[33] On the other hand, in the open air the residue after ignition included significant amounts of Fe_3O_4 together, in some instances, with Fe_2O_3. Considering together the product distributions from those three modes of ignition points to participation of air in the combustion process via, for example, eqs 4 and 5.[7] Thus, the mol fraction of Fe(0) that reacted in samples ignited in air cannot be used as an estimate of the efficiency of the reaction with $LiClO_4$.

$$3\ FeO + \tfrac{1}{2}\ O_2 \longrightarrow Fe_3O_4 \qquad (4)$$

$$2\ Fe_3O_4 + \tfrac{1}{2}\ O_2 \longrightarrow Fe_3O_4 \qquad (5)$$

The amount of heat released from the reaction was calculated based on the product distribution. There was an excellent agreement between the calculated and experimental values obtained with the BC. For example, ignition of **Fe-700** in the BC gave a clean reaction to FeO, whereas the experimental heat release was 58.3 kcal mol^{-1} of Fe(0) reacted, versus a theoretically expected value of 66.64 kcal mol^{-1}.[34] Similarly, ignition of **Fe-600** in the BC gave a small amount of Fe_2O_3 along FeO (FeO:Fe_2O_3 = 13.8 mol/mol); the theoretical heat release was 71.1 kcal per mol of Fe(0) reacted, and the experimental value was 60.1 kcal mol^{-1}. By the same token, the calculated heat release values from ignition in the open air were higher than the values measured in the BC, due to the parallel production of Fe_3O_4 and Fe_2O_3, whose heats of formation per iron atom (89 kcal mol^{-1} and 98.5 kcal mol^{-1}, respectively) are higher than the heat of formation of FeO (65 kcal mol^{-1}). Hence, the heat released in the BC was taken as the lower limit for the possible heat release from ignition of our nanoporous iron samples with $LiClO_4$.

The absence of any explosive behavior from **Fe-500** to **Fe-800** ignited under vacuum confirms that **Fe-temp** do not produce gases (e.g., from traces or unreacted C) and supports our previous conjecture,[17] whereas explosive behavior was attributed to rapid heating and expansion of air confined in nanoporous space. The need for O_2 for the explosive behavior, or to put it differently, whether the heat produced by the reaction of Fe(0) with $LiClO_4$ alone was sufficient to cause explosive behavior, was inferred by igniting samples in tubes sealed under N_2. As stated above, that produced extremely powerful explosions (Movie S.N2.1). Hence, the heat release from the reaction of Fe(0) with $LiClO_4$ was indeed sufficient to heat and expand the pore filling gas resulting to an explosive effect.

2.5.2. Ignition with $NaClO_4$ and $KClO_4$. Selected Fe-temp samples (Fe-400, Fe-600 and Fe-1000) containing those salts were ignited in air. Figure 10 captures the moment of ignition from Movies S.Na.1-3 and Movies S.K.1-3. None of the samples exploded. $NaClO_4$-loaded **Fe-400** and **Fe-600** produced sprays of sparks; **Fe-1000** produced a similar behavior to its $LiClO_4$-loaded counterpart. With $KClO_4$ the overall trend was the same, but effects were weaker. The behavior of **Fe-1000** was close to a thermite. Except **Fe-400** with $NaClO_4$, the residue contained large quantities of unreacted iron whose percentage increases as the mol ratio of the perchlorate decreases. Except **Fe-400** with $KClO_4$, whereas the product was only FeO, in all other cases the residue consisted only of Fe_2O_3 and Fe_3O_4. The iron:perchlorate mol ratio was always sub-stoichiometric even for the formation of FeO (that requires the least amount of perchlorate). As discussed above, in some cases the Fe:perchlorate ratio was extremely high (Table S.1). Thereby, conversions and product distributions as those observed herewith can only be justified by air participation in the combustion process (eqs 4 and 5). No further attempt was made along this study for higher loading with those salts, and discussion of the explosive versus thermite behavior focuses on the $LiClO_4$-loaded samples.

2.6. THE FACTORS CONTROLLING EXPLOSIVE VERSUS THERMITE BEHAVIOR

In most experiments ignition was carried out with a flame whereas temperature reaches levels above the melting points of all three perchlorates, thereby in all three cases the reaction was assumed to be solid-liquid rather than solid-solid. The necessary condition for explosive behavior is undoubtedly that nanopores must be filled with a gas that is heated by the reaction of the iron matrix with the filler: evacuated samples did not explode and

further confinement in tubes sealed under N_2 intensified the explosion. Although the most intense effects were obtained with $LiClO_4$, a parallel trend was noted with $NaClO_4$ and $KClO_4$, but the effects were greatly diminished. The latter is attributed to the sub-stoichiometric amount of perchlorate. Focusing on $LiClO_4$, pores filled with a gas was a necessary, but not a sufficient condition for explosive behavior. That is, even though **Fe-400** and **Fe-500** had similar or higher porosities than **Fe-600** to **Fe-800**, either they did not explore as violently (**Fe-500**), or fizzled out (**Fe-400**). Other factors had to be at work. Thus, turning to the skeletal framework, we noted that successive switching from fizzling to explosive to thermite behavior took place along abrupt particle size increases associated with surface sintering (in the 400 ^oC to 500 ^oC range) and melting-like fusion (above 950 ^oC). Those phenomena were supported by a parallel abrupt increase in electrical conductivity, but most importantly in mechanical strength. The latter was investigated under compression and it was found that **Fe-temp** demonstrated yield behavior similar to that of ductile (polymeric) aerogels. The stress at the yield point increased with the final H_2-reduction temperature. Although compression (Figure 7) is the opposite of outward expansion, yield points along the stress-strain curves of Figure 7A express a fundamental material property and can also serve as a guide for the behavior under internal pressure. Thus, it is noted that the pressure expected to develop inside monoliths by isochoric/adiabatic heating of the pore-filling gas by the iron/perchlorate reaction was on the order of 35 atm (around 3.5 MPa).[35] Semi-quantitatively, the yield point of samples that did not explode was generally above that pressure level. At this point, considering all data together suggests that once pores are filled with gas, fizzling versus explosive versus thermite behavior is primarily controlled by the strength of the Fe(0) framework, which in

turn is controlled by sintering that takes place in two stages: one at the onset of explosive behavior and one at the onset of thermite behavior. For explosive behavior the framework has to be strong enough to contain hot gasses long enough for high pressure to build up before it fails catastrophically. If the framework is not strong enough (at the onset of sintering, samples **Fe-400** and below) failure starts early and samples fizzle out. At the other end, if the network is strengthened by melting-like fusion of skeletal nanoparticles, we observe only a fireball of hot gas escaping from the monolith - no explosions. Clean thermite behavior –no fireball– was observed only with **Fe-1300**. It is plausible that a combination of reduced porosity (50% v/v in **Fe-1300** versus 69% v/v in **Fe-1200**, Table 1), a substantially sub-stoichiometric amount of $LiClO_4$ ($[Fe:LiClO_4]_{\mathbf{Fe\text{-}1300}}$=12.8 mol/mol, Table S.1) and a slower heat release rate (via a slower rate of oxidation – in line with conclusions from the TGA-in-O_2 data of Figure 4A) are all additional contributing factors towards the clean thermite behavior of **Fe-1300**.

3. CONCLUSIONS AND OUTLOOK

Monolithic nanoporous iron aerogels were prepared via carbothermal reduction of interpenetrating networks of polybenzoxazine-iron oxide nanoparticles (PBO-FeOx). The PBO network plays the role of a hard-sacrificial template. Excess unreacted carbon was burned off at 600 ^oC in air. That process partially oxidizes the Fe(0) network. Reduction of oxides back to Fe(0) was carried out with H_2 at different temperatures varying from 300 ^oC to 1300 ^oC. The temperature of the final H_2-reduction step had an annealing effect on the iron framework, thereby upon ignition of samples loaded with stoichiometric amounts of $LiClO_4$ fizzled out, exploded or presented thermite behavior depending mainly on the

mechanical strength of said network. Although explosion by fast heating and expansion of gas confined in nanoporous space is novel and quite impressive, we do not loose sight of the fact that our original objective was thermites, not explosives. Near thermite behavior was demonstrated by **Fe-900** to **Fe-1200** and clean thermite behavior was demonstrated only by **Fe-1300**. What we learned from those samples is that for thermite behavior, higher surface areas and higher porosities are not real advantages. More sturdy, slower-reacting networks associated with lower porosities and thicker skeletal walls from melting-like fusion of skeletal nanoparticles are definitely more desirable. However, that renders filling pores with the necessary amount of perchlorate more difficult. That issue could be addressed by filling monoliths via massive in-place deposition of the salt. The latter almost dictates revisiting $KClO_4$ by taking advantage of its low solubility. In one such approach, $KClO_4$ could be precipitated *in situ* within the pores from KCl and $LiClO_4$. In another approach, "annealing" of the network could be enforced, sort-of-speak, before carbothermal reduction by pyrolyzing compacts of interpenetrating PBO-FeOx aerogels. That method will eliminate most of the porosity of the parent aerogel, thus loading with perchlorate will take place within the empty space that will be created from the carbothermal reduction between carbon and the iron oxide network. This work serves as the point of departure for all those possibilities, several of which are under current investigation.

4. EXPERIMENTAL

4.1. MATERIALS

All reagents and solvents were used as received unless otherwise noted. Iron chloride hexahydrate ($FeCl_3.6H_2O$), paraformaldehyde (96%), aniline, and 4,4'-isopropylidenediphenol (bisphenol A) were obtained from Acros Organics. Dimethylformamide (DMF) and epichlorohydrin were obtained from Sigma-Aldrich. Anhydrous lithium perchlorate was obtained from GFS Chemicals, anhydrous potassium perchlorate was obtained from Fluka Chemika and sodium perchlorate was obtained from Fisher Scientific. Ultra-high purity argon (99.99999%), hydrogen (99.9999%) and compressed air were purchased from either Airgas Co. or Ozark Gas (both of Rolla, MO). Benzoxazine monomer (BO monomer) was synthesized via a modification of literature procedures.[12-16]

4.2. PREPARATION OF POLYBENZOXAZINE-IRON OXIDE INTERPENETRATING NETWORKS (PBO-FeOX AEROGELS)

Solution A was prepared by dissolving 1 g (2.16 mmol) of purified BO monomer in 4.23 mL (4 g) DMF. Solution B was prepared by first dissolving (with ultra-sonication) 2.30 g (8.52 mmol) of iron chloride hexahydrate in 3 mL (2.8 g) DMF, and then adding 2.06 mL (25.56 mmol) of epichlorohydrin. Upon addition of epichlorohydrin, Solution B was immediately added to Solution A waiting in a round bottom flask, the resulting sol was stirred magnetically for 5 min at room temperature and then was poured in 10 mL portions into polypropylene jars (Fisherbrand, part no. 02-912-025, 1.5 inch in diameter), which were screw-capped and placed in an oven at 80 ^{o}C. Gelation took place in 15-20 min. Wet-

gels were aged in their molds at 80 ^{o}C for 2 days. Subsequently, wet-gels were removed from the molds and washed with DMF (2×12 h), followed with DMF:acetone (50:50 v/v, 2×12 h) and finally with pure acetone (4×12 h). Acetone-filled wet-gels were dried in an autoclave with liquid CO_2 that was removed at the end as a supercritical fluid (SCF). The resulting aerogels are referred to as **PBO-FeOx** and were step-cured in air at 160 ^{o}C for 1 h, then at 180 ^{o}C for 1 h, and finally at 200 ^{o}C for 24 h. The resulting materials are referred to as **PBO-FeOx-200**.

4.3. CONVERSION OF PBO-FeOX-200 AEROGELS INTO Fe(0) AEROGELS (Fe-TEMP)

PBO-FeOx-200 aerogels were transferred to a MTI GSL1600X-80 tube furnace (alumina 99.8%, 72 mm and 80 mm inner and outer diameters, respectively, with a 457 mm heating zone), which was flushed with ultra-high purity Ar for 1h (300 mL min^{-1}). Subsequently, the temperature of the furnace was raised to 800 ^{o}C at 5 ^{o}C min^{-1} and was maintained there for 5 h under a 150 mL min^{-1} flow of ultra-high purity Ar. At the end of the period, the temperature was first lowered to 600 ^{o}C at 5 ^{o}C min^{-1}, then the flowing gas was switched to air (at 150 mL min^{-1}) and the new conditions were maintained for 20 min at 600 ^{o}C. Subsequently, the temperature was changed at 5 ^{o}C min^{-1} under constant flow of Ar (150 mL min^{-1}) to various terminal values ranging from 300 ^{o}C to 1300 ^{o}C. Then the flowing gas was switched to H_2 and the flow (150 mL min^{-1}) was maintained for 5 h at constant temperature. At the end, the tube furnace was cooled down to room temperature at 5 ^{o}C min^{-1} under continuous flow of H_2. Those samples are referred to as **Fe-temp** (**temp**: 300-1300).

4.4. METHODS

Drying with SCF CO_2 was conducted in an autoclave (Spe-ed SFE system, Applied Separations, Allentown, PA). Bulk densities (ρ_b) were calculated from the weight and the physical dimensions of the samples. Skeletal densities (ρ_s) were determined with helium pycnometry using a Micromeritics AccuPyc II 1340 instrument. Porosities (Π) as percent of empty space were determined from the ρ_b and ρ_s values via $\Pi = 100 \times [(\rho_s - \rho_b)/\rho_s]$.

4.4.1. Thermogravimetric Analysis (TGA). That was conducted in an O_2 atmosphere with a TA Instruments Model TGA Q50 Thermogravimetric Analyzer, using a heating rate of either 10 $^oC\ min^{-1}$ or 5 $^oC\ min^{-1}$.

4.4.2. Chemical Characterization. That was conducted with powder X-ray diffraction (XRD) using a PANalytical X'Pert Pro multipurpose diffractometer with Cu Kα radiation (λ = 1.54 Å) and a proportional counter detector equipped with a flat graphite monochromator. Phase composition was estimated via Rietveld refinement of the X-ray diffraction patterns utilizing RIQAS software (Materials Data, Inc., version 4.0.0.26).[36] Structural information for each phase was obtained from the ICSD database version 2.01. A Gaussian correction for instrumental broadening was applied utilizing NIST SRM 660a LaB_6 to determine the instrumental broadening.

4.4.3. Visualization of the Skeletal Framework. That was carried out with scanning electron microscopy (SEM) using Au-coated samples on a Hitachi Model S-4700 field-emission microscope.

4.4.4. N_2-Sorption Porosimetry. That was conducted with a Micromeritics ASAP 2020 surface area and porosity analyzer. Surface areas, β, were obtained using the Brunauer-Emmett-Teller (BET) equation. Samples for porosimetry and skeletal density

determination were outgassed under vacuum for 24 h at 80 ^{o}C. Average pore diameters were determined with the $4\times V_{Total}/\beta$ method, where the total pore volume per gram was calculated via $V_{Total} = (1/\rho_b)–(1/\rho_s)$.

4.4.5. Mechanical Characterization. Mechanical testing under quasi-static compression of **Fe-950**, **Fe-1000**, **Fe-1100**, **Fe-1200** and **Fe-1300** was conducted with an Instron 3369 universal testing machine at a strain rate of 2.5 mm/mim, using a 50 kN load cell following a testing procedure in the spirit of ASTM D1621-04a (Standard Test Method for Compressive Properties of Rigid Cellular Plastics). In order to achieve a surface roughness within few μm and ensure that specimens would have no surface scratches and cracks that could act as stress concentrators that might cause premature failure compromising the reliability and reproducibility of the data, both surfaces of the samples were polished with a 3M surface smoothing sand paper (320 grit, part No. 98401). Typical specimen dimensions ranged from 1.00 cm to 1.38 cm in diameter and from 0.30 cm to 0.45 cm in height. The recorded force as a function of displacement (machine-compliance corrected) was converted to stress as a function of strain. The mechanical properties of four samples (**Fe-400**, **Fe-600**, **Fe-800** and **Fe-900)** were determined with a TA Instruments Model Q800 Dynamic Mechanical Analyzer in a controlled force/strain mode using a submersion compression clamp (TA Instruments Part Number 985067.901), which is useful for testing low to medium modulus samples. The experiment was conducted with a force ramp of 1 N min^{-1} (preload force = 0.01 N) up to a maximum of 18 N and typical specimen dimensions of these aerogels for testing were about 10 mm in diameter, 3.5 mm thick.

4.4.6. Electrical Conductivity (σ). That was measured using a four-point-probe conductivity instrument consisting of an Alessi CPS-06 Contact Probe Station with a four point probe head, a Keithley Model 220 programmable current source, and a Model 181 nanovoltmeter. The reliability of the measurements was confirmed with commercially available silicon wafers and indium-tin oxide films of known sheet resistance. The conductivity was calculated via Conductivity = 1/Resistivity, where Resistivity = $2\pi \times s \times T_1(t/s) \times C_o(d/s) \times (V/I)$, where s is the distance between electrodes in the probe (0.1588 cm), and $T_1(t/s)$ and $C_o(d/s)$ are geometric correction factors due to the finite thickness (t) and diameter (d) of the samples.[37,38] For example, for t = 0.428 cm and d = 1. 386 cm, (t/s) = 2.70 and (d/s) = 8.73, and $T_1(t/s)$ = 0.9596, and $C_o(d/s)$ = 0.9059. The surface of the aerogel samples was smoothened for electrical conductivity measurements using the 3M surface smoothing sand paper (320 grit, part No. 98401) and debris was blown off with dry N_2.

4.4.7. Loading with Perchlorates and Ignition. Saturated solutions of anhydrous $LiClO_4$, $KClO_4$ and $NaClO_4$ were prepared in dry acetone. **Fe-temp** monoliths were placed in those acetone solutions for 24 h and were infiltrated with capillary action. Subsequently, wet monoliths were rinsed briefly with acetone and left in a fume hood to dry for 12 h. At the end of that period, samples were placed in a vacuum oven at 80 ^oC until they were used for ignition experiments, at least two days later or longer. The amount of perchlorate was determined gravimetrically in the dry samples. For ignition in the open air, approximately 0.2 g of perchlorate-loaded samples were placed in 5 mL vials and were heated with a Bunsen burner underneath. This procedure was followed with all $LiClO_4$-loaded **Fe-temp** aerogels, and with **Fe-400, Fe-600** and **Fe-1000** aerogels loaded with

either $NaClO_4$ or $KClO_4$. For ignition under vacuum or under N_2, approximately 0.2 g of selected $LiClO_4$-loaded samples (**Fe-600, Fe-700, Fe-800** and **Fe-950**) were placed in test tubes (Pyrex^{TM}, 1 cm diameter), necks were created to those tubes close to their open ends using a hot natural gas-O_2 flame, and the tubes with elongated necks and samples trapped inside were fixed on a vacuum line. When the pressure reached 50 mTorr, tubes were sealed under vacuum at their necks with the gas-O_2 flame. Alternatively, the vacuum line was back-filled with N_2 and re-evacuated three times, before it was backfilled with N_2 and tubes were sealed with the gas-O_2 flame under N_2. All precautions under the Safety Warning above, apply.

4.4.8. Calorimetry. The enthalpy of the reaction of $LiClO_4$-loaded Fe-600, Fe-700 and **Fe-800** was measured using a 400 mL bomb calorimeter (BC, Parr Instrument Company, Model 1672 Thermometer). The heat capacity of the calorimeter was measured using benzoic acid as standard. Each sample (approximately 1.5 g) was ignited with a nichrome fuse wire connected to the terminal socket on the apparatus head, which in turn was connected to the power supply (ignition unit). The heat released by the fuse was also taken into consideration in the calculations. After each experiment, the residue was collected and analyzed with XRD for the fraction of iron reacted and the distribution of the iron products.

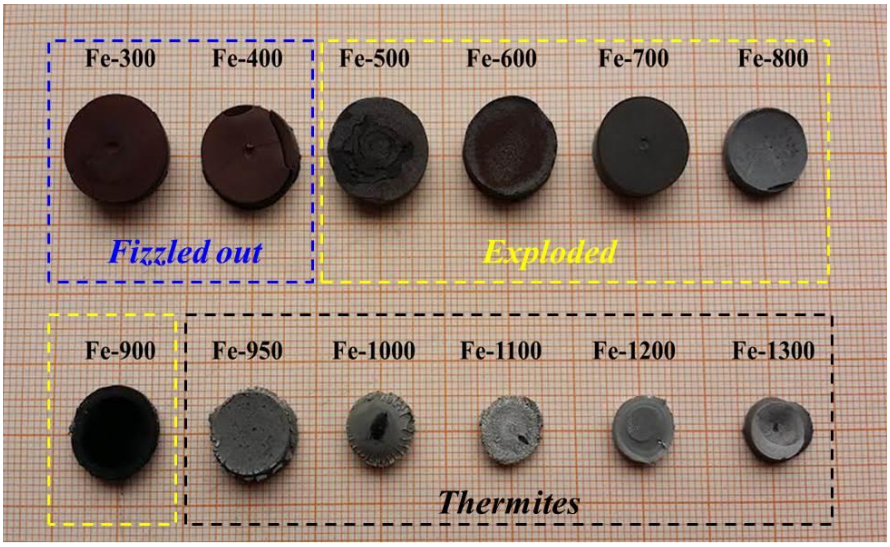

Figure 1. Nanoporous Fe(0) aerogels processed at different final H_2-reduction temperatures (see Scheme 1). Dashed colored lines group samples that when loaded with $LiClO_4$ and ignited (Figure 9) fizzled out, exploded or demonstrated thermite behavior. For relative sizes along synthesis, cross-reference with photographs in Scheme 1.

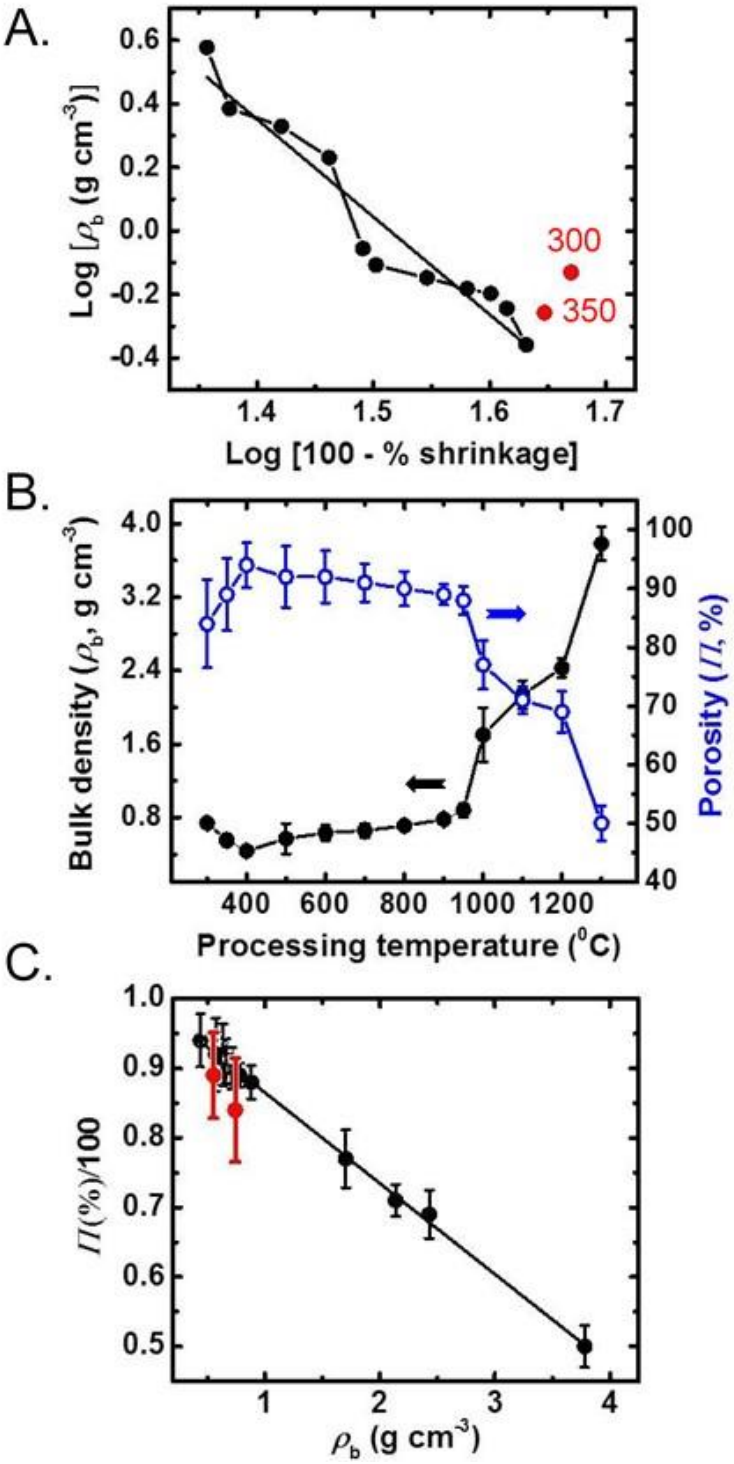

Figure 2. Correlation of basic material properties of **Fe-temp** (bulk density, ρ_b, shrinkage and porosity, Π) as a fuction of the processing temperature (**temp**) at the final H_2-reduction step.

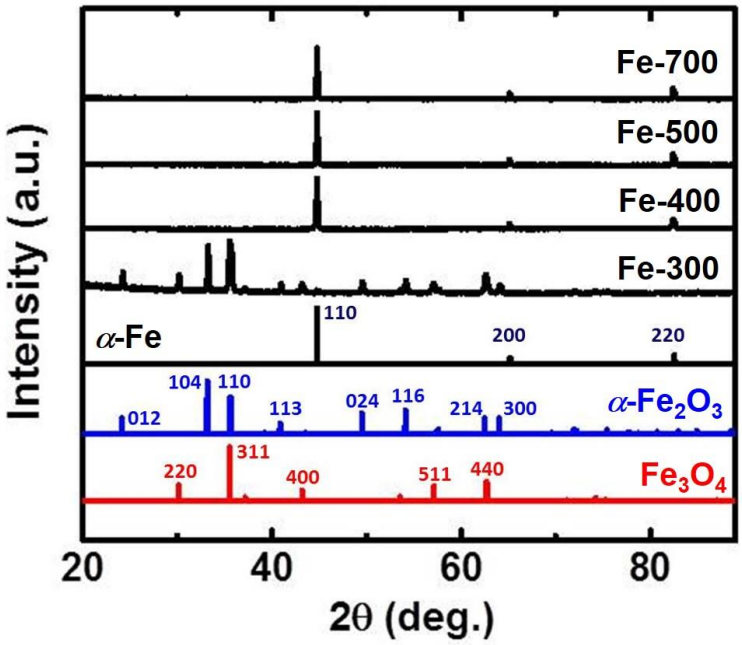

Figure 3. XRD of samples as shown. For samples **Fe-400** and above, only one crystalline phase could be identified, that of α-Fe. Quantitative phase analysis of the **Fe-300** sample gave Fe_2O_3:Fe_3O_4 (63:37 mol/mol).

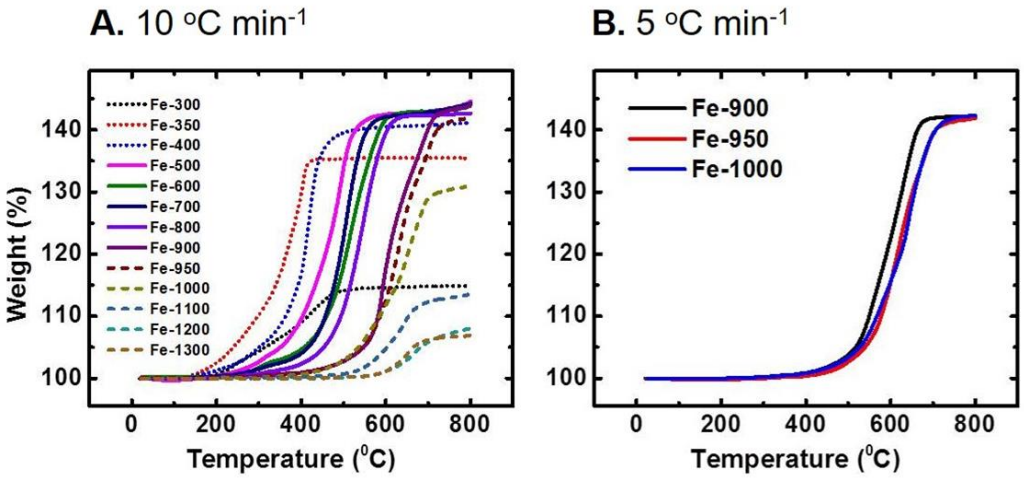

Figure 4. Thermogravimetric analysis (TGA) in an O_2 atmosphere of **Fe-temp** as indicated. (a). Heating rate: 10 °C min^{-1}; (b). Heating rate: 5 °C min^{-1}.

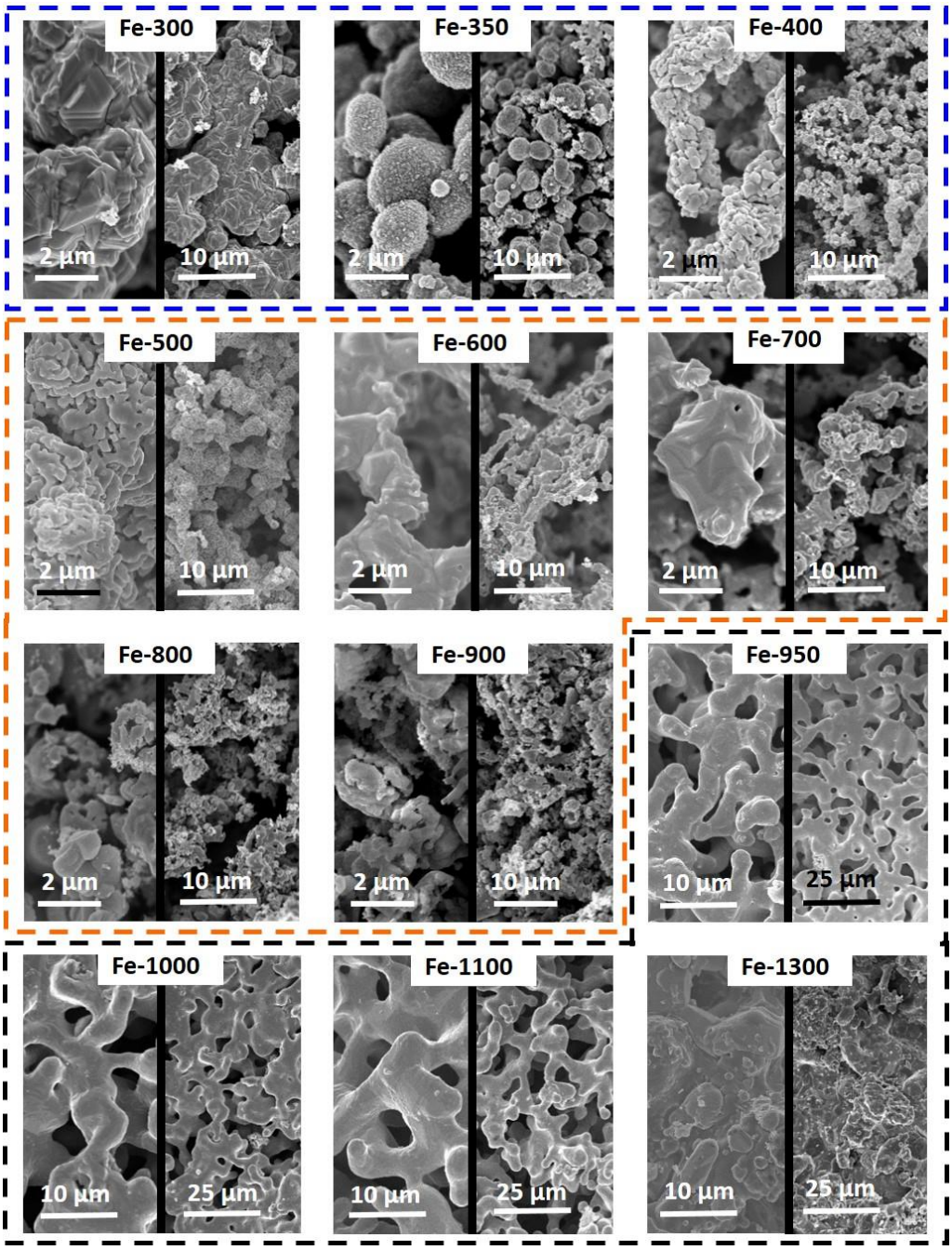

Figure 5. SEM at two different magnifications of samples as indicated. With reference to Figure 1, colored dashed lines group samples that when loaded with $LiClO_4$ and ignited (Figure 9) fizzled out (blue), exploded (orange) or demonstrated thermite behavior (black).

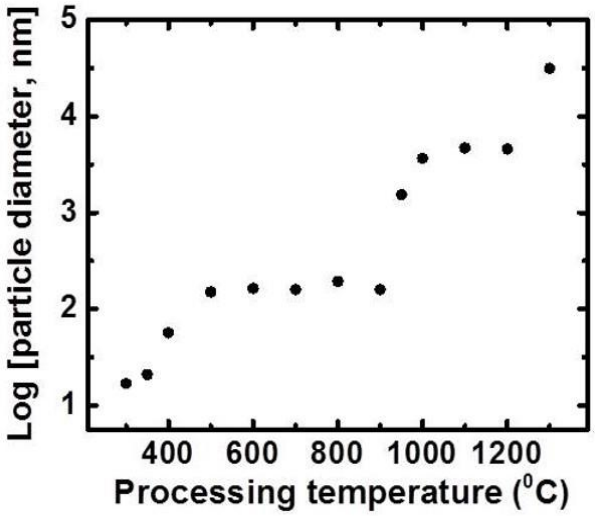

Figure 6. Particle diameters (d) calculated from BET surface areas (β) and skeletal density (ρ_s) data via $d=6/(\rho_s \times \beta)$ as a function of processing temperature at the final H_2-reduction step.

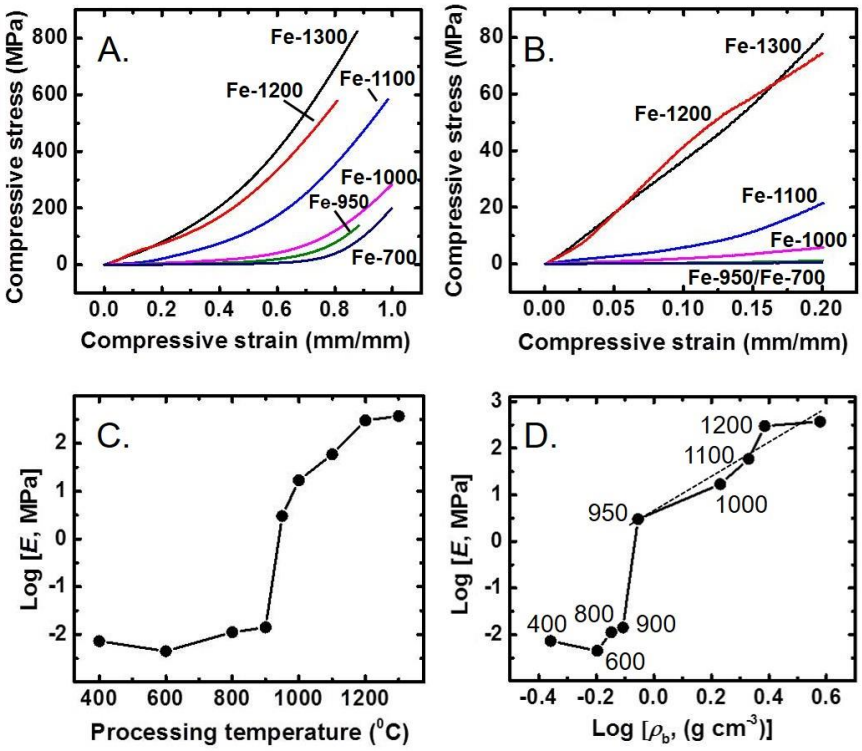

Figure 7. (a). Stress-strain curves under quasi-static compression of samples as indicated. (b). Magnification of the lower-strain part of the curves in (a). (c). Young's modulus, E, as a function of processing temperature. (For the fitted dashed straight line refer to the text.) (d). Young's modulus as a function of bulk density.

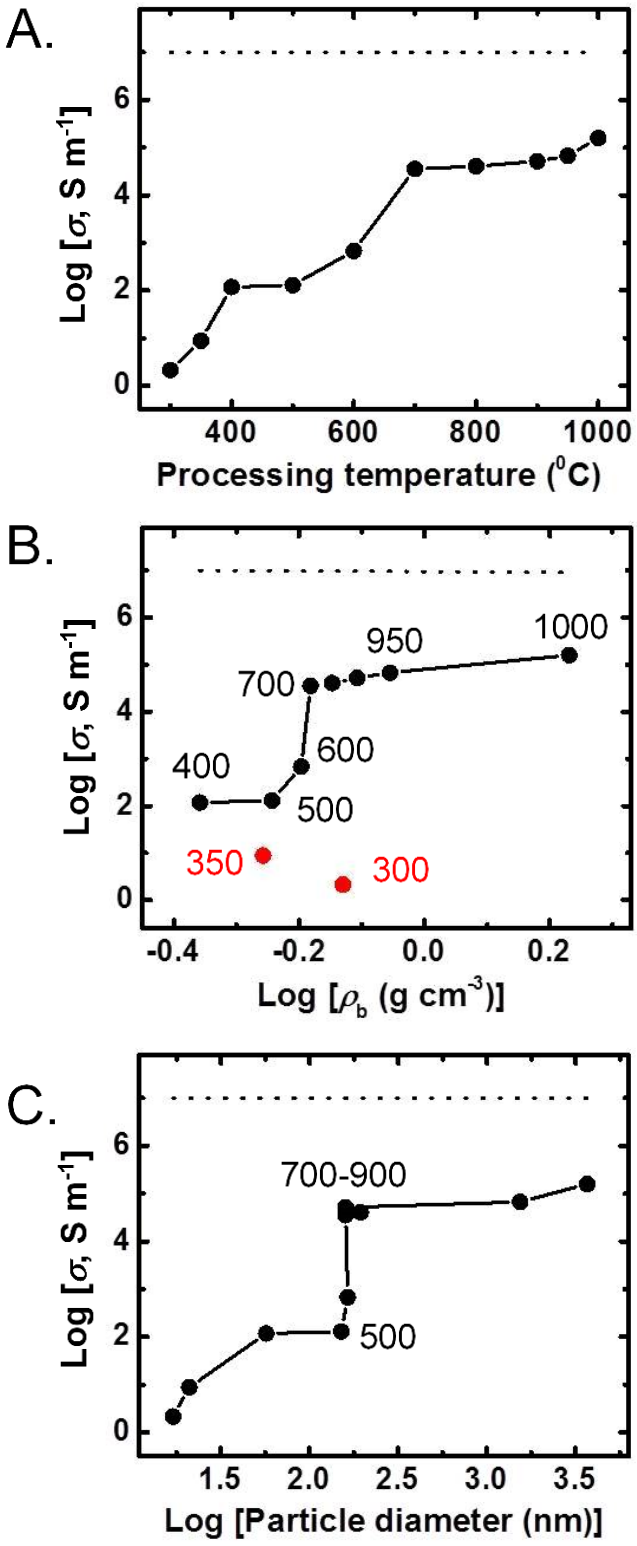

Figure 8. Electrical conductivity (σ, in Siemens (S) per meter) as a function of various parameters as indicated. The horizontal dotted line on top marks the electrical conductivity of pure dense iron.

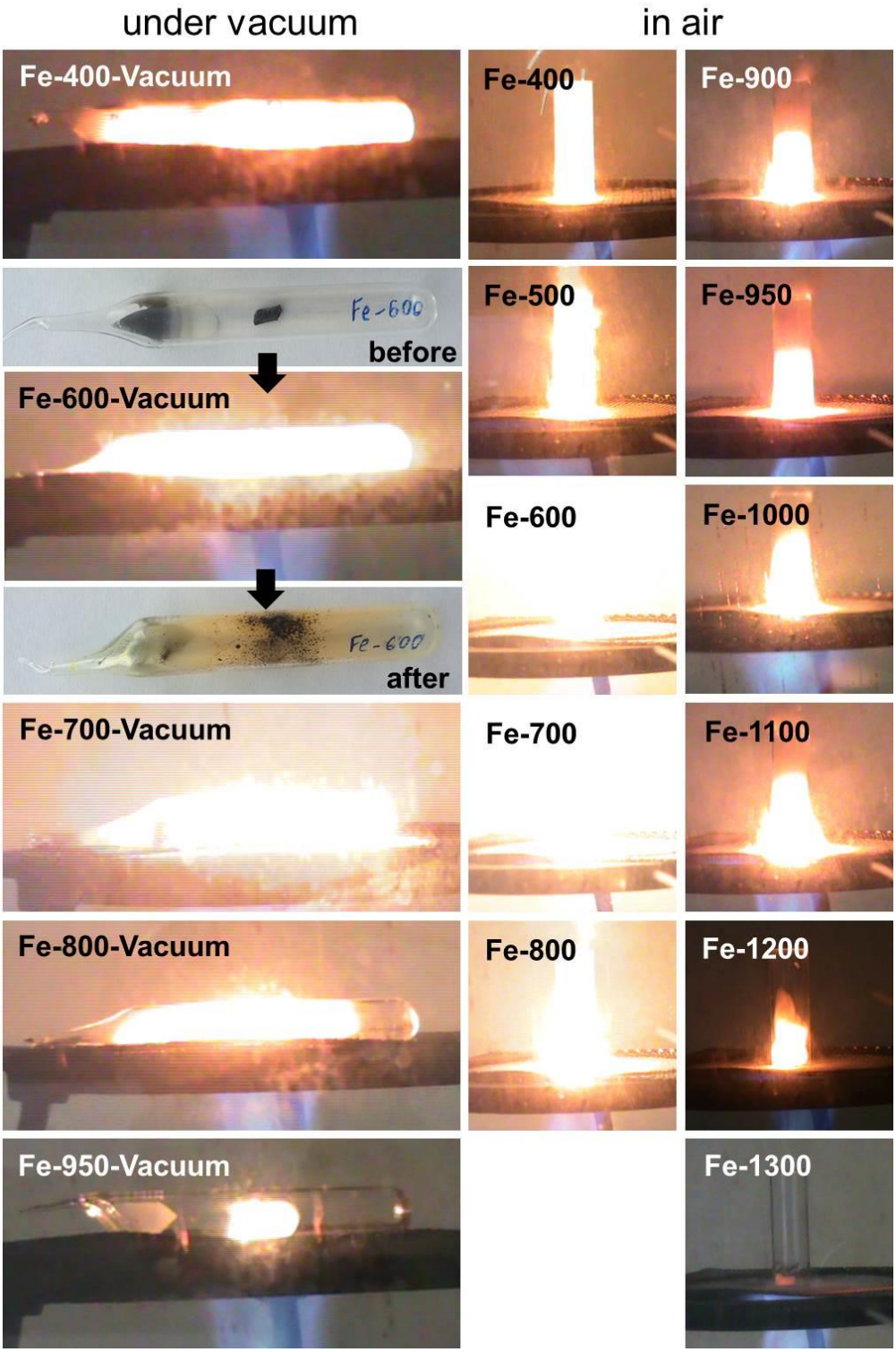

Figure 9. Moment of ignition with a flame of $LiClO_4$-loaded **Fe-temp** samples. Pictures are frames from the videos given in Supporting Information. (Photographs of evacuated ampules with **Fe-600** inside before and after ignition are also included for reference).

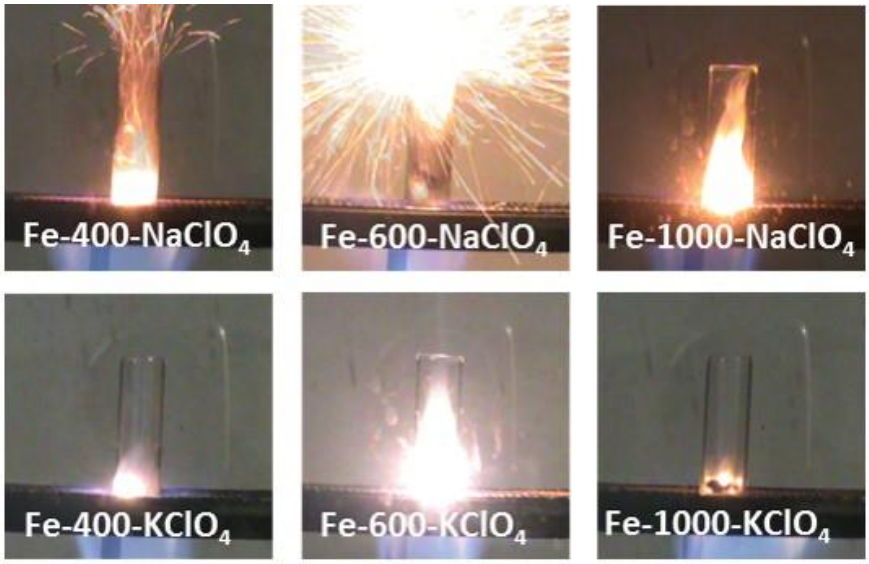

Figure 10. Moment of ignition with a flame in open air of $NaClO_4$ and $KClO_4$-loaded **Fe-temp** samples (refer to Movies S.Na-1-3 and S.K.1-3 in Supporting Information).

A. Formation of the FeOx network

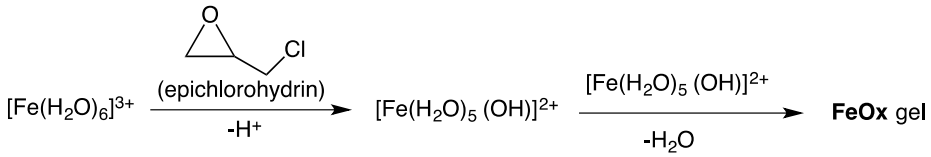

B. Formation of the PBO network

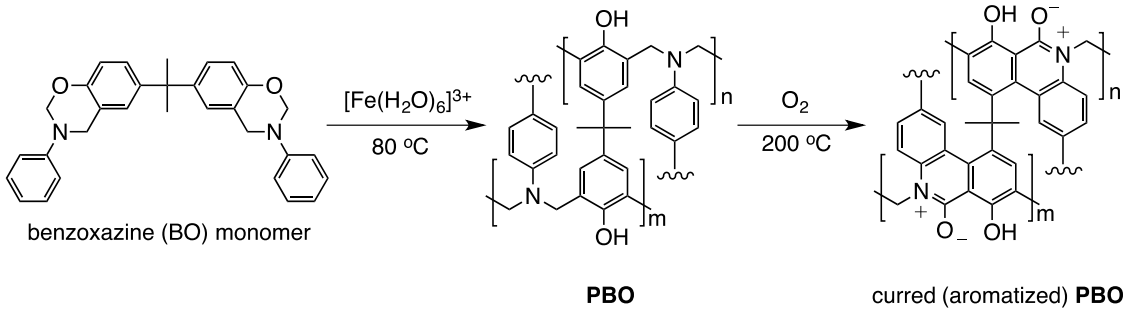

Scheme 1. Co-gelation of iron oxide (FeOx) and polybenzoxazine (PBO) interpenetrating networks.

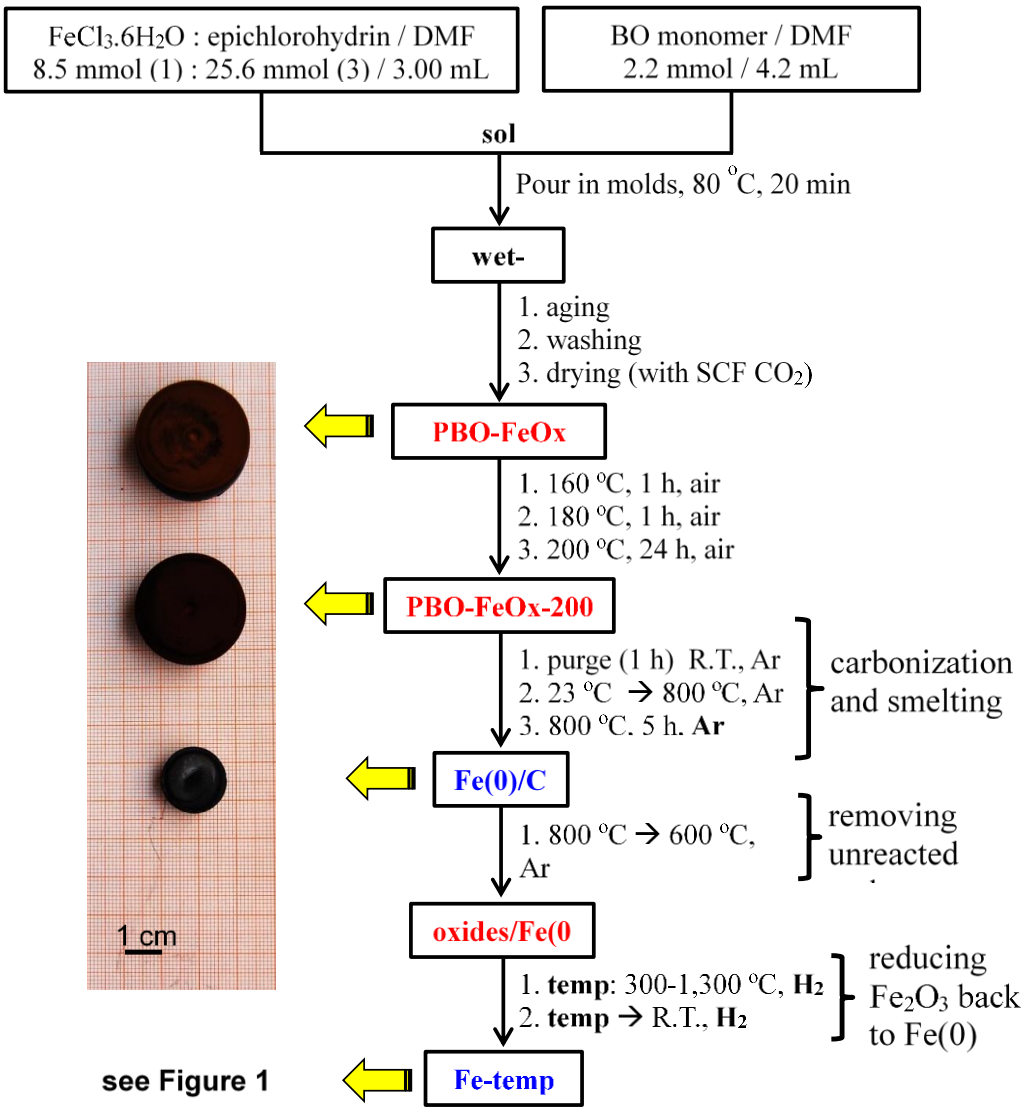

Scheme 2. Preparation Fe(0) aerogels with variable morphology and pore structure.

Table 1. Materials characterization data for samples as shown.

sample	linear shrinkage (%) [a,b]	bulk density, ρ_b (g cm^{-3}) [a]	skeletal density, ρ_s (g cm^{-3}) [c]	porosity, Π (% v/v)	Specific pore volume, (cm^3 g^{-1}) [d]			BET surface area, β (m^2 g^{-1})	Av. pore diameter (nm) [e]	particle diameter (nm) [f]
					V_{Total}	$V_{1.7\text{-}300\_nm}$	$\frac{V_{>300\_nm}}{V_{Total}}$			
Fe-300	53.23±0.93	0.741±0.025	4.573 ± 0.262	84	1.131	0.225	0.80	75.9	60	17
Fe-350	55.63±1.42	0.553±0.064	5.050 ± 0.228	89	1.610	0.148	0.91	56.2	115	21
Fe-400	57.19±0.72	0.438±0.006	7.274 ± 0.202	94	2.146	0.030	0.98_6	14.5	590	57
Fe-500	58.82±3.80	0.571±0.166	7.334 ± 0.256	92	1.615	0.003	0.99_8	5.41	1190	151
Fe-600	60.11±1.51	0.636±0.083	7.462 ± 0.237	92	1.438	0.007	0.99_5	4.90	1170	164
Fe-700	61.92±0.81	0.658±0.078	7.361 ± 0.166	91	1.384	0.006	0.99_6	5.11	1080	160
Fe-800	64.84±1.17	0.712±0.035	7.364 ± 0.159	90	1.269	0.006	0.99_5	4.21	1200	194
Fe-900	68.21±1.16	0.781±0.052	7.302 ± 0.085	89	1.144	0.014	0.98_8	5.15	900	160
Fe-950	69.03±1.55	0.881±0.075	7.305 ± 0.119	88	0.998	0.002	0.99_8	0.534	7480	1540
Fe-1000	71.03±1.54	1.702±0.296	7.292 ± 0.050	77	0.450	0.001	0.99_8	0.224	8040	3670
Fe-1100	73.64±1.72	2.137±0.154	7.248 ± 0.052	71	0.330	0.000	1.00	0.176	7500	4700
Fe-1200	76.20±0.89	2.429±0.102	7.703 ± 0.204	69	0.282	0.000	1.00	0.170	6630	4580
Fe-1300	77.25±1.64	3.782±0.184	7.635 ± 0.124	50	0.133	0.000	1.00	0.025	21350	31430

[a] Average of 5 samples. [b] Shrinkage = 100 × (mold diameter – sample diameter)/(mold diameter). [c] Single sample, average of 50 measurements. [d] V_{Total} was calculated via $V_{Total} = (1/\rho_b) - (1/\rho_s)$. $V_{1.7\text{-}300\_nm}$ from the total N_2-desorption volume. $V_{>300\_nm} = V_{Total} - V_{1.7\text{-}300\_nm}$. [e] By the $4\times V_{Total}/\beta$ method. [f] Diameter = $6/\rho_s\beta$.

ACKNOWLEDGEMENTS

We thank the Army Research Office for financial support under Cooperative Agreement No. W911NF-12-2-0029. We also thank the Materials Research Center of MS&T for support with materials characterization.

REFERENCES

1. Overviews of Recent Research on Energetic Materials; Shaw, R. W., Brill, T. B., Thompson, D. L., Eds.; Advanced Series in Physical Chemistry, Vol. 16; World Scientific Publishing, Co.: London, U.K., 2005.

2. Klasons, V.; Lamp, C. M. Thermal Batteries in *Handbook of Batteries Third Edition*, Linden, D.; Reddy, T. B. Ed.s McGraw Hill, New York, N.Y. 2002, Chapter 21, pp 21.1-21.22.

3. Guidotti, R. A.; Masset, P. "Thermally activated ("thermal") battery technology Part I: An overview," *J. Power Sources* **2006**, *161*, 1443-1449.

4. Goldsmith, H.; Smith, J. T. "Thermal cells in present use," *Electrochem. Technol.* **1968**, *6*, 16-19.

5. Ding, M.; Krieger, F.; Swank, J.; Poret, J.; McMullan, C.; Chen, G. "Use of NanoFoil as a new heat source in thermal batteries II: Its materials properties relevant to thermal batteries," *Proceedings of the 43rd Power Sources Conference*, Philadelphia, PA, July 7-10, 2008, p. 615-619.

6. Leventis, N.; Chandrasekaran, N.; Sotiriou-Leventis, C.; Mumtaz, A. "Smelting in the age of nano: Iron aerogels," *J. Mater. Chem.* **2009**, *19*, 63-65.

7. Leventis, N.; Chandrasekaran, N.; Sadekar, A. G.; Sotiriou-Leventis, C.; Lu, H. "One-pot synthesis of interpenetrating inorganic/organic networks of CuO/resorcinol-formaldehyde aerogels: Nanostructured energetic materials," *J. Am. Chem. Soc.* **2009**, *131*, 4576-4577.

8. Leventis, N.; Chandrasekaran, N.; Sadekar, A. G.; Mulik, S.; Sotiriou-Leventis, C. "The effect of compactness on the carbothermal conversion of interpenetrating metal oxide / resorcinol-formaldehyde nanoparticle networks to porous metals and carbides," *J. Mater. Chem.* **2010**, *20*, 7456-7471.

9. Leventis, N.; Sotiriou-Leventis, C.; Chandrasekaran, N.; Mulik, S.; Larimore, Z. J.; Lu, H.; Churu, G.; Mang, J. T. "Multifunctional polyurea aerogels from isocyanates and water. A structure-property case study," *Chem. Mater.* **2010**, *22*, 6692-6710.

10. Chidambareswarapattar, C.; Xu, L.; Sotiriou-Leventis, C.; Leventis, N. "Robust monolithic multiscale nanoporous polyimides and conversion to isomorphic carbons," *RSC Advances* **2013**, *3*, 26459-26469.

11. Sadekar, A. G.; Mahadik, S. S.; Bang, A. N.; Larimore, Z. J.; Wisner, C. A.; Bertino, M. F.; Kalkan, A. K.; Mang, J. T.; Sotiriou-Leventis, C.; Leventis, N. "´Green´ aerogels and porous carbons by emulsion gelation of acrylonitrile," *Chem. Mater.* **2012**, *24*, 26-47.

12. Ning, X.; Ishida, H. "Phenolic materials via ring-opening polymerization: synthesis and characterization of bisphenol-A based benzoxazines and their polymers," *J. Polym. Sci.: Part A: Polym. Chem.* **1994**, *32*, 1121-1129.

13. Ning, X.; Ishida, H. "Phenolic materials via ring-opening polymerization of benzoxazines: Effect of molecular structure on mechanical and dynamic mechanical properties," *J. Polym. Sci.:Part B: Polym. Phys.* **1994**, *32*, 921-927.

14. Santhosh Kumar K. S. "Polybenzoxazines and state-of-the-art high-temperature polymers," in *Polybenzoxazines: Chemistry and Properties*, Santhosh Kumar, K. S.; Raghunadhan Nair, C. P. Ed.s, iSmithers Rapra Technology: Shrewsbury, Shropshire, 2010, Chapter 1.

15. Lorjai, P.; Chaisuwan, T.; Wongkasemjit, S. "Porous structure of polybenzoxazine-based organic aerogel prepared by sol–gel process and their carbon aerogels," *J. Sol-Gel Sci. Technol.* **2009**, *52*, 56-64.

16. Mahadik-Khanolkar, S.; Donthula, S.; Sotiriou-Leventis, C.; Leventis, N. "Polybenzoxazine aerogels. 1. High-yield room-temperature acid-catalyzed synthesis of robust monoliths, oxidative aromatization and conversion to microporous carbons," *Chem. Mater.* **2014**, *26*, 1303-1317.

17. Mahadik-Khanolkar, S.; Donthula, S.; Bang, A.; Wisner, C.; Sotiriou-Leventis, C.; Leventis, N. "Polybenzoxazine aerogels. 2. Interpenetrating networks with iron oxide and the carbothermal synthesis of highly porous monolithic pure iron(0) aerogels as energetic materials," *Chem. Mater.* **2014**, *26*, 1318-1331.

18. Kearby, K.; Kistler, S. S.; Swann, S. Jr., "Aerogel catalyst: conversion of alcohols to amines," *Ind. Eng. Chem.* **1938**, *30*, 1082-1086.

19. Gash, A. E.; Tillotson, T. M.; Satcher, J. H.; Hrubesh, L. W.; Simpson, R. L. "New sol–gel synthetic route to transition and main-group metal oxide aerogels using inorganic salt precursors," *J. Non-Cryst. Solids* **2001**, *285*, 22-28.

20. Gash, A. E.; Tillotson, T. M.; Satcher, J. H.; Poco, J. F.; Hrubesh, L. W.; Simpson, R. L. "Use of epoxides in the sol−gel synthesis of porous iron(III) oxide monoliths from Fe(III) salts," *Chem. Mater.* **2001**, *13*, 999-1007.

21. Sisk C. N.; Hope-Weeks, J. "Copper(II) aerogels via 1, 2-epoxide gelation," *J. Mater. Chem.* **2008**, *18*, 2607-2610.

22. Therefore, that combination of temperature/reduction time (300 ^{o}C/5 h) was not deemed sufficient to reduce back to Fe(0) all oxide produced at the C-removal step (600 ^{o}C/air).

23. Maldonado-Hódar, F. J.; Moreno-Castilla, C.; Rivera-Utrilla, J.; Hanzawa, Y.; Yamada, Y. "Catalytic graphitization of carbon Aerogels by transition metals," *Langmuir* **2000**, *16*, 4367-4373.

24. Cotet, L. C.; Gich, M.; Roig, A.; Popescu, I. C.; Cosoveanu, V.; Molins, E.; Danciu, V. "Synthesis and structural characteristics of carbon aerogels with a high content of Fe, Co, Ni, Cu, and Pd," *J. Non-Cryst. Solids* **2006**, *352*, 2772-2777.

25. Lu, A.-H.; Li,W.-C.; Salabas, E.-L.; Spliethoff, B.; Schüth, F. "Low temperature catalytic pyrolysis for the synthesis of high surface area, nanostructured graphitic carbon," *Chem. Mater.* **2006**, *18*, 2086-2094.

26. Pierre, A. C.; Pajonk, G. M. "Chemistry of aerogels and their applications," *Chem. Rev.* **2002**, *102*, 4243-4265.

27. Chidambareswarapattar, C.; McCarver, P. M.; Luo, H.; Lu, H.; Sotiriou-Leventis, C.; N. Leventis, N. "Fractal multiscale nanoporous polyurethanes: Flexible to extremely rigid aerogels from multifunctional small molecules," *Chem. Mater.* **2013**, *25*, 3205-3224.

28. Leventis, N.; Chidambareswarapattar, C.; Mohite, D. P.; Larimore, Z. J.; Lu, H.; Sotiriou-Leventis, C. "Multifunctional porous aramids (aerogels) by efficient reaction of carboxylic acids and isocyanates," *J. Mater. Chem.* **2011**, *21*, 11981-11986.

29. Mohite, D. P.; Larimore, Z. J.; Lu, H.; Mang, J. T.; Sotiriou-Leventis, C.; Leventis, N. "Monolithic hierarchical fractal assemblies of silica nanoparticles cross-linked with polynorbornene via ROMP: A structure-property correlation from molecular to bulk through nano," *Chem. Mater.* **2012**, *24*, 3434-3448.

30. Katti, A.; Shimpi, N.; Roy, S.; Lu, H.; Fabrizio, E. F.; Dass, A.; Capadona, L. A.; Leventis, N. "Chemical, Physical and Mechanical Characterization of Isocyanate-Crosslinked Amine-Modified Silica Aerogels," *Chem. Mater.* **2006**, *18*, 285-296.

31. Lu, X.; Nilsson, O.; Fricke, J.; Pekala, R. W. "Thermal and electrical conductivity of monolithic carbon aerogels," *J. Appl. Phys.* **1993**, *73*, 581-584.

32. Pullin, A. D. E.; Pollock, J. McC. "Spectra of solutions of silver and lithium perchlorates in acetone," *Trans. Faraday Soc.* **1958**, *54*, 11-18.

33. Guidotti, R. A.; Odinek, J.; Reinhardt, F. W. "Characterization of Fe/$KClO_4$ heat powders and pellets," *J. Energ. Mater.* **2006**, *24*, 271-305.

34. Cox, J. D., Wagman, D. D., Medvedev, V. A. *CODATA Key Values for Thermodynamics*, Hemisphere Publishing Corp.: New York, N.Y., 1989.

35. That was calculated considering the minimum heat of the Fe(0)/$LiClO_4$ reaction (from BC, around ΔH = 60 kcal mol^{-1} of iron reacting), the heat capacity of Fe(0) (c, about equal to $3R - R$: gas constant) and the gas law: $P_2/P_1=T_2/T_1$ (which translates into $P_2=P_1\times(\Delta H/(c\times T_1)$ with P_1=1 atm and T_1=298 K).

36. Cullity, B. C.; Stock, S. R. *Elements of X-Ray Diffraction*, 3rd Ed., Prentice-Hall Inc.: New York, N.Y., 2001, pp 167-171.

37. Geometric Factors in Four Point Resistivity Measurements, Bulletin No. 472-13, Haldor Topsoe Semiconductor Division: Vedbæk, May 25, 1968, p 37.

38. http://www.fourpointprobes.com/haldor.html (accessed September 27, 2015).

SUPPORTING INFORMATION

Table S.1. Cumulative XRD analysis and thermochemical data of perchlorate-loaded samples before and after ignition under various conditions.

Ignition Movies

Fe-temp *loaded with $LiClO_4$*

Ignition in open air

Movie S.AIR.1…Fe-350-LiClO4

Movie S.AIR.2…Fe-400-LiClO4

Movie S.AIR.3…Fe-600-LiClO4

Movie S.AIR.4…Fe-800-LiClO4

Movie S.AIR.5…Fe-950-LiClO4

Movie S.AIR.6…Fe-1100-LiClO4

Movie S.AIR.7…Fe-1200-LiClO4

Movie S.AIR.8…Fe-1300-LiClO4

Ignition in sealed tubes under vacuum

Movie S.VAC.1…Fe-400-LiClO4

Movie S.VAC.2…Fe-600-LiClO4

Movie S.VAC.3…Fe-700-LiClO4

Movie S.VAC.4…Fe-800-LiClO4

Movie S.VAC.5…Fe-950-LiClO4

Ignition in sealed tubes under nitrogen

Movie S.N2.1…Fe-350-LiClO4

Movie S.N2.2…Fe-700-LiClO4

Movie S.N2.3…Fe-800-LiClO4

Fe-temp *loaded with* $NaClO_4$

Movie S.Na.1…Fe-400-NaClO4

Movie S.Na.2…Fe-600-NaClO4

Movie S.Na.3…Fe-1000-NaClO4

Fe-temp *loaded with* $KClO_4$

Movie S.K.1…Fe-400-KClO4

Movie S.K.2…Fe-600-KClO4

Movie S.K.3…Fe-1000-KClO4

Table S.1. Cumulative XRD analysis and TGA data of perchlorate-loaded samples before and after ignition under various conditions.

Sample [a]	$\frac{Fe(0)}{perchlorate}$ (mol/mol) [b]	$\frac{Fe_{reacted}}{Fe_{initial}}$ (mol/mol) [c]	Fe (mol%) [d]	FeO (mol%) [d]	Fe_3O_4 (mol%) [d]	Fe_2O_3 (mol%) [d]	ΔH (kcal/mol) [e] theoretical [experimental]
			Loaded with $LiClO_4$				
Fe-300 [f]	-	-	-	-	-	-	-
Fe-350	2.675	1.000	0	0	100	0	-91.298
Fe-400	2.929	1.000	0	100	0	0	-66.639
Fe-500	2.959	1.000	0	0	42	58	-95.953
Fe-600	2.634	0.922	11	68	21	0	-78.527
Fe-600-BC	2.634	0.898	11	83	0	6	-71.066 [-60.1]
Fe-700	2.640	[g]	[g]	[g]	[g]	[g]	-66.639
Fe-700-BC	2.640	0.887	11	89	0	0	-66.639 [-58.3]
Fe-700-vac	2.640	0.899	10	90	0	0	-66.639
Fe-800	1.777	0.537	67	0	11	22	-96.675
Fe-800-BC	1.777	0.898	11	83	0	6	-71.066 [-57.5]
Fe-800-vac	1.777	0.734	27	73	0	0	-66.639
Fe-900	5.369	1.000	0	0	100	0	-91.298
Fe-950	5.552	1.000	0	0	100	0	-91.298
Fe-950-vac	5.552	0.203	82	15	0	3	-75.537
Fe-1000	4.252	0.332	67	33	0	0	-66.639
Fe-1100	6.436	0.360	64	36	0	0	-66.639
Fe-1200	6.634	0.705	36	52	12	0	-76.594
Fe-1300	12.836	0.946	15	0	85	0	-91.298

Table S.1. Cumulative XRD analysis and TGA data of perchlorate-loaded samples before and after ignition under various conditions (Continued).

Sample [a]	$\frac{Fe(0)}{perchlorate}$ (mol/mol) [b]	$\frac{Fe_{reacted}}{Fe_{initial}}$ (mol/mol) [c]	Fe (mol%) [d]	FeO (mol%) [d]	Fe_3O_4 (mol%) [d]	Fe_2O_3 (mol%) [d]	ΔH (kcal/mol) [e] theoretical [experimental]
			Loaded with $NaClO_4$				
Fe-400	7.137	0.986	3	0	24	73	-97.794
Fe-600	7.472	0.828	32	0	21	47	-97.177
Fe-1000	21.448	0.263	89	0	11	0	-91.322
			Loaded with $KClO_4$				
Fe-400	12.920	0.671	40	50	10	0	-74.403
Fe-600	162.871	0.202	90	0	3	7	-95.126
Fe-1000	314.407	0.220	91	0	9	0	-89.394

[a] Samples were ignited in air unless otherwise noted (BC: in a bomb calorimeter; vac: in evacuated sealed ampules).
[b] Determined gravimetrically.
[c] Calculated from the iron products in the residue after ignition via:
$[100-\%Fe_{in\text{-}residue}] / 100 \times [\%Fe_{in\text{-}residue} + \%FeO + 2\times\%Fe_2O_3 + 3\times\%Fe_3O_4]$. All % in mol/mol from [d].
[d] Via XRD and quantitative phase analysis.
[e] Based on the amount of iron reacted. Theoretical values were calculated from standard heats of formation assuming no air (O_2) participation and stoichiometrically sufficient amount of perchlorate: $(\Delta H_f)_{LiCl}$ = -97.679 kcal/mol, $(\Delta H_f)_{LiClO4}$ = -91.057 kcal/mol, $(\Delta H_f)_{KCl}$ = -104.324 kcal/mol, $(\Delta H_f)_{KClO4}$ = -103.439 kcal/mol, $(\Delta H_f)_{NaCl}$ = -98.277 kcal/mol, $(\Delta H_f)_{NaClO4}$ = -91.609 kcal/mol, $(\Delta H_f)_{Fe}$ = 0 kcal/mol, $(\Delta H_f)_{FeO}$ = -65.008 kcal/mol, $(\Delta H_f)_{Fe2O3}$ = -196.984 kcal/mol, $(\Delta H_f)_{Fe3O4}$ = -267.298 kcal/mol. Experimental values were measured with a bomb calorimeter.
[f] Sample consisted mostly of oxides.
[g] No residue could be recovered.

SECTION

2. CONCLUSIONS

Aerogels with varying morphology and interparticle connectivity were synthesized and studied for their applications as energy storage materials. Polyurethane chemistry was employed for the first time to make shape memory aerogels using cheap monomers. The effect of particle interconnectivity or the framework in iron aerogels was related with the explosive or thermite behavior when those aerogels were loaded with oxidizing agents and ignited in air.

In paper I, shape memory superelastic poly(isocyanurate-urethane) (PIR-PUR) aerogels were successfully synthesized and showed applications as in deployable panels and biomimetic devices. As shown here, the isocyanurate ring of the isocyanate monomer effectively acts as a cross-linking node for imparting both rubber-like elasticity and insolubility of a developing polyurethane network. Both these conditions are necessary for the shape memory effect and the synthesis of polymeric aerogels, respectively that were achieved with the help of design of experiments. Those resulting aerogels showed a robust shape memory effect with high strain fixity, strain recovery ratios and fill factors.

In paper II, PIR-PUR aerogels were prepared with mixed diols and an aliphatic triisocyanate whose synthetic parameters were varied systematically using a statistical design-of-experiments model. The chemical composition of each sample reflected its formulation, as designed. Microstructures could be put in two groups, one consisting of micron-size particles connected with large necks, and a second one classified as bicontinuous. The two groups could be explained consistently by a gelation mechanism

involving spinodal decomposition and early versus late phase separation relative to the gel point. The overall figure of merit, the fill factor, was found in the range of 0.35-0.71; that variability was traced to a variability in the shape recovery rates, $R_t(N)$, which in turn were related to the micromorphology. The inverse correlation between $R_t(N)$ and the elastic modulus, E, provides a means for a qualitative predictability of the shape recovery rates, thereby the fill factor, and in turn the overall quality of the shape memory effect. Quantitatively, the correlation of Rt(N) and E (Eq. 10) was traced to a linear correlation of the activation barrier for shape recovery and the elastic modulus which represents a rigorous thermodynamic-kinetic correlation, analogous to the Marcus expression for electron transfer reactions.

In paper III, monolithic nanoporous iron aerogels were prepared via carbothermal reduction of interpenetrating networks of polybenzoxazine-iron oxide nanoparticles (PBO-FeOx). The PBO network played the role of a hard-sacrificial template in the carbothermal process and excess unreacted carbon was burned off at 600 °C in air. That step partially oxidized the Fe(0) network which was reduced back to Fe(0) with H_2 at different temperatures varying from 300 to 1300 °C. The final H_2-reduction temperature had an annealing effect on the iron framework, thereby upon ignition of samples loaded with stoichiometric amounts of LiClO4 that fizzled out, exploded or presented thermite behavior depending mainly on the mechanical strength of said network. The explosion behavior was explained due to the fast heating and expansion of gas confined in nanoporous space.

BIBILIOGRAPHY

1. Dunn, B.; Kamath, H.; Tarascon, J. M. Electrical Energy Storage for the Grid: A Battery of Choices. *Science* **2011**, *334*, 928.

2. Manthiram, A.; Murugan, A. V.; Sarkar, A.; Muraliganth, T. Nanostructured Electrode Materials for Electrochemical Energy Storage and Conversion. *Energy Environ. Sci.* **2008**, *1*, 621-638.

3. Alva, G.; Liu, L.; Huang, X.; Fang, G. Thermal energy storage materials and systems for solar energy applications. *Renew. Sustain. Energy Rev.* **2017**, *68*, 693-706.

4. Scarfogliero, U.; Stefanini, C.; Dario, P. The use of compliant joints and elastic energy storage in bio-inspired legged robots. *Mech. Mach. Theory*, **2009**, *44*, 580-590.

5. Tang, C.; Zhang, Q.; Zhao, M.-Q.; Tian, G.-L.; Wei, F. Resilient Aligned Carbon Nanotube/Graphene Sandwiches for Robust Mechanical Energy Storage. *Nano Energy*, **2014**, *7*, 161-169.

6. Chen, K.; Xue, D. Materials Chemistry toward Electrochemical Energy Storage. *J. Mater. Chem. A*, **2016**, *4*, 7522-7537.

7. Guerreiro, L.; Collares-Pereira, M. New Materials for Thermal Energy Storage in Concentrated Solar Power Plants. *AIP Conf. Proc.* **2016**, 1734, 050018-1-8.

8. Zhao, J. M.; Zhang, Z. M. Electromagnetic Energy Storage and Power Dissipation in Nanostructures *J. Quant. Spectrosc. Radiat. Transfer* **2015**, *151*, 49-57.

9. Rasmussen, C. N.; Altiparmakis, A.; Däumling, M. Electromagnetic and electrostatic storage. *DTU International Energy Report* **2013**.

10. IUPAC, Compendium of Chemical Terminology (the "Gold Book"), second ed., Blackwell Scientific Publications, Oxford, 1997.

11. Vareda, J. P.; Lamy-Mendes, A.; Durães, L. A Reconsideration on the Definition of the Term Aerogel Based on Current Drying Trends. *Microporous Mesoporous Mater.* **2018**, *258*, 211−216.

12. Kistler, S. S. Coherent Expanded Aerogels and Jellies. *Nature* **1931**, *127*, 741.

13. Leventis, N.; Sadekar, A.; Chandrasekaran, N.; Sotiriou-Leventis, C. Click Synthesis of Monolithic Silicon Carbide Aerogels from Polyacrylonitrile-Coated 3D Silica Networks. *Chem. Mater.* **2010**, *22*, 2790- 2803.

14. L. L. Hench, J. K. West. The Sol-Gel Process. *Chem. Rev*. **1990**, *90*, 33–72.

15. (a) Rao, A. V.; Hegde, N. D.; Hirashima, H. Absorption and Desorption of Organic Liquids in Elastic Superhydrophobic Silica Aerogels. *J. Colloid Interface Sci.* **2007**, *305*, 124–132. (b) Rao, A. V.; Bhagat, S. D.; Hirashima, H.; Pajonk, G. M. Synthesis of Flexible Silica Aerogels Using Methyltrimethoxysilane (MTMS) Precursor. *J. Colloid Interface Sci.* **2006**, *300*, 279–285.

16. Wang, C. T.; Wu, C. L.; Chen, I. C.; Huang, Y. H. Humidity Sensors Based on Silica Nanoparticle Aerogel Thin Films. *Sens. Actuators, B* **2005**, *107*, 402–410.

17. Li, Y. K.; Yang, D. K.; Chen, Y. C.; Su, H. J.; Wu, J. C.; Chen-Yang, Y. W. A Novel Three-Dimensional Aerogel Biochip for Molecular Recognition of Nucleotide Acids. *Acta Biomater.* **2010**, *6*, 1462–1470.

18. Rousset, J. L.; Boukenter, A.; Champagnon, B.; Dumas, J.; Duval, E.; Quison, J. F.; Serughetti, J. Granular Structure and Fractal Domains of Silica Aerogels. *J. Phys.* **1990**, *2*, 8445–8455.

19. Pajonk, G. M.; Manzalji, T. Synthesis of Acrylonitrile from Propylene and Nitric Oxide Mixtures on Pbo_2-Zro_2 Aerogel Catalyst. *Catal. Lett.* **1993**, *21*, 361–369.

20. Sayari, A.; Ghorbel, A.; Pajonk, G. M.; Teichner, S. J. Kinetics of The Catalytic Transformation of Isobutene into Methacrylonitrile with NO on Supported Nickel Oxide Aerogel. *React. Kinet. Catal. Lett.* **1981**, *15*, 459–465.

21. Saeed, A. M.; Wisner, C. A.; Donthula, S.; Majedi Far, H.; Sotiriou-Leventis, C.; Leventis, N. Reuseable Monolithic Nanoporous Graphite-Supported Nanocatalysts (Fe, Au, Pt, Pd, Ni, and Rh) from Pyrolysis and Galvanic Transmetalation of Ferrocene-Based Polyamide Aerogels. *Chem. Mater.* **2016**, *28*, 4867−4877.

22. Thapliyal, P. C.; Singh, K. Aerogels as Promising Thermal Insulating Materials: An Overview. *J. Mater.* **2014**, 127049-1-10.

23. Hamann, T. W.; Martinson, A. B. F.; Elam, J. W.; Pellin, M. J.; Hupp, J. T. Atomic Layer Deposition of TiO_2 on Aerogel Templates: New Photoanodes for Dye-Sensitized Solar Cells. *J. Phys. Chem. C* **2008**, *112*, 10303–10307.

24. Anandan, S.; Hebalkar, N.; Sarada, B. V.; Rao, T. N. In *Aerospace Materials and Material Technologies*; Prasad, N. E., Wanhill, R. J. H., Eds.; Springer: Singapore, **2017**; Chapter 5, pp 85-101.

25. Coffman, B.; Fesmire, J.; White, S.; Gould, G.; Augustynowicz, S. Aerogel Blanket Insulation Materials for Cryogenic Applications. *Adv. Cryog. Eng.* **2010**, *1218*, 913-920.

26. Xia, W.; Qu, C.; Liang, Z.; Zhao, B.; Dai, S.; Qiu, B.; Jiao, Y.; Zhang, Q.; Huang, X.; Guo, W.; Dang, D.; Zou, R.; Xia, R.; Xu, R.; Liu, M. High-Performance Energy Storage and Conversion Materials Derived from a Single Metal–Organic Framework/Graphene Aerogel Composite. *Nano Lett.* **2017**, *17*, 2788-2795.

27. Beiner, J.; Stadermann, M.; Suss, M.; Worsley, M. A.; Beiner, M. M.; Rose, K. A.; Baumann, T. F. Advanced Carbon Aerogels for Energy Applications. *Energy Environ. Sci.* **2011**, *4*, 656-667.

28. Meador, M. A. B.; McMillon, E. Sandberg, A.; Barrios, E.; Wilmoth, N. G.; Mueller, C. H.; Miranda, F. A. Dielectric and Other Properties of Polyimide Aerogels Containing Fluorinated Blocks. *ACS Appl. Mater. Interfaces* **2014**, *6*, 6062–6068.

29. Meador, M. A. B.; Wright, S.; Sandberg, A.; Nguyen, B. N.; Keuls, F. W. V.; Mueller, C. H. Rodriguez-Solis, R.; Miranda, F. A. Low Dielectric Polyimide Aerogels as Substrates for Lightweight Patch Antennas. *ACS Appl. Mater. Interfaces* **2012**, *4*, 6346–6353.

30. Hong, J.-Y.; Wie, J. J.; Xu, Y.; Park, H. S. Chemical Modification of Graphene Aerogels for Electrochemical Capacitor Applications. *Phys. Chem. Chem. Phys.* **2015**, *17*, 30946-30962.

31. (a) Kistler, S. S. Coherent Expanded Aerogels and Jellies. *Nature* **1931**, *127*, 741. (b) Kistler, S. S. The Relation between Heat Conductivity and Structure in Silica Aerogel. *J. Phys. Chem.* **1934**, *39*, 79-86. (c) Lu, X.; Caps, R.; Fricke, J.; Pekala, R. W. Correlation between Structure and Thermal Conductivity of Organic Aerogels. *J. Non-Cryst. Solids* **1995**, *188*, 226-234.

32. http://www.aerogeltechnologies.com/silica-aerogel-samples.

33. Pierre, A. C.; Pajonk, G. M. Chemistry of Aerogels and Their Applications. *Chem. Rev*. **2002**, *102*, 4243−4265.

34. (a) Gould, G. L.; Lee, J. K.; Stepanian, C. J.; Lee, K. P. High Strength, Nanoporous Bodies Reinforced with Fibrous Materials. U. S. Patent Application 20070222116, 2007. (b) Ryu, J. Flexible Aerogel Superinsulation and its Manufacture. U. S. Patent 6068882A, 2000.

35. Harasim, S. Building Envelope Applications for Reinforced Flexible Aerogel Insulation Blankets. Aspen Aerogels Inc. 2011.

36. (a) Wittwer, V. Development of Aerogel Windows. *J. Non-Cryst. Solids* **1992**, *145*, 233–236. (b) Gerlach, R.; Kraus, O.; Fricke, J.; Eccardt, P. C.; Kroemer, N.; Magori, V. Modified SiO_2 Aerogels as Acoustic Impedance Matching Layers in Ultrasonic devices. *J. Non-Cryst. Solids* **1992**, *145*, 227–232.

37. Pajonk, G. M. Aerogel Catalysts. *Appl. Catal.* **1991**, *72*, 217–266.

38. Cantin, M.; Casse, M.; Koch, L.; Jouan, R.; Mestreau, P.; Roussel, D.; Saclay, C.; Bonnin, F.; Moutel, J.; Teichner, S. J. Silica aerogels used as Cherenkov radiators. *Nucl.Instrum.Meth.* **1974**, *118*, 177-182.

39. Lagamba, L.; Cisbani, E.; Colilli, S.; Crateri, R.; Leo, R. D.; Frullani, S.; Garibaldi, F.; Giuliani, F.; Gricia, M.; Iodice, M.; Iommi, R.; Leone, A.; Lucentini, M.; Mostarda, A.; Nappi, E.; Perrino, R.; Pierangili, L.; Santavenere, F.; Urciuoli, G. M. Silica Aerogel Threshold Cherenkov Counters for the Jlab Hall A Spectrometers: Improvements and Proposed Modifications. *Nucl. Instr. Meth. Phys. Res. A.* **2001**, *471*, 325–332.

40. (a) Leventis, N. Three-Dimensional Core-Shell Superstructures: Mechanically Strong Aerogels. *Acc. Chem. Res.* **2007**, *40*, 874-884. (b) Leventis, N.; Mulik, S.; Wang, X.; Dass, A.; Sotiriou-Leventis, C.; Lu, H. Stresses at the Interface of Micro with nano. *J. Am. Chem. Soc.* **2007**, *129*, 10660-10661. (c) Leventis, N.; Sotiriou-Leventis, C.; Zhang, G.; Rawashdeh, A.-M. M. Nano Engineering Strong Silica Aerogels. *Nano Lett.* **2002**, *2*, 957-960.

41. Han, Q.; Urban, M. W. J. Kinetics and Mechanisms of Catalyzed and Noncatalyzed Reactions of OH and NCO in Acrylic Polyol–1,6-Hexamethylene Diisocyanate (HDI) Polyurethanes. VI. *Appl. Polym. Sci.* **2002**, *86*, 2322-2329.

42. Han, J. L.; Yu, C. H.; Lin, Y. H.; Hsieh, K. H. Kinetic Study of the Urethane and Urea Reactions of Isophorone Diisocyanate. *J. Appl. Polym. Sci.* **2008**, *107*, 3891-3902.

43. Chang, M. C.; Chen, S. A. Kinetics and Mechanism of Urethane Reactions: Phenyls Isocyanate-Alcohol Systems. *J. Polym. Sci. Part A: Polym. Chem.* **1987**, *25*, 2543-2559.

44. Donohoe, G.; Satchell, D. P. N.; Satchell, R. S. The Kinetics and Mechanism of Addition of Bulky Alcohols to Dimethyl Ketene and P-Nitrophenyl Isocyanate in Iso-Octane and Carbon Tetrachloride Solutions. *J. Chem. Soc. Perkin Trans.* **1990**, *210*, 1671-1674.

45. Bayer, O. Das Di-Isocyanat-Polyadditionsverfahren (Polyurethane). *Angew. Chem.* **1947**, *59*, 257–272.

46. Rausch, K.W.; Sayigh, A. A. R. Structure Property Relationships in Polyurethane Elastomers Prepared by One-Step Reaction. *Ind. Eng. Chem. Prod. Res. Dev.* **1965**, *4*, 92-98.

47. Islam, M. R.; Beg, M. D. H.; Jamari, S. S. Development of Vegetable-Oil-Based Polymers, *J. Appl. Polym. Sci*. **2014**, *131*, 40787–40790.

48. Delebecq, E.; Pascault, J.-P.; Boutevin, B.; Ganachaud, F. O. On the Versatility of Urethane/Urea Bonds: Reversibility, Blocked Isocyanate, and Nonisocyanate Polyurethane. *Chem. Rev.* **2012**, *113*, 80–118.

49. Pigott, K.A. Polyurethanes, in Encyclopedia of Polymer Science and Technology, Vol. 11.; John Wiley & Sons, Inc.: New York, NY, 1989; pp 506–563.

50. Wilkes, G.L.; Dziemianowicz, T.S.; Ophir, Z.H.; and Wildnauer, R. Thermally Induced Time Dependence of Mechanical Properties in Biomedical Grade Polyurethanes. *J. Biomed. Mater. Res.* **1979**, *13*, 189–206.

51. Dzierza, W. Stress-Relaxation Properties of Segmented Polyurethane Rubbers. *J. Appl. Polym. Sci.* **1982**, *27*, 1487–1499.

52. Wong, E.W.C. Development of a biomedical polyurethane. In Urethane Chemistry and Applications, ACS Series, 1981; pp 489–504.

53. Engels, H. W.; Pirkl, H. G.; Albers, R.; Albach, R. W.; Krause, J.; Hoffmann, A.; Casselmann, H.; Dormish, J. Polyurethanes: Versatile Materials and Sustainable Problem Solvers for Today's Challenges. *Angew. Chem. Int. Ed.* **2013**, *52*, 9422-9441.

54. Singhal, P.; Small, W.; Cosgriff-Hernandez, E.; Maitland D. J.; Wilson, T. S. Low Density Biodegradable Shape Memory Polyurethane Foams for Embolic Biomedical Applications. *Acta Biomater*. **2014**, *10*, 67–76.

55. Hodlur, R.; Rabinal, M. Self Assembled Graphene Layers on Polyurethane Foam as a Highly Pressure Sensitive Conducting Composite. *Compos. Sci. Technol.* **2014**, *90*, 160–165.

56. Kang, S.; Kwon, S.; Park, J.; Kim, B. Carbon Nanotube Reinforced Shape Memory Polyurethane Foam. *Polym. Bull.* **2013**, *70*, 885–893.

57. Liu, H. D.; Liu, Z. Y.; Yang, M. B.; He, Q. Surperhydrophobic Polyurethane Foam Modified by Graphene Oxide. *J. Appl. Polym. Sci.* **2013**, *130*, 3530–3536.

58. Chen, T.; Qiu, J.; Zhu, K.; Li, J. Electro-Mechanical Performance of Polyurethane Dielectric Elastomer Flexible Micro-Actuator Composite Modified with Titanium Dioxide–Graphene Hybrid Fillers. *Mater. Des.* **2016**, *90*, 1069–1076.

59. Yan, R.; Wang, R.; Lou, C. W.; Huang, S. Y.; Lin, J. H. Quasi-Static and Dynamic Mechanical Responses of Hybrid Laminated Composites Based on High-Density Flexible Polyurethane Foam. *Composites Part B*, **2015**, *83*, 253–263.

60. Anisur, M. R.; Kibria, M. A.; Mahfuz, M. H.; Saidur, R. Metselaar, I. H. S. C. In *Energy Sustainability Through Green Energy*; Sharma, A., Kar, S. K., Eds.; Springer: New york, NY, 2015; Chapter 10, pp 245–263.

61. Heinen, M.; Gerbase, A. E.; Petzhold, C. L. Vegetable Oil Based Rigid Polyurethanes and Phosphorylated Flame Retardants Derived from Epoxydized Soybean Oil. *Polym. Degrad. Stab.* **2014**, *108*, 76–86.

62. Factsheet PU-Europe, Applications for polyurethane insulation-today's solution for tomorrow's needs, 2011, http://www.pu-europe.eu.

63. (a) Zhang, M.; Luo, Z.; Zhang, J.; Chen, S.; Zhou, Y. Effects of a Novel Phosphorus–Nitrogen Flame Retardant on Rosin Based Rigid Polyurethane Foams. *Polym. Degrad. Stab.* **2015**, *120*, 427–434. (b) Kordomenos, P. I.; Kresta, J. E. Thermal Stability of Isocyanate-Based Polymers. 1. Kinetics of the Thermal Dissociation of Urethane, Oxazolidone, and Isocyanurate Groups. *Macromolecules* **1981**, *14*, 1434-1437. (c) Liszkowska, J.; Czuprynski, B.; Paciorek-Sadowska, J. Thermal Properties of Polyurethane-Polyisocyanurate (PUR-PIR) Foams Modified with Tris(5-hydroxypentyl) Citrate. *J. Adv. Chem. Eng.* **2016**, *6*, 1000148.

64. Claeys, B.; Vervaeck, A.; Hillewaere, X. K.; Possemiers, S.; Hansen, L.; Beer, T. D. Thermoplastic Polyurethanes for the Manufacturing of Highly Dosed Oral Sustained Release Matrices via Hot Melt Extrusion and Injection Molding. *Eur. J. Pharm. Biopharm.* **2015**, *90*, 44–52.

65. Unverferth, M.; Kreye, O.; Prohammer, V.; Meier, M. A. Renewable Non-Isocyanate Based Thermoplastic Polyurethanes via Polycondensation of Dimethyl Carbamate Monomers with Diols. *Macromol. Rapid Commun.* **2013**, *34*, 1569–1574.

66. Lingier, S.; Espeel, P.; Suarez, S. S.; T¨ur¨unç, O.; Wildeman, S. D.; Prez, F. E. D. Renewable Thermoplastic Polyurethanes Containing Rigid Spiroacetal Moieties. *Eur. Polym. J.* **2015**, *70*, 232–239.

67. More, A. S.; Lebarb´e, T.; Maisonneuve, L.; Gadenne, B.; Alfos, C.; Cramail, H. Novel Fatty Acid Based Diisocyanates Towards the Synthesis of Thermoplastic Polyurethanes. *Eur. Polym. J.* **2013**, *49*, 823–833.

68. Petrovi´c, Z. S.; Wan, X.; Bili´c, O.; Zlatani´c, A.; Hong, J.; Javni, I. Polyols and Polyurethanes from Crude Algal Oil. *J. Am. Oil Chem. Soc.* **2013**, *90*, 1073–1078.

69. Rajput, S. D.; Hundiwale, D. G.; Mahulikar, P. P.; Gite, V. V. Fatty Acids Based Transparent Polyurethane Films and Coatings. *Prog. Org. Coat.* **2014**, *77*, 1360–1368.

70. Gaikwad, M. S.; Gite, V. V.; Mahulikar, P. P.; Hundiwale, D. G.; Yemul, O. S. Eco-Friendly Polyurethane Coatings from Cottonseed and Karanja Oil. *Prog. Org. Coat.* **2015**, *86*, 64– 172.

71. Chattopadhyay, D.; Webster, D. C. Thermal Stability and Flame Retardancy of Polyurethanes. *Prog. Polym. Sci.* **2009**, *34*, 1068–1133.

72. Szycher, M. *Szycher's handbook of polyurethanes;* CRC Press, Taylor & Francis: Boca Raton, FL, 1999; Chapter 2.

73. Zia, K. M.; Bhatti, H. N.; Bhatti, I. A. Methods for Polyurethane and Polyurethane Composites, Recycling and Recovery: A Review. *React. Funct. Polym.* **2007**, *67*, 675–692.

74. Charlon, M.; Heinrich, B.; Matter, Y.; Couzigne, E.; Donnio, B.; Averous, L. Synthesis, Structure and Properties of Fully Bio-Based Thermoplastic Polyurethanes, Obtained from a Diisocyanate Based on Modified Dimer Fatty Acids, and Different Renewable Diols. *Eur. Polym. J.* **2014**, *61*, 197–205.

75. (a) Buehler, W. J.; Gilfrich, J. V.; Wiley, R. C. Effect of Low-Temperature Phase Changes on the Mechanical Properties of Alloys near Composition TiNi. *J. Appl. Phys.* **1963**, *34*, 1475-1477. (b) Perkins, J.; Hodgson, D. In *Engineering Aspects of Shape Memory Alloys*; Duerig, T. W., Melton, K. N., Stockel, D., Wayman, C. M., Eds.; Butterworth-Heinemann: London, 1990.

76. Wayman, C. M. In *Shape Memory Materials*; Otsuka, K., Wayman, C. M., Eds.; Cambridge University Press: Cambridge, UK, 1999.

77. Beloshenko, V. A.; Varyukhin, V. N.; Voznyak, Y. V. The Shape Memory Effect in Polymers. *Russ. Chem. Rev.* **2005**, *74*, 265.

78. Lendlein, A.; Kelch, S. Shape-Memory Polymers. *Angew. Chem., Int. Ed.* **2002**, *41*, 2034.

79. Liu, C.; Qin, H.; Mather, P. T. Review of Progress in Shape-Memory Polymers. *J. Mater. Chem.* **2007**, *17*, 1543–1558.

80. Hager, M. D.; Bode, S.; Weber, C.; Schubert, U. S. Shape Memory Polymers: Past, Present and Future Developments. *Prog. Polym. Sci.* **2015**, *49*, 3–33.

81. Jiang, Z. -C.; Xiao, Y. -Y.; Kang, Y.; Pan, M.; Li, B. J.; Zhang, S. Shape Memory Polymers Based on Supramolecular Interactions. *ACS Appl. Mater. Interfaces* **2017**, *9*, 20276−20293.

82. Pilate, F.; Toncheva, A.; Dubois, P.; Raquez, J.-M. Shape-Memory Polymers for Multiple Applications in the Materials World. *Eur. Polym. J.* **2016**, *80*, 268-294.

83. Peterson, G. I.; Dobrynin, A. V.; Becker, M. L. Biodegradable Shape Memory Polymers in Medicine. *Adv. Healthcare Mater.* **2017**, *6*, 1700694-1-16.

84. Xiao, X.; Kong, D.; Qiu, X.; Zhang, W.; Zhang, F.; Liu, L.; Liu, Y.; Zhang, S.; Hu, Y.; Leng, J. Shape-Memory Polymers with Adjustable High Glass Transition Temperatures. *Macromolecules* **2015**, *48*, 3582−3589.

85. Bellin, I., Kelch, S., Langer, R.; Lendlein, A. Polymeric Triple-Shape Materials. *Proc. Natl Acad. Sci.* **2006**, *103*, 18043–18047.

86. Behl, M.; Bellin, I.; Kelch, S. Wagermaier, W.; Lendlein, A. One-Step Process for Creating Triple-Shape Capability of AB Polymer Networks. *Adv. Funct. Mater.* **2009**, *19*, 102–108.

87. Xie, T.; Xiao, X.; Cheng, Y. T. Revealing Triple-Shape Memory Effect by Polymer Bilayers. *Macromol. Rapid Commun.* **2009**, *30*, 1823–1827.

88. Xie, T. Tunable Polymer Multi-Shape Memory Effect. *Nature* **2010**, *464*, 267-270.

89. Rivero, G.; Nguyen, L. -T. T.; Hillewaere, X. K. D.; Prez, F. E. D. One-Pot Thermo-Remendable Shape Memory Polyurethanes. *Macromolecules* **2014**, *47*, 2010-2018.

90. Li, G.; Fei, G.; Xia, H.; Han, J.; Zhao, Y. Spatial and Temporal Control of Shape Memory Polymers and Simultaneous Drug Release Using High Intensity Focused Ultrasound. *J. Mater. Chem.* **2012**, *22*, 7692-7696.

91. (a) Rao, A. V.; Pajonk, G. M. Effect of Methyltrimethoxysilane as a Co-Precursor on the Optical Properties of Silica Aerogels. *J. Non-Cryst. Solids.* **2001**, *285*, 202-209. (b) Rao, A. V.; Kulkarni, M. M. Superhydrophobic Silica Aerogels Based on Methyltrimethoxysilane Precursor. *J. Non-Cryst. Solids*, **2003**, *330*, 187-195.

92. Meador, M. A. B.; Malow, E. J.; Silva, R.; Wright, S.; Quade, D.; Vivod, S. L.; Guo, H.; Guo, J.; Cakmak, M. Mechanically Strong, Flexible Polyimide Aerogels Cross-Linked with Aromatic Triamine. *ACS Appl. Mater. Interfaces* **2012**, *4*, 536-544.

93. Bang, A.; Buback, C.; Sotiriou-Leventis, C.; Leventis, N. Flexible Aerogels from Hyperbranched Polyurethanes: Probing the Role of Molecular Rigidity with Poly(Urethane Acrylates) Versus Poly(Urethane Norbornenes). *Chem. Mater.* **2014**, *26*, 6979-6993.

94. Michal, B. T.; Brenn, W. A.; Nguyen, B. N.; McCorkle L. S.; Meador, M. A. B.; Rowan, S. J. Thermoresponsive Shape-Memory Aerogels from Thiol–Ene Networks. *Chem. Mater.* **2016**, *28*, 2341−2347.

95. Liu, C.; Qin, H.; Mather, P. T. Review of Progress in Shape-Memory Polymers. *J. Mater. Chem.* **2007**, 17, 1543–58.

96. Pekala, R. Organic Aerogels from The Polycondensation of Resorcinol with Formaldehyde. *J. Mater. Sci.* **1989**, *24*, 3221-3227.

97. (a) Li, W.-C.; Lu, A.-H.; Sch¨uth, F. Preparation of Monolithic Carbon Aerogels and Investigation of Their Pore Interconnectivity by a Nanocasting Pathway. *Chem. Mater.* **2005**, *17*, 3620–3626.

98. Ruben, G. C.; Pekala, R. W. High-resolution Transmission Electron Microscopy of The Nanostructure of Melamine-formaldehyde Aerogels. *J. Non- Cryst. Solids* **1995**, *186*, 219-231. (b) Li, W.; Guo, S. Preparation of Low-density Carbon Aerogels from a Cresol/formaldehyde mixture. *Carbon* **2000**, *38*, 1520- 1523. (c) Pekala, R. W.; Alviso, C. T.; Lu, X.; Gross, J.; Fricke, J. New Organic Aerogels Based Upon a Phenolic-furfural Reaction. *J. Non-Cryst. Solids* **1995**, *188*, 34-40.

99. Mayer, S. T.; Pekala R. W.; Kaschmitter, J. L. The Aerocapacitor: An Electrochemical Double-Layer Energy-Storage Device. *J. Electrochem. Soc.* **1993**, *140*, 446–451.

100. Al-Muhtaseb, S.; Ritter, J. Preparation and Properties of Resorcinol–Formaldehyde Organic and Carbon Gels. *Adv. Mater* **2003**, *15*, 101-114.

101. Mulik, S.; Sotirious-Leventis, C.; Leventis, N. Time-Efficient Acid-Catalyzed Synthesis of Resorcinol−Formaldehyde Aerogels. *Chem. Mater.* **2007**, *19*, 6138-6144.

102. Holly, F. W.; Cope, A. C. Condensation Products of Aldehydes and Ketones with O-Aminobenzyl Alcohol and O-Hydroxybenzylamine. *J. Am. Chem. Soc.* **1944**, *66*, 1875–1879.

103. Ishida, H.; Agag, T. *Handbook of Benzoxazine Resins*; Elsevier: Amsterdam, 2011, pp 355–362.

104. Ishida, H. Process for Preparation of Benzoxazine Compounds in Solventless Systems. U.S. Patent No. 5543516A, 1996.

105. Lorjai, P.; Chaisuwan, T.; Wongkasemjit, S. Porous Structure of Polybenzoxazine-Based Organic Aerogel Prepared by Sol–Gel Process and Their Carbon Aerogels *J. Sol-Gel Sci. Technol.* **2009**, *52*, 56-64.

106. Khanolkar, S. M.; Donthula, S.; Bang, A; Sotirious-Leventis, C.; Leventis, N. Polybenzoxazine Aerogels. 2. Interpenetrating Networks with Iron Oxide and the Carbothermal Synthesis of Highly Porous Monolithic Pure Iron(0) Aerogels as Energetic Materials. *Chem. Mater.* **2014**, *26*, 1318-1331.

107. Wang, Y. X.; Ishida, H. Cationic Ring-Opening Polymerization of Benzoxazines. *Polymer* **1999**, *40*, 4563–4570.

108. Agag, T.; Tsuchiya, H.; Takeichi, T. Novel Organic-Inorganic Hybrids Prepared from Polybenzoxazine and Titania Using Sol-Gel Process. *Polymer* **2004**, *45*, 7903–7910.

109. Sudo, A.; Hirayama, S.; Endo, T. Highly Efficient Catalysts-Acetylacetonato Complexes of Transition Metals in the 4th Period for Ring-Opening Polymerization of 1,3-Benzoxazine. *J. Polym. Sci. A Polym. Chem.* **2010**, *48*, 479–484.

110. Ran, Q.-C.; Gao, N.; Gu, Y. Thermal Stability of Polybenzoxazines with Lanthanum Chloride and Their Crosslinked Structures. *Polym. Degrad. Stab.* **2011**, *96*, 1610–1615.

111. (a) Ohnaga, T.; Chen, W.; Inoue, T. Structure Development by Reaction Induced Phase Separation in Polymer Mixtures: Computer Simulation of the Spinodal Decomposition under the Non-Isoquench Depth. *Polymer* **1994**, *35*, 3774–3781. (b) Kyu, T.; Lee, J.-H. Nucleation Initiated Spinodal Decomposition in a Polymerizing System. *Phys. Rev. Lett.* **1996**, *76*, 3746–3749. (c) Chan, P. K.; Rey, A. D. Polymerization-Induced Phase Separation. 1. Droplet Size Selection Mechanism. *Macromolecules* **1996**, *29*, 8934–8941. (d) Inoue, T. Reaction-Induced Phase Decomposition in Polymer Blends, *Prog. Polym. Sci.* **1995**, *20*, 119–153.

112. Huang, J.-M.; Kuo, S.-W.; Lee, Y.-J.; Chang, F.-C. Synthesis and Characterization of a Vinyl-Terminated Benzoxazine Monomer and its Blends with Poly(Ethylene Oxide). *J. Polym. Sci. B Polym. Phys.* **2007**, *45*, 644–653.

113. (a) Takeichi, T.; Kusakabe, Y. Performance Improvement of Polybenzoxazine by Alloying with Polyimide. *J. Net. Polym.* **2002**, *23*, 195–202. (b) Takeichi, T.; Guo, Y.; Rimdusit, S. Performance Improvement of Polybenzoxazine by Alloying with Polyimide: Effect of Preparation Method on the Properties. *Polymer* **2005**, *46*, 4909–4916. (c) Tiptipakorn, S.; Damrongsakkul, S.; Ando, S.; Hemvichian, K.; Rimdusit, S. Thermal Degradation Behaviors of Polybenzoxazine and Silicon-Containing Polyimide Blends. *Polym. Degrad. Stab*. **2007**, *92*, 1265–1278. (d) Zhao, P.; Liang, X.; Chen, J.; Ran, Q.; Gu, Y. Poly (Ether Imide)- Modified Benzoxazine Blends: Influences of Phase Separation and Hydrogen Bonding Interactions on the Curing Reaction. *J. Appl. Polym. Sci.* **2013**, *128*, 2865–2874.

114. (a) Ishida, H.; Lee, Y. H. Synergism Observed in Polybenzoxazine and Poly (e-Caprolactone) Blends by Dynamic Mechanical and Thermogravimetric Analysis. *Polymer* **2001**, *42*, 6971–6979. (b) Ishida, H.; Lee, Y.-H. Study of Hydrogen Bonding and Thermal Properties of Polybenzoxazine and Poly-(e-Caprolactone) Blends. *J. Polym. Sci. B Polym. Phys.* **2001**, *39*, 736–749. (c) Su, Y.-C.; Chen, W.-C.; Ou, K-I.; Chang, F.-C. Study of the Morphologies and Dielectric Constants of Nanoporous Materials Derived from Benzoxazine-Terminated Poly(e-Caprolactone)/Polybenzoxazine Copolymers. *Polymer* **2005**, *46*, 3758–3766. (d) Huang, J.-M.; Yang, S.-J. Studying the Miscibility and Thermal Behavior of Polybenzoxazine/Poly(e-Caprolactone) Blends Using DSC, DMA, and Solid State ^{13}CNMR Spectroscopy. *Polymer* **2005**, *46*, 8068–8078.

115. Liang, X.; Zhao, P.; Gu, Y. Morphology and Properties of Benzoxazine/ Poly(Ether Sulfone) System. *Polym. Mater. Sci. Eng.* **2012**, *28*, 109–111.

116. Grishchuk, S.; Mbhele, Z.; Schmitt, S.; Karger-Kocsis, J. Structure, Thermal and Fracture Mechanical Properties of Benzoxazine-Modified Amine-Cured DGEBA Epoxy Resins. *Express Polym. Lett.* **2011**, *5*, 273–282.

117. (a) Takeichi, T.; Saito, Y.; Agag, T.; Muto, H.; Kawauchi, T. High Performance Polymer Alloys of Polybenzoxazine and Bismaleimide. *Polymer* **2008**, *49*, 1173–1179. (b) Kumar, K. S. S.; Nair, C. P. R.; Sadhana, R.; Ninan, K. R. Benzoxazine–Bismaleimide Blends: Curing and Thermal Properties. *Eur. Polym. J.* **2007**, *43*, 5084–5096.

118. (a) Li, X.; Gu, Y. The Co-Curing Process of a Benzoxazine-Cyanate System and Tthe Thermal Properties of the Copolymers. *Polym. Chem.* **2011**, *2*, 2778–2781. (b) Kumar, K. S. S.; Nair, C. P. R.; Ninan, K. R. Investigations on the Cure Chemistry and Polymer Properties of Benzoxazine–Cyanate Ester Blends. *Eur. Polym. J.* **2009**, *45*, 494–502. (c) Kimura, H.; Ohtsuka, K.; Matsumoto, A. Curing Reaction of Bisphenol-A Based Benzoxazine with Cyanate Ester Resin and the Properties of the Cured Thermosetting Resin. *Express Polym.Lett.* **2011**, *5*, 1113–1122.

119. Leventis, N.; Donthula, S. In *Advanced and Emerging Polybenzoxazine Science and Technology*; Ishida, H., Froimowicz, P. Eds.; Elsevier: Amsterdam, 2016; Chapter 34, pp 673-695.

120. Lorjai, P.; Wongkasemjit, S.; Chaisuwan, T.; Jamieson, A. M. Significant Enhancement of Thermal Stability in the Non-Oxidative Thermal Degradation of Bisphenol-A/Aniline Based Polybenzoxazine Aerogel. *Polym. Degrad. Stabil.* **2011**, *96*, 708-718.

121. Far, H. M.; Donthula, S.; Taghvaee, T.; Saeed, A. M.; Garr, Z.; Sotiriou-Leventis, C.; Leventis, N. Air-Oxidation of Phenolic Resin Aerogels: Backbone Reorganization, Formation of Ring-Fused Pyrylium Cations, and the Effect on Microporous Carbons with Enhanced Surface Areas. *RSC Adv.* **2017**, *7*, 51104–51120.

122. Ding, Y. Erlebacher, J. Nanoporous Metals with Controlled Multimodal Pore Size Distribution. *J. Am. Chem. Soc.* **2003**, *125*, 7772-7773.

123. Nath, O.; Stephen, A.; Rosler, J.; Vollertsen, F. *J. Mater. Process. Technol.* **2009**, *209*, 4739-4743.

124. Liao, C. L.; Chu, C. W.; Fung, K. Z.; Leu, I. C. Fabrication of Nanoporous Metal Electrode by Two-Step Replication Technique. *J. Alloys Compd.* **2007**, *441*, L1-L6.

125. Nyce, G. W.; Hayes, J. R.; Hamza, A. V.; Satcher, J. H. Synthesis and Characterization of Hierarchical Porous Gold Materials. *Chem. Mater.* **2007**, *19*, 344-346.

126. Brock, S.L.; Arachchige, I. U.; Mohanan, J. L. Porous Semiconductor Chalcogenide Aerogels. *Science* **2005**, *307*, 397-400.

127. Tappan, B. C.; Huynh, M. H.; Hiskey, M. A.; Chavez, D. E.; Luther, E. P.; Mang, J. T.; Son, S. F. Ultralow-Density Nanostructured Metal Foams: Combustion Synthesis, Morphology, and Composition. *J. Am. Chem. Soc.* **2006**, *128*, 6589-6594.

128. Jiang, P.; Cizeron, J.; Bertone, J. F.; Colvin, V. L. Preparation of Macroporous Metal Films from Colloidal Crystals. *J. Am. Chem. Soc.* **1999**, *121*, 7957-7958.

129. Yan, H.; Blanford, C. F.; Holland, B. T.; Parent, M.; Smyrl, W. H.; Stein, A. A Chemical Synthesis of Periodic Macroporous NiO and Metallic Ni. *Adv. Mater.* **1999**, *11*, 1003-1006.

130. Burpo, F.; Nagelli, E.; Morris, L.; McClure, J.; Ryu, M.; Palmer, J. Direct Solution-Based Reduction Synthesis of Au, Pd, And Pt Aerogels. *J. Mater. Res.* **2017**, *32*, 4153-4165.

131. Liu, W.; Herrmann, A. -K.; Bigall, N. C.; Rodriguez, P.; Wen, D.; Oezaslan, M.; Schmidt, T. J.; Gaponik, N.; Eychmüller, A. Noble Metal Aerogels—Synthesis, Characterization, and Application as Electrocatalysts. *Acc. Chem. Res.* **2015**, *48*, 154−162.

132. (a) Mohanan, J. L.; Brock, S. L. A New Addition to the Aerogel Community: Unsupported CdS Aerogels with Tunable Optical Properties. *J. Non-Cryst. Solids* **2004**, *350*, 1–8. (b) Mohanan, J. L.; Arachchige, I. U.; Brock, S. L. Porous Semiconductor Chalcogenide Aerogels. *Science* **2005**, *307*, 397-400. (c) Arachchige, I. U.; Brock, S. L. Sol−Gel Assembly of CdSe Nanoparticles to Form Porous Aerogel Networks. *J. Amer. Chem. Soc.* **2006** *128*, 7964-7971. (d) Gaponik, N.; Wolf, A.; Marx, R.; Lesnyak, V.; Schilling, K.; Eychmüller, A. Three-Dimensional Self-Assembly of Thiol-Capped CdTe Nanocrystals: Gels and Aerogels as Building Blocks for Nanotechnology. *Adv. Mater.* **2008**, *20*, 4257–4262.

133. Hitihami-Mudiyanselage, A.; Senevirathne, K.; Brock, S. L. Assembly of Phosphide Nanocrystals into Porous Networks: Formation of InP Gels and Aerogels. *ACS Nano* **2013**, *7*, 1163-1170.

134. (a) Oyama, S. T. Novel Catalysts for Advanced Hydroprocessing: Transition Metal Phosphides. *J. Catal.* **2003**, *216*, 343-352. (b) Li, K.; Wang, R.; Chen, J. Hydrodeoxygenation of Anisole over Silica-Supported Ni2P, MoP, and NiMoP Catalysts. *Energy Fuels* **2011**, *25*, 854-863. (c) Liu, P.; Rodriguez, J. A.; Takahashi, Y.; Nakamura, K. Water–Gas-Shift Reaction on a Ni2P(001) Catalyst: Formation of Oxy-Phosphides and Highly Active Reaction Sites. *J. Catal.* **2009**, *262*, 294-303. (d) Popczun, E. J.; McKone, J. R.; Read, C. G.; Biacchi, A. J.; Wiltrout, A. M.; Lewis, N. S.; Schaak, R. E. Nanostructured Nickel Phosphide as an Electrocatalyst for the Hydrogen Evolution Reaction. *J. Amer. Chem. Soc.* **2013**, *135*, 9267-9270.

135. Tappan, B. C.; Steiner, S. A.; Luther, E. P. Nanoporous Metal Foams. *Angew. Chem. Int. Ed.* **2010**, *49*, 4544-4565.

136. Kumar, T. N.; Sivabalan, S.; Chandrasekaran, N.; Phani, K. L. Synergism Between Polyurethane and Polydopamine in the Synthesis of Ni–Fe Alloy Monoliths. *Chem. Commun.* **2015**, *51*, 1922-1925.

137. Chandrasekaran, N.; and Muthusamy, S. Binderless, Free-Standing Porous Interconnects of Ni–Fe Alloy Decorated Reduced Graphene Oxide for Oxygen Evolution Reaction. *Langmuir* **2017**, *33*, 2−10.

138. Liu, Y.; Gorgutsa, S.; Santato, C.; Skorobogatiy, M. Flexible, Solid Electrolyte-Based Lithium Battery Composed of $LiFePO_4$ Cathode and $Li_4Ti_5O_{12}$ Anode for Applications in Smart Textiles. *J. Electrochem. Soc.* **2012**, *159*, A349-A356.

139. Khang, D. Y.; Jiang, H.; Huang, Y.; Rogers, J. A. A Stretchable Form of Single-Crystal Silicon for High-Performance Electronics on Rubber Substrates. *Science* **2006**, *311*, 208-212.

140. (a) Leventis, N.; Chandrasekaran, N.; Sadekar, A. G.; Sotiriou-Leventis, C.; Lu, H. One-Pot Synthesis of Interpenetrating Inorganic/Organic Networks of CuO/Resorcinol-Formaldehyde Aerogels: Nanostructured Energetic Materials. *J. Am. Chem. Soc.* **2009**, *131*, 4576-4577. (b) Leventis, N.; Chandrasekaran, N.; Sotiriou-Leventis, C.; Mumtaz, A. Smelting in the Age of Nano: Iron Aerogels. *J. Mater. Chem.* **2009**, *19*, 63-65.

141. Guidotti, R. A.; Masset, P. Thermally activated ("thermal") battery technology Part I: An overview. *J. Power Sources* **2006**, *161*, 1443−1449.

VITA

Suraj Donthula, a native of India, received his 5-year Integrated Master of Science degree in Chemistry from Indian Institute of Technology (Indian School of Mines) (IIT-ISM), Dhanbad, India in 2012. In the summer of 2011, he worked as a research assistant at University of Minnesota, Minneapolis, MN, USA under Prof. Wayland E. Noland. He came to Missouri University of Science and Technology to pursue his Ph.D. degree in chemistry in the fall of 2012. He joined the Prof. Nicholas Leventis group and his research work focused on polymeric and metal aerogels for energy storage applications. During the course of his Ph.D., he coauthored eleven (11) journal articles, submitted one (1) article for publishing, and has contributed to 29 national and regional ACS meetings. He received the Chemistry Department's Outstanding Teaching Assistant Award in 2014, the outstanding Graduate Researcher Award in 2017, and the ACS Midwest Regional Meeting Graduate Student Award in 2017. In May 2018, he received his PhD in Chemistry from Missouri University of Science & Technology.